

# Cosmic Gold Mining: Hunting for the Astrophysical Sites of $r$ -Process Nucleosynthesis

Thesis by  
Shreya Anand

In Partial Fulfillment of the Requirements for the  
Degree of  
Doctor of Philosophy

The logo for the California Institute of Technology (Caltech), featuring the word "Caltech" in a bold, orange, sans-serif font.

CALIFORNIA INSTITUTE OF TECHNOLOGY  
Pasadena, California

2024  
Defended May 24, 2024

© 2024

Shreya Anand

ORCID: 0000-0003-3768-7515

All rights reserved

## ACKNOWLEDGEMENTS

I would like to recognize and express my gratitude towards the following people, who have contributed towards making my academic journey through a PhD at Caltech fruitful and fulfilling:

First and foremost, Mansi. Little did I know that there was no turning back once I decided to cross the street to come to Cahill, and I have you to thank for that. You have given me the courage to ask bold questions and address them head-on, and deepened my appreciation for the uncharted discovery space in the transient world. I have learned from you to always “leave no stone unturned” and to pull the trigger when a high-risk, high-reward transient presents itself.

Alan, for always being a genuinely positive and supportive presence throughout my PhD. Thanks for helping me stay connected with the LIGO Lab, which has been an enriching experience that I have learned so much from. I am ever grateful for the amount of care and effort you put towards the LIGO SURF program; my experience as a LIGO SURF truly jumpstarted my career at Caltech!

Thanks to my thesis committee, Jim, Alan, Katerina, and Dimitri, for your useful suggestions to improve my thesis work.

Important characters from my life pre-Caltech: Doc, Leo, Cole, Brad, Alex U., and Sukanta, without whom I would not have made it to the PhD program at Caltech. Thanks to Alex U. for giving me the opportunity to work on my first PhD project with you at the LIGO Livingston detector site.

The Palomar staff: Joel, Carolyn, Kajsa, Paul, Isaac, Diana, Kathleen, and others for supporting me during many nights of WIRC, TSPEC, and DBSP observations. Thanks to the Palomar kitchen staff for the fantastic multi-course dinners and night lunches, and especially Alex M. for many enlightening discussions on spirituality and sadhana.

The Keck staff: Greg, Josh, Percy, Sherry, Michael, Heather, Julie, Rita, and others for your help during many nights of observing on LRIS and NIRES, and especially during high-risk, high-reward ToO operations.

My mentors, with whom I was lucky to overlap with at Caltech: Michael and Igor. Michael, for exposing me to many academic “life-skills”, including grant-writing, student recommendation letters, paper refereeing, proposals, and undergraduate

mentoring. Thank you for cheering me on, providing timely advice, and introducing me to Jill the squirrel :) Thank you Igor, for being someone I know I can always confide in with any problem, and for helping me to network meaningfully at many conferences. Your trailblazing work has been a great inspiration to me during my PhD.

Shri, for hosting me at many gatherings at your house and for all of the valuable life and career advice.

The amazing TDA community, past and present: Jacob, Kaew, Kishalay, Yuhan, Yashvi, Viraj, Kaustav, Nicholas, and Sam; Lin and Christoffer; Matt, Robert, Tomás, Yu-jing, Theo, Andy, Aishwarya, Gokul and others. I have learned so much from you, and you have made my experience in the TDA group so much more fulfilling.

Kishalay, thanks for your incredible patience in teaching me many observational techniques and checking in on me during countless observing runs. Viraj, I've thoroughly enjoyed having you as an academic peer, friend, and recently office-mate at Caltech. To Tomás, my academic partner-in-crime, I have so many wonderful memories working with you throughout my PhD, through the challenges of the pandemic, during observing campaigns in the middle of the night, and sitting in the little nook outside my office. I am definitely NOT going to miss you roasting me every day in the hallway ;) Robert, thanks for bringing a shared sense of community to the group after the pandemic. I fondly remember watching Christmas movies and tending the fireplace during our snowed-out December observing run at Palomar. Nicholas, it was great being paired with you for Physics peer mentoring.

The LIGO Data analysis group, for several enlightening discussions during group meeting and for broadening my understanding of GW data analysis.

Thanks to many others who have been key collaborators or provided me with mentorship, including: Jenni, Mattia, Tim, David, Varun, and Jesper. Thanks also to the broader GROWTH collaboration and ZTF MMA community that have played an integral role in my PhD. Special thanks to Ivona for handling all our ZTF-related logistics and doing fantastic public outreach efforts.

Former undergraduate summer students that I have mentored and co-mentored: Mouza, Olivia, Priya, Nick, Faith, and Marianna. Thanks to you, I have become a better research mentor and look forward to mentoring new students each year.

The wonderful GWiPMA community for serving as an inspiration to improve the

climate in physics and astronomy. Thanks to Dave, Marcia, Nam, Mika, and Freddy for giving me the incredible opportunity to serve on the FUTURE organizing committee. Thanks to the FUTURE cohorts of 2020 and 2021 that made FUTURE one of the most memorable experiences I had at Caltech. Thanks also to the CCID staff for hosting fantastic workshops and bonding spaces.

Gita, and Judy, for making the logistics of my PhD go as smoothly as possible. Anu, Patrick, Carl, and James, for helping me resolve many technical issues I encountered with the astro machines.

My former housemates, Yashvi and Jean, for in-the-stairwell impromptu astro discussions, all the tea (quite literally!), and for all the excellent food. My former housemates, Merri and Pippin (Yashvi's cats), for luring me away from my computer to play with them every so often.

Kunal pr., Yamini Akka, and kids for the weekly sangha program I always looked forward to, and for so much delicious home-cooked food (especially when I was sick with covid!). Thanks to the other members of the wonderful PoY community: Akshay, Raju, Guru, Pranav, Saransh, Ashesha, Ben-Ben, and Karla.

Many other friends I have been fortunate to meet during my time at Caltech, including: Neeraja, Xenia, Nitika M., Nitika Y., Apurva, Nabha, Nivedita, Renée, and Katie. Thanks to my dear friend, Dr. Jacob Bringewatt, who has been there for me throughout, and with whom I have often shared many of my experiences during these past six years.

Last, but not least, I am immensely grateful to my family. My parents, Amma and Appa, who have wholly supported my choice of a very unconventional career in astronomy from the start, and who have helped me achieve my dream of being an astronomer. Divya and Gita, for listening to my astronomy-related ramblings and constantly giving me something to laugh about. GM, for saving newspaper clippings of astronomy articles to discuss with me during the next phone call. My extended family for cheering me on, and especially to Vidya Chiti and Atif Chitappa for advice on navigating a career in STEM and academia. My new set of parents, Amma and Anna, for supporting and encouraging me in all of my career pursuits. Paatti, for sharing many good recipes, and for your care and affection during the final phases of my thesis-writing. Finally, my best friend and binary companion, Dr. Navin Sridhar, without whom I truly could not have made it through my PhD (and these past six years) successfully, and our growing baby, who has been a source

of great joy during these final stages of pregnancy and PhD.

## ABSTRACT

One of the major open questions in astronomy is where the heaviest elements in the Universe are formed. These elements, generated via the rapid neutron-capture process ( $r$ -process), require environments abundant with free neutrons, present only in extreme cosmic explosions, which are by nature inherently rare. To date, vivid, direct evidence of heavy element nucleosynthesis has been seen and most extensively studied in the binary neutron star (BNS) merger GW170817. However, neutron star–black hole (NSBH) mergers, some collapsing massive stars (collapsars), and other explosions have also been proposed as alternative sites of  $r$ -process production. This thesis explores BNS mergers, NSBH mergers, and collapsars as  $r$ -process sites through observational studies. In this work, we first investigate whether  $r$ -process signatures are present in the light curves of broadlined type Ic supernovae (SNe Ic-BL) associated with long-duration gamma-ray bursts. For this study, we conduct optical imaging with the Zwicky Transient Facility (ZTF) and near-infrared imaging with the Wide-Field Infrared Camera on the Palomar 200-in Hale telescope of ZTF-discovered SNe Ic-BL. Second, we study the chemical distribution of ejecta in the kilonova (KN)—an optical/near-infrared transient powered by the radioactive decay of  $r$ -process elements—counterpart to GW170817, using new state-of-the-art KN models and incorporating precise inclination information on GW170817 into our inference. Third, we describe systematic searches conducted with ZTF for KNe associated with both BNS and NSBH mergers detected by the LIGO Virgo KAGRA detector network during its third and fourth observing runs. Based on our non-detections, we place constraints on the properties of KNe from both BNS and NSBH merger sites. Finally, we summarize the unique insights we have gained on the nature of  $r$ -process sites from observations and non-detections. We also discuss prospects for discovering and characterizing these transients with upcoming surveys such as the Vera C. Rubin Observatory and the Nancy Grace Roman Space Telescope.

PUBLISHED CONTENT AND CONTRIBUTIONS IN THIS  
THESIS

Ahumada, T. & Anand, S., Coughlin, M. W., Gupta, V., et al. 2024, Searching for gravitational wave optical counterparts with the Zwicky Transient Facility: summary of O4a, arXiv e-prints, arXiv:2405.12403, . S. A. conducted observations with ZTF, performed candidate vetting and follow-up, simulated KNe with sim-survey and calculated luminosity function constraints, and wrote the manuscript along with T. Ahumada. Submitted to PASP. <https://arxiv.org/abs/2405.12403>

Anand, S., Pang, P. T. H., Bulla, M., et al. 2023, Chemical Distribution of the Dynamical Ejecta in the Neutron Star Merger GW170817, arXiv e-prints, arXiv:2307.11080, . S. A. trained the surrogate kilonova models, performed light curve fitting along with P. T. H. Pang, and wrote the manuscript along with other co-authors. Under review in MNRAS. <https://arxiv.org/abs/2307.11080>

Anand, S., Barnes, J., Yang, S., et al. 2024, Collapsars as Sites of r-process Nucleosynthesis: Systematic Photometric Near-infrared Follow-up of Type Ic-BL Supernovae, *The Astrophysical Journal*, 962, 68, . S. A. participated in the conception of the project, performed observations, reduced data, analyzed the light curves and fit models to the data, and wrote most of the manuscript. Published in *ApJ*. <https://doi.org/10.3847/1538-4357/ad11df>

Anand, S. & Coughlin, M.W., Kasliwal, M. M., Bulla, M., Ahumada, T., et al. 2021, Optical follow-up of the neutron star–black hole mergers S200105ae and S200115j, *Nature Astronomy*, 5, 46, . S. A. conducted observations with ZTF, vetted candidates and performed follow-up, and wrote the manuscript along with M. C. Coughlin. Published in *Nature Astronomy*. <https://doi.org/10.1038/s41550-020-1183-3>

## OTHER RELEVANT PUBLISHED CONTENT OUTSIDE OF THIS THESIS

- Ahumada, T., Singer, L. P., Anand, S., et al. 2021, Discovery and confirmation of the shortest gamma-ray burst from a collapsar, *Nature Astronomy*, 5, 917, . S. A. participated in the real-time follow-up of the GRB with ZTF, helped obtain follow-up observations of the GRB afterglow, and participated in writing the manuscript. <https://doi.org/10.1038/s41550-021-01428-7>
- Ahumada, T., Anand, S., Coughlin, M. W., et al. 2022, In Search of Short Gamma-Ray Burst Optical Counterparts with the Zwicky Transient Facility, *The Astrophysical Journal*, 932, 40., . S. A. triggered ZTF, vetted counterpart candidates, and performed follow-up observations with various telescopes. <https://doi.org/10.3847/1538-4357/ac6c29>
- Almualla, M., Anand, S., Coughlin, M. W., et al. 2021, Optimizing serendipitous detections of kilonovae: cadence and filter selection, *Monthly Notices of the RAS*, 504, 2822, . S. A. co-mentored the lead author (Mouza) on this project, and participated in writing and editing the manuscript. <https://doi.org/10.1093/mnras/stab1090>
- Andreoni, I., Goldstein, D. A., Anand, S., et al. 2019, GROWTH on S190510g: DECam Observation Planning and Follow-up of a Distant Binary Neutron Star Merger Candidate, *The Astrophysical Journal, Letters*, 881, L16, . S. A. aided in planning the DECam follow-up of the GW event, vetted DECam candidates, and participated in writing the manuscript. <https://doi.org/10.3847/2041-8213/ab3399>
- Corsi, A., Ho, A. Y. Q., Cenko, S. B., et al. 2023, A Search for Relativistic Ejecta in a Sample of ZTF Broad-lined Type Ic Supernovae, *The Astrophysical Journal*, 953, 179, . S. A. analyzed the optical spectra of SNe Ic-BL in the sample and performed photospheric velocity measurements for each of the SNe. <https://dx.doi.org/10.3847/1538-4357/acd3f2>
- Coughlin, M. W., Ahumada, T., Anand, S., et al. 2019, GROWTH on S190425z: Searching Thousands of Square Degrees to Identify an Optical or Infrared Counterpart to a Binary Neutron Star Merger with the Zwicky Transient Facility and Palomar Gattini-IR, *The Astrophysical Journal, Letters*, 885, L19, . S. A. aided in planning ZTF observations, vetting candidates, performing follow-up observations, and writing the manuscript. <https://doi.org/10.3847/1538-4357/ac3981>
- Kasliwal, M. M., Anand, S., Ahumada, T., et al. 2020, Kilonova Luminosity Function Constraints Based on Zwicky Transient Facility Searches for 13 Neutron Star Merger Triggers during O3, *The Astrophysical Journal*, 905, 145, . S.

A. triggered ZTF, performed candidate vetting, compiled the candidate tables, performed the `simsurvey` analysis, and participated in editing the manuscript. <https://doi.org/10.3847/1538-4357/abc335>

Mohite, S. R., Rajkumar, P., Anand, S., et al. 2022, Inferring Kilonova Population Properties with a Hierarchical Bayesian Framework. I. Nondetection Methodology and Single-event Analyses, *The Astrophysical Journal*, 925, 58, . S. A. performed the `simsurvey` analysis for this paper, mentored the second author (Priya) on her contribution to the astrophysical priors section, and participated in writing and editing the manuscript. <https://dx.doi.org/10.3847/1538-4357/ac3981>

Rana, J., Anand, S., & Bose, S. 2019, Optimal Search Strategy for Finding Transients in Large-sky Error Regions under Realistic Constraints, *The Astrophysical Journal*, 876, 104, . S. A. wrote the slew optimization algorithm, generated plans for simulated skymaps, and participated in writing the manuscript. <https://doi.org/10.3847/1538-4357/ab165a>

## TABLE OF CONTENTS

Acknowledgements . . . . .	iii
Abstract . . . . .	vii
Published Content and Contributions in this Thesis . . . . .	viii
Other Relevant Published Content Outside of this Thesis . . . . .	ix
Table of Contents . . . . .	x
List of Illustrations . . . . .	xiii
List of Tables . . . . .	xxvi
Chapter I: Introduction . . . . .	1
1.1 Evidence Indicates that $r$ -Process Sites Must Be Rare and Prolific . . . . .	5
1.2 $r$ -Process from Collapsars . . . . .	7
1.3 $r$ -Process from Binary Neutron Star Mergers . . . . .	8
1.4 $r$ -Process from Neutron Star– Black Hole Mergers . . . . .	10
1.5 Thesis Outline . . . . .	11
Chapter II: $r$ -Process from Collapsars . . . . .	13
Abstract . . . . .	14
2.1 Introduction . . . . .	15
2.2 Sample Selection . . . . .	19
2.3 Observations . . . . .	20
2.4 Description of ZTF Candidates . . . . .	25
2.5 Literature sample . . . . .	33
2.6 Collapsar Light Curve Models . . . . .	35
2.7 Analysis . . . . .	37
2.8 Results of Light Curve Model Fitting . . . . .	42
2.9 Discussion and Outlook . . . . .	60
Chapter III: $r$ -Process from GW170817 . . . . .	71
Abstract . . . . .	72
3.1 Introduction . . . . .	73
3.2 Methodology . . . . .	75
3.3 Parameter Inference . . . . .	78
3.4 Summary . . . . .	78
3.5 Appendix . . . . .	80
Chapter IV: $r$ -Process from Neutron Star-Black Hole Mergers . . . . .	85
Abstract . . . . .	86
4.1 Methods . . . . .	99
4.2 Extended Data . . . . .	107
4.3 Supplementary Information . . . . .	115
Chapter V: $r$ -Process from IGWN-Detected Neutron Star Mergers . . . . .	132
Abstract . . . . .	133
5.1 Introduction . . . . .	134

5.2 Zwicky Transient Facility Follow-up . . . . .	136
5.3 Analysis Pipelines . . . . .	139
5.4 Summary of ZTF Triggers . . . . .	147
5.5 Discussion . . . . .	152
5.6 Conclusion . . . . .	158
5.7 Acknowledgements . . . . .	162
5.8 Appendix . . . . .	163
Chapter VI: Lessons Learned and Future Outlook . . . . .	180
6.1 Collapsars . . . . .	180
6.2 Neutron Star Mergers . . . . .	182
Bibliography . . . . .	190

## LIST OF ILLUSTRATIONS

<i>Number</i>	<i>Page</i>
1.1 Periodic table color-coded by astrophysical origin. Origin of the Elements in the Solar System by Jennifer Johnson is licensed under a Creative Commons Attribution-ShareAlike 4.0 International License.	2
1.2 A diagram of neutron captures and beta decays in the <i>s</i> -process from Ag to Sb by Rursus Siderespector. This file is licensed under the Creative Commons Attribution-Share Alike 3.0 Unported license. . . .	3
1.3 A diagram of neutron captures and beta decay in the <i>r</i> -process. Image credit: Lawrence Livermore National Laboratory (July 2014) published here. . . . .	3
1.4 The solar <i>r</i> -process abundance pattern, showing first peak, second peak, lanthanides peak, and third peak elements. Modified from (Hotokezaka et al., 2018; Kasliwal et al., 2017a). . . . .	4
2.1 Classification spectra for the SNe Ic-BL in our sample, along with their SNID best-match templates, labeled by name, supernova phase relative to the peak light, and corresponding template name, and template phase from SNID. GRB190829A only has a host spectrum, which we do not display here. The spectra for SN 2018gep and SN 2020bvc are published in Ho et al. (2019) and Ho et al. (2020a) so we do not show them here. The spectra show broad Fe II, Si II and O I lines. The Na I D absorption line, an indicator of host extinction (Stritzinger et al., 2018a), is plotted for reference. None of the SNe appear to have strong Na I D features. . . . .	21
2.2 SN velocities measured from the Fe II 5169Å line as a function of the spectroscopic phase for each supernova in our sample (black points) plotted along with the measured velocities of SNe Ic-BL from the literature and from PTF (Taddia et al., 2018). The velocities we measure here are broadly consistent with both the literature and PTF sample. . . . .	39

- 2.3  $r - J$ ,  $r - H$ , and  $r - K_s$  color evolution plots for the  $r$ -process enriched models for a representative set of model parameters, compared to color measurements for the SNe in our sample. Each model is shown in a separate linestyle: “solid”:  $M_{\text{ej}} = 7.93M_{\odot}$ ,  $\beta_{\text{ej}} = 0.25c$ ,  $M_{56} = 0.85M_{\odot}$ , “dotted”:  $M_{\text{ej}} = 2.62M_{\odot}$ ,  $\beta_{\text{ej}} = 0.038c$ ,  $M_{56} = 0.39M_{\odot}$ , and “dashed”:  $M_{\text{ej}} = 1.00M_{\odot}$ ,  $\beta_{\text{ej}} = 0.033c$ ,  $M_{56} = 0.07M_{\odot}$ . When possible, the  $r - X$  color of observed SNe was estimated using either concurrent  $r$ -band photometry or the closest optical photometry within 3 days of a given NIR datapoint (filled markers). Otherwise, the  $r$ -band magnitude is extrapolated from a stretched and scaled light curve of SN 2020bvc (unfilled markers). Left: Fixing the mixing fraction to a moderate value of 0.3, we vary  $r$ -process ejecta masses [0.01, 0.03, 0.08, 0.13]  $M_{\odot}$ . Right: Fixing the  $r$ -process mass to a conservative value of 0.01  $M_{\odot}$ , we vary the mixing coordinate from 0.1 to 0.9. In general, the objects in our sample appear to have bluer colors relative to the models (with the exception of SN 2007I). . . . . 41
- 2.4 Corner plots showing the posterior probability distributions for each of the parameters in the  $r$ -process enriched models for the subset of objects satisfying our  $\chi^2$  cut, ordered by the amount of  $r$ -process mass inferred. The posterior probability plots are more well constrained for the objects with low inferred  $M_{\text{rp}}$ ; in the remaining cases, the posterior distributions are poorly constrained.  $M_{\text{ej}}$  and  $\beta_{\text{ej}}$  inferred here are generally in agreement with HAFET, but discrepancies exist in the amount of nickel mass inferred. . . . . 49
- 2.5 Plots of light curve models from Barnes & Metzger (2022) with best fit parameters (red dotted line) and corresponding  $1\sigma$  uncertainties (black) with photometric data overplotted, for both ZTF candidates and candidates from the literature shown in Figure 2.4 which pass our  $\chi^2$  cut, ordered by inferred  $M_{\text{rp}}$ . The objects whose optical and NIR photometry are both well described by the models are consistent with  $M_{\text{rp}} \lesssim 0.01M_{\odot}$ . The remaining objects do not show convincing fits to the  $r$ -process enriched models. . . . . 54

- 2.6 Color evolution as a function of time for both SN 2007ce (top) and SN 2007I (bottom). Similar to Figure 2.3, the filled circles with errorbars represent the  $r - J/H/K_s$  color estimated directly from the data, while the unfilled circles correspond to a stretched and scaled  $r$ -band model of SN 2020bvc used as a proxy to estimate the color at each NIR photometric epoch, in the absence of  $r$ -band photometry. The dashed line represents the color evolution of the best fit  $r$ -process enriched model, and the shaded regions encompass the  $\pm 1\sigma$  uncertainty on the model parameters from our fits. Using the same convention as in Figure 2.3, magenta is  $r - J$ , brown is  $r - H$  and cyan is  $r - K_s$ . As shown here, the color evolution of both SN 2007I and SN 2007ce appear to be inconsistent with their best fitting  $r$ -process enriched model colors and associated  $1\sigma$  uncertainties. . . . . 56
- 2.7 Light curve fits to the literature supernova events from HAFFET. The dashed cyan line is the best fit bolometric light curve, while the remaining dashed lines show the fits to each of the broadband light curves. Broadband light curves are calculated by fitting bolometric corrections in each band, and using these corrections to rescale the Arnett fitted bolometric light curves. The circles are the photometry for each object in  $griJHK_s$  bands. In the bolometric light curve plot, the points correspond to bolometric luminosity estimated from both  $g$ - and  $r$ - bands, or from a single band, and using GPR to estimate the flux in the other band. For SNe with photometry in the Johnson filter system, we convert the photometry to SDSS assuming photometric conversions from Jordi et al. (2006). We find that the HAFFET models are good fits to the photometric data from our sample. . . . . 57
- 2.8 Light curve fits to ZTF SNe from HAFFET, similar to Figure 2.7. . . . . 59
- 3.1 Schematic diagram of the ejecta distribution for AT2017gfo as inferred from the BU2023YE grid. The two distinct regions of the dynamical ejecta are represented in blue, corresponding to the lanthanide-poor, squeezed polar dynamical ejecta, and the red, representing the lanthanide-rich, equatorial tidal component. The disk wind ejecta is represented by the light grey annulus in the center. The solid lines show the boundary between the lanthanide-rich and lanthanide-poor regions of the dynamical ejecta. . . . . 74

3.2	Contribution to the total bolometric light curve (black) of the squeezed-polar dynamical ( $Y_e \geq 0.25$ , blue), tidal-equatorial dynamical ( $Y_e < 0.25$ , red) and wind (grey) ejecta components. Light curves have been computed with a dedicated POSSIS simulation with $N_{\text{ph}} = 10^7$ using the parameters described below and for an observer viewing angle of $\theta_{\text{obs}} = 18.6^\circ$ . . . . .	81
3.3	Parameter estimation for the BU2019LM model with (orange) and without (blue) the inclusion of the tight viewing angle prior. . . . .	82
3.4	Light curves comparison between the BU2019LM grid (orange) and the BU2023YE grid for different choices of the wind composition $Y_{e,\text{wind}}$ and for a viewing angle and the rest of the ejecta parameters fixed to the same values (see text). The BU2019LM should be compared to the BU2023YE light curve with $Y_{e,\text{wind}} = 0.25$ , which matches the lanthanide-intermediate composition assumed in the BU2019LM grid. . . . .	84
4.1	<b>Absolute magnitudes corresponding to ZTF pointings in the skymap.</b> We map the absolute magnitudes corresponding to the distance provided in the GW LALInference skymap, measured at the center of each field, and the deepest limiting magnitude in either $g$ - or $r$ -bands (computed as a median over the CCDs in a particular field) for S200105ae (a) and S200115j (b). We also show the 90% probability region contours to guide the eye. . . . .	93

4.2 **Spectra of all of the candidates ruled out spectroscopically during both campaigns.** In order to visualize all the spectra on the same figure, we have applied a vertical offset to the flux, and plotted each spectrum at mean signal-to-noise ratio. The vertical dashed lines correspond to common spectral absorption and emission features in SN spectra. (a) Spectra of five S200105ae candidates taken with the Optical System for Imaging and low Resolution Integrated Spectroscopy (OSIRIS) on the Gran Telescopio Canarias (GTC) of the Roque de los Muchachos Observatory in La Palma, Spain (Castro-Tirado et al., 2020; Valeev et al., 2020). The top three spectra were taken on Jan 11th, and the bottom two were taken on Jan 10th. From top to bottom, ZTF20aaertpj was classified as a SN Ib at  $z(s) = 0.026$ , ZTF20aaerqbx was classified as a SN IIP at  $z(s) = 0.098$ , ZTF20aaervyn was shown to be a SN Ia at  $z(s) = 0.112$ , ZTF20aaerxsd is a SN Ia at  $z(s) = 0.055$ , and ZTF20aaervoa was classified as a SN IIP at  $z(s) = 0.046$ . (b) Top: all spectra taken with the SED Machine (SEDM) on the Palomar 60-inch telescope (P60); from top to bottom, ZTF20aafanxk (S200105ae) was classified as a SN Ia at  $z(s) = 0.103$  on January 18th, the spectrum of ZTF20aafqulk (S200115j), observed on January 24th, indicates that it is likely stellar, and ZTF20aafujqk (S200105ae), also observed on January 18th, was classified as a SN Ia at  $z(s) = 0.074$ . (b) Bottom: The spectrum of ZTF20aaevbzl (S200105ae) taken by the Double Spectrograph (DBSP) on the Palomar 200-inch telescope (P200) obtained on January 18th, 2020, contains a  $H\alpha$  feature in a mostly featureless blue continuum that is indicative of it being a cataclysmic variable. . 94

- 4.3 **Detection efficiency of simulated KNe based on ZTF observations.** Ratio of recovered vs injected KNe (efficiency) identified in observations in a skymap for an analytic model varying absolute magnitude and change in magnitude per day for (a) S200105ae and (b) S200115j in both  $g$  and  $r$ -bands. Here, the magnitude corresponds to the peak absolute magnitude of the injected kilonovae for a linear model with a given rise or decay rate. The maximum of the colorbar scale is set to the maximum efficiency achieved (at  $M = -20$ ), which for S200105ae was 53% and 29% for S200115j. We include approximate peak absolute magnitudes and approximate rise rates for some common SNe types; for GW170817, we plot the absolute magnitude at detection and the approximate decline rate to guide the eye. . . . . 95
- 4.4 **Constraints on kilonova model parameters based on median limiting magnitudes.** We display all KN light curves ruled out by *median*  $5\text{-}\sigma$  limits on (a) S200105ae (ZTF), (b) S200115j (ZTF) and (c) S190814bv (DECam). For S200105ae and S200115j, median AB magnitudes are shown with filled triangles, while individual limits are shown with open triangles. Limits shown for S190814bv are median depth values from table 1 of Andreoni et al. (2020). KN light curves are calculated with POSSIS (Bulla, 2019); we show in blue when they are ruled out by the limits at three different distances (corresponding to median distances and  $\pm 1\sigma$  distance uncertainties from LIGO) and in grey otherwise. For each distance, the shaded area represents the range spanned by different models and different viewing angles (with the brighter end generally corresponding to higher masses and polar orientations while the fainter end to lower masses and equatorial orientations). The median limits for S200105ae do not constrain any kilonova models for any distance assumptions, while for S200115j they place constraints only on the models for nearby kilonovae (light blue). For S190814bv, median limits constrain kilonova models for all distance assumptions. . . . . 96

- 4.5 **Automatic preliminary filtering criteria for transient detection.** Here we show results for each step of the ZTF filtering scheme for three representative nights covering the events discussed in this paper. Each cell shows the number of candidates that successfully pass a particular filter. The number shown is the result of running a filtering step on the alerts that met previous requirements. We define as “Real” any alert with a real-bogus score greater than 0.25 and “not moving” the candidates that have more than two detections separated by at least 15 minutes. The highlighted numbers represent the amount of candidates that required further vetting, as described in Section 4.1. . . . . 108
- 4.6 **ZTF coverage and candidates discovered within skymap.** Top row: Coverage of S200105ae, showing the tiles on the 90% probability region of the initial BAYESTAR (a) and final LALInference (b) skymaps. The color intensity is proportional to the 2-D probability. The mapping of candidates to numbers is 1: ZTF20aaervoa, 2: ZTF20aaertpj, 3: ZTF20aaervyn, 4: ZTF20aaerqbx, 5: ZTF20aaerxsd, 6: ZTF20aaafduvt, 7: ZTF20aaevbzl, 8: ZTF20aaafndh, 9: ZTF20aaexpwt, 10: ZTF20aafaoki, 11: ZTF20aafukgx, 12: ZTF20aagijez, 13: ZTF20aafanxk, 14: ZTF20aafujqk, 15: ZTF20aagiiik, 16: ZTF20aafdxxkf, 17: ZTF20aagiipi, 18: ZTF20aagjemb, 19: ZTF20aafksha, 20: ZTF20aaertil, 21: ZTF20aafexle and 22: ZTF20aafefxe. Bottom row: Same for S200115j, with the BAYESTAR coverage shown in (c) and LALInference coverage shown in (d). The mapping of candidates to numbers is 1: ZTF20aagjqxg, 2: ZTF20aafqyyc, 3: ZTF20aahenrt, 4: ZTF20aafqpum, 5: ZTF20aafqulk, and 6: ZTF20aahakkp. We note that we include candidates up to and including within the 95% probability region, and therefore some are outside of the fields we plot here. . . . . 109

- 4.7 **Limiting magnitudes at each epoch of observations.**  $5\text{-}\sigma$  limiting magnitudes as a function of time for (a) S200105ae (ZTF), (b) S200115j (ZTF), and (c) S190814bv (DECam) with the left, middle, and right panels corresponding to observations on the first, second, and third nights for S200105ae and S190814bv and first, second, and fourth nights for S200115j. The red and green triangles correspond to the  $r$ - and  $g$ -band limits for ZTF, while the yellow and black triangles correspond to the  $i$ - and  $z$ -band limits for DECam; the open triangles correspond to serendipitous observations and closed ToO observations. The large differences in limiting magnitude from observation to observation are due to poor weather. . . . . 110
- 4.8 **Potential constraints on kilonova model parameters based on the deepest limiting magnitudes.** We display constraints on (a) S200105ae (ZTF), (b) S200115j (ZTF) and (c) S190814bv (DECam) for the models in the NSBH grid used here. *Top panels:* same as Figure 4.4 but using the deepest (filled triangles) rather than the median limits for each set of S200105ae and S200115j observations. The panel for S190814bv is the same as in Figure 4.4, with all limits corresponding to the median magnitudes. *Bottom panels:* regions of the  $M_{\text{ej,dyn}} - M_{\text{ej,pm}}$  parameter space that are ruled out at different distances and for different viewing angle ranges (moving from pole to equator from top to bottom panel). . . . . 111
- 4.9 **Broadband NSBH light curve models from POSSIS.** Light curves predicted with POSSIS (Bulla, 2019) for a NSBH model with  $M_{\text{dyn}} = 0.05M_{\odot}$  and  $M_{\text{pm}} = 0.05M_{\odot}$  as seen from a polar (a) and equatorial (b) viewing angle. . . . . 112
- 4.10 **Comparison of peak magnitudes between optical and near-IR bands for NSBH models.** We plot the difference in peak magnitudes between the (a)  $g$ -band and the near-IR  $i$ - and  $z$ -bands for the models in the NSBH grid used here. Similarly, in (b) we show the difference between  $r$ -band and the same near-IR bands. . . . . 112

- 4.11 **Potential constraints on the parameters of a NSBH binary associated with S200105ae.** Here we assume that  $M_{ej,dyn} \leq 0.02M_{\odot}$  and  $M_{ej,pm} \leq 0.04M_{\odot}$ , appropriate for the deepest observations of S200105ae in a face-on orientation. We show the maximum value of the aligned component of the BH spin as a function of the neutron star radius  $R_{NS}$  and the binary mass ratio  $Q = M_{BH}/M_{NS}$ . The two panels show results assuming that low (a) and high (b) fractions of the post-merger accretion disk are ejected (see text). Both plots assume  $M_{NS} = 1.35$ . Results for different neutron star masses can be estimated from this plot simply by considering a binary with the same  $Q, \chi$  and compaction  $M_{NS}/R_{NS}$ . . . . . 113
- 4.12 **Potential constraints on the parameters of a NSBH binary associated with S190814bv.** Here we assume that  $M_{ej,dyn} \leq 0.01M_{\odot}$  and  $M_{ej,pm} \leq 0.01M_{\odot}$ , as appropriate for S190814bv in a face-on orientation in a similar fashion to 4.11, with low (a) and high (b) fractions of disk ejecta. . . . . 113
- 4.13 **Minimum aligned component of the BH spin above which we cannot rule out the presence of a kilonova.** We cannot exclude this region of parameter space because either the resulting kilonova evolves too slowly, or the ejected mass is outside of the grid of models used in this study. In this plot, we consider the worse-case scenario of  $f_{rem} = 0.5$ . . . . . 114
- 4.14 **light curves for all objects ruled out photometrically.** In each panel, filled circles represent ZTF forced photometry and the photometry from the ZTF alert production pipeline, with error bars corresponding to  $1-\sigma$  uncertainties. Filled triangles display  $5-\sigma$  upper limits for non-detections. The  $r$ -,  $g$ -, and  $i$ -band data is presented in red, green and yellow respectively. . . . . 119

- 4.15 **Plot of the decay rate (mag/day) in  $g$ -band (a) and  $r$ -band (b) for all the ejecta masses and viewing angles of the modeled grid presented in Section 4.1.** Blue histograms are for time windows from 1 to 4 days after merger ( $\Delta t = 3$  days), orange from 1 to 6 days ( $\Delta t = 5$  days), green from 1 to 8 days ( $\Delta t = 7$  days). In general, 96 % of models show faster decay than 0.3 mags/day (dashed vertical line) in  $g$ -band, while 82 % of models show faster decay than 0.3 mags/day in  $r$ -band. The more slowly fading models are the higher mass ones. Particularly, our threshold was chosen based on the 7 days baseline, as all the candidates meet that requirement. . . . . 122
- 4.16 **ZTF  $r$ -band cutouts of the slow moving asteroid ZTF20aaegqfp.** The yellow circles show the position of the ZTF candidate in both cutouts. Panel (a) shows a cutout of the region one day before the trigger. There, it is possible to see a source to the right of ZTF20aaegqfp position, marked with a yellow circle. This source was located at 7.3'' from our candidate. Panel (b) shows the discovery image of our candidate ZTF20aaegqfp, which is located within the circle. The cutouts are 0.7 sq. arcmin and north and east are up and to the left respectively. . . . . 125
- 4.17 **light curves and  $r$ -band cutouts for a subset of the most well-sampled light curves for ZTF candidates that were ruled out photometrically.** Colors were used to represent the different bands: green, red and yellow for  $g$ -,  $r$ - and  $i$ - bands. The triangles in the light curve represent upper limits and filled circles are the detected magnitudes of the object. On each panel, the left cutout is the ZTF discovery image and the right one is the corresponding ZTF reference image. The transient is marked with a cross and the size of the cutouts is 0.7 sq. arcmin with north being up and east to the left. The candidates highlighted here are as follows: (a) ZTF20aaertil, (b) ZTF20aafksha, (c) ZTF20aagjemb, and (d) ZTF20aahenrt. . . . . 127
- 5.1 The Fritz page for a GW event displays information in tags located below the date of the event. In the Properties tab, it presents information originally available in the GCN. The page exhibits the most up-to-date information available, as well as the history of changes circulated through GCNs. . . . . 140

- 5.2 A snapshot illustrating the spatial and temporal constraints set on *Fritz* for transients selection. This feature is used to refine the candidate query, limiting it to a specific region (Cumulative Probability) on a skymap within a designated time-frame. . . . . 143
- 5.3 Snapshot of the GCN Analysis *Fritz* page. In this case, we display the sources within the 90% localization of the GW event S230627c passing the EM+GW filter in the corresponding GW skymap. . . . . 144
- 5.4 Snapshot of the GCN Analysis *Fritz* page showing the rejection criteria for candidates discovered within the 90% localization of S231029k. 145
- 5.5 Two examples of auto-generated GCN circular text for the GW event S230521k. Top: a summary of the actual ZTF observations conducted. Bottom: selected and rejected candidates within the GW localization. . . . . 148
- 5.6 Constraints on KN model parameters based on the ZTF limiting magnitudes on GW230529. Top panels. the  $g$  (left),  $r$  (middle) and  $i$  (right) band non-detections are shown together with NSBH KN models: the blue areas encompass light curves that are ruled out by the limits at three different distances (corresponding to median distances and  $\pm 1\sigma$  distance uncertainties from LIGO), while those in grey encompass light curves that are compatible with the limits. These NSBH-specific models are computed with POSSIS (Anand et al., 2020a; Bulla, 2019) and have three free parameters: the mass of the lanthanide-rich dynamical ejecta ( $M_{ej,dyn}$ ), the mass of the post-merger disk-wind ejecta ( $M_{ej,pm}$ ) and the viewing angle ( $\theta_{jobs}$ ). Bottom panels. Regions of the  $M_{ej,pm}$ - $M_{ej,dyn}$  parameter space that are ruled out at different distances and for different viewing angle ( $\theta_{jobs}$ ) ranges (from a face-on to a edge-on view of the system from left to right), assuming the KN fell within the ZTF footprint. . . . . 150
- 5.7 Localization of S230627c, overplotted with the ZTF coverage (black squares) and the 90% probability contour. We show the candidates associated to this event as white stars in the localization region. The rest of the skymaps can be found in the Appendix 5.8, in Figs. 5.12-5.18. . . . . 151

- 5.8 The `nimbus` results of the combined posterior probability for KN model parameters assuming the *Tophat* model using events followed up by ZTF only during O4a. The x-axis shows the initial absolute magnitude  $M_0$  of a model, while the y-axis shows its evolution rate  $\alpha$ . The color bar shows the posterior probability of each model, in the combined dataset, where yellow regions show the favored regions of parameter space given the non-detection of KNe from ZTF observations, and the bluer regions show less preferred combinations for initial  $M_0$  and  $\alpha$ . We also mark the position of the average  $r$ -band decay rate for a GW170817-like KN over its first 3 days of evolution. . . . . 153
- 5.9 Filtered kilonova efficiency with `simsurvey` for the *Tophat* model evolution. The filtering cuts we apply include a requirement of a minimum of two detections separated by 15 minutes at  $5\sigma$ . The color bar shows the fraction of sources detected after the filtering versus the number of sources ingested in the GW volume for the O3 and O4a combined set of skymaps. Similar to Figure 5.8, we mark the position of a GW170817-like KN on this plot. For this dataset, GW170817 has 36% of efficiency. . . . . 154
- 5.10 Kilonova luminosity function for events surviving O3, and high significance O4a events. We show in orange the models with flat evolution ( $\alpha = 0$ ), and in green the fading models ( $\alpha = 1 \text{ mag day}^{-1}$ ). The solid lines show the unfiltered results, while the dashed lines show the results after selecting sources consistent with the ZTF filtering criteria (i.e. two detections). The green dotted line weights models with fading evolution passing the filtering criteria by the event's terrestrial probability ( $t_i$ ). The black and blue lines show the fraction of Kasen and Bulla models whose peak magnitudes fall within a particular luminosity bin. . . . . 155
- 5.11 Spectra of the counterpart candidates taken during O4a. . . . . 165
- 5.12 Localization of the high-significance event S230529ay, overplotted with the ZTF tiles and the 90% probability contour. . . . . 166
- 5.13 Localization of the high-significance event S230731an, overplotted with the ZTF tiles and the 90% probability contour. We show the candidates discovered in the region as white stars. We note that even though we covered  $\sim 2500 \text{ deg}^2$ , the total enclosed probability is only 7%. . . . . 166

5.14	Localization of the high-significance event S231113bw, over plotted with the ZTF tiles and the 90% probability contour. No candidates were found in this region. . . . .	167
5.15	Localization of S230521k, overplotted with the ZTF tiles and the 90% probability contour. We show the candidates in the region as white stars. . . . .	167
5.16	Localization of S230528a, overplotted with the ZTF tiles and the 90% probability contour. We show the transients consistent with KNe candidates as white stars. . . . .	168
5.17	Localization of S230615az, overplotted with the ZTF tiles and the 90% probability contour. We show the candidates as white stars. . . . .	169
5.18	Localization of S231029k, overplotted with the ZTF tiles and the 90% probability contour. We show the candidates as white stars. . . . .	169
5.19	Light-curves for ZTF candidates found during O4a. These candidates correspond to the high-significant events S230529ay and S230627c. . . . .	177
5.20	Light-curves for ZTF candidates found during O4a. These candidates correspond to the events S230521k and S230528a. . . . .	178
5.21	These candidates correspond to the events S230521k, S230528a and S231029k. . . . .	179
6.1	Luminosity function from O4a, updated with the inclusion of S240422ed.	185
6.2	A schematic diagram showing the recommended observing strategy with filters and cadence for Rubin during GW ToO observations for both "gold" and "silver" events. Figure credit: Igor Andreoni. Published in the Rubin ToO 2024 workshop final report linked here. . . . .	188

## LIST OF TABLES

<i>Number</i>	<i>Page</i>
2.1	
<p>Sample summary table of Ic-BL supernova properties, estimated <math>r</math>-process ejecta mass and mixing fraction along with their <math>1\sigma</math> uncertainties, and first radio/X-ray detection. In the absence of any X-ray/radio detections we quote an upper limit; if the source was not observed we mark the cell with a dash. a) Flux density in <math>\mu\text{Jy}</math> with the VLA. We list only the first VLA observation at <math>\lesssim 50</math> days from the first ZTF detection as reported in Corsi et al. (2023). b) <i>Swift</i> XRT flux in units of <math>10^{-14}\text{erg cm}^{-2}\text{ s}^{-1}</math>, taken from Corsi et al. (2023). *This SN Ic-BL is also categorized as a fast blue optical transient (FBOT), and was published in Ho et al. (2019). The quoted radio detection with the VLA could be galaxy-dominated. **This Ic-BL had a double-peaked light curve from shock-cooling; X-ray and radio measurements taken from Ho et al. (2020a).</p>	
	66
2.2	
<p>Central wavelengths for the optical and NIR filters assumed during the analysis and fitting of our light curves.</p>	
	66
2.3	
<p>Explosion properties and inferred <math>r</math>-process ejecta masses and mixing fractions of low-redshift SNe with contemporaneous optical and NIR imaging from our literature search. Where available, we quote the <math>1\sigma</math> uncertainties on the parameters in brackets. For SN 1998bw and SN 2002ap, we quote the ranges of explosion parameters corresponding to the best fitting light curve models. *Clocchiatti et al. (2011) already corrected for host extinction; we use the assumed host extinction to correct only the NIR photometry. **For SN 2007I and SN 2007ce, as explosion properties were not estimated in the literature, we conduct light curve analysis to derive the best fit properties as described in Section 2.7.</p>	
	67
2.4	
<p>Table containing the explosion properties of all of the ZTF-discovered SNe in our sample that have not yet been published. Our methods for deriving the quantities given above are described in Section 2.7. The velocities shown here are measured at various different phases, so do not represent the photospheric velocity of the supernova at peak. We report effective temperatures from blackbody fits around <math>\sim 30</math> days post-peak for each of the objects that has one or more NIR detections.</p>	
	69

3.1	Parameter priors used for the Bayesian analyses. $\mathcal{U}(a, b)$ refers to an uniform prior in the interval $[a, b)$ . This table excludes the priors on the inclination angle, which we describe in Section 3.3. . . . . .	78
4.1	Follow-up table for all spectroscopically classified transients. Our spectra were obtained with GTC (Castro-Tirado et al., 2020; Valeev et al., 2020), ePESSTO (Schulze et al., 2020), P60+SEDM, and P200+DBSP. The spectroscopic redshifts are listed as well. The objects with a star (*) were first reported to TNS by ALerCE. Discovery magnitudes reported are extinction-corrected. . . . . .	131
4.2	Follow-up table of the candidates identified for S200105ae, reported in Ahumada et al. (2020b). The ZTF objects with a star (*) in the TNS column were first reported to TNS by ALerCE. The spectroscopic (s) or photometric (p) redshifts of the respective host galaxies are listed as well. As a reference, the all-sky averaged distance to the source is $283 \pm 74$ Mpc, corresponding to a redshift range $z = 0.045\text{--}0.077$ . We use the same rejection criteria described in more detail in section 4.1 here, as follows: slow photometric evolution (slow), hostless, stellar, and slow moving asteroid (asteroid). . . . . .	131
4.3	Follow-up table of the candidates identified for S200115j, reported in Anand et al. (2020b). As a reference, the all-sky averaged distance to the source is $340 \pm 79$ Mpc, corresponding to a redshift range $z = 0.056\text{--}0.089$ . . . . . .	131
5.1	Summary of ZTF observations and GW properties of the 5 GW events selected and analyzed in this paper. We required their FAR to be less than $1 \text{ year}^{-1}$ , and one of the following: $p_{BNS} > 0.1$ , $p_{NSBH} > 0.1$ , or $\text{HasNS} > 0.1$ . We quote other quantities intrinsic to the GW event, such as the mean distance to the merger, the <code>HasRemnant</code> , and the <code>HasMassGap</code> parameters. For each event we summarize the coverage, depth and latency for the ZTF observations. We include the events with $\text{FAR} > 1 \text{ year}^{-1}$ in Table 5.2 in the Appendix 5.8. To determine the areal coverage and the enclosed skymap probability observed by ZTF, we require at least two ZTF observations in a given region. . . . . .	149

5.2	Summary of ZTF observations and GW properties for 5 GW events additionally followed-up with ZTF, with $\text{FAR} > 1 \text{ year}^{-1}$ . Similarly to Table 5.1 we quote other quantities intrinsic to the GW event, such as the mean distance to the merger, the <code>HasRemnant</code> , and the <code>HasMassGap</code> parameters. . . . .	164
5.3	Properties of the candidates that passed manual inspection and their rejection criteria for six of the followed-up LVK events. There are 15 candidates from the follow-up of <i>High-significance</i> events ( $\text{FAR} < 1 \text{ year}^{-1}$ ), and 27 candidates for the <i>Other ZTF triggers</i> with $\text{FAR} > 1 \text{ year}^{-1}$ . .	170
5.4	Compilation of all the 150 IGWN events that had either a probability of BNS ( $p_{\text{BNS}}$ ) greater than 0.1 or their probability of NSBH ( $p_{\text{NSBH}}$ ) greater than 0.1. We divide the events into <i>High-significance</i> ( $\text{FAR} < 1 \text{ year}^{-1}$ ), <i>Other ZTF triggers</i> , and <i>Not followed with ZTF</i> . The events we did not follow-up with ZTF all have $\text{FAR} > 1 \text{ year}^{-1}$ , and were not used in the ZTF non-detection analysis. We additionally quote their FAR, their probability of BBH merger ( $p_{\text{BBH}}$ ), their terrestrial probability ( $p_{\text{Terrestrial}}$ ), and their publicly available properties <code>HasNS</code> , <code>HasRemnant</code> , and <code>HasMassGap</code> . . . . .	176

## *Chapter 1*

### INTRODUCTION

While the origin of the lighter elements in the periodic table is known, the origin of the heaviest elements in the periodic table is a subject of active investigation. Hydrogen, Helium, and a small quantity of Lithium were synthesized during Big Bang nucleosynthesis (Fields et al., 2020). Most Lithium, Beryllium and Boron are attributed to cosmic ray fission (Meneguzzi et al., 1971; Prantzos, 2012; Tatischeff & Gabici, 2018). Massive stars fuse elements up to Iron in their cores (Hoyle, 1954). Core-collapse supernovae (SNe) and Type Ia SNe contribute to elements up to an atomic mass number of 91 (Colgate & McKee, 1969; Hughes et al., 2000; Hughes & Singh, 1994; Rank et al., 1988). Most of the elements heavier than Iron are produced via the *s*-process and the *r*-process (Johnson et al., 2020) (see Figure 1.1). The slow neutron-capture process, or *s*-process, occurs when a heavy seed nucleus captures a neutron to form an unstable isotope of the same element, and then undergoes beta decay to create a stable isotope of a heavier element. Figure 1.2 shows a diagram of neutron capture and beta decay in the *s*-process as it occurs between Ag and Sb. The *s*-process occurs over timescales of  $10^3 - 10^6$  years, in asymptotic giant branch stars, terminating at Bismuth ( $A \sim 208$ ), the heaviest stable element in the periodic table (Käppeler et al., 2011). In contrast, the rapid neutron-capture process, or *r*-process, occurs over timescales of seconds. Seed nuclei of  $^{56}\text{Fe}$ -peak elements execute a series of neutron captures until they reach the nuclear drip line, or the boundary beyond which nuclei can no longer retain their neutrons (Thoennessen, 2004). In contrast to the *s*-process, *r*-process nuclei do not have time to beta-decay to stability between successive neutron captures (see Figure 1.3). Thus the *r*-process enables the formation of extremely heavy, neutron-rich isotopes, which then radioactively decay to form the heaviest elements in the periodic table (Johnson et al., 2020).

A prerequisite for the *r*-process is an environment with a high density of free neutrons. Namely, the viability of *r*-process production is determined by the electron fraction,  $Y_e$ , of the environment. The electron fraction is defined as follows (Metzger, 2019):

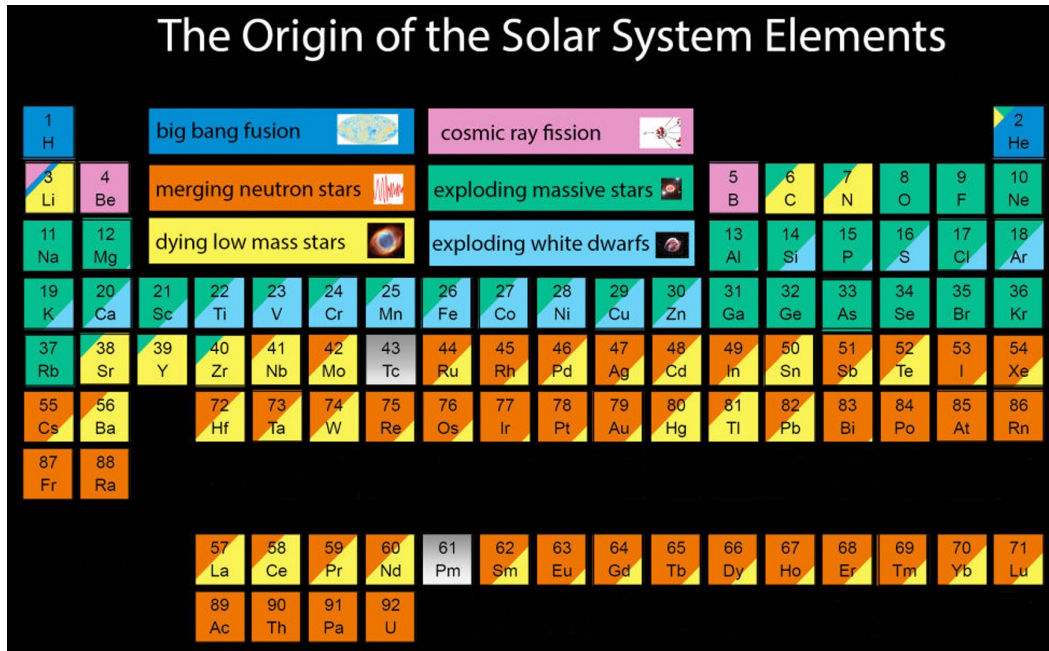


Figure 1.1: Periodic table color-coded by astrophysical origin. Origin of the Elements in the Solar System by Jennifer Johnson is licensed under a Creative Commons Attribution-ShareAlike 4.0 International License.

$$Y_e \equiv \frac{n_p}{n_p + n_n} \quad (1.1)$$

where  $n_p$  is the number of protons, and  $n_n$  is the number of neutrons, assuming charge-neutrality. Low values of  $Y_e$  correspond to high numbers of neutrons, which are required for the  $r$ -process to occur.

Another requirement for  $r$ -process sites is to be able to explain the heavy element abundances we observe in the Solar neighborhood. Studies (Cameron, 1957; Urey, 1952) have constructed an atomic abundance curve, primarily derived from solar, meteoritic, and terrestrial sources that exhibits distinct peaks, or overabundances, at particular atomic mass numbers, that point towards different astrophysical nucleosynthesis sites. The  $s$ - and  $r$ -processes contribute sets of twin peaks to the solar abundance pattern at high atomic mass numbers ( $A \gtrsim 80$ ), suggesting that these two distinct processes occur in independent astrophysical sites (Burbidge et al., 1957). Separating out the contribution of  $r$ -process alone yields the solar  $r$ -process abundance pattern. The solar  $r$ -process abundance pattern exhibits four main peaks (see Figure 1.4): 1) first peak ( $A \sim 80$ ; light  $r$ -process elements), 2) second peak

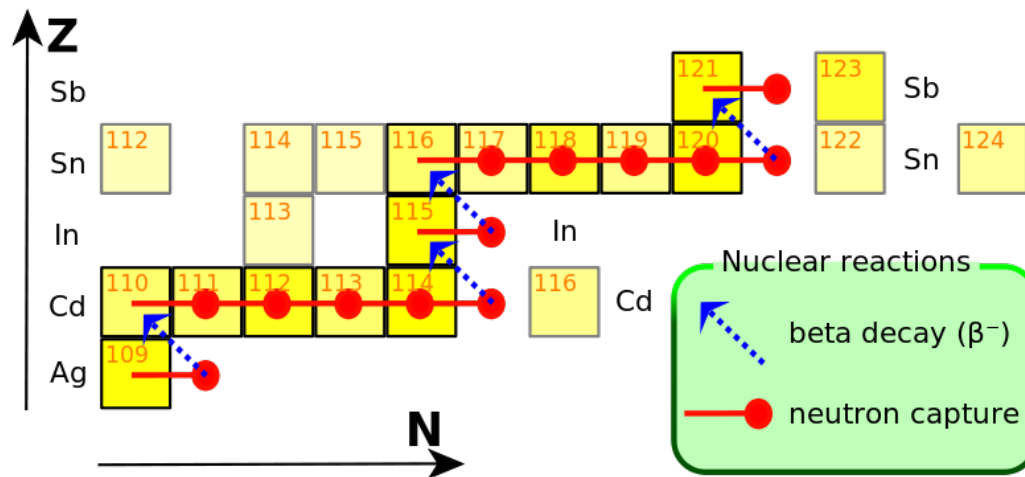


Figure 1.2: A diagram of neutron captures and beta decays in the *s*-process from Ag to Sb by Rursus Siderespector. This file is licensed under the Creative Commons Attribution-Share Alike 3.0 Unported license.

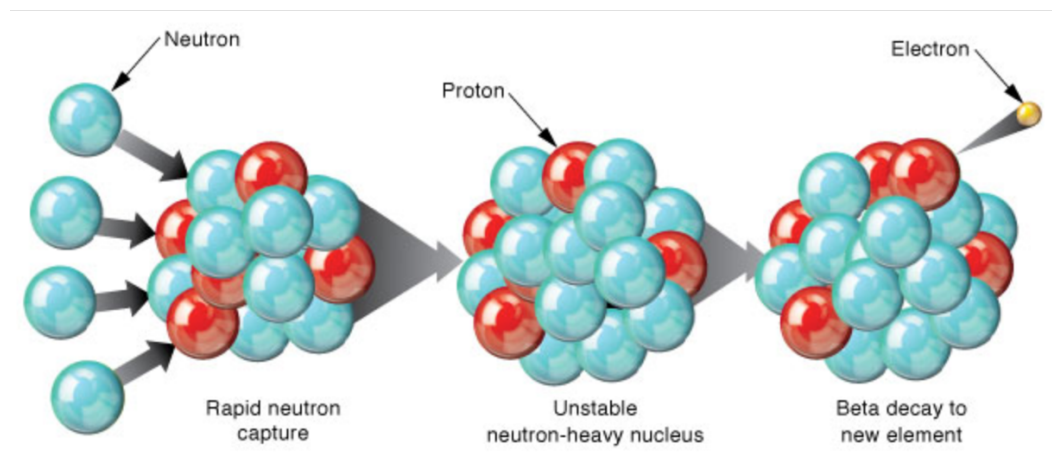


Figure 1.3: A diagram of neutron captures and beta decay in the *r*-process. Image credit: Lawrence Livermore National Laboratory (July 2014) published here.

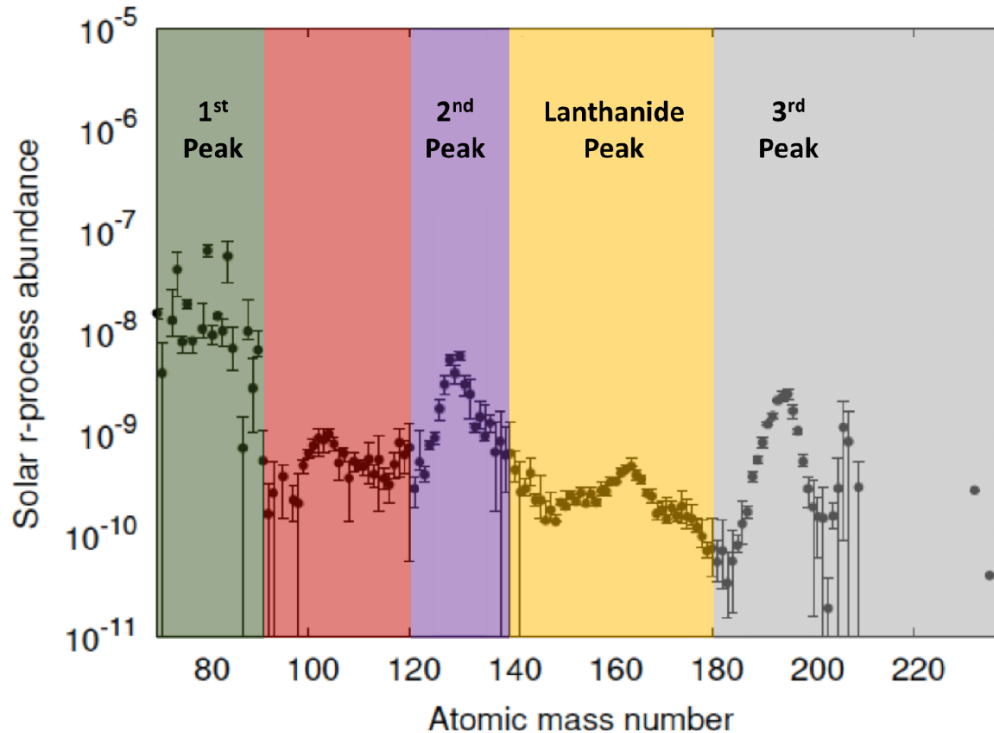


Figure 1.4: The solar  $r$ -process abundance pattern, showing first peak, second peak, lanthanides peak, and third peak elements. Modified from (Hotokezaka et al., 2018; Kasliwal et al., 2017a).

( $A \sim 130$ ; moderate  $r$ -process elements), 3) lanthanides peak ( $A \sim 160$ ), and 4) third peak ( $A \sim 194$ ; heavy  $r$ -process elements) (Goriely, 1999; Lodders, 2003). The astrophysical sites of  $r$ -process nucleosynthesis must therefore synthesize from the lightest to the heaviest  $r$ -process elements in the correct ratios to explain the observed solar  $r$ -process abundance pattern.

Many studies have investigated whether this  $r$ -process abundance pattern we observe in the solar neighborhood is universal. Europium, one of the few elements purely produced via the  $r$ -process, can be useful as a robust tracer of the universality of the solar  $r$ -process pattern. The measurements of excess  $[\text{Ba}/\text{Fe}]$  and  $[\text{Eu}/\text{Fe}]$  abundances in the dwarf galaxy Reticulum II are consistent with solar abundances (Ji et al., 2016a). The second- and third-peak abundance patterns derived from Europium detections in metal-poor stars in the Galactic Halo also match those of the solar neighborhood, pointing towards the non-locality of the *heavy* solar  $r$ -process abundance pattern (Kajino et al., 2019). Using light  $r$ -process elemental tracers

such as Sr/Y/Zr in the spectra of metal-poor Galactic Halo stars, studies (Cowan et al., 2006; Siqueira Mello et al., 2014) have found differences in the first-peak  $r$ -process abundance ratios relative to Solar abundance ratios, indicating that the abundance of light  $r$ -process elements in the Solar neighborhood may not be universal. The fact that we observe variations in light  $r$ -process enrichment amongst stellar spectra may hint at multiple  $r$ -process sites that each produce different ratios of light and heavy  $r$ -process elements. This begs the question: what were the  $r$ -process site(s) that contributed towards the Solar  $r$ -process abundance pattern we observe today?

### 1.1 Evidence Indicates that $r$ -Process Sites Must Be Rare and Prolific

Lattimer & Schramm (1974a) and Lattimer & Schramm (1976) first proposed that the decompression of cold, neutron-rich matter ejected during the merging process of a neutron star with a black hole could provide the right conditions for  $r$ -process to occur. It was only following the discovery of the first binary pulsar system (Hulse & Taylor, 1975) that BNS mergers were also proposed as viable  $r$ -process sites (Symbalisty & Schramm, 1982). Numerical simulations showed that  $\sim 2\%$  of the mass in these NS mergers is unbound as  $r$ -process ejecta (Davies et al., 1994), making them prolific  $r$ -process sites. Rosswog et al. (1999) performed hydrodynamical simulations of BNS mergers, confirming that the composition of the NS merger ejecta is broadly consistent with measurements of  $r$ -process abundances in the Solar neighborhood.

In the 1990s, core-collapse SNe were also proposed as a dominant site for  $r$ -process (Woosley et al., 1994). The neutrino-heated winds from a proto neutron star (NS), following a SN explosion, were considered to be the primary mechanism for generating  $r$ -process elements (Takahashi et al., 1994; Woosley et al., 1994). However, detailed simulations soon revealed that the neutrino-driven winds did not reach  $Y_e \lesssim 0.5$ , and therefore were not conducive for  $r$ -process nucleosynthesis (Martínez-Pinedo et al., 2012; Roberts et al., 2010).

However, a rare supernova (SN) subtype, known as a hypernova, was proposed as a viable alternative  $r$ -process site (e.g., Fujimoto et al., 2007). In this scenario, the hypernova leaves behind a rapidly rotating black hole remnant that can power a relativistic jet and form an accretion disk around it. Neutronization of the accretion disk material could then create the optimal conditions for  $r$ -process (Siegel et al., 2019). Hypernovae could also yield a proto-NS central engine whose winds, if

strongly magnetized, can give rise to  $r$ -process enriched wind ejecta (Desai et al., 2023; Metzger et al., 2011). Given that these hypernovae comprise  $< 1/1000$ th of the core-collapse SN rate (Podsiadlowski et al., 2004), they must be prolific (producing  $\gtrsim 10^{-2}M_{\odot}$  of  $r$ -process ejecta per event) in order to be a dominant  $r$ -process site.

Meteoritic, geochemical, and galactic archaeological studies have also provided indirect clues that rare SNe contribute to  $r$ -process enrichment in the Universe. Comparisons of the derived decay timescale of  $^{247}\text{Cm}$  measured in a Calcium-Aluminum Inclusion meteorite with previous meteoritic measurements suggest that multiple  $r$ -process events could have occurred in the solar systems' history (Tissot et al., 2016). Wallner et al. 2015 detected the presence of live  $^{244}\text{Pu}$ , a short-lived  $r$ -nuclide part of the actinides branch, with abundances 2 – 3 orders of magnitude lower than expected from a continuous galactic production scenario, indicating that the  $r$ -process production site must be rare. However, simultaneous detections of  $^{60}\text{Fe}$  and  $^{244}\text{Pu}$  influxes point towards  $\geq 2$  galactic events within the last  $\sim 10$  Myr that insinuate a rare subtype of core-collapse SNe (Wallner et al., 2021). A recent discovery of *heavy*  $r$ -process enrichment in a disrupted dwarf in the Milky Way Halo, Gaia Sausage Enceladus (GSE), with a 3.6 Gyr star formation duration, but not in the very similar disrupted dwarf Kraken ( $\approx 2$  Gyr star formation duration) also implies two different enrichment sites. Detections of both Eu (along with Mg) for all stars in Kraken indicates that rare SNe may be responsible for its early-time enrichment (Naidu et al., 2021), while the longer star formation duration in GSE can still be explained by NS mergers that possess  $\gtrsim 500$  Myr time delays between their formation and production of  $r$ -process elements.

The  $r$ -process enrichment of metal-poor dwarf galaxies also contributes interesting clues towards the nature of astrophysical  $r$ -process sites. Chemical abundance analyses of the stars in many of these dwarf galaxies have revealed excess  $[\text{Ba}/\text{Fe}]$  and  $[\text{Eu}/\text{Fe}]$  that have been shown to be attributed to the  $r$ -process. The fact that these dwarf galaxies are chemically simple argues for a rare  $r$ -process site capable of enriching the galaxies early in their evolution (Ji et al., 2016a; Tarumi et al., 2020). While Duggan et al. (2018) argue that NS merger time delays are needed to explain the delayed Barium enrichment relative to core-collapse SNe in metal-poor dwarf galaxies, the  $r$ -process deposits in Reticulum II's early evolution is compatible only with the shortest NS merger time delays (Ji et al., 2016a; Roederer et al., 2016; Tarumi et al., 2020). Furthermore, low-mass dwarf galaxies need a way to retain

heavy elements despite NS merger kicks (Komiya & Shigeyama, 2016) that could exceed the dwarf galaxies' escape velocities. Low-kick, fast-merging channels for neutron star mergers have been invoked to explain dwarf galaxy enrichment (Beniamini et al., 2016; Bonetti et al., 2019). However, core-collapse SNe could also provide a convenient solution to this conundrum, as their timescales for enriching the surrounding environment are quicker, generally following star formation, and they have lower kick velocities that allow the SNe to remain within the galaxy (Côté et al., 2019).

Based on clues from the solar  $r$ -process abundance pattern and various studies of geochemistry, galactic archaeology, and meteorites, three viable  $r$ -process sites emerge, which are the subject of further investigation in this thesis: hypernovae of collapsar origin, binary neutron star mergers, and neutron star-black hole mergers.

## 1.2 $r$ -Process from Collapsars

The collapse of massive ( $\gtrsim 30 M_{\odot}$ ), rapidly rotating stars directly into black holes (i.e. collapsars) have been suggested as an alternative  $r$ -process site to NS mergers. These collapsars power long-duration gamma-ray bursts (GRBs) and are expected to be accompanied by broad-lined Type Ic supernovae (SNe Ic-BL; MacFadyen & Woosley 1999; MacFadyen et al. 2001; Woosley et al. 1994). SNe Ic-BL are stripped of their Hydrogen and Helium envelopes and possess high photospheric velocities (significantly larger than  $10^4 \text{ km s}^{-1}$ ) that cause line broadening in their spectra (Gal-Yam, 2017; Modjaz et al., 2016).

The black hole central engines to collapsars are key to enabling  $r$ -process production. Simulations suggest that  $r$ -process elements originate in an outflow from the accretion disk (Metzger et al., 2008, 2009) surrounding the newly born central black hole (Shibata & Taniguchi, 2006), that could be seen in both short GRBs associated with NS mergers as well as collapsar-powered long GRBs. Many works have suggested that collapsars could produce between  $M_{\odot}$  of  $r$ -process material (Fujimoto et al., 2007; Nakamura et al., 2015; Ono et al., 2012; Soker & Gilkis, 2017). However, the question of whether collapsars harbor  $r$ -process continues to be heavily debated. For example, Surman et al. (2006) concluded that only light  $r$ -process elements could be produced in the neutrino-driven winds originating from collapsar accretion disks. Siegel et al. (2019) conducted 3-D, magnetohydrodynamical simulations of collapsar disks, and found that the accretion disks became neutron-rich through weak interactions, enabling the production of heavy  $r$ -process up to

the third peak, in sufficient quantities to contribute as a dominant  $r$ -process site. On the other hand, studies of the full radiation-transport and  $\alpha$ -viscosity in collapsar disks have revealed that collapsars may actually be inefficient in synthesizing  $r$ -process elements (Fujibayashi et al., 2022; Just et al., 2022; Miller et al., 2020). Whether or not collapsars produce  $r$ -process elements is still under active investigation, both theoretically and observationally. The black hole central engines to collapsars are key to enabling  $r$ -process production. Simulations suggest that  $r$ -process elements originate in an outflow from the accretion disk (Metzger et al., 2008, 2009) surrounding the newly born central black hole (Shibata & Taniguchi, 2006), that could be seen in both short GRBs associated with NS mergers as well as collapsar-powered long GRBs. Many works have suggested that collapsars could produce between  $0.01 - 0.10 M_{\odot}$  of  $r$ -process material (Fujimoto et al., 2007; Nakamura et al., 2015; Ono et al., 2012; Soker & Gilkis, 2017). However, the question of whether collapsars harbor  $r$ -process continues to be heavily debated. For example, Surman et al. (2006) concluded that only light  $r$ -process elements could be produced in the neutrino-driven winds originating from collapsar accretion disks. Siegel et al. (2019) conducted 3-D, magnetohydrodynamical simulations of collapsar disks, and found that the accretion disks became neutron-rich through weak interactions, enabling the production of heavy  $r$ -process up to the third peak, in sufficient quantities to contribute as a dominant  $r$ -process site. On the other hand, studies of the full radiation-transport and  $\alpha$ -viscosity in collapsar disks have revealed that collapsars may actually be inefficient in synthesizing  $r$ -process elements (Fujibayashi et al., 2022; Just et al., 2022; Miller et al., 2020). Whether or not collapsars produce  $r$ -process elements is still under active investigation, both theoretically and observationally.

### 1.3 $r$ -Process from Binary Neutron Star Mergers

Mergers of two neutron stars produce both gravitational and electromagnetic radiation. The inspiral process of the two neutron stars in the system generates gravitational radiation; as the neutron stars' mutual orbit circularizes and the neutron stars merge, their radiation is detectable by ground-based gravitational wave (GW) detectors (Misner et al., 1973). The merger is also expected to produce a number of detectable electromagnetic (EM) signatures, or counterparts (Metzger & Berger, 2012), including a relativistic jet known as a short-duration gamma-ray burst (GRB; Narayan et al. 1992), a multi-wavelength afterglow, arising from the interaction of the GRB jet with the surrounding interstellar medium (ISM; Fong et al. 2015, and

a kilonova (KN), the optical/NIR signatures of radioactive decay of  $r$ -process elements (Barnes & Kasen, 2013; Kasen et al., 2013; Li & Paczynski, 1998; Metzger et al., 2010).

Studies reveal that while KN emission appears to be quasi-isotropic, its ejecta is stratified into multiple components. Simulations have shown that during the merging process of two neutron stars, matter is tidally stripped from the two stars on a timescale of milliseconds (Freiburghaus et al., 1999). More ejecta is expelled from the system as the neutron stars come into contact, squeezing the ejecta into the polar regions (Sekiguchi et al., 2016). The tidal ejecta is cold and neutron-rich, and thus expected to produce heavy  $r$ -process elements, while the composition of the polar ejecta is comprised of only light  $r$ -process elements due to neutrino irradiation and weak interactions in the polar regions (Metzger & Fernandez, 2014; Perego et al., 2014; Sekiguchi et al., 2016; Wanajo et al., 2014). These two components are known together as the *dynamical* ejecta of the KN (Kasen et al., 2017).

Another ejecta component is known as the *postmerger*, or *disk wind* ejecta. When the two neutron stars merge, they will either temporarily form a hypermassive neutron star (HMNS; Margalit & Metzger 2019; Metzger 2019) that then collapses to form a black hole, or promptly form a black hole remnant (Bauswein et al., 2013; Hotokezaka et al., 2011). Disk wind ejecta originates from the accretion disk that forms around the remnant black hole or HMNS on timescales of a second after the merger (Metzger, 2019). The accretion disk becomes neutron-rich through weak interactions, and liberates the matter through disk winds, with velocities of  $0.05-0.1c$  (Just et al., 2015; Perego et al., 2014). The nature of the remnant determines the composition of the disk wind ejecta; a HMNS remnant may increase the electron fraction of the disk wind through neutrino irradiation, while a prompt black hole collapse could lead to disk winds that are very rich in lanthanides, and therefore harbor heavy  $r$ -process elements (Metzger, 2019).

The ejecta composition of KNe from binary neutron star (BNS) and neutron star-black hole (NSBH) mergers has implications for observables. Ejecta composed of light  $r$ -process elements has low opacities, and radiates blue optical light that fades quickly within a few days. A lanthanide-rich ejecta composition results in a high density of lines that blocks out most of the optical radiation, shifting the peak of the emission to the infrared (Kasen et al., 2013, 2017). This heavy  $r$ -process ejecta has longer diffusion times, resulting in the IR light curves peaking later than the optical light curves and lasting up to a week after merger (Barbieri

et al., 2019; Kasliwal et al., 2019; Kawaguchi et al., 2020; Rosswog et al., 2017). KNe from BNS mergers are predicted to possess both a “blue”, fast-fading and a “red”, long-lasting component to their light curves (Kasen et al., 2017), while NSBH KN light curves are more likely to have reddened emission, delayed peaks, and slower evolution timescales (Kawaguchi et al., 2016, 2020).

### ***r*-Process from GW170817**

On August 17, 2017, the LIGO and Virgo detectors discovered the binary neutron star merger GW170817 at 40 Mpc (Abbott et al., 2017a). Two seconds later, the Fermi Gamma Ray Burst Monitor detected a coincident short burst of gamma-rays (Abbott et al., 2017b), followed by a multi-wavelength afterglow (Haggard et al., 2017; Hallinan et al., 2017; Margutti et al., 2017; Mooley et al., 2018; Pozanenko et al., 2018; Troja et al., 2017). The Swope Supernova Survey first identified the KN counterpart, AT2017gfo, in a galaxy-targeted search within the 31 sq. deg. localization (Coulter et al., 2017a). In-depth photometric and spectroscopic observations in the optical and NIR bands revealed telltale signatures of radioactive decay of heavy elements from the BNS merger (Andreoni et al., 2017a; Arcavi, 2018; Chornock et al., 2017; Cowperthwaite et al., 2017; Drout et al., 2017; Evans et al., 2017a; Kasen et al., 2017; Kasliwal et al., 2017b; Kasliwal et al., 2019; Kilpatrick et al., 2017; Lipunov et al., 2017a; Soares-Santos et al., 2017; Utsumi et al., 2017; Valenti et al., 2017; Villar et al., 2017; Watson et al., 2019).

The discovery of GW170817 unambiguously solidified the connection between BNS mergers and KNe, confirming that BNS mergers are *r*-process sites (Hotokezaka et al., 2018). The weak, non-standard short-duration GRB accompanying GW170817 (Abbott et al., 2017b) pointed towards a cocoon shock-breakout powering the gamma-ray emission (Gottlieb et al., 2018; Kasliwal et al., 2017a; Nakar & Piran, 2016), ultimately leading to a successful jet breakout (Mooley et al., 2018). GW170817 also provided constraints on the neutron star equation of state (Coughlin et al., 2020; Dietrich et al., 2020a) and the Hubble constant (Coughlin et al., 2020a; Kashyap et al., 2019).

### **1.4 *r*-Process from Neutron Star– Black Hole Mergers**

All BNS mergers are expected to be accompanied by a KN counterpart. This is not the case for NSBH mergers, however. The fate of the neutron star—that is, whether it is tidally ripped apart, or swallowed whole by its black hole companion—determines the presence of an EM counterpart. This outcome ultimately relies on

the mass of the black hole and the tidal radius of the neutron star, or the distance at which the neutron star’s gravitational force becomes equivalent to the black hole’s tidal force (Foucart, 2012). If the black hole mass is  $\lesssim 3 - 5x$  the mass of the neutron star, the tidal radius will be outside the black hole’s innermost stable circular orbit (ISCO), and some matter from the neutron star will likely be unbound as tidal dynamical ejecta (Foucart et al., 2017). Unlike the BNS merger scenario where the two NSs touch at the surface, squeezing ejecta into the polar regions, no polar dynamical ejecta component is expected from an NSBH merger (Kasen et al., 2017). The remainder of the neutron star’s matter is predicted to form an accretion disk surrounding the black hole; similar to the BNS merger prompt black hole collapse case, heavy  $r$ -process elements will be ejected via disk winds (Foucart, 2012; Foucart et al., 2015). Alternatively, if the tidal radius of the neutron star falls within the black hole’s ISCO, which is likely to occur for black holes that are  $\gtrsim 5x$  the mass of the neutron star, the neutron star will be swallowed whole, and no matter will remain outside the final black hole remnant (Foucart, 2012). Such NSBH mergers will be electromagnetically dark. While the mass ratio may be the dominant factor in determining whether or not an EM counterpart is produced, other factors, such as the tidal deformability of the NS ( $\tilde{\Lambda}$ ) and the spin of the black hole ( $\chi_{\text{eff}}$ ) also play a role in whether or not any matter remains outside the final black hole remnant. In particular, the ISCO for highly spinning black holes will shrink, increasing the probability of matter remaining outside the final black hole (Foucart et al., 2018b). NSs with large radii that are less compact will have larger tidal deformabilities, indicating that they can more easily deform in the presence of tidal effects from the black hole (Chatziioannou, 2020). All of these factors affect whether or not NSBH mergers produce detectable signatures of  $r$ -process nucleosynthesis.

## 1.5 Thesis Outline

My thesis chapters explore observational studies of various potential  $r$ -process sites primarily using the Zwicky Transient Facility (ZTF) mounted on the Samuel Oschin 48-in telescope at Palomar Observatory. In Chapter 1, we investigate  $r$ -process enrichment in the light curves of SNe Ic-BL discovered by ZTF and followed up by the Wide-Field Infrared Camera (WIRC) on the Palomar Hale 200-in telescope. In Chapter 2 we perform Bayesian inference on the early photometric data of GW170817 to infer its geometry and ejecta composition with and without the inclusion of tight viewing angle constraints. In Chapter 3, we describe ZTF’s observational constraints on KNe from NSBH mergers. In Chapter 4, we present

our extensive ZTF follow-ups of neutron star mergers during the first half of the International Gravitational Wave Network's fourth observing run and subsequent constraints on the kilonova luminosity function. Finally, in Chapter 5, I provide a high-level summary of the work presented herein and discuss future prospects for understanding  $r$ -process sites through observational studies.

*Chapter 2**r*-PROCESS FROM COLLAPSARS**Collapsars as Sites of *r*-Process Nucleosynthesis: Systematic Photometric Near-Infrared Follow-Up of Type Ic-BL Supernovae**

Anand, S., Barnes, J., Yang, S., et al. 2024, Collapsars as Sites of *r*-process Nucleosynthesis: Systematic Photometric Near-infrared Follow-up of Type Ic-BL Supernovae, *The Astrophysical Journal*, 962, 68, . S. A. participated in the conception of the project, performed observations, reduced data, analyzed the light curves and fit models to the data, and wrote most of the manuscript. Published in *ApJ*. <https://doi.org/10.3847/1538-4357/ad11df>

S. A. participated in the conception of the project, performed observations, reduced data, analyzed the light curves and fit models to the data, and wrote most of the manuscript.

## ABSTRACT

One of the open questions following the discovery of GW170817 is whether neutron star mergers are the only astrophysical sites capable of producing  $r$ -process elements. Simulations have shown that  $0.01\text{-}0.1M_{\odot}$  of  $r$ -process material could be generated in the outflows originating from the accretion disk surrounding the rapidly rotating black hole that forms as a remnant to both neutron star mergers and collapsing massive stars associated with long-duration gamma-ray bursts (collapsars). The hallmark signature of  $r$ -process nucleosynthesis in the binary neutron star merger GW170817 was its long-lasting near-infrared emission, thus motivating a systematic photometric study of the light curves of broadlined stripped-envelope (Ic-BL) supernovae (SNe) associated with collapsars. We present the first systematic study of 25 SNe Ic-BL—including 18 observed with the Zwicky Transient Facility and 7 from the literature—in the optical/near-infrared bands to determine what quantity of  $r$ -process material, if any, is synthesized in these explosions. Using semi-analytic models designed to account for  $r$ -process production in SNe Ic-BL, we perform light curve fitting to derive constraints on the  $r$ -process mass for these SNe. We also perform independent light curve fits to models without  $r$ -process. We find that the  $r$ -process-free models are a better fit to the light curves of the objects in our sample. Thus we find no compelling evidence of  $r$ -process enrichment in any of our objects. Further high-cadence infrared photometric studies and nebular spectroscopic analysis would be sensitive to smaller quantities of  $r$ -process ejecta mass or indicate whether all collapsars are completely devoid of  $r$ -process nucleosynthesis.

## 2.1 Introduction

The dominant process responsible for producing elements heavier than iron is the rapid neutron capture process, known as the  $r$ -process (Burbidge et al., 1957; Cameron, 1957), which only has a few plausible astrophysical sites. While standard core-collapse supernovae (SNe) were previously considered as candidate sites for  $r$ -process nucleosynthesis (Qian & Woosley, 1996; Takahashi et al., 1994; Woosley et al., 1994), they have since been disfavored because simulations of neutrino-driven winds in core-collapse SNe fail to create conducive conditions for  $r$ -process production (Hotokezaka et al., 2018; Martínez-Pinedo et al., 2012; Roberts et al., 2010; Thompson et al., 2001). On the other hand, before 2017, many studies (Lattimer & Schramm, 1974a; Lattimer & Schramm, 1976; Symbalisky & Schramm, 1982) predicted that mergers of two neutron stars (NSs) or neutron stars with black holes were capable of generating  $r$ -process elements during the decompression of cold, neutron-rich matter ensuing from the tidal disruption of the neutron stars. Li & Paczynski (1998) first suggested that the signature of such  $r$ -process nucleosynthesis would be detectable in an ultraviolet, optical and near-infrared (NIR) transient powered by the radioactive decay of neutron-rich nuclei, termed as a “kilonova” for its brightness, which was predicted to be  $1000\times$  that of a classical nova (Metzger et al., 2010). Other studies proposed that  $r$ -process elements could be synthesized in a rare SN subtype known as a hypernova (e.g. Fujimoto et al., 2007). In this scenario, the SN explosion produces a rapidly rotating central BH surrounded by an accretion disk. Accretion onto the BH is thought to power a relativistic jet, while material in the disk may neutronize, allowing the  $r$ -process to occur when the newly neutron-rich material is unbound as a disk wind.

Galactic archaeological studies (Ji et al., 2016a,b), geochemical studies (Wallner et al., 2021), and studies of the early solar system (Tissot et al., 2016) offer unique insights into which astrophysical sites could plausibly explain observed  $r$ -process elemental abundances. A recent study of  $r$ -process abundances in the Magellanic Clouds indicate that the astrophysical  $r$ -process site has a time-delay longer than for core-collapse SNe (Reggiani et al., 2021). Second- and third-peak abundance patterns inferred from metal-poor Galactic halo stars show consistency with the solar  $r$ -process abundance pattern at high atomic number, but scatter at low atomic number that could be attributed to enrichment from multiple sources, including magneto-rotational hypernovae (Yong et al., 2021). Measurements of excess  $[Ba/Fe]$  and  $[Eu/Fe]$  abundances in the dwarf galaxy Reticulum II argue for not only a rare and prolific event, but one capable of enriching the galaxy early in its history (Ji

et al., 2016a; Tarumi et al., 2020), pointing towards a potential rare SN subtype whose  $r$ -process production would follow star formation (Côté et al., 2019; Siegel et al., 2019). Further evidence of *heavy*  $r$ -process enrichment in the disrupted dwarf galaxy Gaia Sausage Enceladus ( $\sim 3.6$  Gyr star formation duration) but not in the disrupted dwarf galaxy Kraken (with  $\approx 2$  Gyr star formation duration) points towards multiple  $r$ -process enrichment sites operating on different timescales (Naidu et al., 2021).

Overall, geological studies and studies of the early solar system and Galactic chemical evolution exemplify the need for rare and prolific astrophysical sites to explain observed abundances, and insinuate that the solar  $r$ -process abundance pattern could be universal. While NS mergers are compatible with many facets of the above findings (Côté et al., 2018; Hotokezaka et al., 2018; Metzger, 2019), assuming that mergers are the *sole* producers of  $r$ -process material presents some potential hurdles. For example, the time delay between formation and merger of NS systems must be short enough to enrich old, ultra-faint dwarf galaxies with heavy elements (Côté et al., 2019; Ji et al., 2016a; Roederer et al., 2016). Furthermore, natal merger kicks present a challenge for low-mass galaxies to retain pre-merger compact binaries (Komiya & Shigeyama, 2016). The question of whether NS mergers alone can explain the relative abundances of  $r$ -process elements (e.g. [Eu/Fe] vs. [Fe/H]) in the solar neighborhood remains unanswered (Beniamini et al., 2016; Bonetti et al., 2019).

The multi-messenger detection of the binary neutron star merger GW170817 (Abbott et al., 2017a), an associated short burst of gamma-rays GRB170817 (Abbott et al., 2017b) and the kilonova AT2017gfo (Andreoni et al., 2017a; Chornock et al., 2017; Coulter et al., 2017b; Cowperthwaite et al., 2017; Drout et al., 2017; Evans et al., 2017b; Kasliwal et al., 2017a, 2022; Kilpatrick et al., 2017; Lipunov et al., 2017b; McCully et al., 2017; Nicholl et al., 2017; Pian et al., 2017a; Shappee et al., 2017; Smartt et al., 2017; Soares-Santos et al., 2017; Tanvir et al., 2017; Utsumi et al., 2017; Villar et al., 2017) relayed the first direct evidence that NS mergers are an astrophysical site of  $r$ -process nucleosynthesis and short GRB progenitors. Multi-band photometry and optical/NIR spectroscopy of AT2017gfo indicated that the KN ejecta was enriched with  $r$ -process elements (Chornock et al., 2017; Cowperthwaite et al., 2017; Drout et al., 2017; Kasliwal et al., 2017a; Kilpatrick et al., 2017; Pian et al., 2017a; Smartt et al., 2017; Tanvir et al., 2017; Watson et al., 2019) including heavier species occupying the second- and third-peak (Gillanders et al.,

2021; Kasliwal et al., 2022; Tanvir et al., 2017; Watson et al., 2019).

Although GW170817 confirmed NS mergers as  $r$ -process nucleosynthesis sites, some fundamental open questions on the nature of  $r$ -process production still remain. Namely, can the rates of and expected yields from NS mergers explain the *total* amount of  $r$ -process production measured in the Universe? Or, do the direct and indirect clues about  $r$ -process production in the Universe point towards an alternative  $r$ -process site, such as rare core-collapse SNe?

The discovery of the broadlined Type Ic supernova SN 1998bw at 40 Mpc (Galama et al., 1998), following the long GRB 980425 was a watershed event that provided the first hints that some GRBs were connected to stellar explosions (Galama et al., 1999; Kulkarni et al., 1998). However, due to the anomalous nature of the explosion, it was not until GRB 030329 that a direct long GRB–SN connection was securely established (Fynbo et al., 2004). The spectra of these SNe exhibit broad features due to high photospheric velocities ( $\gtrsim 20,000 \text{ km s}^{-1}$ ). They have higher inferred kinetic energies than typical SNe (at  $\sim 10^{52}$  erg), and are stripped of both hydrogen and helium (Gal-Yam, 2017; Modjaz et al., 2016). Since SN 1998bw, several other SNe Ic-BL have been discovered in conjunction with long GRBs (e.g. Cano et al. (2017b); Corsi & Lazzati (2021); Kocevski et al. (2007); Olivares E. et al. (2012)), boosting the existing collapsar theory (MacFadyen & Woosley, 1999; MacFadyen et al., 2001; Woosley et al., 1994) as a mechanism to explain long GRBs and their associated SN counterparts. The term collapsar refers to a rapidly-rotating, massive star that collapses into a black hole, forming an accretion disk around the central black hole. Collapsars are distinct from the magnetar-powered explosions (referred to as “magnetohydrodynamic (MHD) SNe”) also proposed to be related to SNe Ic-BL (Kashiyama et al., 2016; Metzger et al., 2011). However, puzzling discoveries including that of GRB060505 and GRB060614 which lacked a clear SN counterpart to deep limits (Gehrels et al., 2006) and that of GRB211211A, a long-duration GRB associated with a kilonova (Rastinejad et al., 2022) have shifted the paradigm from the traditional conception that all long GRBs have a collapsar or magnetar origin. Thus some fraction of long-duration GRBs may also originate from compact binary mergers.

Several works (Fujimoto et al., 2007; Nakamura et al., 2015; Ono et al., 2012; Soker & Gilkis, 2017) have since hypothesized that the explosions that give rise to SNe Ic-BL and (in some cases) to their accompanying long GRBs (i.e. collapsars) are capable of producing 0.01-0.1 $M_{\odot}$  of  $r$ -process material per event. Simulations

suggest that in the case of a NS merger, an accretion disk forms surrounding the merger’s newly-born central black hole (Shibata & Taniguchi, 2006) and  $r$ -process elements originate in the associated disk outflows (Metzger et al., 2008, 2009). Such accretion flows are not only central to the short GRBs associated with NS mergers, but also with the long classes of GRBs associated with collapsars. However, predictions about  $r$ -process-production in the collapsar context are sensitive to assumptions about the magnetic field, the disk viscosity model, and the treatment of neutrinos, among other factors. Surman et al. (2006) argued that only light  $r$ -process elements can be synthesized in collapsar accretion disks due to neutrino-driven winds. More recently, Siegel et al. (2019) conducted 3D general-relativistic, magnetohydrodynamic simulations demonstrating sufficient  $r$ -process yields to explain the observed abundances in the Universe. Siegel et al. (2019) found that the disk material becomes neutron-rich through weak interactions, enabling the production of even 2nd and 3rd peak  $r$ -process elements in disk-wind outflows. Other works in the literature (Fujibayashi et al., 2022; Just et al., 2022; Miller et al., 2020) have argued that collapsars are inefficient producers of  $r$ -process elements based on studies of the full radiation transport and  $\alpha$ -viscosity in collapsar disks. Whether or not collapsars are sites of  $r$ -process nucleosynthesis is still an active area of investigation, motivating detailed studies of the photometric evolution of  $r$ -process enriched SNe.

Recently, Barnes & Metzger (2022), motivated by Siegel et al. (2019), created semi-analytic models of the light curves of SNe from collapsars producing  $r$ -process elements, yielding concrete predictions for the photometric evolution of  $r$ -process-enriched SNe Ic-BL. Our work is focused on observationally testing the models from Barnes & Metzger (2022).

In this work, we report our findings from an extensive observational campaign and compilations from the literature to determine whether collapsars powering SNe Ic-BL are capable of synthesizing  $r$ -process elements. We present optical and near-infrared photometric observations and compare both color evolution and absolute light curves against the predictions from Barnes & Metzger (2022). Our paper is structured as follows: First, we detail our sample selection criteria in Section 2.2, then Section 2.3 describes our optical and NIR observations, followed by Section 2.4 which provides the discovery details about each candidate. Section 2.5 introduces the objects from the literature used in our study, and in Section 2.6 we introduce the latest collapsar  $r$ -process models. In Section 2.7, we show how we de-

rive explosion properties. The results of our light curve model fits are presented in Section 2.8, and finally we discuss our conclusions and future work in Section 2.9.

## 2.2 Sample Selection

To test the hypothesis that SNe Ic-BL generate  $r$ -process elements, we require a statistically robust sample size of SNe with contemporaneous NIR and optical light curves. To obtain optical light curves, we use data from the Zwicky Transient Facility (ZTF; Bellm et al. 2019a; Graham et al. 2019; Masci et al. 2019), a 47 sq. deg. field-of-view mosaic camera with a pixel scale of  $1''/\text{pixel}$  (Dekany et al., 2020) installed on the Palomar 48 in. telescope. ZTF images the entire Northern sky every  $\sim 2$  nights in  $g$ - and  $r$ -bands, attaining a median  $5\sigma$  detection depth of  $20.5 m_{\text{AB}}$ . Amongst the systematic efforts aimed at SN detection with ZTF, our SNe draw from two surveys in particular: “Bright Transient Survey” (BTS; Fremling et al. 2020) and the ZTF “Census of the Local Universe” survey (CLU; De et al. 2020b) which are conducted as a part of ZTF’s nightly operations. BTS is a magnitude-limited survey aimed at spectroscopically classifying all SNe  $< 18.5$  mag at peak brightness (Perley et al., 2020). CLU, in contrast, is a volume-limited survey aimed at classifying all SNe within 150 Mpc whose hosts belong to the CLU galaxy catalog (Cook et al., 2019a). The CLU galaxy catalog is designed to provide spectroscopic redshifts of all galaxies within 200 Mpc, and is 90% complete (for an  $H\alpha$  line flux of  $4 \times 10^{-14}$  erg  $\text{cm}^2 \text{s}^{-1}$ ). Hence the two surveys provide complementary methods for SN identification. Our sample consists of 18 spectroscopically-confirmed ZTF SNe Ic-BL within  $z \lesssim 0.05$ . Due to our low redshift cut, we assume that the photometric K-corrections are negligible (Taddia et al., 2018). The details of the instruments and configurations used to take our classification spectra are described in Section 2.3 (see also Figure 4.2). Where available, we use the spectroscopic redshift from the SDSS galaxy host (especially for sources falling in the CLU sample) and otherwise determine the SN redshift from spectral fitting to the narrow galaxy  $H\alpha$  feature. For each spectrum, we use the Supernova Identification code (SNID; Blondin & Tonry 2007a) to determine the best match template (also plotted in Figure 4.2), fixing the redshift to the value determined using the methods described above. We overplot the characteristic spectroscopic lines for SNe Ic-BL including O I, Fe II, and Si II in dashed lines, along with Na I D, an indicator of the amount of supernova host galaxy extinction (Stritzinger et al., 2018a). For all of the ZTF SNe, we assume zero host attenuation; this assumption is backed by the lack of any prominent Na I D absorption features in the spectra (see Figure 4.2). Higher host

attenuation results in redder observed SN colors.

We impose a redshift cut to eliminate distant SNe that might fade rapidly below ZTF detection limits within 60 days post-peak. ZTF yields an average rate of SNe Ic-BL discovery of  $\sim 1/\text{month}$ , but due to visibility and weather losses, we followed-up  $\sim 10$  SNe per year. As a consequence of our sample selection from ZTF, probing only the local volume, we are biased against GRB-SNe. However, amongst our sample, we include one LLGRB (GRB 190829A), SN 2018gep, a published SN with fast and luminous emission (Ho et al., 2019), and another published SN with a mildly-relativistic ejecta, SN 2020bvc (Ho et al., 2020a), which contribute diversity to our ZTF sample. The two SNe exhibited broad features in their spectra and were classified as SNe Ic-BL, while the LLGRB was too faint for spectroscopy, and only had photometric evidence of an associated SN bump.

In the analyses in subsequent sections, we assume the following cosmological parameters:  $H_0 = 67.3 \text{ km s}^{-1} \text{ Mpc}^{-1}$ ,  $\Omega_m = 0.307$ .

### 2.3 Observations

Here we describe the photometric and spectroscopic observations obtained by various facilities in our follow-up campaign.

#### Photometry

##### ZTF

We use the ZTF camera on the Palomar 48-in telescope for supernova discovery and initial follow-up. ZTF’s default observing mode consists of 30 s exposures. Alerts ( $5\sigma$  changes in brightness relative to the reference image) are disseminated in avro format (Patterson et al., 2019) and filtered based on machine-learning real-bogus classifiers (Mahabal et al., 2019), star-galaxy classifiers (Tachibana & Miller, 2018), and light curve properties. Cross-matches with solar-system objects serve to reject asteroids. ZTF’s survey observations automatically obtain  $r$ –,  $g$ – and sometimes  $i$ – band imaging lasting  $\approx 60$  days after peak, while the supernova is brighter than 20.5 mag. Masci et al. (2019) provides more information about the data processing and image subtraction pipelines. More details about specific surveys used to obtain these data are provided in Sec 2.2.

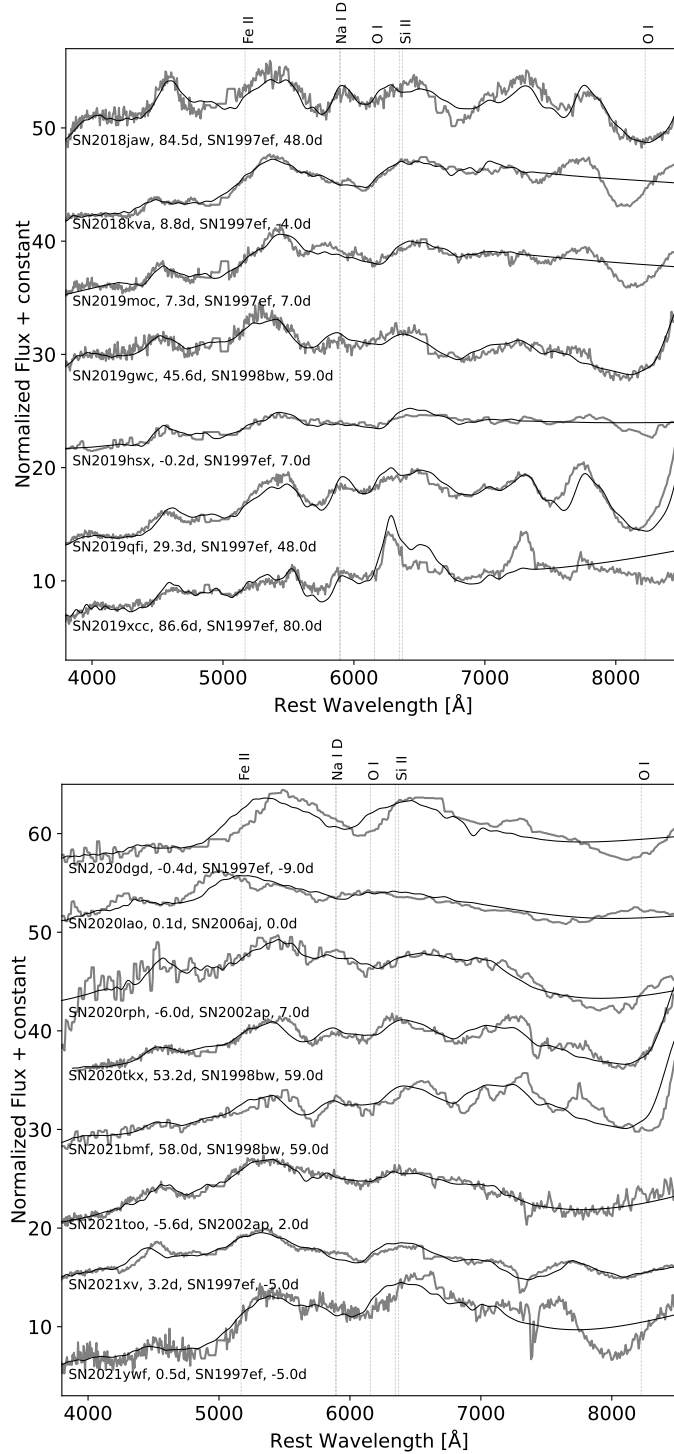


Figure 2.1: Classification spectra for the SNe Ic-BL in our sample, along with their SNID best-match templates, labeled by name, supernova phase relative to the peak light, and corresponding template name, and template phase from SNID. GRB190829A only has a host spectrum, which we do not display here. The spectra for SN 2018gep and SN 2020bvc are published in Ho et al. (2019) and Ho et al. (2020a) so we do not show them here. The spectra show broad Fe II, Si II and O I lines. The Na I D absorption line, an indicator of host extinction (Stritzinger et al., 2018a), is plotted for reference. None of the SNe appear to have strong Na I D features.

## **LCOGT**

We performed photometric follow-up of our SNe with the Sinistro and Spectral cameras on the Las Cumbres Observatory Global Telescope (LCOGT; Brown et al. 2013a) Network’s 1-m and 2-m telescopes respectively. The Sinistro (Spectral) camera has a field of view of  $26.5 (10.5)' \times 26.5 (10.5)'$  and a pixel scale of  $0.389 (0.304)''/\text{pixel}$ . The observations relied on two separate LCO programs: one aimed at supplementing ZTF light curves of Bright Transient Survey objects and the other intending to acquire late-time  $r$ - and  $i$ - band follow-up of stripped-envelope SNe fainter than 21 mag. The exposure times and number of images requested varied based on filter and desired depth, ranging from 160 s to 300 s and from 1 to 5 images. The data are automatically flat-fielded and bias-subtracted. Though both programs use different data reduction pipelines, the methodology is nearly the same. Both pipelines extract sources using the Source Extractor package (Bertin & Arnouts, 2010) and calibrate magnitudes against Pan-STARRS1 (PS1) (Chambers et al., 2016a; Flewelling, 2018) objects in the vicinity. The BTS-targeted program uses the High Order Transform of Psf ANd Template Subtraction code (HOTPANTS; Becker 2015) to subtract a PSF scaled Pan-STARRS1 template previously aligned using SCAMP (Bertin, 2006a). For the late-time LCOGT follow-up program, our pipeline performed image subtraction with pyzogy (Guevel & Hosseinzadeh, 2017a), based on the ZOGY algorithm (Zackay et al., 2016). Both pipelines stack multiple images to to increase depth.

## **WASP**

We performed deep imaging with the WAfer-scale imager for Prime (WASP), mounted on the Palomar 200-in. prime focus with a  $18.5' \times 18.5'$  field of view and a plate scale of  $0.18''/\text{pixel}$ . We obtained data from WASP for the transients at late times in the  $g'$ -,  $r'$ - and  $i'$ - filters. The data were reduced using a python based pipeline that applied standard optical reduction techniques (as described in ?), and the photometric calibration was obtained against PS1 sources in the field. Image subtraction was performed with HOTPANTS with references from PS1 and SDSS.

## **SEDM**

We obtained additional photometric follow-up with the Spectral Energy Distribution Machine (SEDM; Blagorodnova et al. 2018a; Kim et al. 2022a; Rigault et al. 2019a) on the Palomar 60-inch (P60) telescope which has a field of view of  $13'$

x 13' and a plate scale of 0.378''/pixel. The processing is automated, and can be triggered using the Fritz marshal (Duev et al., 2019; Kasliwal et al., 2019; van der Walt et al., 2019). Standard imaging requests involve  $g-$ ,  $r-$ , and  $i-$  band 300s exposures with the Rainbow Camera on SEDM. The data are later reduced using a python-based pipeline that applies standard reduction techniques and applies a customized version of FPipe (Fremling Automated Pipeline; Fremling et al. 2016a) for image subtraction.

### **Liverpool IO:O**

We acquired late-time, multi-band imaging with the Liverpool Telescope (Steele et al., 2004) using the IO:O camera with the Sloan *griz* filter set. The IO:O camera has a 10'x10' field of view with a plate scale of 0.15''/pixel. An automatic pipeline reduces the images, performing bias subtraction, trimming of the overscan regions, and flat fielding. Once a PS1 template is aligned, the image subtraction takes place, and the final photometry comes from the analysis of the subtracted image.

### **GROWTH-India Telescope**

We obtained photometric follow-up of our SNe with the 0.7m robotic GROWTH-India Telescope (GIT; Kumar et al. 2022) equipped with a 4096x4108 pixel back-illuminated Andor camera. GIT has a circular field of view of 0.86deg x 0.86 deg (corresponding to 51.6' x 51.6') and has a pixel scale of 0.676''/pixel. GIT is located at the IAO (Hanle, Ladakh). Targeted observations were conducted in SDSS  $r'$ , and  $i'$  filters with varying exposure times. All data were downloaded in real time and processed with the automated GIT pipeline. Zero points for photometry were calculated using the PanSTARRS catalogue (Flewelling, 2018), downloaded from Vizier (Ochsenbein et al., 2000). We performed image subtraction with pyzogy and PSF photometry with PSFEx (Bertin, 2011).

### **WIRC**

We obtained near-infrared follow-up imaging of candidates with the Wide-field Infrared Camera (WIRC; Wilson et al. 2003), on the Palomar 200-inch telescope (P200) in  $J-$ ,  $H-$  and  $K$ -short ( $Ks-$ ) bands. WIRC's field of view is 8.7' x 8.7' with a pixel scale of 0.2487''/pixel. The WIRC data was reduced using the same pipeline as described above for WASP, but it was additionally stacked using Swarp (Bertin, 2010) while the calibration was done using the 2MASS point source cata-

log (Skrutskie et al., 2006). We obtained the WIRC data during classical observing runs on a  $\sim$ monthly cadence between January 2019 and December 2021. Due to the fact that the 2MASS Catalog is far shallower ( $J = 15.8, H = 15.1, K_s = 14.3$   $m_{AB}$ ; Skrutskie et al. 2006) compared to WIRC’s limiting magnitudes ( $J = 22.6, H = 22.0, K_s = 21.5$ , in AB mag), we obtained reference images with WIRC after the SNe had faded in order to perform reference image subtraction. We perform image subtraction using the HOTPANTS algorithm and obtain aperture photometry using PHOTUTILS (Bradley et al., 2020).

## **Spectroscopy**

### **SEDM**

We also used the SEDM’s low-dispersion ( $R \sim 100$ ) integral field spectrograph (IFU) to obtain classification spectra for several of our objects. The field of view is  $28'' \times 28''$  with a pixel scale of  $0.125''/\text{pixel}$ . The SEDM is fully roboticized from the request submission to data acquisition to image reduction and uploading. The IFU images are reduced using the custom SEDM IFU data reduction pipeline (Blagorodnova et al., 2018a; Rigault et al., 2019a), which relies on the steps flat-fielding, wavelength calibration, extraction, flux calibration, and telluric correction.

### **DBSP**

We obtained low to medium resolution ( $R \sim 1000-10000$ ) classification spectra of many of the SNe in our sample with Double Spectrograph (DBSP; Oke & Gunn 1982) on the Palomar 200-in telescope. Its plate scale is  $0.293''/\text{pixel}$  (red side) and  $0.389''/\text{pixel}$  (blue side) and field of view is  $120'' \times 70''$ . The setup included a red grating of 316/7500, a blue grating of 600/400, a D55 dichroic, and slitmasks of  $1'', 1.5'',$  and  $2''$ . Some of our data was reduced using a custom PyRAF DBSP reduction pipeline (Bellm & Sesar, 2016a) while the rest were reduced using a custom DBSP Data Reduction pipeline relying on Pypeit (Prochaska et al., 2019; Roberson et al., 2022).

### **LRIS**

Some of the SNe in our sample also have spectra from the Low Resolution Imaging Spectrometer (LRIS; Oke et al. 1995) mounted on the 10 m Keck I telescope. LRIS has a  $6' \times 7.8'$  field of view and a pixel scale of  $0.135''/\text{pixel}$ . We used the 400/3400 grism on the blue arm and the 400/8500 grating on the red arm, with a central

wavelength of 7830 Å to cover the bandpass from 3,200-10,000 Å. We used longslit masks of 1.0'' and 1.5'' width. We typically used an exposure time of 600 s to obtain our classification spectra. The spectra were reduced using LPipe (Perley, 2019).

## NOT

We obtained low-resolution spectra with the Alhambra Faint Object Spectrograph and Camera (ALFOSC)<sup>1</sup> on the 2.56 m Nordic Optical Telescope (NOT) at the Observatorio del Roque de los Muchachos on La Palma (Spain). The ALFOSC has a field of view of 6.4' x 6.4' and a pixel scale of 0.2138''/pixel. The spectra were obtained with a 10 wide slit and grism #4. The data were reduced with IRAF and PyeIt. The spectra were calibrated with spectrophotometric standard stars observed during the same night and the same instrument setup.

### 2.4 Description of ZTF Candidates

In the section below we include descriptions of all of the 18 candidates with ZTF data that were analyzed in this paper, including details about its discovery, coincident radio and X-ray data and any other notable characteristics about the objects. Our literature sample is described in Section 2.5. Some of these candidates are part of a companion study (Corsi et al., 2023) focusing on radio properties of SNe Ic-BL; the full ZTF sample of SNe Ic-BL will be presented in Srinivasaragavan et al., in prep. For all Swift XRT fluxes reported from the companion study, we assume a spectral model of a power-law spectrum with photon index  $\Gamma = 2$  corrected for Galactic absorption only. The 90% flux upper limits for Swift XRT reported below are calculated by converting counts to flux using the same power-law model. All Swift fluxes have an energy range of 0.3-10 keV. For a more thorough discussion of whether the reported X-ray and radio emission correspond to transient or host-only emission, see Sections 3.4 and 3.5 of Corsi et al. (2023).

The objects described here range from  $M_r = -16.58$  to  $M_r = -20.60$  mag and from  $z = 0.017$  to  $z = 0.056$  (excluding the LLGRB, at  $z = 0.077$ ). All of the transients included below are ZTF SNe, but we hereafter refer to them by their IAU names. We performed forced photometry (using the MCMC method) for all of the candidates using ForcePhotZTF<sup>2</sup> (Yao et al., 2019).

We found no coincident *Fermi*, *Swift*, *MAXI*, *AGILE*, or *INTEGRAL* GRB trig-

<sup>1</sup><http://www.not.iac.es/instruments/alfosc>

<sup>2</sup><https://github.com/yaoyuhan/ForcePhotZTF>

gers or serendipitous *Chandra* or *XMM* X-ray coverage for these SNe based on their derived explosion dates. Though several candidate counterparts were found in temporal coincidence with *KONUS* instrument on the Wind satellite, the explosion epoch uncertainties hinder our ability to make any firm association to the *KONUS* sources. These objects are summarized in Tables 2.1, and their classification spectra are shown in Figure 4.2.

### SN 2021ywf

Our first ZTF photometry of SN 2021ywf (ZTF21acbnfos) was obtained on 2021 September 12 (MJD = 59469.47) with the P48. This first detection was in the  $r$ -band, with a host-subtracted magnitude of  $20.03 \pm 0.20$ , at  $\alpha = 05^h 14^m 11.00^s$ ,  $\delta = +01^\circ 52' 52.3''$  (J2000.0). The discovery was reported to TNS on 2021 September 14 (Nordin et al., 2021), with a note saying that the latest non-detection from ZTF was just 1 day prior to discovery ( $r = 20.2$  mag). The high cadence around discovery allows for a well constrained explosion date. With power-law fits to the early  $g$ - and  $r$ - band data, we estimate the explosion date as  $\text{MJD}_{\text{explosion}}^{\text{SN2021ywf}} = 59467.70 \pm 0.2$  (see below).

We classified the transient as a Type Ic-BL using a spectrum from P200+DBSP obtained on 2021 September 27 (Chu et al., 2021). The first spectrum was actually obtained using the P60+SEDM. However, the quality of that spectrum was not good enough to warrant a classification. SN 2021ywf exploded in the outskirts of the spiral galaxy CGCG 395-022 with a well established redshift of  $z = 0.028249$ , which corresponds to a luminosity distance of 127.85 Mpc and a distance modulus of 35.534. This redshift is confirmed with narrow host lines in our classification spectrum.

On 2021 September 30, SN 2021ywf was detected ( $3.2\sigma$  significance) both with the *Swift* XRT with  $5.3_{-3.3}^{+4.9} \times 10^{-14}$  erg cm $^{-2}$  s $^{-1}$  in a 7.2 ks observation, and with the VLA at  $83 \pm 10 \mu\text{Jy}$  at 5.0 GHz (see Corsi et al. 2023 for details).

### SN 2021xv

Our first ZTF photometry of SN 2021xv (ZTF21aadatfg) was obtained on 2021 January 10 (MJD = 59224.52) with the P48. The transient was discovered in the public ZTF alert stream and reported by ALERCE (Forster, 2021). This first detection was in the  $r$ - band, with a host-subtracted magnitude of 19.93, at  $\alpha = 16^h 07^m 32.82^s$ ,  $\delta = +36^\circ 46' 46.07''$  (J2000.0). The discovery was reported to TNS (Förster et al., 2021), with a note saying that the last non-detection was 3 days before discovery

(on 2021 January 07 at  $r = 19.52$  mag). We classified the transient as a Type Ic-BL using a spectrum from the NOT+ALFOSC obtained on 2021 Jan 25 (Schulze & Sollerman, 2021). The transient appears to be associated with the galaxy host SDSS J160732.83+364646.1. We measure a redshift of  $z = 0.041$  from the narrow host lines in the NOT spectrum, corresponding to a luminosity distance of 187.29 Mpc and a distance modulus of 36.363. SN 2021xv was marginally detected with the VLA on 2021 May 19 at  $F_\nu = 34.3 \pm 8.1 \mu\text{Jy}$  at 5.2 GHz, but the detection is consistent with host galaxy emission (see Corsi et al. 2023 for details).

### **SN 2021too**

SN 2021too (ZTF21abmjgwf) was reported first by the PS1 Young Supernova Experiment on 2021 July 17 (MJD = 59412.60) with the internal name PS21iap, but the first ZTF alerts are from 2021 July 16. This first detection was in the  $i$ -band, with a host-subtracted magnitude of 19.5, at  $\alpha = 21^{\text{h}}40^{\text{m}}54.28^{\text{s}}$ ,  $\delta = +10^{\circ}19'30.3''$  (J2000.0). The discovery was reported to TNS (Jones et al., 2021). Our last non-detection with ZTF was on 2021 July 16 at  $r = 20.4$  mag. The transient was classified as a Type Ic-BL using a spectrum from EFOSC2-NTT obtained on 2021 August 02 by ePESSTO (Pessi et al., 2021). The object was positioned in the star-forming galaxy SDSS J214054.29+101930.5. We measure a redshift of 0.035 from the narrow host lines in its P200+DBSP spectrum taken on 2021 Aug 07. This corresponds to a luminosity distance of 159.19 Mpc and a distance modulus of 36.01.

### **SN 2021bmf**

SN 2021bmf (ZTF21aagtpro) was discovered by ATLAS on 2021 January 30 (MJD = 59244.0) with the internal name ATLAS 21djt, and later by ZTF (MJD = 59248.0). This first detection was in the  $o$  band, with a host-subtracted magnitude of 18.12, at  $\alpha = 16^{\text{h}}33^{\text{m}}29.41^{\text{s}}$ ,  $\delta = -06^{\circ}22'49.53''$  (J2000.0). The discovery was reported to TNS (Tonry et al., 2021), with a note saying that the last non-detection was on 2021 January 16 at  $c = 18.4$  mag. The transient was classified as a Type Ic-BL using a spectrum from ePESSTO obtained on 2021 February 03 (Magee et al., 2021). SN 2021bmf was found in the faint host galaxy SDSS J163329.48-062249.9, which was determined to be at  $z = 0.0175$  based on narrow host lines in the Keck I LRIS spectrum taken on 2021 July 09, which corresponds to a luminosity distance of 78.57 Mpc and a distance modulus of 34.476.

### SN 2020tkx

Our first ZTF photometry of SN 2020tkx (ZTF20abzoeiw) was obtained on 2020 September 16 (MJD = 59108.26) with the P48. This first detection was in the  $g$ -band, with a host-subtracted magnitude of  $18.09 \pm 0.08$ , at  $\alpha = 18^h 40^m 09.01^s$ ,  $\delta = +34^\circ 06' 59.5''$  (J2000.0). The discovery was done by Gaia two days earlier (Hodgkin et al., 2020). The last ZTF non-detection is from 2021 September 07, a full week before discovery, and the constraints on the explosion date are therefore imprecise.

The transient was classified as a Type Ic-BL by Srivastav et al. (2020) based on a spectrum from the Spectrograph for the Rapid Acquisition of Transients (SPRAT) on LT, obtained on 2020 September 18. Our sequence of P60 spectra taken in 2020 confirm this classification.

SN 2020tkx exploded in a faint host galaxy without a known redshift. Using the spectral template fitting SNID for our best NOT+ALFOOSC spectrum taken on 2020 November 18, the redshift can be constrained to  $z \sim 0.02 - 0.03$ , and our adopted redshift of  $z = 0.027$  is based on a weak, tentative  $H\alpha$  line from the host galaxy in the spectrum. The adopted redshift translates to a luminosity distance of 122.09 Mpc and a distance modulus of 35.433.

The object has an upper limit of  $< 3.3 \times 10^{-14}$  erg cm $^{-2}$  s $^{-1}$  with the *Swift* XRT (8.1 ks exposure) on 2020 October 03, 8.9 days after peak light. SN 2020tkx was detected with the VLA at  $286 \pm 15$   $\mu$ Jy (10 GHz) on 2021 September 25 (see Corsi et al. 2023 for more details).

### SN 2020rph

Our first ZTF photometry of SN 2020rph (ZTF20abswdbg) was obtained on 2020 August 11 (MJD = 59072.49) with the P48. The transient was discovered in the public ZTF alert stream and reported by ALERCE. This first detection was in the  $r$  band, with a host-subtracted magnitude of 20.36, at  $\alpha = 03^h 15^m 17.82^s$ ,  $\delta = +37^\circ 00' 50.57''$  (J2000.0). The discovery was reported to TNS (Förster et al., 2020a), with the last non-detection just 1 hour before discovery at  $r = 19.88$  mag. We classified the transient as a Type Ic-BL using a spectrum from the P60+SEDM obtained on 2020 August 24 (Dahiwalé & Fremling, 2020a). The supernova was found offset from the galaxy WISEA J031517.67+370055.3. We measure a redshift of  $z = 0.042$  based on a Keck I LRIS spectrum taken on 2020 October 19, which corresponds to a luminosity distance of 192.0 Mpc and a distance modulus

of 36.42. SN 2020rph has a *Swift* XRT upper limit of  $f < 3.6 \times 10^{-14}$  erg cm<sup>-2</sup> s<sup>-1</sup> on 2020 August 27, 3.5 days after peak, in a 7.5 ks observation. It is detected with the VLA at  $42.7 \pm 7.4 \mu\text{Jy}$  (5.5 GHz) one day later, but the detection is consistent with host galaxy emission (see Corsi et al. 2023 for details).

### SN 2020lao

Our first ZTF photometry of SN 2020lao (ZTF20abbplei) was obtained on 2020 May 25 (MJD = 58994.41) with the P48. This first detection was in the *g*-band, with a host-subtracted magnitude of  $19.69 \pm 0.10$ , at  $\alpha = 17^h 06^m 54.61^s$ ,  $\delta = +30^\circ 16' 17.3''$  (J2000.0). The discovery was reported to TNS on the same day (Förster et al., 2020b). The field was well covered both before and after this first detection, and the P60 telescope was immediately triggered to provide *ugr* photometry 1.4 hours after first detection. The high cadence around discovery allows for a well constrained explosion date. With power-law fits to the early *g*- and *r*- data, we estimate the explosion date as  $\text{MJD}_{\text{explosion}}^{\text{SN2020lao}} = 58993.07 \pm 0.75$ .

SN 2020lao was also reported in a paper by the Transient Exoplanet Satellite Survey (TESS; Vallely et al. 2021) with high cadence photometry. The TESS paper finds a slightly different rise time ( $13.5 \pm 0.22$  days) relative to our ZTF observations; however this can be attributed to their broad peak and bandpass that may also contain NIR flux. On the other hand, we find that our narrow *i*-band peak is consistent with our estimated *r*-band peak.

Our first spectrum of this event was obtained with the P60+SEDM on 2020 May 26. It was mainly blue and featureless and did not warrant any classification. We obtained several more inconclusive spectra the following days, and the transient was finally classified as a Type Ic-BL by the Global SN Project on 2020 June 02 (Burke et al., 2020). Our subsequent P60+SEDM and NOT+ALFOSC spectra taken in 2020 confirmed this classification based on its broad Fe II features.

SN 2020lao exploded in the face on spiral galaxy CGCG 169-041 with a well established redshift of  $z = 0.030814$ , which corresponds to a luminosity distance of 141.3 Mpc and a distance modulus of 35.8. This redshift is confirmed with narrow host lines in our later spectra.

On 2020 June 07, 3.5 days after peak light, we obtained an upper limit on the *Swift* XRT flux of  $f < 2.9 \times 10^{-14}$  erg cm<sup>-2</sup> s<sup>-1</sup> (14 ks).

### SN 2020dgd

Our first ZTF photometry of SN 2020dgd (ZTF20aapcbmc) was obtained on 2020 February 19 (MJD = 58898.52) with the P48. This first detection was in the  $r$ - band, with a host-subtracted magnitude of 18.99, at  $\alpha = 15^h45^m35.57^s$ ,  $\delta = +29^\circ18'38.4''$  (J2000.0). The discovery was reported to TNS (Nordin et al., 2020), with a note saying that the last non-detection was 5 days before discovery (on 2020 February 14 at  $r = 20.03$  mag). We classified the transient as a Type Ic-BL using a spectrum from the P60 SEDM obtained on 2020 March 05 (Dahiwale & Fremling, 2020b). The transient appears to be separated by  $14''$  from any visible host galaxy in the vicinity; however with a Keck I LRIS spectrum taken on 2020 June 23 in the nebular phase (not shown in Figure 4.2), we measure weak host lines at a redshift of  $z = 0.032$ , corresponding to a distance of 145.2 Mpc and a distance modulus of 35.8. In addition, that LRIS spectrum of the SN exhibits strong Ca II emission features.

### SN 2020bvc

Our first ZTF photometry of SN 2020bvc (ZTF20aalxlis) was obtained on 2020 February 04 (MJD = 58883.0) with the P48. This first detection was in the  $i$ - band, with a host-subtracted magnitude of 17.48, at  $\alpha = 14^h33^m57.01^s$ ,  $\delta = +40^\circ14'37.5''$  (J2000.0). SN 2020bvc, reported originally in Ho et al. (2020a), shows very similar optical, X-ray and radio properties to SN 2006aj, which was associated with the low-luminosity GRB 060218. See Ho et al. (2020a) for more details about this object.

### SN 2019xcc

Our first ZTF photometry of SN 2019xcc (ZTF19adaiomg) was obtained on 2019 December 19 (MJD = 58836.48) with the P48. This first detection was in the  $r$ - band, with a host-subtracted magnitude of  $19.40 \pm 0.13$ , at  $\alpha = 11^h01^m12.39^s$ ,  $\delta = +16^\circ43'29.1''$  (J2000.0). The discovery was reported to TNS on the same day (Förster et al., 2019), with a note saying that the latest non-detection from ZTF was five days prior to discovery ( $r = 19.3$ ). This transient has very sparse light curves with only four data points from P48 in the alert stream, all in the  $r$ - band, but forced photometry also retrieved detections in the  $g$ - band.

The transient was classified as a Type Ic-BL by Prentice et al. (2019), based on a spectrum from SPRAT on the Liverpool Telescope obtained on 2019 December 20. We could confirm this classification with a spectrum from the Keck telescope a few

days later, using the LRIS instrument.

SN 2019xcc exploded close to the centre of the face on grand spiral CGCG 095-091 with a well established redshift of  $z = 0.028738$ , which corresponds to a luminosity distance of 129.8 Mpc, and a distance modulus of 35.6. This redshift is confirmed with narrow host  $H\alpha$  in our Keck spectrum.

### **SN 2019qfi**

SN 2019qfi (ZTF19abzwaen) was discovered by ATLAS on 2019 September 07 (MJD = 58743.29) with the internal name ATLAS2019vdc, with the first ZTF alerts around the same time. This first detection was in the  $o$  band, with a host-subtracted magnitude of 18.81, at  $\alpha = 21^h51^m07.90^s$ ,  $\delta = +12^\circ25'38.5''$  (J2000.0). The discovery was reported to TNS (Tonry et al., 2019a), with a note saying that the last non-detection was 6 days before the discovery at  $o = 18.69$  mag. We classified the transient as a Type Ic-BL using a spectrum from the P60+SEDM obtained on 2019 Sep 21 (Fremling et al., 2019a). SN 2019qfi was identified in the starforming galaxy SDSS J215107.99+122542.5 with a known spectroscopic redshift of  $z = 0.028$ . This corresponds to a luminosity distance of 129.0 Mpc and a distance modulus of 35.5.

### **SN 2019moc**

SN 2019moc (ZTF19ablesob) was first reported by ATLAS on 2019 August 04 (MJD = 58699.47) with the internal name ATLAS2019rgu. This first detection was in the  $c$  band, with a host-subtracted magnitude of 18.54, at  $\alpha = 23^h55^m45.95^s$ ,  $\delta = +21^\circ57'19.67''$  (J2000.0). However, its first ZTF detection preceded that of ATLAS, on 2019 July 31. The discovery was reported to TNS (Tonry et al., 2019b), with a note saying that the last non-detection was 6 days before discovery at  $c = 19.44$  mag. We classified the transient as a Type Ic-BL using a spectrum from the P200 DBSP obtained on 2019 Aug 10 (Dahiwale et al., 2019). The SN was found in the galaxy SDSS J235545.94+215719.7 with a known spectroscopic redshift of 0.055, corresponding to a luminosity distance of 257.6 Mpc and a distance modulus of 37.1.

### **SN 2019gwc**

Our first ZTF photometry of SN 2019gwc (ZTF19aaxfcpq) was obtained on 2019 June 04 (MJD = 58638.28) with the P48. This first detection was in the  $r-$  band,

with a host-subtracted magnitude of 19.73, at  $\alpha = 16^h 03^m 26.88^s$ ,  $\delta = +38^\circ 11' 02.6''$  (J2000.0). The discovery was reported to TNS (Nordin et al., 2019), with a note saying that the last non-detection was three days before discovery (2019 Jun 01 at  $r = 20.98$  mag). We classified the transient as a Type Ic-BL using a spectrum from the P60 SEDM obtained on 2019 Jun 16 (Fremling et al., 2019b). The transient was identified in the starforming host galaxy SDSS J160326.65+381057.1 at a known spectroscopic redshift of  $z = 0.038$ , corresponding to a distance of 173.2 Mpc, and a distance modulus of 36.2.

### SN 2019hsx

Our first ZTF photometry of SN 2019hsx (ZTF19aawqcgj) was obtained on 2019 June 02 (MJD = 58636.31) with the P48. This first detection was in the  $r$ -band, with a host-subtracted magnitude of  $18.62 \pm 0.08$ , at  $\alpha = 18^h 142^m 56.22^s$ ,  $\delta = +68^\circ 21' 45.2''$  (J2000.0). The discovery was reported to TNS (Fremling, 2019), with a note saying that the latest non-detection from ZTF was 3 days prior to discovery (May 30;  $g = 20.3$ ). We classified the transient as a Type Ic-BL using a spectrum from P60+SEDM obtained on June 14 (Fremling et al., 2019c). SN 2019hsx exploded fairly close to the center of NGC 6621 with redshift  $z = 0.020652$ . This corresponds to a distance of 92.9 Mpc and a distance modulus of 34.8. SN 2019hsx was detected with a *Swift* XRT flux of  $6.2_{-1.8}^{+2.3} \times 10^{-14} \text{ erg cm}^{-2} \text{ s}^{-1}$  (at  $\sim 6\sigma$ ) in a 15 ks observation on 2019 July 20, 36.7 days after peak.

### SN 2018kva

Our first ZTF photometry of SN 2018kva (ZTF18aczqzrj) was obtained on 2018 December 23 (MJD = 58475.51) with the P48. This first detection was in the  $r$ -band, with a host-subtracted magnitude of 19.08, at  $\alpha = 08^h 35^m 16.21^s$ ,  $\delta = +48^\circ 19' 03.4''$  (J2000.0). The discovery was reported to TNS (Fremling, 2018), with a note saying that the latest non-detection was 3 days before discovery, at  $g = 20.33$  mag. We classified the transient as a Type Ic-BL using a spectrum from the P60+SEDM obtained on 2019 Jan 03 (Fremling et al., 2019d). The object was identified in the host galaxy WISEA J083516.34+481901.2 at a known redshift of  $z = 0.043$ , which corresponds to a luminosity distance of 196.2 Mpc and a distance modulus of 36.5.

### SN 2018jaw

Our first ZTF photometry of SN 2018jaw (ZTF18acqphpd) was obtained on 2018 November 20 (MJD = 58442.51) with the P48. This first detection was in the  $g$ -band, with a host-subtracted magnitude of 18.39, at  $\alpha = 12^h54^m04.10^s$ ,  $\delta = +13^\circ32'47.9''$  (J2000.0). The discovery was reported to TNS (Nordin et al., 2018), with a note that the object was missing ZTF non-detection limits. We classified the transient as a Type Ic-BL using a spectrum from the P60+SEDM obtained on 2018 Dec 12 (Fremling et al., 2018), and tentatively estimated its redshift to be  $z = 0.037$ . However, the narrow host lines in the Keck I-LRIS spectrum taken on 2019 April 06 indicate that the object is at a redshift of  $z = 0.047$ . This corresponds to a luminosity distance of 168.5 Mpc and a distance modulus of 36.1. SN 2018jaw was identified in the galaxy host WISE J125404.15+133244.9.

### SN 2018gep

Our first ZTF photometry of SN 2018gep (ZTF18abukavn) was obtained on 2018 September 09 (MJD = 58370.16) with the P48. This first detection was in the  $r$ -band, with a host-subtracted magnitude of 20.5, at  $\alpha = 16^h43^m48.22^s$ ,  $\delta = +41^\circ02'43.4''$  (J2000.0).

SN 2018gep belongs to the class of Fast Blue Optical Transients (FBOTs) with its rapid rise time, high peak luminosity, and blue colors at peak (Pritchard et al., 2021). It was classified as a Ic-BL supernova whose early multi-wavelength data can be explained by late-stage eruptive mass loss. The transient is detected with the VLA over three epochs (9, 9.7 and 14 GHz), but the emission is likely galaxy-dominated. See Ho et al. (2019) for more details on the discovery of this supernova.

## 2.5 Literature sample

In addition to the ZTF SNe in our sample we examine the Open Supernova Catalog<sup>3</sup> for historical low-redshift SNe Ic-BL with  $\geq 3$  epochs of multi-band NIR photometry concurrent with the optical coverage. Our requirement for the minimum number of epochs is to probe the color evolution over time, which then can be compared against the  $r$ -process models. We exclude those objects with only NIR observations of the afterglow and early ( $\lesssim 10$  days from explosion) SN light curve, in the case of a GRB association. We find that SN 1998bw (Clocchiatti et al., 2011; Patat et al., 2001), SN 2002ap (Tomita et al., 2006; Yoshii et al., 2003), SN 2010bh (Olivares E. et al., 2012), and SN 2016coi (Terreran et al., 2019) match our criteria. We also find

<sup>3</sup><https://github.com/astrocatalogs/supernovae>

that SN 2016jca has extensive optical and NIR follow-up (Ashall et al., 2019; Cano et al., 2017b) but exclude it from further study because the reported NIR photometry is neither host- nor afterglow-subtracted.

SN 2016coi uniquely shows a huge  $4.5\ \mu\text{m}$  excess in the mid-infrared with archival WISE coverage in its late-time light curve. This object also has detections in the H-band past 300 days post-peak which coincide with the mid-IR detections. Given that it also has a bright radio counterpart, the mid-IR excess could be attributed to CO formation in the ejecta (Liljegren et al., 2022), or dust formation due to adiabatic cooling (Omand et al., 2019), or metal cooling in highly mixed SN ejecta (Omand & Jerkstrand, 2022). Though we lack model predictions in the mid-IR bands, we test whether the long-lived NIR emission could also be attributed to  $r$ -process production.

In addition, Bianco et al. (2014) collected optical and NIR photometry for a set of 61 stripped envelope SNe that also satisfy our low-redshift cut after conducting template-based subtraction in order to subtract host galaxy emission (for most SNe). Amongst the SNe in that sample classified as Type Ic-BL, only two SNe have observations in the  $J$ ,  $H$ , or  $K_s$  bands: SN 2007I and SN 2007ce. Similar to the case of our ZTF SNe, during the earlier epochs ( $< 60$  days post-peak) these two SNe have well sampled optical photometry, while later in time there is only NIR coverage. The second study, Stritzinger et al. (2018b), acquired optical light curves for 34 stripped-envelope SNe, 26 of which have NIR follow-up in the  $YJH$  bands as a part of the Carnegie Supernova Project. Explosion and bolometric light curve properties for some of these SNe were released in a companion paper (Taddia et al., 2018). Of the 26 SNe, only one (SN 2009bb) has adequate coverage at late times in the NIR.

Li et al. (2022) perform detailed blackbody fits to several SNe from the Open SN Catalog that have optical and NIR coverage to search for SNe that show NIR excesses in their SEDs that could be attributed to dust formation. Amongst the sample they consider, the authors find SN 2007I and SN 2009bb to be consistent with blackbody emission with a slight NIR excess that evolves from a photospheric temperature of  $\sim 5000$  ( $\sim 7000$ ) to 4300 K over the course of 51 (33) days in the case of SN 2007I (SN 2009bb). The same authors find that the SED of SN 2007ce is inconsistent with a blackbody, though they use only the early-time measurements of the object (at 1.9 days). Furthermore, Li et al. (2022) find no evidence for intrinsic dust formation or significant host extinction in order to explain their SEDs. In contrast

to their study, we note that our analysis includes photometry for these SNe over a much longer baseline taken from Bianco et al. (2014) and Stritzinger et al. (2018b). For each of the above-mentioned SNe, we correct for Galactic extinction where extinction has not been accounted for, and convert from Vega to AB magnitudes. We also correct the light curves for host attenuation for all of these SNe except for SN 1998bw (light curve already corrected for Galactic and host extinction) and SN 2007ce (lacks host galaxy extinction information); the assumed host  $E(B-V)$  values are listed in Table 2.3. We include host extinction here as it is significant for the literature SNe. The measurements of total ejecta mass, kinetic energy, and nickel mass for each object are recorded in Table 2.3, along with the appropriate reference we took these estimates from. We include the following seven SNe: SN 1998bw, SN 2002ap, SN 2010bh, SN 2016coi, SN 2009bb, SN 2007I and SN 2007ce in our analysis, described in Section 2.8.

## 2.6 Collapsar Light Curve Models

We model the evolution of the emission from  $r$ -process-enriched collapsars using a semi-analytic model of Barnes & Metzger (2022). While the details of our method are described there, we present an outline here.

The models comprise a series of concentric shells whose densities ( $\rho(v)$ ) follow a broken power law in velocity space:

$$\rho(v) \propto \begin{cases} v^{-n}, & v \leq v_t, \\ v^{-\delta} & v > v_t, \end{cases} \quad (2.1)$$

where we set the power-law index  $n$  ( $\delta$ ) equal to 1 (10). Our density profile, varying with velocity, contrasts with that of ?, which uses a one-zone formulation. Such a density profile is necessary to enrich SNe with  $r$ -process elements out to a particular mixing coordinate, as we describe below. In Eq. 2.1,  $v_t$  is a transition velocity chosen to produce the desired total mass  $M_{ej}$  and kinetic energy  $E_{kin}$ , which is parameterized via the average velocity  $v_{ej} = \sqrt{2E_{kin}/M_{ej}}$ . In addition to  $M_{ej}$  and  $v_{ej}$ , each model is characterized by its mass of  $^{56}\text{Ni}$ ,  $M_{56}$ , which we assume is uniformly distributed throughout the ejecta (Suzuki & Maeda, 2021; Taddia et al., 2018; Yoon et al., 2019). This choice departs from the analytical model of Arnett (1982), which assumes the nickel is centrally located. Furthermore, while the Arnett models do not allow for inefficient deposition of gamma-ray energy, these models calculate gamma-ray deposition based on a gray gamma-ray opacity. Thus these models do not match the Arnett models at maximum light. Different  $^{56}\text{Ni}$  profiles will also

affect the distribution of diffusion times, altering the shape of the bolometric light curve.

We assume that some amount  $M_{rp}$  of the ejecta is composed of pure  $r$ -process material, and that this material is mixed evenly into the ejecta interior to a velocity  $v_{mix}$ , which we define such that

$$\int_0^{v_{mix}} \rho(v) dV = M_{rp} M_{ej}, \quad (2.2)$$

with  $M_{rp}$  a parameter of the model, and  $dV$  the volume of the ejecta. (In other words, Eq. 2.2 shows that  $M_{rp}$  is the fraction of the total ejecta mass for which the  $r$ -process mass fraction is non-zero.) By distributing the  $r$ -process mass within a core of mass  $>M_{rp}$ , we account for hydrodynamic (e.g., Kelvin-Helmholtz) instabilities at the wind-ejecta boundary, which may mix the  $r$ -process-rich disk outflow out into the initially  $r$ -process-free ejecta.

The  $r$ -process elements serve as a source of radioactive energy beyond  $^{56}\text{Ni}/\text{Co}$ . More importantly (especially at early times—see Siegel et al. 2019), they impart to the enriched layers the high opacity (Hotokezaka et al., 2013; Kasen et al., 2013) known to be a unique feature of  $r$ -process compositions. This high opacity affects local diffusion times and the evolution of the photosphere, thereby altering SN emission relative to the  $r$ -process-free case.

We model the spectral energy distribution (SED) from the photospheric ejecta layers ( $r \leq R_{ph}$ ) as a black body, and integrate it to get the bolometric luminosity, given by

$$L = 4\pi R_{ph}^2 \sigma_{SB} T_{ph}^4 \quad (2.3)$$

with  $\sigma_{SB}$  the Stefan-Boltzman constant. The opacity in our model is gray and defined for every zone, allowing a straightforward determination of the photospheric radius  $R_{ph}$ . The photospheric temperature  $T_{ph}$  is then chosen so the RHS of Eq. 2.3 is equal to the luminosity emerging from behind the photosphere, which is an output of our calculation.

Since we are equally interested in SN signals beyond the photospheric phase, we also track emission from optically thin regions of the ejecta. These are assumed to have an SED determined by their composition. The  $r$ -process free layers conform to expectations set by observed SNe (e.g. Hunter et al., 2009). For enriched layers, we rely on theoretical studies of nebular-phase  $r$ -process transients (Hotokezaka

et al., 2021). The radioactive heating, opacity, and photospheric and nebular SEDs of each model are thus fully determined, allowing us to predict light curves and colors as a function of time.

## 2.7 Analysis

In the sections below, for the analysis and fitting of our light curves, we assume the central wavelengths for the optical and NIR bandpasses listed in Table 2.2, ignoring any small differences due to non-standard filters.

### Estimation of explosion properties

The combination of using both a volume-limited and a magnitude-limited survey for SN Ic-BL discovery has yielded SNe with a diverse range of absolute magnitudes. In Table 2.1 we summarize the SNe in our sample, which have redshifts ranging from 0.01 to 0.05 and peak  $r$ -band absolute magnitudes from  $M_r \sim -17$  mag to  $M_r \sim -19$  mag. For the purpose of this analysis, we consider distance uncertainty to have a negligible effect on our estimation of the explosion properties (the SNe we are fitting have a distance uncertainty of  $< 5$  Mpc). Here we summarize our process for deriving explosion parameters (i.e. total ejecta mass, kinetic energy, and nickel mass) from these SN light curves.

The details of the methodology behind our analysis of the bolometric light curves in this sample are described at length in a companion paper, Corsi et al. (2023), though only a subset of our sample is included in the companion paper. This analysis is done with the open-source code HAFFET<sup>4</sup> (Yang & Sollerman, 2023). First, we correct the light curves for Milky Way extinction, and then derive bolometric light curves from the  $g$ - and  $r$ - band photometry after calculating bolometric corrections from the empirical relations given in Lyman et al. (2014, 2016). In spite of the diversity in SNe Ic-BL colors and temporal evolution, Lyman et al. (2016) found that the variation in the bolometric magnitude was  $< 0.1$  mag; thus we consider the Lyman+ relations to be valid for our SN sample. We estimate the explosion epoch with power law fits unless the early-time SN data are limited, in which case the explosion times are set as the midpoint between the last non-detection before discovery and the first ZTF detection. We then fit the bolometric light curves to Arnett models (Arnett, 1982) between  $-20$  and  $60$  days from the peak to obtain the  $^{56}\text{Ni}$  mass,  $M_{56}$  and the characteristic timescale  $\tau_m$ .  $\tau_m$  is calculated from  $M_{\text{ej}}$ , the kinetic energy  $E_k$ , and the ejecta opacity  $\kappa$ , which is assumed to be a constant ( $0.07\text{cm}^2\text{g}^{-1}$ ;

<sup>4</sup><https://github.com/saberyoung/HAFFET>

Barbarino et al. 2021; Chugai 2000; Tartaglia et al. 2021). The uncertainties on our explosion epochs propagate into the uncertainties on  $\tau_m$ ,  $M_{ej}$ , and  $M_{56}$ . The early-time optical light curves of typical SNe Ic-BL are well approximated by the Arnett model which describes the  $^{56}\text{Ni}$ -powered light curve during the supernova’s photospheric phase.

For each of the SNe we estimate the photospheric velocity ( $v_{ph}$ ) using the earliest high-quality spectrum taken of the object. We use the IDL routine WOMBAT to remove host galaxy lines and tellurics, and then smooth the spectrum using SNspecFFTsmooth (Liu et al., 2016). The broad Fe II feature at 5169 Å is considered to be a proxy for the photospheric velocity of a Type Ic-BL SN (Modjaz et al., 2016). Thus we use the open source code SESNspectraLib<sup>5</sup> (Liu et al., 2016; Modjaz et al., 2016) to fit for the Fe II velocity by convolving with SN Ic templates. The velocities were measured at different phases for each SN, as shown in Figure 2.2.

We then estimate the kinetic energy,  $E_k$ , and the total ejecta mass  $M_{ej}$  of the explosion using our derived values for  $\tau_m$  and  $v_{ph}$  and the empirical relations from Lyman et al. (2016). In some cases where  $v_{ph}$  was only measured >15 days after the peak, we could only quote lower limits on the kinetic energy and ejecta mass of the explosion.

The explosion properties we derive are given in Table 2.9.

### Comparing color-color predictions to observations

Optical-NIR colors are a useful diagnostic to determine whether SNe Ic-BL could be potential sites of  $r$ -process production. The high opacity of  $r$ -process elements causes emission from the enriched regions to shift to redder wavelengths.

In Figure 2.3, we plot colors with respect to the  $r$ -band as  $r - X$  ( $X = J, H, K_s$ ) for  $r$ -process enriched models corresponding to the following parameters: “high mass, high velocity”:  $M_{ej} = 7.93 M_\odot$ ,  $\beta_{ej} = 0.25c$ ,  $M_{56} = 0.85 M_\odot$  (solid line), “medium mass, medium velocity”:  $M_{ej} = 2.62 M_\odot$ ,  $\beta_{ej} = 0.038c$ ,  $M_{56} = 0.39 M_\odot$  (dotted line), and “low mass, low velocity”:  $M_{ej} = 1.00 M_\odot$ ,  $\beta_{ej} = 0.033c$ ,  $M_{56} = 0.07 M_\odot$  (dashed line). This set of models illustrates how different combinations of assumed parameters affect the color curves. These specific model grids were used to fit the light curves of three objects in our sample and represent the broad range of explosion parameters derived for our SNe.

<sup>5</sup><https://github.com/nyusngroup/SESNspectraLib>

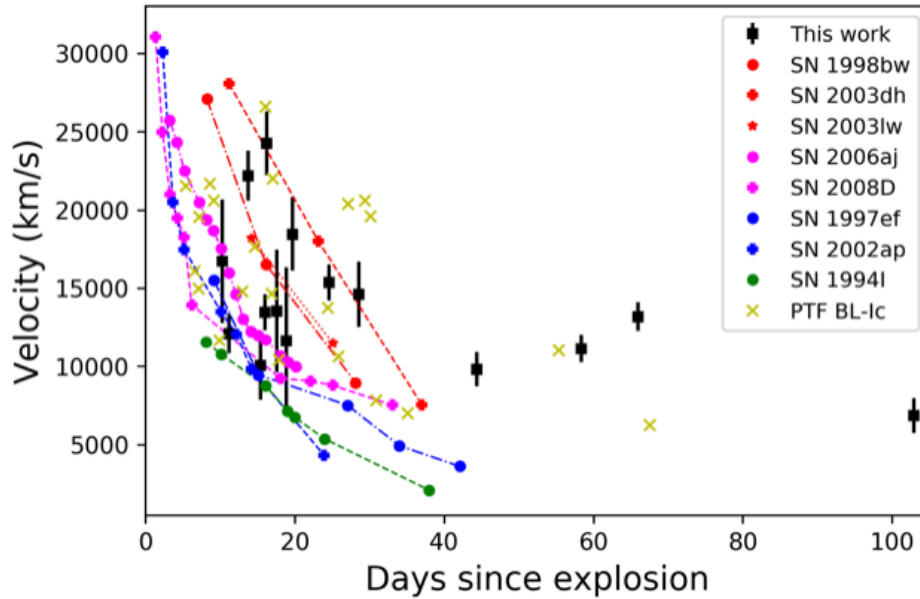


Figure 2.2: SN velocities measured from the Fe II 5169Å line as a function of the spectroscopic phase for each supernova in our sample (black points) plotted along with the measured velocities of SNe Ic-BL from the literature and from PTF (Taddia et al., 2018). The velocities we measure here are broadly consistent with both the literature and PTF sample.

We use these color evolution predictions from the models to compare against the optical-NIR colors of our SNe. Our  $r - X$  color measurements rely on two different methods: if there is an optical data point within three days of the NIR data point, we compute the color difference directly (filled circles); otherwise, we estimate the color by subtracting the NIR photometry from a scaled and shifted optical template (open circles). We construct this template from the light curve of SN 2020bvc, one of the SNe with the most well sampled light curves, and then compute the shift and scale factors needed for the template to fit the data. For the cases in which the optical model does not fit the optical light curve perfectly, there can be a systematic offset between the open and closed circles. For example, the estimated  $r - K_s$  color of SN 2019xcc (Figure 2.3, bottom panel) is  $> 1$  mag, but this is likely attributed to the fact that there is no concurrent optical photometry along with the  $K_s$ -band data point, and the optical light curve fades much faster than that of SN 2020bvc.

The predicted  $r - J$  colors for  $r$ -process collapsar light-curve models range from  $r - J \sim -0.5$  mag to  $r - J \sim 1.5$  mag. In the lefthand-side panels of Figure 2.3, we fix the mixing fraction to a moderate value of  $M_{rp} = 0.3$  and vary the amount of  $r$ -

process ejecta mass. On the righthand-side panels, we fix the  $r$ -process ejecta mass to  $0.01M_{\odot}$  and vary the mixing fraction. The amount of reddening in the model light curves is more strongly affected by the amount of mixing assumed; even for the lowest value of  $M_{rp}$ , we find prolific reddening predictions for high mixing fractions relative to models with moderate mixing fractions and high  $r$ -process yield.

However,  $r$ -process enrichment is not the only factor affecting colors; unenriched SN models also have a range of colors, depending on their masses, velocities, and nickel production. Even amongst different models with identical  $r$ -process composition, color evolution can be sensitive to the explosion properties assumed. Here, the “high mass, high velocity” model set also shows the most dramatic reddening predictions for models that have extreme mixing; in general, higher mass models tend to show larger  $r - X$  colors.

Late-time interaction with the circumstellar medium is also known to affect the color evolution of SNe (Ben-Ami et al., 2014; Kuncarayakti et al., 2022). While this is a rare phenomenon in SNe Ic-BL, SN 2022xxf showed evidence for a clear double-peaked light curve and narrow emission-line profiles in the later-phase spectra characteristic of interaction with a H/He-poor CSM (Kuncarayakti et al., 2023). SN 2022xxf also exhibited a dramatic red-to-blue color evolution as a result of interaction. We do not observe any of the above evidences for CSM interaction in our Ic-BL SNe, and therefore consider it unlikely that interaction could account for bluer colors at later times.

When comparing our color measurements against  $r$ -process models, we find that several of our objects show colors similar to the  $r$ -process models with minimal mixing. However, after 50 days post-peak, our detections and upper limits altogether strongly suggest that our SNe are brighter in the optical compared to the NIR. In particular, as many of our SNe are detected in the  $J$ -band over a wide range of phases, we can constrain the  $r - J$  color to  $< -0.5$  after 50 days post-peak. On the other hand, only one object shows  $r - J/H/K_s$  colors  $\sim 0.5$  mag: SN 2007I. In particular, SN 2007I exhibits an increase in its  $r - J$  color until about 60 days.

While these empirical color comparisons can be useful for identifying any obvious reddening signature that could be a smoking gun for  $r$ -process enrichment, more detailed fitting is required to establish whether or not these SNe are  $r$ -process enriched. Hence, in the next section, we describe our detailed model fitting aimed at determining whether there is room for an  $r$ -process contribution to their light curves.

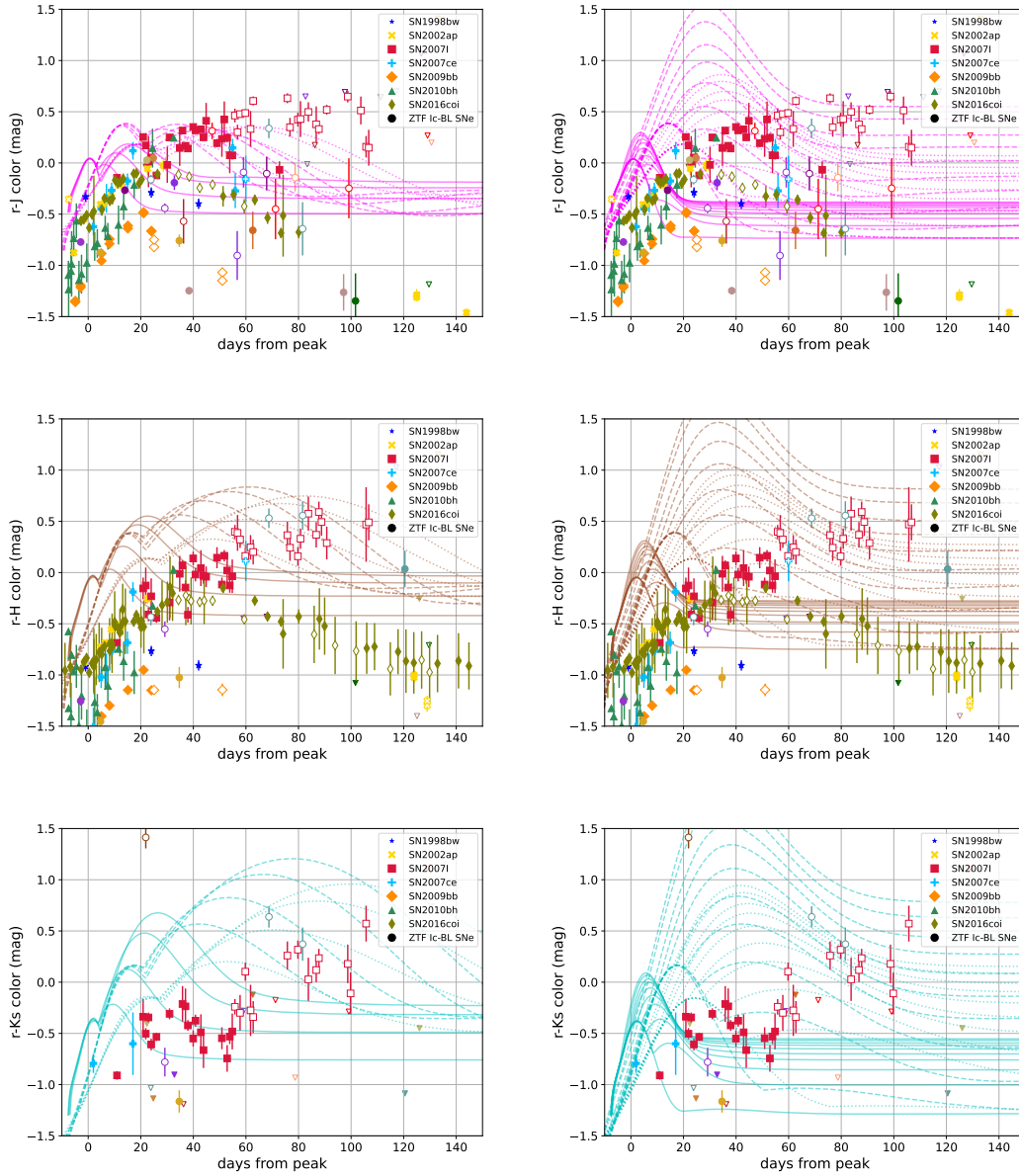


Figure 2.3:  $r - J$ ,  $r - H$ , and  $r - K_s$  color evolution plots for the  $r$ -process enriched models for a representative set of model parameters, compared to color measurements for the SNe in our sample. Each model is shown in a separate linestyle: “solid”:  $M_{\text{ej}} = 7.93 M_{\odot}$ ,  $\beta_{\text{ej}} = 0.25c$ ,  $M_{56} = 0.85 M_{\odot}$ , “dotted”:  $M_{\text{ej}} = 2.62 M_{\odot}$ ,  $\beta_{\text{ej}} = 0.038c$ ,  $M_{56} = 0.39 M_{\odot}$ , and “dashed”:  $M_{\text{ej}} = 1.00 M_{\odot}$ ,  $\beta_{\text{ej}} = 0.033c$ ,  $M_{56} = 0.07 M_{\odot}$ . When possible, the  $r - X$  color of observed SNe was estimated using either concurrent  $r$ -band photometry or the closest optical photometry within 3 days of a given NIR datapoint (filled markers). Otherwise, the  $r$ -band magnitude is extrapolated from a stretched and scaled light curve of SN 2020bvc (unfilled markers). Left: Fixing the mixing fraction to a moderate value of 0.3, we vary  $r$ -process ejecta masses  $[0.01, 0.03, 0.08, 0.13] M_{\odot}$ . Right: Fixing the  $r$ -process mass to a conservative value of  $0.01 M_{\odot}$ , we vary the mixing coordinate from 0.1 to 0.9. In general, the objects in our sample appear to have bluer colors relative to the models (with the exception of SN 2007I).

## 2.8 Results of Light Curve Model Fitting

To quantitatively determine whether  $r$ -process contribution is required to explain the light curves of SNe Ic-BL, we perform nested sampling fits over multi-dimensional parameter space spanned by the  $r$ -process enriched models. However, in order to perform the fitting, we need a distribution over functions with a *continuous* domain. Since these  $r$ -process models are discretely parameterized, we invoke gaussian process regression (GPR) to predict light curves from the training set (which are the  $r$ -process enriched models, in this case) for each linear combination over the continuous ranges of parameters.

We first considered the full grid of  $r$ -process enriched models from Barnes & Metzger (2022). For objects for which it was possible to estimate the total ejecta mass and kinetic energy, we select grids where the parameters fall within the following bounds:  $M_{\text{ej}} \in (M_{\text{ej},0} - 3\sigma, M_{\text{ej},0} + 3\sigma)$ ,  $\beta_{\text{ej}} \in (\beta_{\text{ej},0} - 3\sigma, \beta_{\text{ej},0} + 3\sigma)$ , and  $M_{56} \in (M_{56} - 3\sigma, M_{56} + 10\sigma)$ , where  $M_{\text{ej},0}$ ,  $\beta_{\text{ej},0}$ , and  $M_{56}$  are the independently derived explosion properties for the supernovae (see Table 2.9). We changed the upper bound on  $M_{\text{ej}}$  ( $\beta_{\text{ej}}$ ) to  $M_{\text{ej},0} + 10\sigma$  ( $\beta_{\text{ej},0} + 10\sigma$ ) for those SNe for which only a lower limit on those quantities was derived. We use the entire range of parameters in the grid for  $M_{\text{rp}}$  and  $M_{\text{rp}}$ .

We then perform singular value decomposition on each light curve in the model grid tailored to each supernova and interpolate between model parameters using scikit-learn’s GPR package, sampling between  $-5$  and  $200$  days relative to the supernova peak in a similar fashion to Coughlin et al. (2019) and Pang et al. (2022). We allow GPR to interpolate the range of  $r$ -process ejecta masses and mixing fractions between  $M_{\text{rp}} = 0.01 M_{\odot}$ ,  $M_{\text{rp}} = 0.1$  (which are technically the lowest values in the  $r$ -process enriched grid) and  $M_{\text{rp}} = 0.00$ ,  $M_{\text{rp}} = 0.0$ , though we do not allow it to exceed the maximum values for these quantities (i.e.  $M_{\text{rp}} \leq 0.15 M_{\odot}$  and  $M_{\text{rp}} \leq 0.9$ ). We limit interpolation of the remaining explosion parameters within the maximum and minimum bounds of the original grid. For a given set of explosion parameters ( $M_{\text{ej}}, \beta_{\text{ej}}, M_{56}$ ), each grid also contains an  $r$ -process-free model.

We compute a likelihood function based on the interpolated light curve models and our multi-band ZTF forced photometry, follow-up photometry, and WIRC photometry. Since the errors from GPR are small (i.e. they well approximate the original model grid), we assume a systematic fitting uncertainty of  $0.5$  mag in the NIR bands and a fitting uncertainty of  $1.0$  mag in the optical. We converged upon a  $1.0$  mag systematic uncertainty in the optical after evaluating how different assumed errors

affect the fit quality. The difference in the systematic errors is motivated by the fact that the NIR bands, rather than the optical bands, are a stronger determinant of whether there is evidence for  $r$ -process production. Furthermore, these assumptions on the systematic error compensate for the finer sampling in the optical bands relative to the NIR. In the likelihood calculation, we also impose a condition that rejects samples with a linear least squares fitting error worse than 1.0 mag. For the  $r$ -process enriched model fits, our prior also restricts the inference of parameters within the ranges of the grid ( $0.0 \leq x_{\text{mix}} \leq 0.90$ ;  $0.0 M_{\odot} \leq M_{\text{rp}} \leq 0.15 M_{\odot}$ ) and within physical constraints (i.e.  $M_{\text{rp}} < M_{\text{rp}}(M_{\text{ej}} - M_{56})$ ). We impose this upper limit on  $M_{\text{rp}}$  to satisfy the requirement that the  $r$ -process enriched core also contains  $^{56}\text{Ni}$  (see Figure 8 of Barnes & Metzger 2022). Finally, we employ PyMultinest's (Buchner et al., 2014) nested sampling algorithm to maximize the likelihood and converge on the best fit parameters and their uncertainties.

*Most of the SNe in our sample show no compelling evidence for  $r$ -process production.* In our model fits, the general trend we observe is that the best fit consistently under-predicts the peak of the optical light curve, while performing better at predicting the NIR flux. In some cases, the under-prediction is egregious, while in other cases it is more modest. In general under-prediction indicates that the optical-NIR color of the SN is actually *bluer* than predicted by the models, providing stronger evidence towards favoring  $r$ -process-free models over the enriched models. As mentioned earlier, as  $M_{\text{rp}}$  increases, the NIR light curve gets brighter; as  $M_{\text{rp}}$  increases, the optical light curve peak diminishes and the optical flux is suppressed more at later times.

To quantitatively assess the fit quality, we compute  $\chi^2$  values between the best fit model and the data points. We adopt the convention that if  $\chi^2 > \chi^2_{\text{crit}}$  (at the  $> 5\%$  level), we can reject our hypothesis that these SNe are well described by the best fit  $r$ -process enriched model. Therefore, given that our fits have 4 degrees of freedom, a  $\chi^2 > 9.49$  is indicative that the  $r$ -process enriched models are poor fits to the data. Applying this criteria suggests that SN 2018gep, SN 2019xcc and SN 2020rph are very unlikely to harbor  $r$ -process material in their ejecta.

Similarly, we select the subset of objects for which  $\chi^2 < \chi^2_{\text{crit}}$  for a p-value of 0.90 ( $\chi^2_{\text{crit}} = 1.06$ , for 4 degrees of freedom). Based on their  $\chi^2$  values, SN 1998bw, SN 2007ce, SN 2018kva, SN 2019gwc, SN 2020lao, SN 2020tkx, SN 2021xv and SN 2021bmf show the most convincing fits to the  $r$ -process enriched models. Upon visual inspection of the remainder of the light curve fits, we find that none of the

other objects are well described by the  $r$ -process model predictions. We display the corner plots showing the posterior probability distributions on the derived parameters in Figure 2.4 for the objects passing our  $\chi^2$  cut, along with the best fit light curves in Figure 2.5.

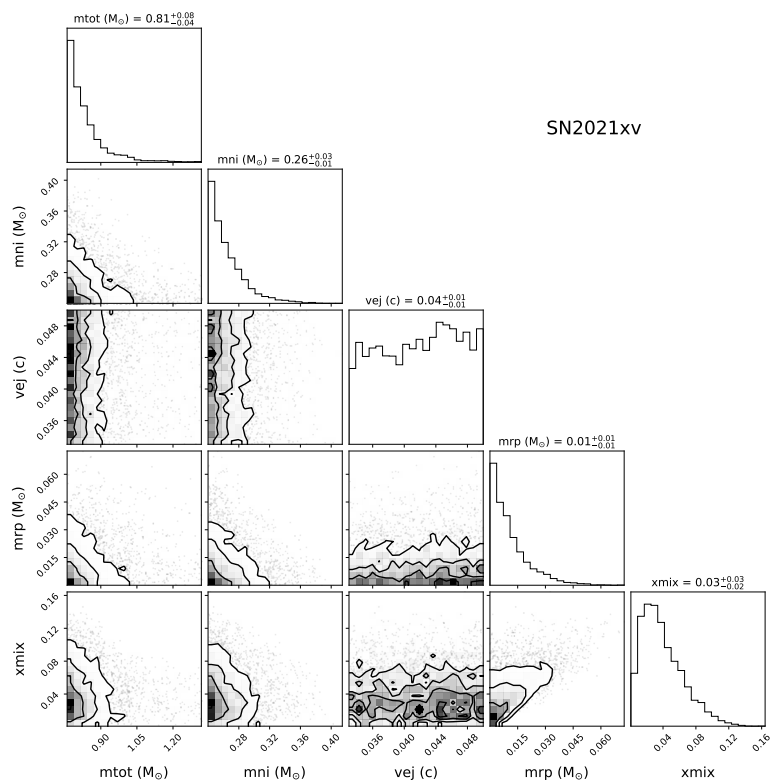
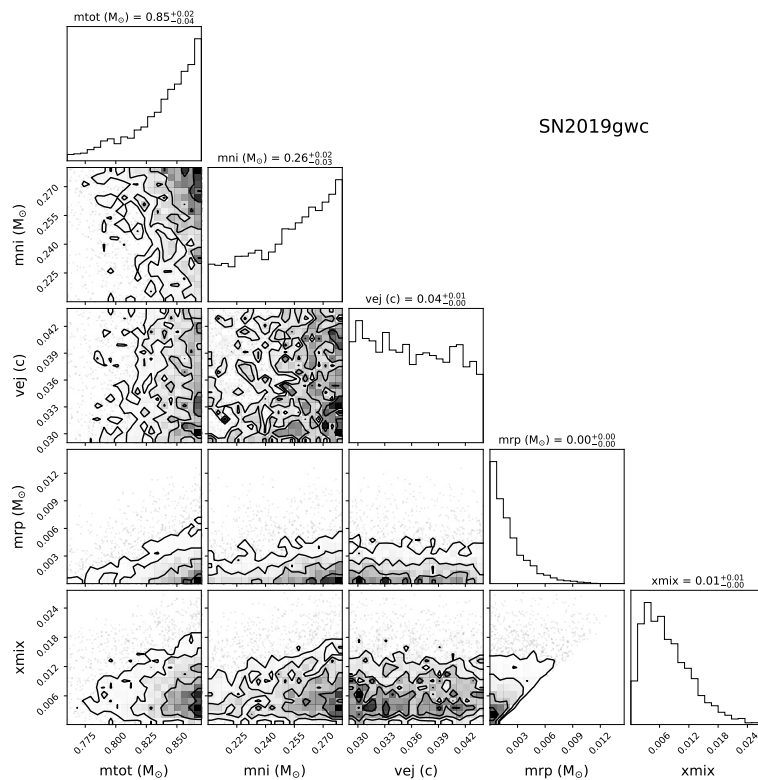
### **$r$ -process Candidate ZTF SNe**

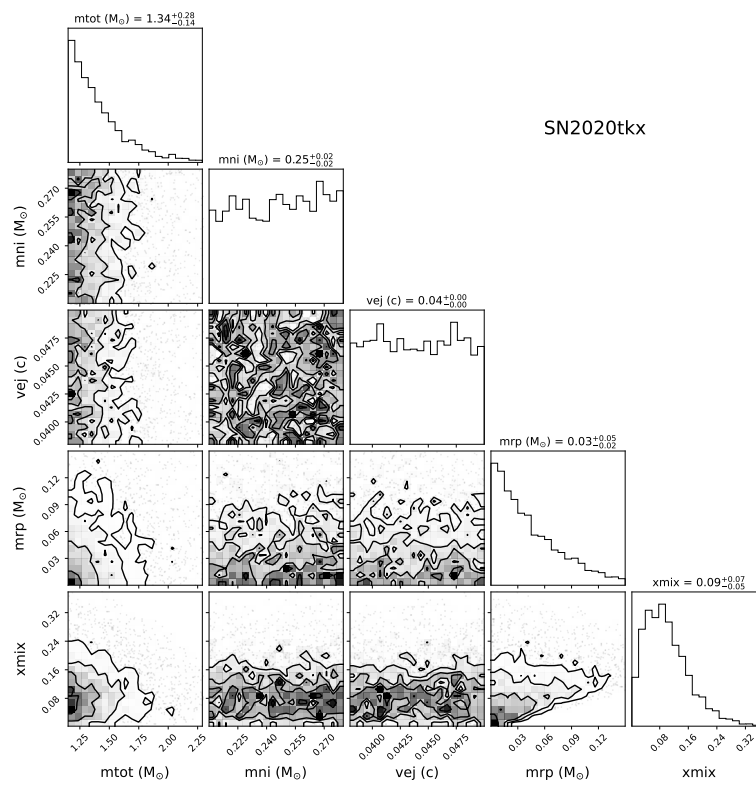
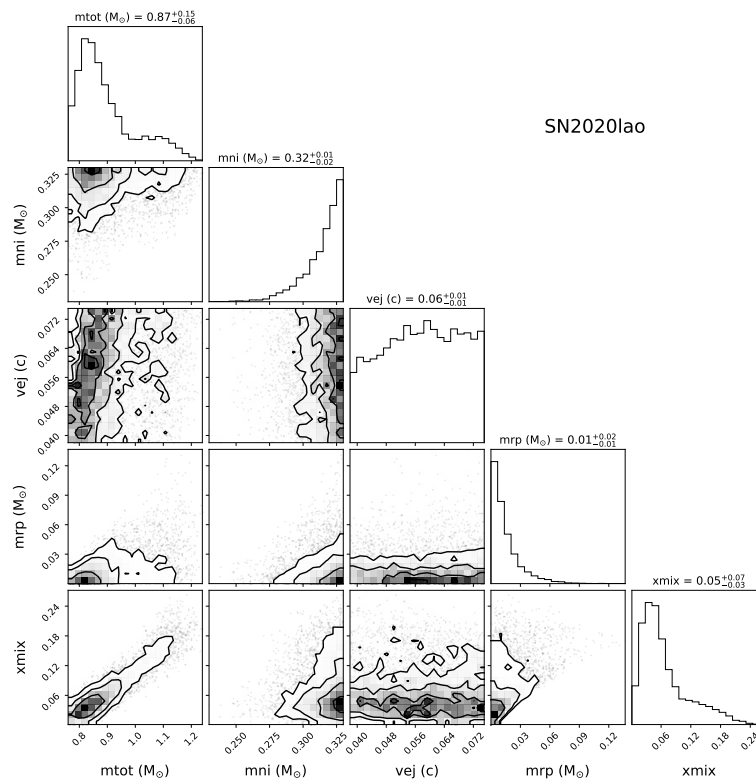
Only two of the SNe in this subset have well constrained parameters derived from the corner plots: SN 2020lao and SN 2021xv. The remainder of the objects have nearly flat posteriors on  $M_{56}$  and  $\beta_{ej}$ . For SN 2019gwc the peaks of the posterior probability distributions for both  $M_{rp}$  and  $M_{rp}$  are consistent with zero. This is supported by the fact that while both the  $r$ -band and  $i$ -band light curves are slightly under-predicted by the models, the  $J$ -band flux is also over-predicted; the observed colors are bluer than a best fit model with negligible  $r$ -process. SN 2020lao and SN 2021xv, in turn, have a best fit value of  $M_{rp} = 0.01 M_{\odot}$  and  $M_{rp} < 0.1$ . In the case of SN 2020lao, the optical flux is under-predicted by the models, and there are no NIR detections. On the other hand, for SN 2021xv, the optical models provide a decent fit to the optical data, but the NIR flux is still slightly over-predicted by the models.

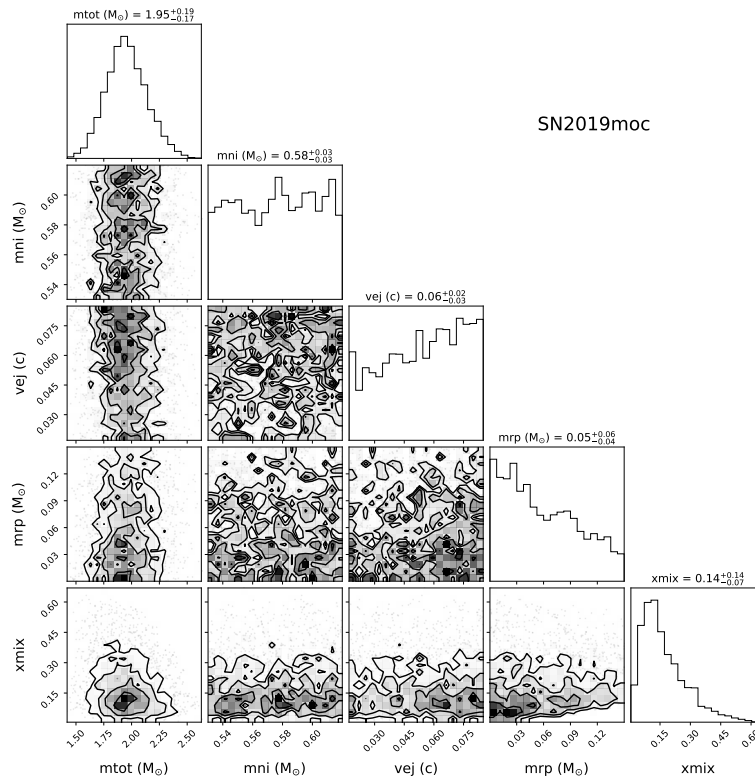
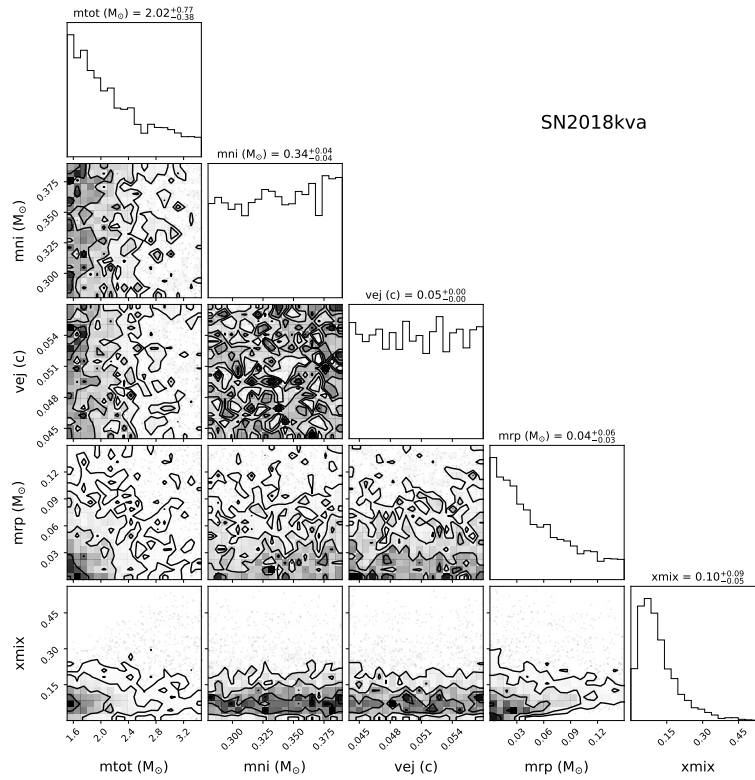
SN 2018kva, SN 2019moc, SN 2020tkx and SN 2021bmf show posterior support for higher  $r$ -process enrichment. SN 2020tkx and SN 2018kva have inferred values of  $M_{rp} \sim 0.03 M_{\odot}$  and  $M_{rp} \lesssim 0.1$ . For these two objects, the model under-predicts the peak of the optical light curve, though for SN 2018kva the  $J$ -band models fit the corresponding photometry. SN 2020tkx has two NIR detections in each of  $J$ ,  $H$ , and  $K_s$  filters which are well below the NIR model prediction, demonstrating that its light curve is inconsistent with the  $r$ -process enriched model. Finally, SN 2019moc and SN 2021bmf have parameter fits consistent with  $M_{rp} \gtrsim 0.03$  and  $M_{rp} \gtrsim 0.1$ . Similar to other cases, the best fit model for SN 2019moc under-predicts its optical light curve. While the model is consistent with the  $K_s$ -band upper limit, it still over-predicts the  $J$ -band flux. SN 2021bmf has one of the best-sampled optical light curves in our sample, and the model provides a beautiful fit to the optical bands. However, the NIR photometry is still vastly over-predicted by the same model.

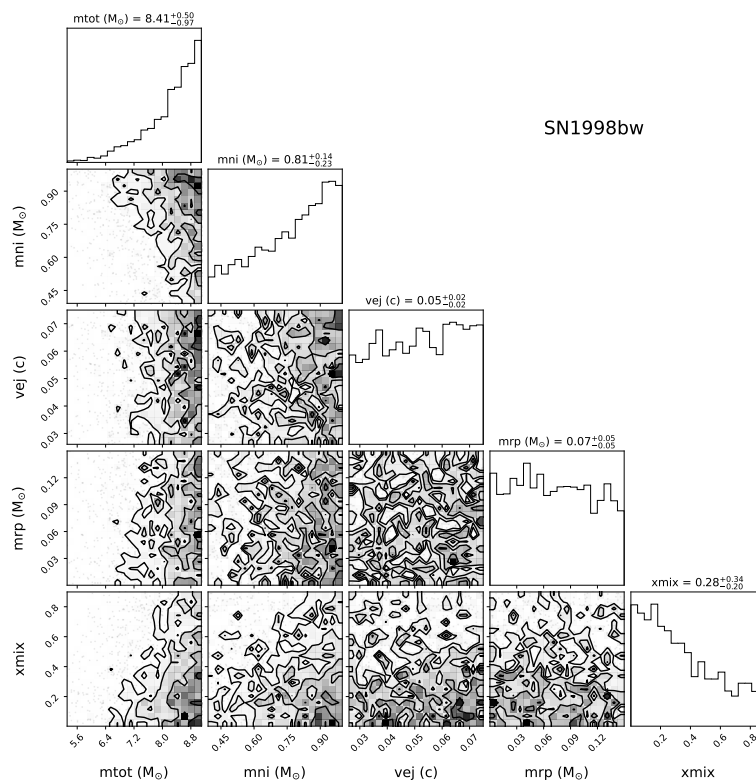
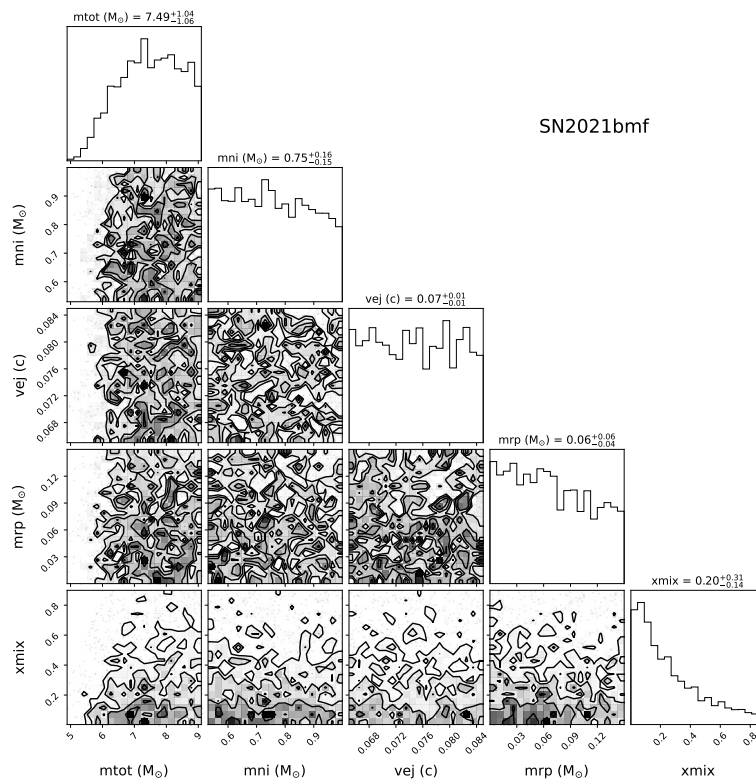
### **$r$ -process Candidate Literature SNe**

Similarly, the two objects with  $\chi^2$  fits that pass our criteria are SN 1998bw and SN 2007ce. In this category we also include SN 2007I because it shows more signif-









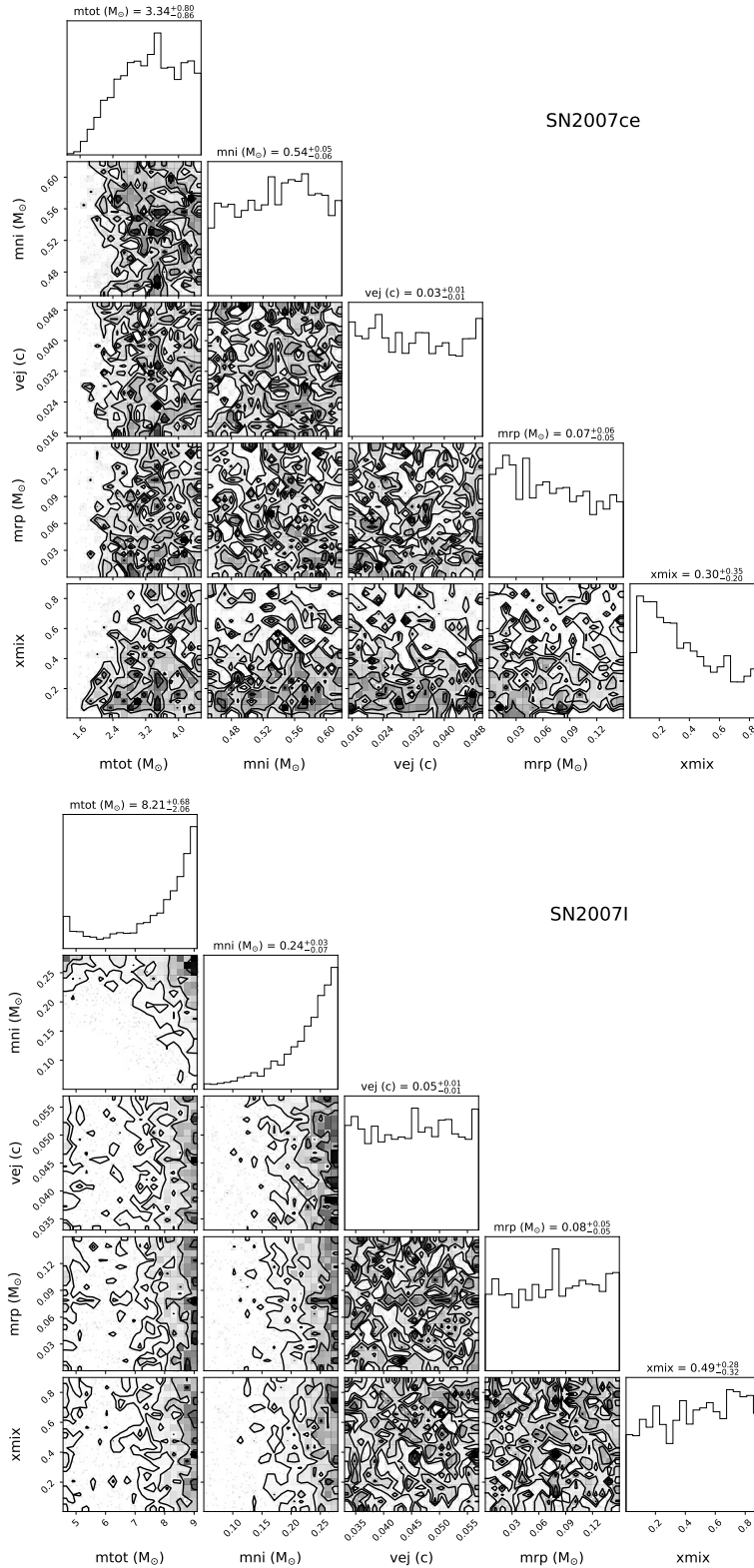
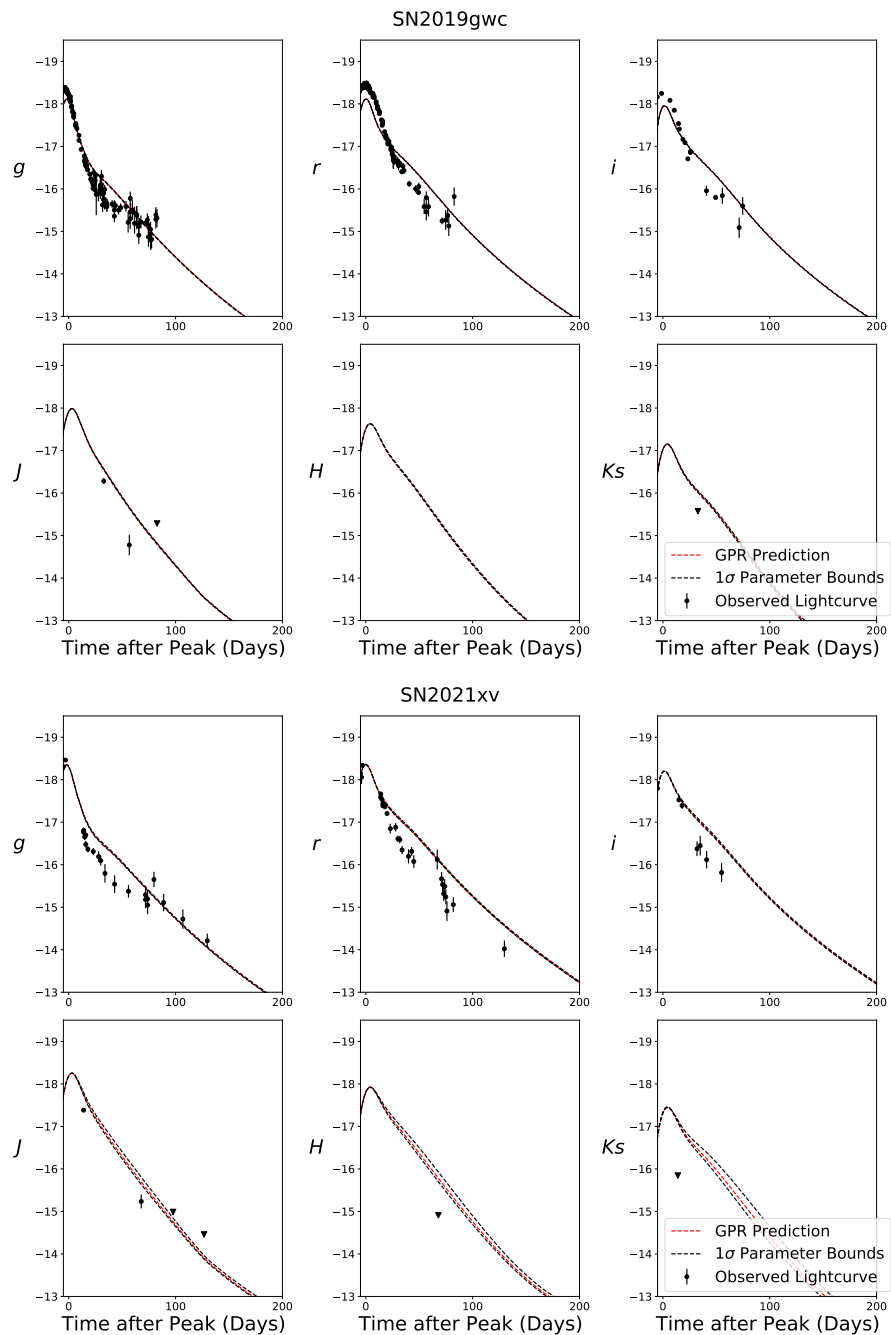
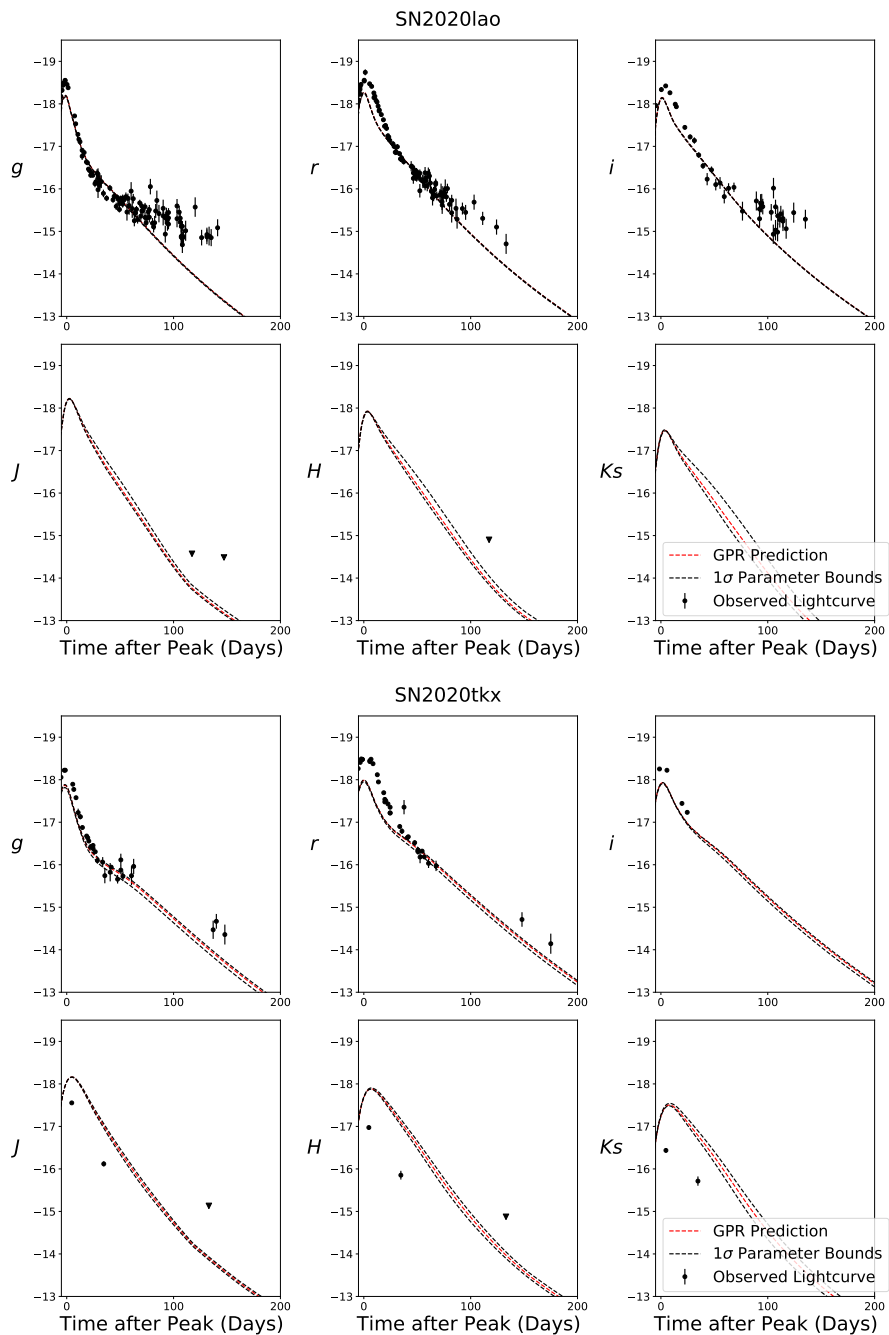
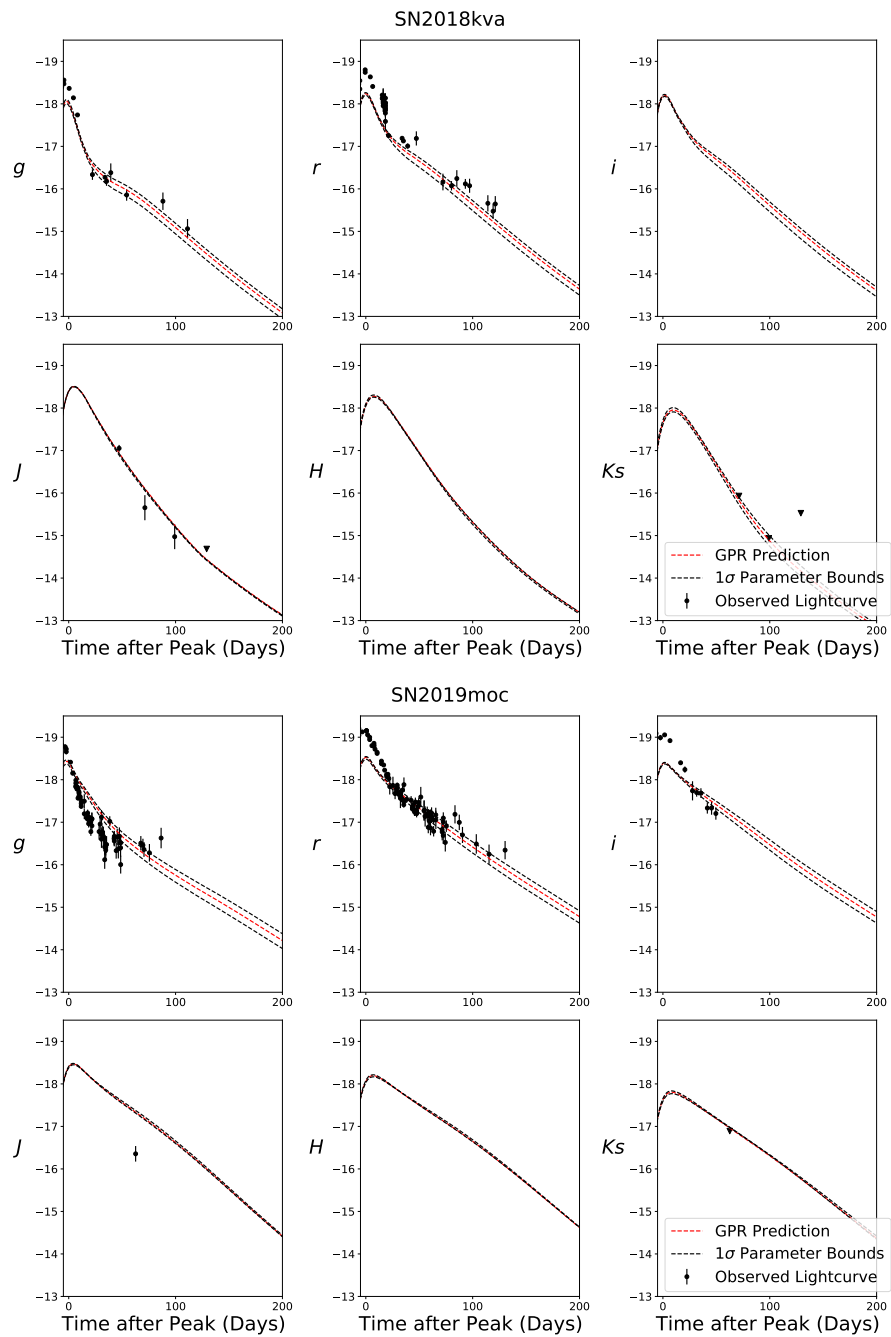
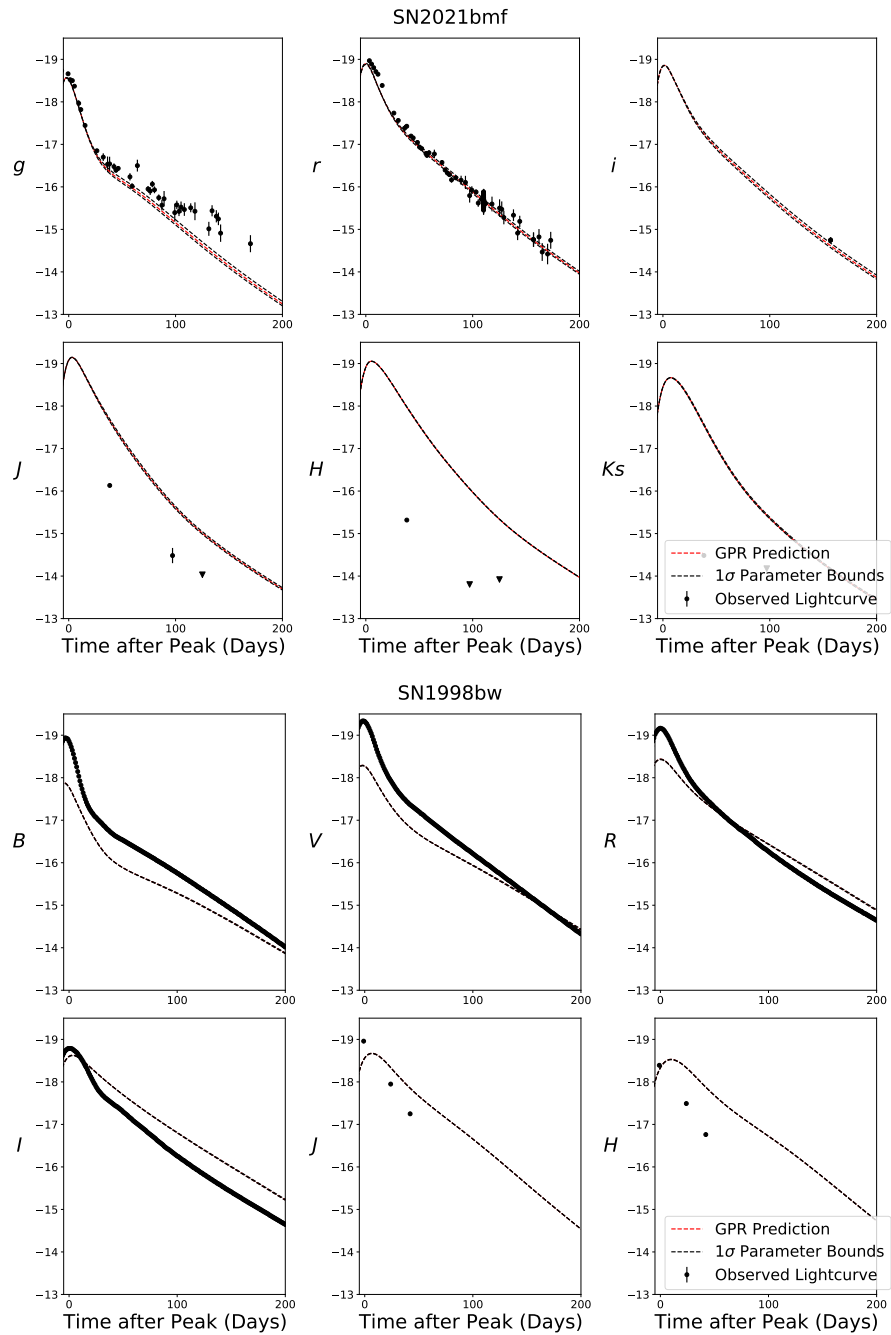


Figure 2.4: Corner plots showing the posterior probability distributions for each of the parameters in the  $r$ -process enriched models for the subset of objects satisfying our  $\chi^2$  cut, ordered by the amount of  $r$ -process mass inferred. The posterior probability plots are more well constrained for the objects with low inferred  $M_{\text{rp}}$ ; in the remaining cases, the posterior distributions are poorly constrained.  $M_{\text{ej}}$  and  $\beta_{\text{ej}}$  inferred here are generally in agreement with HAFJET, but discrepancies exist in the amount of nickel mass inferred.









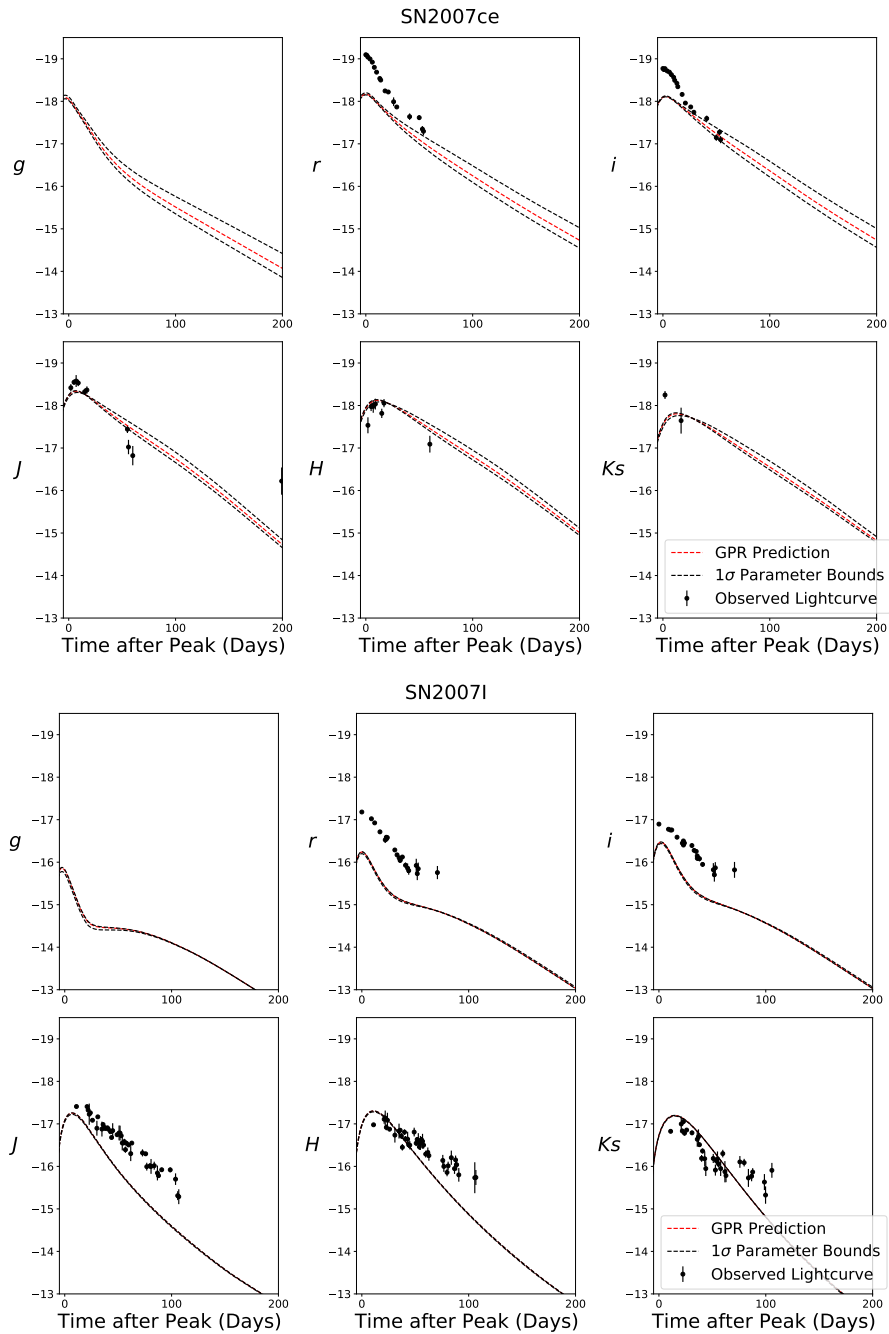


Figure 2.5: Plots of light curve models from Barnes & Metzger (2022) with best fit parameters (red dotted line) and corresponding  $1\sigma$  uncertainties (black) with photometric data overplotted, for both ZTF candidates and candidates from the literature shown in Figure 2.4 which pass our  $\chi^2$  cut, ordered by inferred  $M_{rp}$ . The objects whose optical and NIR photometry are both well described by the models are consistent with  $M_{rp} \lesssim 0.01 M_{\odot}$ . The remaining objects do not show convincing fits to the  $r$ -process enriched models.

icant photometric reddening relative to the other objects in the sample, even though it does not pass our nominal cuts.

The corner plots for these three objects show posterior distributions that are not well constrained. However, all three objects have high predicted values for both  $M_{rp}$  as well as  $M_{rp}$ . The light curve fits show the same phenomenon that we identify for the ZTF SN light curve fits: the peak of the optical light curve is under-predicted, while the NIR data shows better agreement with the models. In the case of SN 1998bw, the low  $\chi^2$  is likely attributed to the fact that the optical data are extremely well sampled, and the model provides a decent fit to its late-time light curve (in the  $B$ ,  $V$ , and  $R$ -bands), but the same model does not describe the decay in the NIR flux accurately. The best fit model for SN 2007ce matches the NIR bands but again under-predicts the optical. For SN 2007I, the  $riJ$ -band fluxes are wholly underestimated, and in the  $HK$ -bands, the light curve appears to be declining much slower than predicted by the models.

As emphasized by Barnes & Metzger (2022), color evolution can be a more powerful metric in comparison to absolute magnitude comparisons between the model light curves and data in determining whether a SN Ic-BL harbors  $r$ -process material. We thus plot color evolution ( $r - J/H/K_s$ ) as a function of time for our two reddest objects, SN 2007I and SN 2007ce. In Figure 2.6 we show their photometric colors along with their best fit  $r$ -process-free and  $r$ -process enriched models. In the shaded regions we include the  $\pm 1\sigma$  uncertainty on the model parameters from our fits. SN 2007ce's colors appear too blue in comparison with its best fit  $r$ -process model. We note that the color measurements for this object are secure because of several contemporaneous optical-NIR epochs. Given that it only attains a maximum  $r - X$  color of  $\sim 0.1$  mag 50 days post-peak, we conclude that SN 2007ce is most likely not an  $r$ -process collapsar. SN 2007I is completely inconsistent with the color evolution of its best fit  $r$ -process model, even within the parameter uncertainties. However, one challenge arises from the fact that in the late-time ( $\gtrsim 50$  days post-peak) SN 2007I lacks any optical photometry. Based on our extrapolation of the  $r$ -band light curve of SN 2007I we see evidence for further reddening which starts to become consistent with the  $r$ -process enriched model predictions in the late-times. Thus, we are unable to rule out the possibility of  $r$ -process production in SN 2007I based on the  $r$ -process fits and the color evolution comparison alone.

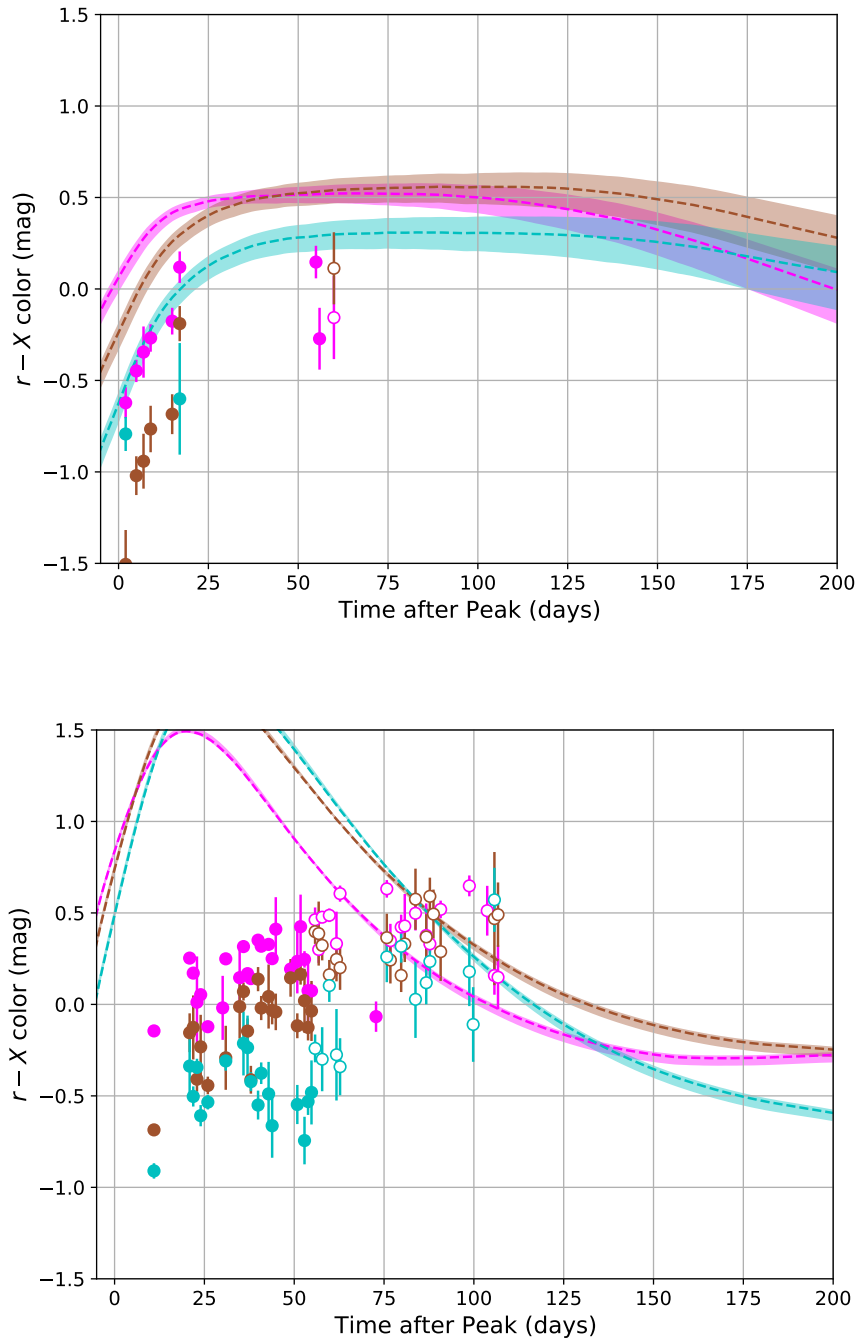


Figure 2.6: Color evolution as a function of time for both SN 2007ce (top) and SN 2007I (bottom). Similar to Figure 2.3, the filled circles with errorbars represent the  $r - J/H/K_s$  color estimated directly from the data, while the unfilled circles correspond to a stretched and scaled  $r$ -band model of SN 2020bvc used as a proxy to estimate the color at each NIR photometric epoch, in the absence of  $r$ -band photometry. The dashed line represents the color evolution of the best fit  $r$ -process enriched model, and the shaded regions encompass the  $\pm 1\sigma$  uncertainty on the model parameters from our fits. Using the same convention as in Figure 2.3, magenta is  $r - J$ , brown is  $r - H$  and cyan is  $r - K_s$ . As shown here, the color evolution of both SN 2007I and SN 2007ce appear to be inconsistent with their best fitting  $r$ -process enriched model colors and associated  $1\sigma$  uncertainties.

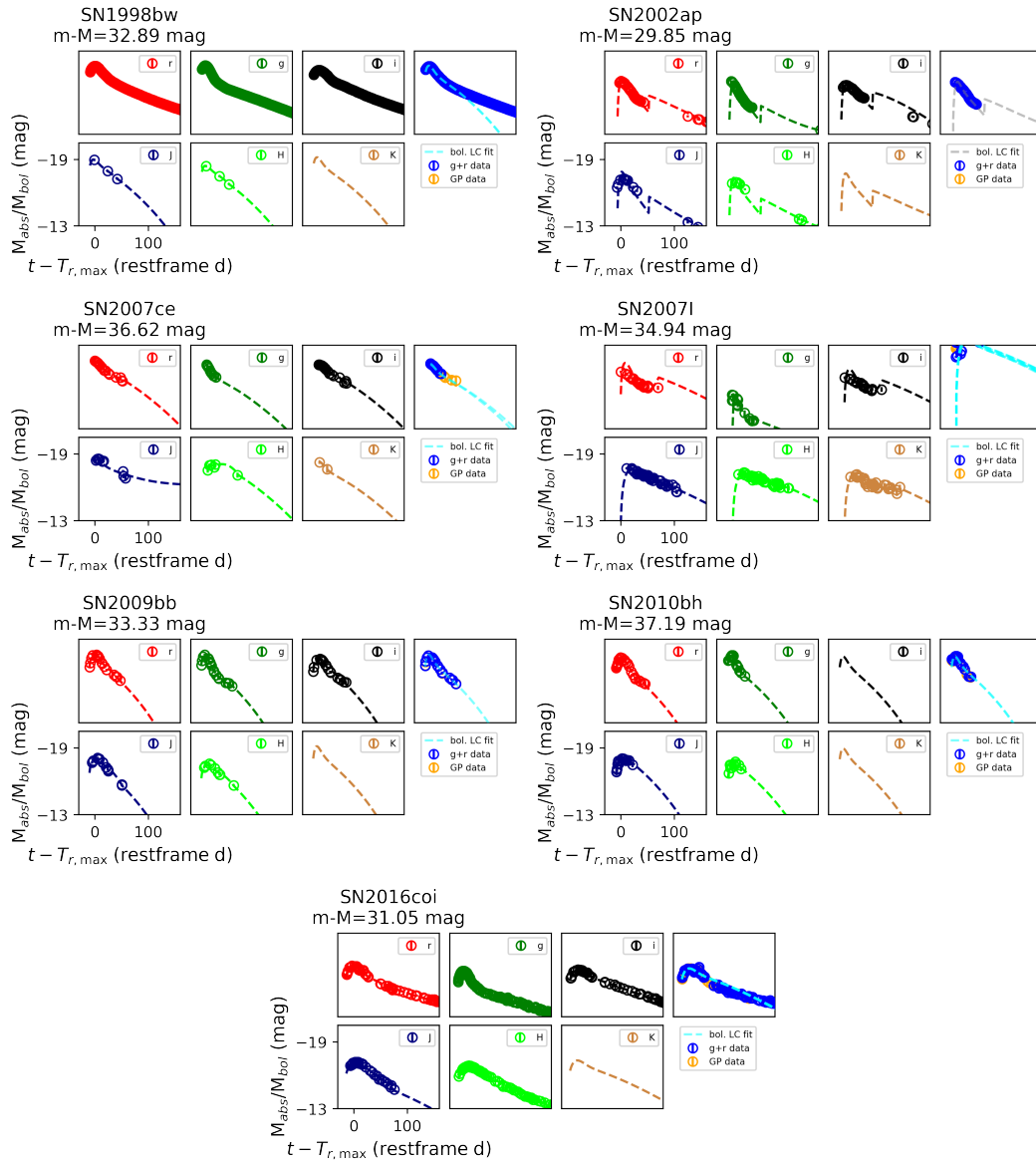
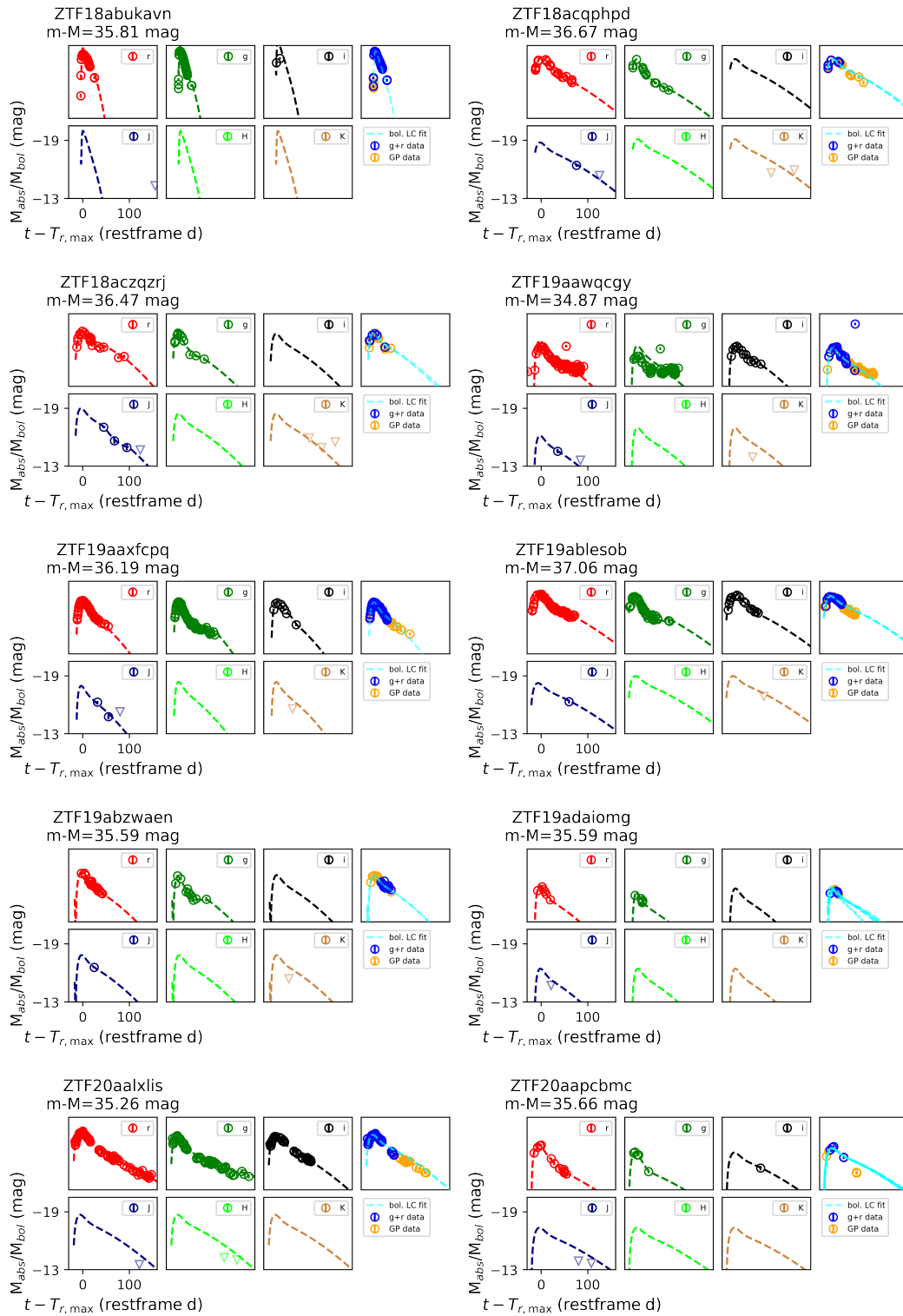


Figure 2.7: Light curve fits to the literature supernova events from HAFET. The dashed cyan line is the best fit bolometric light curve, while the remaining dashed lines show the fits to each of the broadband light curves. Broadband light curves are calculated by fitting bolometric corrections in each band, and using these corrections to rescale the Arnett fitted bolometric light curves. The circles are the photometry for each object in  $griJHK_s$  bands. In the bolometric light curve plot, the points correspond to bolometric luminosity estimated from both  $g-$  and  $r-$  bands, or from a single band, and using GPR to estimate the flux in the other band. For SNe with photometry in the Johnson filter system, we convert the photometry to SDSS assuming photometric conversions from Jordi et al. (2006). We find that the HAFET models are good fits to the photometric data from our sample.



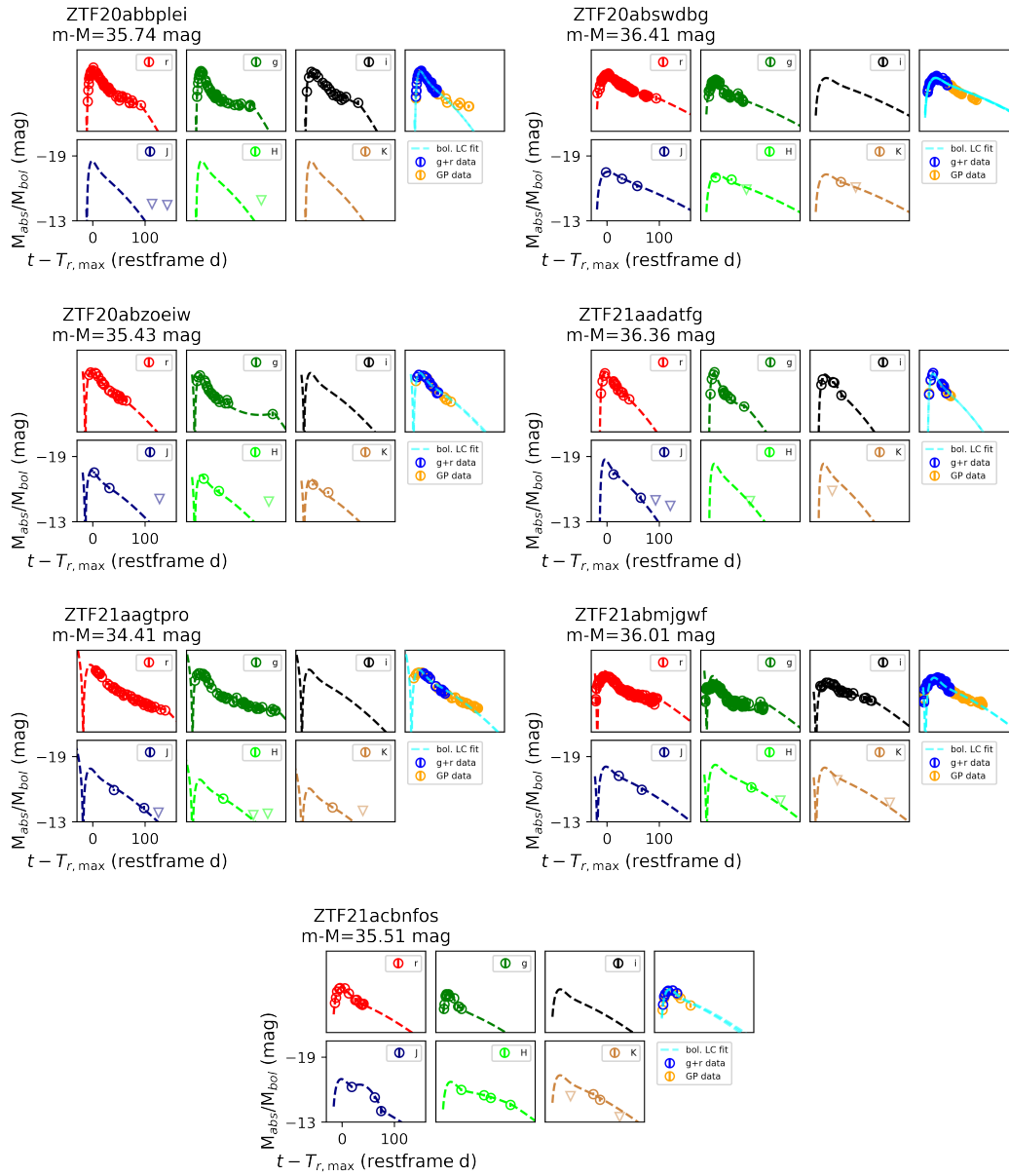


Figure 2.8: Light curve fits to ZTF SNe from HAFET, similar to Figure 2.7.

### Independent Arnett Fits

To supplement our fits to  $r$ -process enriched models we use HAFET to construct a bolometric light curve from our optical data and fit to the standard Arnett model (as described in more detail in Section 2.7). We then calculate broadband light curve models by fitting bolometric corrections in each band, and using these corrections to rescale the Arnett fitted bolometric light curve models. Our fits are shown in Figures 2.7 and 2.8.

In order to compare the two models, we compute  $\chi^2$  for each of the broadband light curves in the same way as we did using the  $r$ -process-enriched models. We find that all of the objects, except for SN 2021xv, have lower  $\chi^2$  values with the HAFET fits compared to the  $r$ -process model fits, insinuating that the  $r$ -process-free models are a better descriptor of these SN light curves. Aside from 3 objects, all other objects pass our criteria of  $\chi^2 < 1.06$  (i.e. well described by the  $r$ -process-free models) and none of them have  $\chi^2 > 9.49$  (i.e. poorly described by the  $r$ -process-free models). Upon visual inspection, we find convincing fits to both the early optical light curves and the NIR light curves of these objects for the  $r$ -process-free models. In the case of SN 2021xv, we note that the  $r$ -process parameter estimation favors little to no  $r$ -process mass and mixing, and the  $r$ -process-enriched models overestimate the NIR flux. Thus we consider SN 2021xv to still be consistent with an  $r$ -process-free scenario.

Furthermore, we derive blackbody effective temperatures for the closest epoch to 30 days post-peak where both optical and NIR photometry are available. The effective temperatures range from 4000 – 15000 K; the SED colors are well described by a single-component blackbody at this phase. Based on the quality of our Arnett fits, and the fact that the SED for these SNe in the photospheric phase is well described by a blackbody, we conclude that no  $r$ -process contribution is needed to explain the color evolution of the objects in our sample, including SN 2007I.

Thus, we find no compelling evidence of  $r$ -process enrichment in any of the SNe in our sample.

## 2.9 Discussion and Outlook

From our systematic study in optical and NIR of the SNe Ic-BL associated with collapsars discovered by ZTF and reported in the literature, we do not find any evidence of  $r$ -process enrichment based on theoretical models which predict observable NIR excesses in the SN light curves. After constructing GPR models from

the  $r$ -process-enriched model grid and performing fitting, the SNe that pass our nominal  $\chi^2$  cuts still do not show convincing fits in both the optical and NIR to the  $r$ -process enriched broadband light curve predictions. On the other hand, for the  $r$ -process-free models, when computing broadband light curves from the bolometric corrections, we get compelling fits in both optical and NIR for each SN. Our single-component blackbody fits at  $\sim 1$  month after peak (see Table 2.9) further suggest that no additional  $r$ -process enrichment is required to explain the SN SED colors.

Our use of two models, one for  $r$ -process-free SNe and another for  $r$ -process enriched cases, complicates our efforts to derive global constraints on  $r$ -process production in SNe. To estimate the level of enrichment our analysis is sensitive to, we take the reddest object in our sample that is consistent with the  $r$ -process enriched models, and compare the color measurements with the predicted color evolution from the models. To derive these global constraints, we focus on SN 2007ce. Amongst our sample, SN 2007ce has the highest inferred  $r$ -process ejecta mass of  $0.07M_{\odot}$  while passing the  $\chi^2$  cut (we ignore SN 1998bw, whose extremely well sampled light curve could be influencing the final  $\chi^2$  value). Though SN 2007I is redder than SN 2007ce, it shows color evolution that is completely inconsistent with the models (see Figure 2.6) making it unsuitable for deriving  $r$ -process constraints. In Figure 2.6 we display the predicted color evolution of the best fit model bounded by its  $1\sigma$  uncertainties on the parameters, where the lower bound corresponds to a model with  $M_{rp} = 0.02M_{\odot}$  and the upper bound corresponds to a model with  $M_{rp} = 0.12M_{\odot}$ . SN 2007ce's color measurements exhibit a similar shape to the model color evolution, but show a significant offset with bluer colors compared to the best fit models. As shown in Figure 2.3, a model with a higher  $M_{ej}$  can yield a slightly bluer color evolution for the same  $r$ -process mass, so it is difficult to confidently exclude the possibility that  $M_{rp} = 0.02M_{\odot}$  (the lower bound on the parameter inference) was synthesized in SN 2007ce. In addition, relaxing the assumptions on the SED underlying the models could also alter the color evolution of the model. Thus, based on the the upper bound of these color curves, which corresponds to an  $r$ -process mass of  $0.12M_{\odot}$ , we conservatively argue here that no more than  $0.12M_{\odot}$  of  $r$ -process material was generated in SN 2007ce (assuming  $M_{rp} = 0.7$ ). Furthermore, since SN 2007ce has the highest inferred  $r$ -process mass amongst the objects passing our  $\chi^2$  cut, we suggest that  $M_{rp} \lesssim 0.12M_{\odot}$  represents a tentative global  $r$ -process constraint on all of the models in our sample, based on the observations. Future improvements in the models as well as more systematic observations will

allow for tighter and more robust constraints on the  $r$ -process nucleosynthesis in SNe Ic-BL.

We also examine any other associated relativistic outflows to check whether that may introduce a bias. Only three objects in our full sample are counterparts to GRBs: GRB980425 (SN 1998bw), GRB100316D (SN 2010bh) and GRB190829A. Amongst these three, GRB980425 and GRB190829A are considered to be LLGRBs based on their peak  $\gamma$ -ray luminosities (Dichiara et al., 2019; Galama et al., 1998; Ho et al., 2020b). GRB100316D is a more energetic GRB, but its emission shows a soft spectral peak, similar to other X-ray flashers (Bufano et al., 2012). While none of the other objects in our sample have any coincident  $\gamma$ -ray emission, some have X-ray and radio detections and upper limits. SN 2018gcp, the FBOT/SN Ic-BL, has both X-ray and radio detections that are consistent with the host galaxy emission (Ho et al., 2019). On the other hand, SN 2020bvc has mildly-relativistic X-ray and radio ejecta characteristic of LLGRBs (Ho et al., 2020a). Corsi et al. (2023) also obtained radio and X-ray follow-up for several ZTF SNe, a subset of which are part of the sample discussed in this work. In Table 2.1 we display radio observations with the Very Large Array (VLA) and X-ray observations with the *Swift* X-ray Telescope (XRT) for those SNe; the remainder of SNe which lack radio/X-ray coverage have dashes in those respective columns. Only two of the objects in the sample presented here (SN 2020tkx and SN 2021ywf) have a detected point-source-like radio counterpart, but their low velocities suggest that they are not the same as GRB-associated SNe (Corsi et al., 2023).

The fact that none of these SNe are linked to standard, classical long GRBs prevents us from exploring the proposed theoretical connection between the GRB energetics and  $r$ -process production. If the GRB jet energy, which scales with the mass accreted by the disk, correlates with the amount of  $r$ -process mass produced in the disk winds, then collapsars with no GRBs may not be able to produce detectable  $r$ -process signatures. Siegel et al. (2019) find that for black hole accretion rates between  $0.003\text{--}1.0 M_{\odot} \text{ s}^{-1}$  needed to power relativistic outflows, the disk winds are neutron-rich and can synthesize heavy and light  $r$ -process elements. The association of a GRB with a SN Ic-BL could point towards a central engine that harbors high enough accretion rates to potentially generate  $r$ -process elements. Barnes & Duffell (2023) also find that hydrodynamical mixing between the  $r$ -process enriched and  $r$ -process-free layers of collapsar increases with wind mass and duration, suggesting that SNe accompanying the longest duration long GRBs may be the most

promising sites to search for obvious  $r$ -process signatures.

It is yet unclear to what extent the populations of SNe Ic-BL and long GRBs overlap (Barnes et al., 2018; Bissaldi et al., 2007; Cano et al., 2017a; Woosley & Bloom, 2006), as some long GRBs lack SNe (Della Valle et al., 2006; Fynbo et al., 2006; Tanga et al., 2018), and most Ic-BL SNe have no associated gamma-ray emission (Bianco et al., 2014; Corsi et al., 2023). Furthermore, LLGRBs, short-duration GRBs with collapsar progenitors (Ahumada et al., 2021a) and long-duration GRBs from compact binaries (Rastinejad et al., 2022) present evidence towards a broad diversity in collapsar central engines, ranging from mildly relativistic to ultra-relativistic explosion energies. One possibility is that a subset of SNe Ic-BL could correspond to failed GRBs with low black hole accretion rates (Huang et al., 2002; MacFadyen & Woosley, 1999; Xu et al., 2023). Multi-wavelength observations of SN 2006aj suggest that another subset may be associated with a progenitor whose jet runs into a cocoon of extended stellar material (Nakar, 2015), even when an LLGRB is not detected, as in the case of SN 2017iuk (Izzo et al., 2019). Yet another subset could be off-axis GRBs.

This diversity of collapsar central engines and jet properties could lend itself naturally to a scenario where some collapsars are capable of producing  $r$ -process elements while others are not. However, given that only  $\sim$ half of the SNe in our sample have X-ray or radio observations, a more systematic NIR follow-up campaign with SNe Ic-BL associated with classical long GRBs, LLGRBs, X-ray/radio counterparts, and lacking any multi-wavelength counterparts is needed to investigate whether only those SNe that produce relativistic ejecta are able to create conditions conducive to  $r$ -process nucleosynthesis.

Another possibility we acknowledge is that collapsars could be a very low-yield source of  $r$ -process nucleosynthesis. The expected yields from the Siegel et al. 2019 and Barnes & Metzger 2022 models ( $0.01$ - $0.1M_{\odot}$ ) are mainly set by the joint constraints from the literature on  $r$ -process nucleosynthesis sites (see for e.g. Hotokezaka et al., 2018). However, the discovery of minuscule amounts of Sr and Ba in an extremely metal-poor star (Casey & Schlaufman, 2017) motivates the need for core-collapse supernovae with an extremely low yield of  $r$ -process material whose nucleosynthesis is consistent with the Solar  $r$ -process abundance pattern. Due to the limitations of these models and the dataset presented here, our study only searches for enrichment levels of  $M_{rp} \gtrsim 0.01M_{\odot}$ . Detailed analysis of the nebular-phase spectra of SNe Ic-BL would likely be required to probe such low levels of enhancement

robustly.

Despite the fact that we find no evidence for  $r$ -process enrichment in the SNe Ic-BL in our sample, we must also acknowledge a number of caveats to this work.

First, we note that the  $r$ -process enriched and  $r$ -process-free models make different predictions about the relationship between nickel mass and SN luminosity. While the inferred central values from the GPR inference of both  $\beta_{ej}$  and  $M_{ej}$  based on the  $r$ -process grid are generally within the  $1\sigma$  errorbar of our explosion property estimates, the nickel mass inferred shows a larger deviation from the Arnett value. Arnett-like models are constructed such that the radioactive energy-generation rate crosses the bolometric light curve precisely at peak luminosity. The  $r$ -process enriched models, in which energy diffuses through a series of concentric shells, do not reproduce this behavior; they generally have  $L_{bol}(tpk) < Q_{dot}(tpk)$ . As a result, the amounts of nickel inferred by each model for a given luminosity are inconsistent, and the Arnett-like models do not match the Barnes & Metzger (2022) models when  $M_{rp}$  is set to zero (see Section 2.6 for other differences between the Barnes & Metzger (2022)-like models and the Arnett-like models). To compensate for these differences, we fit the  $r$ -process enriched models over a wide range of nickel masses.

Given the differences between the  $r$ -process enriched and  $r$ -process-free models we use, a more robust approach would be to conduct an apples-to-apples comparison between  $r$ -process-free and  $r$ -process enriched models from the same underlying grid. Initially, we performed fitting to both the  $r$ -process-free and  $r$ -process enriched models from (Barnes & Metzger, 2022), but found that the colors of the  $r$ -process-free models were consistently much redder than the observed colors of our objects at all epochs. To construct the  $r$ -process-free SED, Barnes & Metzger (2022) uses the light curve of SN 2007gr as it has well sampled  $B$ - to  $K$ -band photometry up to late-times, but the detection of the CO molecule in its nebular phase NIR spectra may affect the  $K$ -band flux of the object (Hunter et al., 2009). Unfortunately, the semi-empirical approach to converting between bolometric and broadband light curves using HAFET and the fact that the Arnett models do not allow us to define a spatial or velocity mixing coordinate renders the alternative possibility of enriching the HAFET models with  $r$ -process material infeasible. Our inability to use  $r$ -process enriched and  $r$ -process-free models from the same grid makes our investigation to search for  $r$ -process production less robust. The authors are currently investigating whether varying additional parameters controlling the

*r*-process-free SED may lead to better fits to the data. This will be discussed in a future work.

Furthermore, our understanding of the emission of *r*-process ejecta in the nebular phase is quite limited. The radiation from *r*-process-enriched ejecta layers has a strong impact on the predictions of late-time photometry for the *r*-process grid. Barnes & Metzger (2022) adopts a temperature of 2500 K for the *r*-process SED because a black-body at this temperature reproduces the optical and NIR photometric colors of the nebular-phase kilonova model spectrum of Hotokezaka et al. (2021). However, kilonova nebular-phase modeling is still a topic of active investigation. Future studies of kilonova nebulae, both observational and theoretical, may refine our understanding of nebular emission from pure *r*-process outflows. Furthermore, differences between kilonovae and *r*-process-enriched SN (e.g., in their densities or their compositions) may mean that nebular-phase emission from the former is not a perfect predictor of nebular-phase emission from the latter.

Finally, we acknowledge the limitations of the dataset we present here for testing whether collapsars synthesize *r*-process elements. Due to the nature of our classical observing runs with WIRC, our NIR light curves are very sparse, and in some cases our upper limits are too shallow to be constraining. In contrast, future wide field of view NIR facilities (i.e. WINTER, DREAMS, PRIME) will enable systematic follow-up of nearby SNe Ic-BL discovered by contemporaneous wide-field optical surveys (i.e. ZTF, Pan-STARRS, ATLAS, Vera Rubin Observatory, etc) as well as counterparts to nearby long GRBs to late-times. The James Webb Space Telescope will grant the unique ability to probe the mid-infrared wavelengths and acquire IR spectroscopy to search for further signatures of *r*-process production. Higher cadence NIR photometry and nebular spectroscopy to search for the *r*-process signatures from collapsars would substantiate the results of this paper as well as determine whether the presence of a relativistic jet in the explosion is required for heavy element production. The authors plan to investigate the relative contribution of collapsars, neutron star mergers, and neutron star–black hole mergers towards the *r*-process abundance in the Universe in a future work. The next generation of optical and IR telescopes will open new windows to discoveries providing valuable insights into the open questions about *r*-process nucleosynthesis from collapsars.

IAU name	ZTF name	type	RA	Dec	z	$F_y^a$ ( $\mu\text{Jy}$ )	$F_{0.3-10\text{keV}}^b$ ( $10^{-14} \text{ erg cm}^{-2} \text{ s}^{-1}$ )
2018gep	ZTF18abukavn	FBOT*	16:43:48.21	+41:02:43.29	0.032	$< 34 \pm 4$ (9.7 GHz)	$< 9.9$
2018jaw	ZTF18acqphpd	Ic-BL	12:54:04.10	+13:32:47.9	0.047	-	-
2018kva	ZTF18aczqzrj	Ic/Ic-BL	08:35:16.21	+48:19:03.4	0.043	-	-
2019gwc	ZTF19aaxfcpq	Ic-BL	16:03:26.88	+38:11:02.6	0.038	-	-
2019hsx	ZTF19aawqcggy	Ic-BL	18:12:56.22	+68:21:45.2	0.021	$\lesssim 19$ (6.2 GHz)	$6.2^{+2.3}_{-1.8}$
2019moc	ZTF19ablesob	Ic-BL	23:55:45.95	+21:57:19.67	0.056	-	-
2019qfi	ZTF19abzwaen	Ic-BL	21:51:07.90	+12:25:38.5	0.029	-	-
2019xcc	ZTF19adaiomg	Ic-BL	11:01:12.39	+16:43:29.30	0.029	$< 62.7 \pm 8.7$ (6.3 GHz)	-
GRB190829A	-	LLGRB	2:58:10.580	-8:57:29.82	0.077	-	-
2020bvc	ZTF20aalxlis	Ic-BL**	14:33:57.01	+40:14:37.5	0.025	$63 \pm 6$ (10 GHz)	$9.3^{+10.6}_{-6.1}$
2020dgd	ZTF20aapcbmc	Ic-BL	15:45:35.57	+29:18:38.4	0.03	-	-
2020lao	ZTF20abbplei	Ic-BL	17:06:54.61	+30:16:17.3	0.031	$\lesssim 33$ (5.2 GHz)	$< 2.9$
2020rph	ZTF20abswdbg	Ic-BL	03:15:17.82	+37:00:50.57	0.042	$< 42.7 \pm 7.4$ (5.5 GHz)	$< 3.6$
2020tkx	ZTF20abzoeiw	Ic-BL	18:40:09.01	+34:06:59.5	0.027	$272 \pm 16$ (10 GHz)	$< 3.3$
2021bmf	ZTF21aagtpro	Ic-BL	16:33:29.41	-06:22:49.53	0.017	-	-
2021xv	ZTF21aadatfg	Ic-BL	16:07:32.82	+36:46:46.07	0.041	$< 34.3 \pm 8.1$ (5.2 GHz)	-
2021ywf	ZTF21acbnfos	Ic-BL	05:14:11.00	+01:52:52.28	0.028	$83 \pm 10$ (5.0 GHz)	$5.3^{+4.9}_{-3.3}$
2021too	ZTF21abmjgwf	Ic-BL	21:40:54.28	+10:19:30.33	0.035	-	-

Table 2.1: Sample summary table of Ic-BL supernova properties, estimated  $r$ -process ejecta mass and mixing fraction along with their  $1\sigma$  uncertainties, and first radio/X-ray detection. In the absence of any X-ray/radio detections we quote an upper limit; if the source was not observed we mark the cell with a dash. a) Flux density in  $\mu\text{Jy}$  with the VLA. We list only the first VLA observation at  $\lesssim 50$  days from the first ZTF detection as reported in Corsi et al. (2023). b) *Swift* XRT flux in units of  $10^{-14} \text{ erg cm}^{-2} \text{ s}^{-1}$ , taken from Corsi et al. (2023). \*This SN Ic-BL is also categorized as a fast blue optical transient (FBOT), and was published in Ho et al. (2019). The quoted radio detection with the VLA could be galaxy-dominated. \*\*This Ic-BL had a double-peaked light curve from shock-cooling; X-ray and radio measurements taken from Ho et al. (2020a).

filter	central wavelength ( $\text{\AA}$ )
<i>g</i>	4770
<i>r</i>	6231
<i>i</i>	7625
<i>U</i>	3600
<i>B</i>	4380
<i>V</i>	5450
<i>R</i>	6410
<i>I</i>	7980
<i>J</i>	12350
<i>H</i>	16620
$K_s$	21590
<i>K</i>	21900

Table 2.2: Central wavelengths for the optical and NIR filters assumed during the analysis and fitting of our light curves.

SN	$M_{ej}$ ( $M_{\odot}$ )	$E_K$ (foe)	$M_{Ni}$ ( $M_{\odot}$ )	$E(B-V)_{host}$	$T_{eff}$ [phase] (K [day])	Ref.
1998bw	10	50	0.4	0.06*	5919 [24.5]	Clocchiatti et al. (2011); Nakamura et al. (2001)
2002ap	2.5-5	4-10	0.07 (0.02)	0.09	5126 [30.5]	Mazzali et al. (2002)
2007ce	2.90 (0.63)	1.85 (0.89)	0.48 (0.01)	0.00	6310 [18.5]	Modjaz et al. (2008)**
2007I	6.87 (0.80)	7.63 (1.99)	0.10 (0.00)	0.34	4064 [33.5]	Modjaz et al. (2008)**
2009bb	3.4 (0.4)	6.2 (0.8)	0.20 (0.02)	0.540	3584 [22.6]	Taddia et al. (2018)
2010bh	2.21 (0.10)	11.34 (0.52)	0.21 (0.03)	0.30	6102 [23.5]	Olivares E. et al. (2012)
2016coi	4-7	7-8	0.15	0.00	4727 [32.1]	Terreran et al. (2019)

Table 2.3: Explosion properties and inferred  $r$ -process ejecta masses and mixing fractions of low-redshift SNe with contemporaneous optical and NIR imaging from our literature search. Where available, we quote the  $1\sigma$  uncertainties on the parameters in brackets. For SN 1998bw and SN 2002ap, we quote the ranges of explosion parameters corresponding to the best fitting light curve models. \*Clocchiatti et al. (2011) already corrected for host extinction; we use the assumed host extinction to correct only the NIR photometry. \*\*For SN 2007I and SN 2007ce, as explosion properties were not estimated in the literature, we conduct light curve analysis to derive the best fit properties as described in Section 2.7.

The authors express gratitude towards Ehud Nakar, Daniel Siegel, Leo Singer, Navin Sridhar, and Peter Tsun Ho Pang for helpful discussions in preparing this work. All light curves presented in this work will be made public via WISEREP upon publication. Based on observations obtained with the Samuel Oschin Telescope 48-inch and the 60-inch Telescope at the Palomar Observatory as part of the Zwicky Transient Facility project. ZTF is supported by the National Science Foundation under Grants No. AST-1440341 and AST-2034437 and a collaboration including current partners Caltech, IPAC, the Weizmann Institute of Science, the Oskar Klein Center at Stockholm University, the University of Maryland, Deutsches Elektronen-Synchrotron and Humboldt University, the TANGO Consortium of Taiwan, the University of Wisconsin at Milwaukee, Trinity College Dublin, Lawrence Livermore National Laboratories, IN2P3, University of Warwick, Ruhr University Bochum, Northwestern University and former partners the University of Washington, Los Alamos National Laboratories, and Lawrence Berkeley National Laboratories. Operations are conducted by COO, IPAC, and UW. SED Machine is based upon work supported by the National Science Foundation under Grant No. 1106171. Based on observations made with the Nordic Optical Telescope, owned in collaboration by the University of Turku and Aarhus University, and operated jointly by Aarhus University, the University of Turku and the University of Oslo, representing Denmark, Finland and Norway, the University of Iceland and Stockholm University at the Observatorio del Roque de los Muchachos, La Palma, Spain, of the Instituto de Astrofísica de Canarias. S. Anand acknowledges support from the National Science Foundation GROWTH PIRE grant No. 1545949. J. Barnes is supported by the Gordon and Betty Moore Foundation through Grant GBMF5076. S. Yang is supported by the National Natural Science Foundation of China under Grant No. 12303046. M. W. Coughlin acknowledges support from the National Science Foundation with grant numbers PHY-2010970 and OAC-2117997. S. Schulze acknowledges support from the G.R.E.A.T research environment, funded by *Vetenskapsrådet*, the Swedish Research Council, project number 2016-06012. L.T. acknowledges support from MIUR. A.C. acknowledges support from the NASA Swift Guest Investigator program (80NSSC22K0203).

Source Extractor (Bertin & Arnouts, 2010), HOTPANTS (Becker, 2015), SCAMP (Bertin, 2006a), pyzogy (Guevel & Hosseinzadeh, 2017a), PSFEx (Bertin, 2011), Pypeit (Prochaska et al., 2019; Roberson et al., 2022), LPipe (Perley, 2019), ForcePhotZTF (Yao et al., 2019), HAFFET (Yang & Sollerman, 2023), SNspecFFTSmooth (Liu et al., 2016), SESNspectraLib (Liu et al., 2016; Modjaz et al., 2016), PyMulti-

SN	$t_{\text{peak}}$ (MJD)	$M_{\text{peak,r}}$ (mag)	$t_{\text{expl}}$ (day)	$M_{\text{Ni}}$ ( $M_{\odot}$ )	$\tau_m$ (day)	$M_{\text{ej}}$ ( $M_{\odot}$ )	$E_{\text{kin}}$ ( $10^{51}$ erg)	$v_{\text{ph}}$ (c)	$T_{\text{eff}}$ [phase] (K [day])
2018jaw	58455.70	-18.63 (0.08)	-18.74 <sup>+0.66</sup> <sub>-0.66</sub>	0.33 <sup>+0.02</sup> <sub>-0.02</sub>	13.63 <sup>+1.10</sup> <sub>-1.38</sub>	> 1.41 (0.33)	> 0.40 (0.16)	0.022 (0.004)	—
2018kva	58487.05	-18.70 (0.02)	-15.81 <sup>+0.49</sup> <sub>-0.60</sub>	0.29 <sup>+0.01</sup> <sub>-0.01</sub>	12.13 <sup>+1.06</sup> <sub>-0.87</sub>	2.51 (0.39)	3.53 (0.76)	0.051 (0.004)	5431 [47.2]
2019gwc	58650.58	-18.48 (0.01)	-12.78 <sup>+0.46</sup> <sub>-0.46</sub>	0.22 <sup>+0.01</sup> <sub>-0.01</sub>	6.96 <sup>+0.12</sup> <sub>-0.15</sub>	> 0.60 (0.05)	> 0.44 (0.08)	0.037 (0.003)	5953 [33.6]
2019hsx	58647.07	-17.08 (0.02)	-15.63 <sup>+0.38</sup> <sub>-0.53</sub>	0.07 <sup>+0.01</sup> <sub>-0.01</sub>	12.12 <sup>+1.10</sup> <sub>-1.26</sub>	1.64 (0.43)	0.99 (0.50)	0.033 (0.007)	11002 [36.1]
2019moc	58715.76	-19.16 (0.03)	-20.02 <sup>+0.27</sup> <sub>-3.23</sub>	0.52 <sup>+0.01</sup> <sub>-0.02</sub>	10.60 <sup>+0.37</sup> <sub>-0.30</sub>	2.09 (0.50)	3.48 (1.85)	0.056 (0.013)	8537 [63.0]
2019qfi	58753.56	-18.01 (0.02)	-15.09 <sup>+1.40</sup> <sub>-1.40</sub>	0.13 <sup>+0.01</sup> <sub>-0.01</sub>	10.58 <sup>+1.44</sup> <sub>-1.71</sub>	> 1.22 (0.33)	> 0.70 (0.24)	0.032 (0.004)	5698 [25.0]
2019xcc	58844.59	-16.58 (0.06)	-10.62 <sup>+2.51</sup> <sub>-2.51</sub>	0.04 <sup>+0.01</sup> <sub>-0.01</sub>	5.04 <sup>+1.36</sup> <sub>-0.95</sub>	0.68 (0.30)	2.40 (1.14)	0.081 (0.007)	—
2020dgd	58914.05	-17.74 (0.02)	-18.03 <sup>+2.50</sup> <sub>-2.50</sub>	0.13 <sup>+0.03</sup> <sub>-0.03</sub>	13.68 <sup>+3.78</sup> <sub>-2.70</sub>	2.81 (1.50)	3.07 (2.42)	0.045 (0.013)	—
2020lao	59003.92	-18.66 (0.02)	-10.60 <sup>+0.99</sup> <sub>-0.99</sub>	0.23 <sup>+0.01</sup> <sub>-0.01</sub>	7.71 <sup>+0.22</sup> <sub>-0.21</sub>	1.22 (0.16)	2.48 (0.71)	0.048 (0.005)	—
2020rph	59092.34	-17.48 (0.02)	-19.88 <sup>+0.02</sup> <sub>-0.02</sub>	0.07 <sup>+0.01</sup> <sub>-0.01</sub>	17.23 <sup>+1.19</sup> <sub>-0.89</sub>	3.83 (1.59)	3.08 (2.81)	0.039 (0.016)	5857 [30.5]
2020tkx	59116.50	-18.49 (0.05)	-12.77 <sup>+4.54</sup> <sub>-4.54</sub>	0.22 <sup>+0.01</sup> <sub>-0.01</sub>	10.95 <sup>+0.67</sup> <sub>-0.77</sub>	> 1.75 (0.24)	> 1.82 (0.35)	0.044 (0.003)	7116 [32.8]
2021bmf	59265.12	-20.60 (0.04)	-23.76 <sup>+5.68</sup> <sub>-5.52</sub>	0.98 <sup>+0.16</sup> <sub>-0.17</sub>	18.08 <sup>+6.64</sup> <sub>-7.94</sub>	8.05 (5.37)	23.63 (16.14)	0.073 (0.005)	15618 [41.4]
2021too	59434.09	-19.66 (0.02)	-23.23 <sup>+0.41</sup> <sub>-0.41</sub>	0.92 <sup>+0.03</sup> <sub>-0.03</sub>	17.67 <sup>+0.65</sup> <sub>-0.66</sub>	5.06 (0.78)	6.42 (2.09)	0.048 (0.007)	5363 [23.5]
2021xv	59235.56	-18.92 (0.07)	-12.79 <sup>+0.24</sup> <sub>-0.33</sub>	0.30 <sup>+0.01</sup> <sub>-0.02</sub>	7.72 <sup>+0.66</sup> <sub>-0.49</sub>	0.89 (0.15)	0.96 (0.23)	0.045 (0.004)	5969 [13.5]
2021ywf	59478.64	-17.10 (0.05)	-10.67 <sup>+0.49</sup> <sub>-0.49</sub>	0.06 <sup>+0.01</sup> <sub>-0.01</sub>	8.87 <sup>+0.81</sup> <sub>-0.81</sub>	1.06 (0.19)	0.92 (0.26)	0.040 (0.004)	5238 [19.5]

Table 2.4: Table containing the explosion properties of all of the ZTF-discovered SNe in our sample that have not yet been published. Our methods for deriving the quantities given above are described in Section 2.7. The velocities shown here are measured at various different phases, so do not represent the photospheric velocity of the supernova at peak. We report effective temperatures from blackbody fits around  $\sim 30$  days post-peak for each of the objects that has one or more NIR detections.

nest's (Buchner et al., 2014)

*Chapter 3**r*-PROCESS FROM GW170817**Chemical Distribution of the Ejecta in the Neutron Star Merger GW170817**

Anand, S., Pang, P. T. H., Bulla, M., et al. 2023, Chemical Distribution of the Dynamical Ejecta in the Neutron Star Merger GW170817, arXiv e-prints, arXiv:2307.11080, . S. A. trained the surrogate kilonova models, performed light curve fitting along with P. T. H. Pang, and wrote the manuscript along with other co-authors. Under review in MNRAS. <https://arxiv.org/abs/2307.11080>

S. A. trained the surrogate kilonova models, performed light curve fitting along with P. T. H. Pang, and wrote the manuscript along with other co-authors.

## ABSTRACT

GW170817 and its associated electromagnetic counterpart AT2017gfo continue to be a treasure trove as observations and modeling continue. Recent precision astrometry of AT2017gfo with the Hubble Space Telescope combined with previous constraints from Very Long Baseline Interferometry (VLBI) narrowed down the inclination angle to  $19\text{-}25^\circ$  (90% confidence). This paper explores how the inclusion of precise inclination information can reveal new insights about the ejecta properties, particularly about the composition of the dynamical ejecta of AT2017gfo. Our analysis relies on updated kilonova modeling, which includes state-of-the-art heating rates, thermalization efficiencies, and opacities and is parameterized by  $\bar{Y}_{e,\text{dyn}}$ , the average electron fraction of the dynamical ejecta component, and  $Y_{e,\text{wind}}$ , the electron fraction of the disk wind ejecta component. Using this model, we incorporate the latest inclination angle constraint of AT2017gfo into a light curve fitting framework to derive updated parameter estimates. Analysis is ongoing to obtain the final results from the light curve fits.

### 3.1 Introduction

More than five years since its discovery, the binary neutron star (BNS) merger GW170817 remains the only gravitational-wave event with a definitive electromagnetic (EM) counterpart (Abbott et al., 2017a): a low-luminosity short gamma-ray burst (Goldstein et al., 2017a; Savchenko et al., 2017), a kilonova peaking at ultraviolet to infrared wavelengths (Andreoni et al., 2017b; Chornock et al., 2017; Coulter et al., 2017a; Evans et al., 2017b; Kasliwal et al., 2017a, 2022; Kilpatrick et al., 2017; Lipunov et al., 2017b; McCully et al., 2017; Shappee et al., 2017; Tanvir et al., 2017; Utsumi et al., 2017), and a gamma-ray burst (GRB) afterglow with multi-wavelength emission (Fong et al., 2019; Lamb et al., 2019; Margutti et al., 2017). The precise localization of GW170817 to the lenticular galaxy NGC 4993 at 40 Mpc (Coulter et al., 2017a) enabled a detailed study of the energetics of the different outflow components, such as the dynamical ejecta, the disk wind ejecta, and the relativistic jet, responsible for the EM counterparts.

Detectable emission from AT2017gfo lasted for a few weeks post-merger. Due to the initially dominant ultraviolet and blue emission, numerical-relativity simulations indicated the presence of at least two components associated with the kilonova:  $\sim 0.01M_{\odot}$  of lanthanide-poor ejecta (i.e., blue component) traveling at an average speed of  $\sim 0.3c$ , and  $\sim 0.05M_{\odot}$  of lanthanide-rich material (i.e., red component) traveling at  $\sim 0.1c$  (Arcavi et al., 2017; Cowperthwaite et al., 2017; Drout et al., 2017; Kasen et al., 2017; Kasliwal et al., 2017a; Nicholl et al., 2017; Pian et al., 2017b; Smartt et al., 2017; Soares-Santos et al., 2017; Tanvir et al., 2017; Valenti et al., 2017; Villar et al., 2017). The blue component was interpreted as originating preferentially in the polar regions due to irradiation from neutrinos from a short-lived hypermassive neutron star (HMNS), while the red component to be preferentially equatorial, due to shielding of the neutrinos by the accretion disk (Kasen et al., 2017; Metzger, 2019; Metzger & Fernandez, 2014). However, ejecta masses and velocities inferred for these two components did not agree well with those predicted by numerical-relativity simulations (Siegel, 2019). While additional explanations like magnetar-energized wind (Metzger et al., 2018; Yu et al., 2018) have been proposed for the kilonova emission, there is no evidence for a long-lived magnetar in GW170817 (Kawaguchi et al., 2022; Makhathini et al., 2021; Margutti et al., 2018; Mooley et al., 2022; Pooley et al., 2018).

The above general conclusions have been drawn from one-dimensional, inclination-independent analyses. This scenario has changed with the proper motion measure-

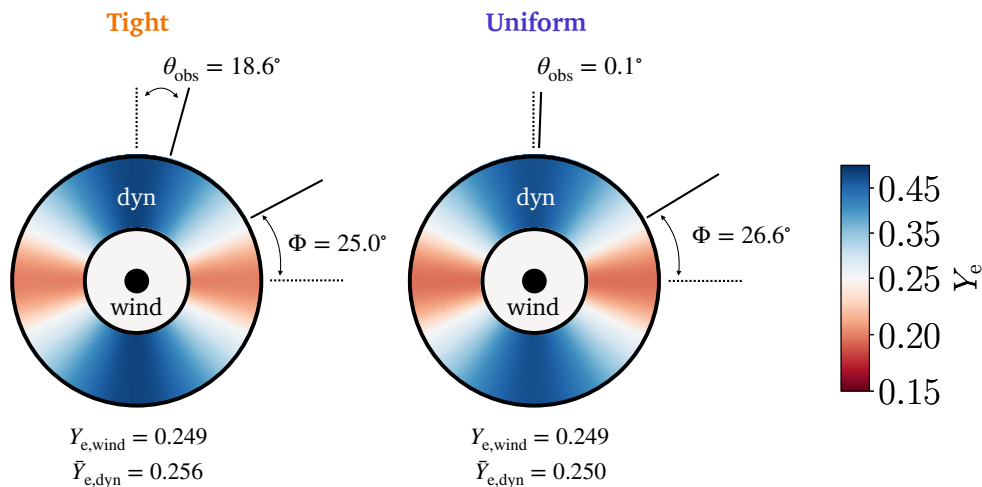


Figure 3.1: Schematic diagram of the ejecta distribution for AT2017gfo as inferred from the Bu2023Y<sub>E</sub> grid. The two distinct regions of the dynamical ejecta are represented in blue, corresponding to the lanthanide-poor, squeezed polar dynamical ejecta, and the red, representing the lanthanide-rich, equatorial tidal component. The disk wind ejecta is represented by the light grey annulus in the center. The solid lines show the boundary between the lanthanide-rich and lanthanide-poor regions of the dynamical ejecta.

ments of the relativistic jet in GW170817, made with the Hubble Space Telescope (HST) and very long baseline interferometry (VLBI) (Ghirlanda et al., 2019; Moolley et al., 2022, 2018), yielding a precise viewing angle constraint of  $19 < \theta_{\text{obs}} < 25^\circ$  (90% confidence). Precise measurements of the inclination angle of GW170817 can allow for a more accurate inference of the properties of the associated kilonova, including the ejecta masses, velocities, and composition.

In this work, we present inference results using the tight inclination angle constraint for AT2017gfo and determine whether the inclusion of inclination angle constraints affects the ejecta parameters. We employ a new grid based on an improved version (Bulla, 2023) of POSSIS (Bulla, 2019), a three-dimensional Monte Carlo code for modeling the radiation transport in kilonovae. We use idealized outflow properties (geometry and distributions of density and composition) guided by numerical-relativity simulations combined together with the inclination angle constraint.

## 3.2 Methodology

### Kilonova Models

We make use of the three-dimensional, time-dependent Monte Carlo (MC) radiative transfer code POSSIS (Bulla, 2019, 2023) for simulating kilonova light curves. The code simulates the propagation of MC photon packets as they diffuse out of an expanding medium and interact with matter. Each grid cell in the model is assigned a density  $\rho$  (evolved with time assuming homologous expansion), an electron fraction  $Y_e$  (constant throughout the simulation), and a temperature  $T$  (estimated from the mean intensity of the radiation field). At the start of the simulation, MC photon packets are assigned an initial location sampled from the distribution of energy from radioactive-decay of  $r$ -process nuclei (i.e., depending on the mass and heating rates distribution within the model). The energy available at each time-step is estimated from heating rates (Rosswog & Korobkin, 2022) and thermalization efficiencies (Barnes et al., 2016; Wollaeger et al., 2018) that depend on local properties of the ejecta and split equally among MC packets (Lucy, 1999). The propagation of MC packets is controlled by the opacity of the ejecta, which is dominated by bound-bound transitions and electron scattering. The most recent version of POSSIS (Bulla, 2023) uses time-dependent opacities that depend on local properties of the ejecta such as  $\rho$ ,  $T$ ,  $Y_e$ , and on the photon frequency/wavelength in the case of bound-bound transitions (Tanaka et al., 2020). We refer the reader to Bulla (2019) and Bulla (2023) for more details about the code.

In this article, we computed a new kilonova grid based on the BNS ejecta model described in Bulla (2023). The ejecta are modeled following Kawaguchi et al. (2020) and with an idealized geometry assuming two main components: the dynamical ejecta, which is ejected during the merger, and the wind ejecta, which is ejected from the debris disk formed around the central remnant post-merger. The dynamical ejecta, which extend from  $0.1c$  to  $v_{\max, \text{dyn}}$ , where  $c$  is the speed of light, have a density profile depending on both the radius  $r$  and polar angle  $\theta$  as

$$\rho(r, t, \theta) \propto \begin{cases} \sin^2(\theta) r^{-4} t^{-3}, & 0.1c \leq r/t \leq 0.4c \\ \sin^2(\theta) r^{-8} t^{-3}, & 0.4c \leq r/t \leq v_{\max, \text{dyn}} \end{cases} \quad (3.1)$$

and an electron fraction depending on  $\theta$  as

$$Y_{e, \text{dyn}}(\theta) = a \cos^2(\theta) + b \quad (3.2)$$

Specifically, we scale the densities and  $v_{\max,\text{dyn}}$  to achieve a desired mass  $M_{\text{ej,dyn}}$  and mass-weighted averaged velocity  $\bar{v}_{\text{ej,dyn}}$ , respectively, and assume that the parameters  $a$  and  $b$  are linked as in Setzer et al. (2023) ( $a \sim 0.71 b$ ) and  $a$  scaled to obtain a desired mass mean-weighted averaged electron fraction  $\bar{Y}_{\text{e,dyn}}$ . The wind ejecta extend from 0.02 to  $v_{\max,\text{wind}}$ , with a density profile  $\rho(r) \propto r^{-3} t^{-3}$  and a uniform electron fraction  $Y_{\text{e,wind}}$ . The densities and  $v_{\max,\text{wind}}$  are scaled to obtain a desired  $M_{\text{ej,wind}}$  and mass-weighted averaged velocity  $\bar{v}_{\text{ej,wind}}$ , respectively. If  $v_{\max,\text{wind}} > 0.1c$  (i.e., the minimum velocity of the dynamical ejecta), we follow Kawaguchi et al. (2020) and assume that the wind ejecta replaces the dynamical ejecta at velocities larger than 0.1c and for angles  $\theta < \pi/4$  (see, e.g., their Figure 2, bottom panel).

The new kilonova grid, hereafter referred to as BU2023YE, depends on six free parameters in addition to the viewing angle  $\Theta_{\text{obs}}$ :  $M_{\text{ej,dyn}}$ ,  $\bar{v}_{\text{ej,dyn}}$ ,  $\bar{Y}_{\text{e,dyn}}$ ,  $M_{\text{ej,wind}}$ ,  $\bar{v}_{\text{ej,wind}}$  and  $Y_{\text{e,wind}}$ . Values for these parameters are chosen to cover the expected ranges from numerical-relativity simulations of binary neutron star mergers (e.g. Nedora et al., 2021; Radice et al., 2018):  $M_{\text{ej,dyn}} = [0.001, 0.005, 0.010, 0.020] M_{\odot}$ ,  $\bar{v}_{\text{ej,dyn}} = [0.12, 0.15, 0.20, 0.25]c$ ,  $\bar{Y}_{\text{e,dyn}} = [0.15, 0.20, 0.25, 0.3]$ ,  $M_{\text{ej,wind}} = [0.01, 0.05, 0.09, 0.13] M_{\odot}$ ,  $\bar{v}_{\text{ej,wind}} = [0.03, 0.05, 0.10, 0.15]c$ , and  $Y_{\text{e,wind}} = [0.2, 0.3, 0.4]$ . This results in a total of  $4 \times 4 \times 4 \times 4 \times 4 \times 3 = 3072$  configurations, corresponding to 33792 different kilonova light curves when counting the  $N_{\text{obs}} = 11$  different viewing angles  $\theta_{\text{obs}}$  (equally spaced in cosine from a face-on / jet-axis to an edge-on / merger-plane view of the system). Each simulation employs a number  $N_{\text{ph}} = 10^6$  of MC photon packets,  $N_{\text{times}} = 100$  time-steps from 0.1 to 30 d after the merger (logarithmic binning of  $\Delta \log t = 0.025$ ) and  $N_{\lambda} = 1000$  wavelength bins from 500 Å to 10 μm (logarithmic binning of  $\Delta \log \lambda = 0.0023$ ).

Figure 3.1 shows a sketch of the ejecta for the preliminary fitting results found in this work. We note that the constraint on the averaged  $\bar{Y}_{\text{e,dyn}}$ , coupled with the  $Y_{\text{e,dyn}}(\theta)$  angular dependence in Eq. (3.2), leads to a constraint on the chemical distribution of the dynamical ejecta and specifically on the half-opening angle  $\Phi$  of the lanthanide-rich ( $Y_{\text{e}} < 0.25$ ) region, see below.

Our model employs a simplified geometry relative to numerical simulations. We note that the kilonova ejecta has a complex structure that may not be fully captured by our model. In particular, the model explores the angular, but not the radial dependence of  $Y_{\text{e,dyn}}$ , and assumes that  $Y_{\text{e,wind}}$  has fixed values instead of an angular and radial dependence. Such simplifications allow us to compute the kilonova model

grid with our available computational resources and limit the grid dimensionality (higher grid dimensionalities become increasingly challenging for surrogate models to handle reliably).

### Bayesian analysis using NMMA

To analyse AT2017gfo, we use the Nuclear physics and Multi-Messenger Astronomy framework NMMA (Dietrich et al., 2020a; Pang et al., 2022)<sup>1</sup> that allows us to perform joint Bayesian inference of multi-messenger events containing gravitational waves, kilonovae, supernovae, and GRB afterglows.

To perform Bayesian analysis on the light curve data using the grid of predicted light curves, an interpolation scheme is required. Here, we employ a feed-forward neural network (NN) to predict the kilonova light curves based on the input parameters (Almualla et al., 2021). We used a NN to create a continuous mapping between merger parameters and light curve eigenvalues. The NN architecture begins with an input layer followed by one dense layer with 2048 neurons. A dropout layer subsequently removes 60% of the dense layer’s outputs before connecting to the output layer, yielding ten eigenvalues. This regularized, wide and shallow NN approximates a Gaussian process (see e.g., Lee et al. 2017) in a fraction of its runtime. We used 90% of learning set examples to train the models over 100 epochs, reserving the remaining 10% for validation.

The inference of kilonovae is based on the AB magnitude for a specific filter  $j$ ,  $m_i^j(t_i)$ . The measurements are given as a time series at times  $t_i$  with a corresponding statistical error  $\sigma_i^j \equiv \sigma^j(t_i)$ . The likelihood function  $\mathcal{L}(\vec{\theta})$  is given by Pang et al. (2022):

$$\mathcal{L}(\vec{\theta}) \propto \exp\left(-\frac{1}{2} \sum_{ij} \frac{(m_i^j - m_i^{j,\text{est}}(\vec{\theta}))^2}{(\sigma_i^j)^2 + (\sigma_{\text{sys}})^2}\right) \propto \exp\left(-\frac{1}{2} \chi^2(\vec{\theta})\right), \quad (3.3)$$

where  $m_i^{j,\text{est}}(\vec{\theta})$  is the estimated AB magnitude for the parameters  $\vec{\theta}$  using the interpolation scheme.  $\sigma_{\text{sys}}$  is the additional error budget included to account for the systematic uncertainty within the kilonova modeling. Such a likelihood is equivalent to including an additional shift to the light curve by  $\Delta m$ , and marginalizing it with a normal distribution with mean of 0 and variance of  $\sigma_{\text{sys}}^2$ . Similar to Pang et al. (2022) and motivated by the study of Heinzl et al. (2021),  $\sigma_{\text{sys}}$  is taken to be 1mag.

---

<sup>1</sup><https://github.com/nuclear-multimessenger-astronomy/nmma>

Parameter	Prior
$\log_{10}(M_{\text{ej,dyn}} [M_{\odot}])$	$\mathcal{U}(-3, -1)$
$\bar{Y}_{\text{e,dyn}}$	$\mathcal{U}(0.15, 0.30)$
$\bar{v}_{\text{ej,dyn}} [c]$	$\mathcal{U}(0.12, 0.25)$
$\log_{10}(M_{\text{ej,wind}} [M_{\odot}])$	$\mathcal{U}(-2, -0.89)$
$Y_{\text{e,wind}}$	$\mathcal{U}(0.2, 0.4)$
$\bar{v}_{\text{ej,wind}} [c]$	$\mathcal{U}(0.03, 0.15)$

Table 3.1: Parameter priors used for the Bayesian analyses.  $\mathcal{U}(a, b)$  refers to an uniform prior in the interval  $[a, b)$ . This table excludes the priors on the inclination angle, which we describe in Section 3.3.

The nested sampling algorithm implemented in `PyMultiNest` (Buchner et al., 2014; Feroz et al., 2009) is used for exploring the likelihood landscape and obtaining posterior samples.

### 3.3 Parameter Inference

As described in Section 3.2, Bayesian analyses are performed using `Bu2023YE`, for which we have considered two sets of priors. The *uniform* prior has a uniform prior on the viewing angle  $\theta_{\text{obs}}$ . Instead, the *tight* prior, applying the constraint in Mooley et al. (2022, 2018), has a Gaussian prior on the viewing angle with a mean of  $21.3^\circ$  and a standard deviation of  $2.5^\circ$ . In contrast to the uniform prior, our tight prior is constrained by the precise inclination measurement of GW170817 and its associated uncertainty, which can be used to gauge how precise inclination constraints can influence the inference of other intrinsic ejecta properties. The priors on the rest of the parameters are shown in Table 3.1.

### 3.4 Summary

In this work, we use a tight inclination constraint for GW170817/AT2017gfo from recent HST and VLBI observations (Mooley et al., 2022) and explore how this affects parameter inference on the ejecta, with a particular focus on the composition/chemical distribution within the dynamical ejecta component. We present a new grid of 1024 kilonova models computed with the three-dimensional Monte Carlo radiative transfer code `POSSIS` that depends on six parameters: the mass ( $M_{\text{ej,dyn}}$ ), averaged velocity ( $\bar{v}_{\text{ej,dyn}}$ ) and averaged electron fraction ( $\bar{Y}_{\text{e,dyn}}$ ) of the dynamical ejecta, and the mass ( $M_{\text{ej,wind}}$ ), averaged velocity ( $\bar{v}_{\text{ej,wind}}$ ) and electron fraction ( $Y_{\text{e,wind}}$ ) of the post-merger disk-wind ejecta. Guided by numerical-relativity simulations, an angular dependence of both density and electron fraction is assumed

for the dynamical ejecta. Employing this grid, we train a feed-forward NN that allows us to compute generic light curves to perform Bayesian parameter estimation.

Our study highlights the importance of using tight inclination constraints and state-of-the-art multi-dimensional kilonova modeling for parameter inference of the ejecta properties. Furthermore, we underscore our ability to probe the nucleosynthesis of heavy elements using just the early-time kilonova photometry alone. Given the sensitivity of current ground-based gravitational-wave detectors to distant neutron star mergers, detailed spectroscopy of associated kilonova counterparts to gravitational-wave sources may not always be tenable. With a precise inclination angle measurement from an associated on-axis GRB or via other means, one can employ this methodology to infer the chemical distribution of any kilonova's ejecta using well-sampled early light curve data. This approach, paired with spectroscopic studies of nearby KNe, can enable a better understanding of the nucleosynthetic yields from a population of kilonovae.

Analysis is currently underway to determine the final results from the fitting. We have computed new models after fixing a heating rate extrapolation issue in the original models, and are in the process of training updated surrogate models that will be used to fit the early photometric data of GW170817. These models described here have been updated from the original arXiv version of the paper to include one additional parameter: the electron fraction of the disk wind ejecta.

### **Acknowledgements**

SA acknowledges support from the National Science Foundation GROWTH PIRE grant No. 1545949. PTHP is supported by the research program of the Netherlands Organization for Scientific Research (NWO). MWC and BH acknowledge support from the National Science Foundation with grant numbers PHY-2010970 and OAC-2117997. TD acknowledge funding from the EU Horizon under ERC Starting Grant, no. SMArt-101076369. TD and AN acknowledge support from the Deutsche Forschungsgemeinschaft, DFG, project number DI 2553/7. TD and VN acknowledge support through the Max Planck Society funding the Max Planck Fellow group 'Multi-messenger Astrophysics of Compact Binaries'. The simulations were performed on the national supercomputer HPE Apollo Hawk at the High-Performance Computing (HPC) Center Stuttgart (HLRS) under the grant number GWanalysis/44189 and on the GCS Supercomputer SuperMUC\_NG at the Leibniz Supercomputing Centre (LRZ) [project pn29ba].

### Data Availability

The datasets used and the software used for the analysis can be found at (<https://github.com/nuclear-multimessenger-astronomy/nmma>). The interpolation models can be found on Zenodo (<https://doi.org/10.5281/zenodo.8039909>). The raw data will be made public once the paper is accepted to the journal.

## 3.5 Appendix

### Flux contribution from different ejecta components

Figure 3.2 shows the contribution to the bolometric light curves of the squeezed-polar dynamical ( $Y_e \geq 0.25$ , blue), the tidal dynamical ( $Y_e < 0.25$ , red) and the wind (grey) ejecta components. The light curves were generated from a dedicated ( $N_{\text{ph}} = 10^7$ ) BU2023YE simulation from POSSIS for the following parameters:  $\log_{10}(M_{\text{ej,dyn}}) = -2.827$ ,  $\bar{Y}_{\text{e,dyn}} = 0.256$ ,  $v_{\text{ej,dyn}} = 0.139c$ ,  $\log_{10}(M_{\text{ej,wind}}) = -1.472$ ,  $Y_{\text{e,wind}} = 0.249$ ,  $v_{\text{ej,wind}} = 0.030c$ , and  $\theta_{\text{obs}} = 18.6^\circ$ . At early times ( $\lesssim 2$  d), a significant fraction ( $\gtrsim 60\%$ ) of the escaping radiation originates in the squeezed-polar lanthanide-poor component.

### Comparison to BU2019LM

For comparison, we also make use of the grid introduced in Dietrich et al. (2020a), parameterized by  $M_{\text{ej,dyn}}$ ,  $M_{\text{ej,wind}}$ ,  $\Phi$ , and  $\theta_{\text{obs}}$ . This kilonova grid uses an earlier version of POSSIS (Bulla, 2019) with analytic functions for the opacities and simpler prescriptions for heating rates and thermalization efficiencies. The model built upon the old grid is referred to as BU2019LM. We repeat the analysis described in Section 3.3 with the BU2019LM model.

For the analyses using the BU2019LM model, the inclusion of the tight prior on the viewing angle noticeably changes the posterior and the best fit value of the viewing angle and the opening angle of the tidal dynamical ejecta,  $\Phi$ . On the other hand, the rest of the parameters are only marginally affected by such an inclusion. Such a phenomenon can be explained by the simpler geometry in the BU2019LM model and the opening angle's major role in the anisotropic geometry of the ejecta. The inclusion of the viewing angle constraint causes an increase in the opening angle ( $49.74^\circ \rightarrow 58.26^\circ$ ) and decrease in the disk wind ejecta mass ( $0.060M_\odot \rightarrow 0.056M_\odot$ ).

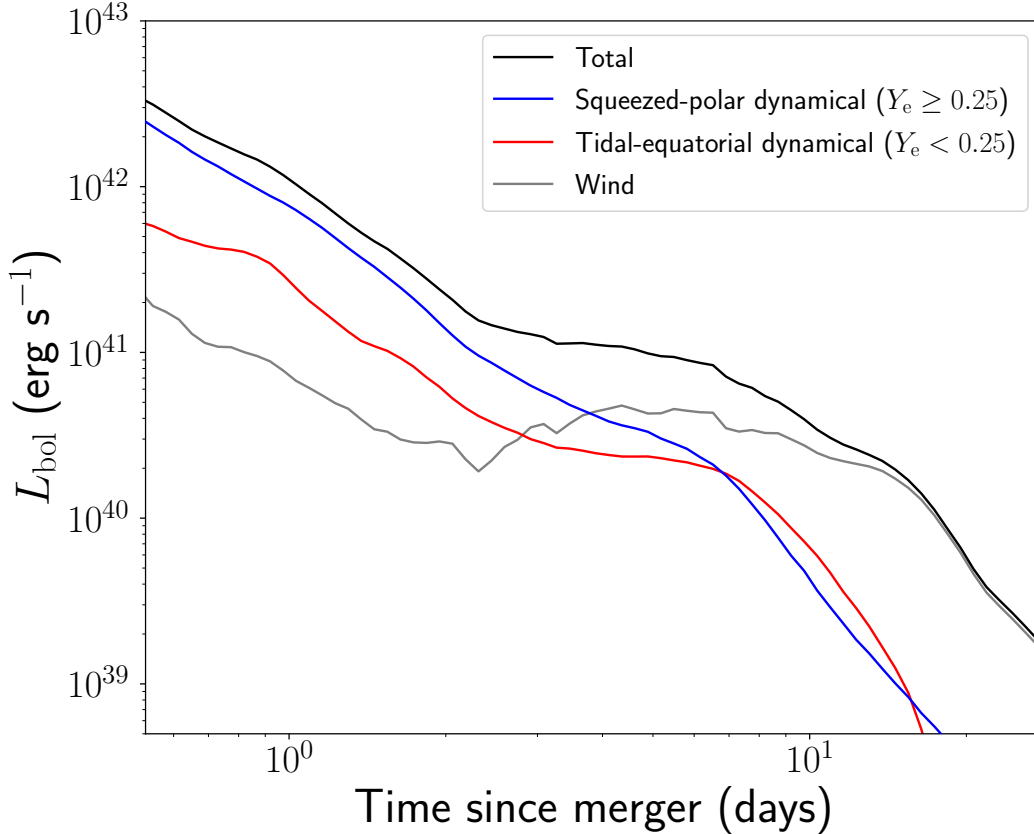


Figure 3.2: Contribution to the total bolometric light curve (black) of the squeezed-polar dynamical ( $Y_e \geq 0.25$ , blue), tidal-equatorial dynamical ( $Y_e < 0.25$ , red) and wind (grey) ejecta components. Light curves have been computed with a dedicated POSSIS simulation with  $N_{\text{ph}} = 10^7$  using the parameters described below and for an observer viewing angle of  $\theta_{\text{obs}} = 18.6^\circ$ .

### Robustness against the input ejecta model and physics

The BU2023YE and BU2019LM (Appendix 3.5) grids are significantly different in terms of assumptions on the ejecta structures (e.g. density profiles) and input physics (heating rates, thermalization efficiencies and opacities), see Bulla (2023) for more details. In Figure 3.4, we compare light curves predicted by the two grids for the same viewing angle ( $\theta_{\text{obs}} = 20^\circ$ ) and ejecta parameters:  $M_{\text{ej,dyn}} = 0.005 M_{\odot}$ ,  $\bar{v}_{\text{ej,dyn}} = 0.17c$ ,  $\bar{Y}_{\text{e,dyn}} = 0.24$  (corresponding to  $\Phi = 30^\circ$  in the BU2019LM grid),  $M_{\text{ej,wind}} = 0.05 M_{\odot}$ ,  $\bar{v}_{\text{ej,wind}} = 0.05c$  and  $Y_{\text{e,wind}} = 0.25$  (corresponding to the lanthanide-intermediate composition in the BU2019LM grid). Despite the differences between the two grids in terms of ejecta structures and input physics, we find that the predicted light curves (orange and pink lines) agree reasonably well with each others

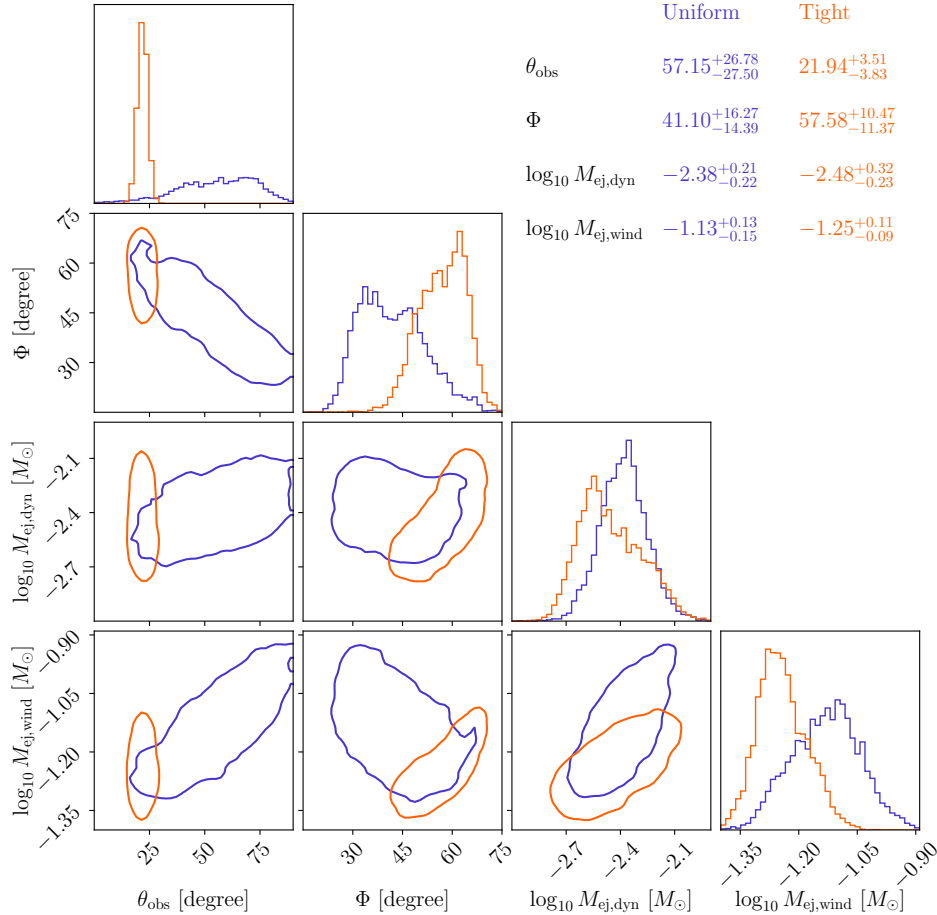


Figure 3.3: Parameter estimation for the BU2019LM model with (orange) and without (blue) the inclusion of the tight viewing angle prior.

(at a  $\lesssim 0.5$  mag level) at phases between  $\sim 1$  and  $\sim 5$  days after the merger. Deviations are instead larger at other phases. At early times, this is caused by the different opacities  $\kappa$  assumed in the two grids: the analytic ones in the BU2019LM grid are typically higher than those from Tanaka et al. (2020) used for the BU2023YE grid and therefore tend to produce fainter light curves at optically-thick early phases. At late times, the differences are likely a combination of different heating rates (assumed to be uniform in the BU2019LM grid while a function of ejecta properties in the BU2023YE grid) and different diffusion timescales caused by the different opacities at early times. While we consider the BU2023YE grid more reliable in terms of the input physics and ejecta structures, it is reassuring the two grids show reasonable agreement at phases that are well observed in the case of AT2017gfo and will likely be for future and more distant KNe.

Figure 3.4 also shows predictions for two different values of the wind composition

in the BU2023YE grid. We find that the wind composition has a relatively strong impact on the light curves and it is therefore an important parameter to vary within the grid.

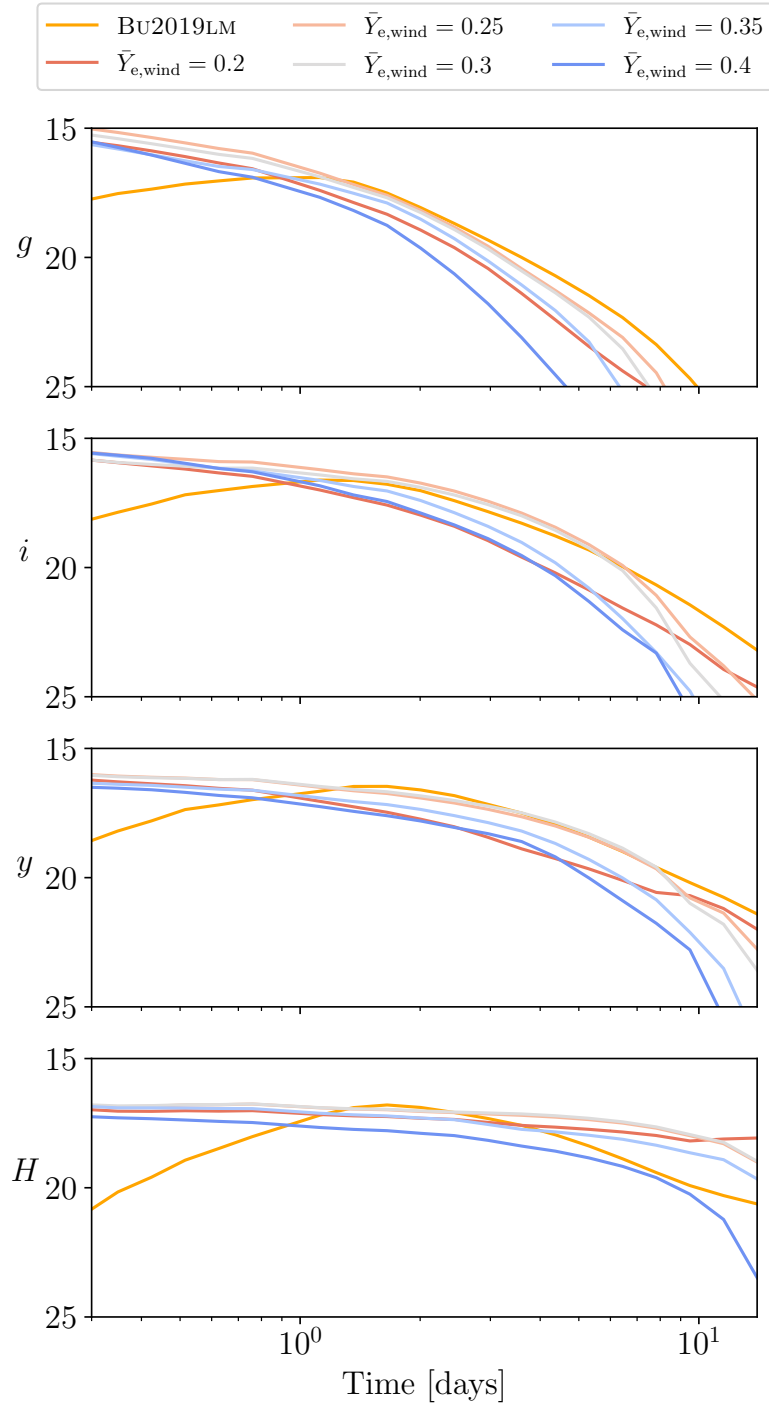


Figure 3.4: Light curves comparison between the BU2019LM grid (orange) and the BU2023YE grid for different choices of the wind composition  $Y_{e,\text{wind}}$  and for a viewing angle and the rest of the ejecta parameters fixed to the same values (see text). The BU2019LM should be compared to the BU2023YE light curve with  $Y_{e,\text{wind}} = 0.25$ , which matches the lanthanide-intermediate composition assumed in the BU2019LM grid.

*Chapter 4****r*-PROCESS FROM NEUTRON STAR-BLACK HOLE MERGERS****Optical Follow-Up of the Neutron Star-Black Hole Mergers S200105ae and S200115j**

Anand, S. & Coughlin, M.W., Kasliwal, M. M., Bulla, M., Ahumada, T., et al. 2021, Optical follow-up of the neutron star–black hole mergers S200105ae and S200115j, *Nature Astronomy*, 5, 46, . S. A. conducted observations with ZTF, vetted candidates and performed follow-up, and wrote the manuscript along with M. C. Coughlin. Published in *Nature Astronomy*. <https://doi.org/10.1038/s41550-020-1183-3>

S. A. conducted observations with ZTF, vetted candidates and performed follow-up, and wrote the manuscript along with M. C. Coughlin.

## ABSTRACT

LIGO and Virgo’s third observing run (O3) revealed the first neutron star–black hole (NSBH) merger candidates in gravitational waves. These events are predicted to synthesize r-process elements (Lattimer & Schramm, 1974b; Li & Paczynski, 1998) creating optical/near-IR “kilonova” (KN) emission. The joint gravitational-wave (GW) and electromagnetic detection of an NSBH merger could be used to constrain the equation of state of dense nuclear matter (Coughlin et al., 2018a), and independently measure the local expansion rate of the universe (Schutz, 1986). Here, we present the optical follow-up and analysis of two of the only three high-significance NSBH merger candidates detected to date, S200105ae and S200115j, with the Zwicky Transient Facility (Bellm et al. 2018; ZTF). ZTF observed  $\sim 48\%$  of S200105ae and  $\sim 22\%$  of S200115j’s localization probabilities, with observations sensitive to KNe brighter than  $-17.5$  mag fading at  $0.5$  mag/day in g- and r-bands; extensive searches and systematic follow-up of candidates did not yield a viable counterpart. We present state-of-the-art KN models tailored to NSBH systems that place constraints on the ejecta properties of these NSBH mergers. We show that with depths of  $m_{AB} \approx 22$  mag, attainable in meter-class, wide field-of-view survey instruments, strong constraints on ejecta mass are possible, with the potential to rule out low mass ratios, high BH spins, and large neutron star radii.

During O3, LIGO and Virgo detected eight NSBH and six BNS candidate events at various confidence levels, with localization regions spanning a few tens to several thousands of square degrees and median distances in the range  $\sim 108\text{-}630$  Mpc. We do not include S190718a as a BNS merger candidate due to glitches in the detectors near trigger time, which have a very high terrestrial probability ( $> 98\%$ ). All of the NSBH candidates had  $\sim 100\%$  probability of one of the component masses being  $< 3 M_{\odot}$ , and therefore likely to be a neutron star. Only two candidates, S200105ae (LIGO Scientific Collaboration & Virgo Collaboration, 2020a) and S200115j (LIGO Scientific Collaboration & Virgo Collaboration, 2020b), initially had finite probability of leaving behind a non-zero amount of neutron star material outside the final black hole, although S200115j’s updated analysis (LIGO Scientific Collaboration & Virgo Collaboration, 2020c) gives  $< 1\%$  probability of leaving behind a remnant. S200105ae (LIGO Scientific Collaboration & Virgo Collaboration, 2020a) and S200115j (LIGO Scientific Collaboration & Virgo Collaboration, 2020b) were both detected in January, at 2020-01-05 16:24:26.057 and 2020-01-15 04:23:09.742 UTC respectively (see Methods). During O3, ZTF ran a dedicated follow-up program to identify optical counterparts to gravitational-wave (GW) candidates (e.g. Coughlin et al., 2019; LIGO Scientific Collaboration & Virgo Collaboration, 2019a,b). Together with the Global Relay of Observatories Watching Transients Happen (GROWTH) network (<http://growth.caltech.edu>), ZTF rapidly followed up and classified objects that were consistent with the candidates. Over the 3 nights following detection, ZTF covered  $3300 \text{ deg}^2$  and  $1100 \text{ deg}^2$  for S200105ae and S200115j respectively, corresponding to  $\sim 52\%$  of the localization probability for S200105ae, and  $\sim 22\%$  of the localization probability for S200115j (see Methods). S200115j occurred during Palomar nighttime, so our triggered observations began immediately, but poor weather on the two nights following the merger prevented further follow-up observations.

As a metric for understanding the efficacy of ZTF’s observations, we show the mean absolute magnitude to which we are sensitive as a function of sky location in Figure 4.1. This folds in the distance distribution across the skymap compared to our median limiting magnitude in each of the fields (See 4.7). The best limiting magnitudes correspond to absolute magnitudes  $\lesssim -16$  mag for both events, with typical observations ranging from  $M \sim -16.5$  mag to  $M \sim -17.5$  mag. AT2017gfo (Evans et al., 2017a), the optical counterpart to GW170817, peaked at  $M \sim -16$  mag, and KNe from NSBH models are typically brighter than those from BNSs (Barbieri et al., 2019; Kawaguchi et al., 2020; Rosswog et al., 2017), indicating that our ob-

servations are in the magnitude range required for detection.

In addition to requiring multi-epoch coverage of large localizations at sufficient depth, these searches normally yield hundreds of thousands of alerts that require quick and thorough vetting (see Methods for specific criteria and 4.5). We successfully narrowed this list down to a select few candidates consistent with our criteria within minutes for both events; only 22 candidates for S200105ae and 6 candidates of S200115j remained (see Methods for selection criteria). GROWTH obtained follow-up photometry and spectroscopy for the candidates passing our requirements to assess their relation to either event. Using a global array of telescopes (see Methods for observatories and instruments), we reject each of our candidates based on the following criteria:

- Spectroscopic Classification: candidates spectroscopically determined to be supernovae or other transient (see Figure 4.2 and 4.17).
- Slow photometric evolution: candidates evolving at  $< |0.3|$  mag/day, below the expected fast evolution for KNe over the course of a week (see Methods and 4.15 for justification and 4.14 for candidate light curves).
- Stellar Variables: candidates coincident with point sources, likely to be variable stars or cataclysmic variables in the Milky Way.
- Slow-moving asteroids: candidates that are later determined to be asteroids or other solar-system objects (see 4.16).

After thorough vetting, we found no candidate remaining that could plausibly be associated with either event (see the candidates spatial distribution in 4.6 and the list of the candidates in Supplementary Information Tables 4.1, 4.2, and 4.3).

The non-detection in our searches allows us to impose both empirical and model-based constraints on photometric evolution for a counterpart falling within the observed region. To place the coverage and limits in context, we compare our observations to empirical models of evolution with a linear rise and decay (Figure 4.3), and KN models, which allow ejecta masses to vary (Figure 4.4). Using `simsurvey` (Feindt et al., 2019) to inject and recover simulated KNe, we show in Figure 4.3 that ZTF should have detected a KN in the observed region of either skymap brighter than  $M \lesssim -17.5$  mag and fading slower than 0.5 mag per day in both  $g$  and  $r$ -bands.

We simulate kilonovae with various absolute magnitudes and evolution rates assuming no color evolution. Our recovery criteria requires a single kilonova detection in either filter. We plot the KN absolute magnitudes at peak along with their evolution rates. We also mark AT2017gfo, which had a peak absolute magnitude of about  $-16$  mag in optical bands, fading at  $\sim 1.0$  mag per day in  $g$ - and  $r$ -bands. Lack of observations on the first night for S200105ae, owing to a delay in the release of the initial skymap, worsened constraints compared to S200115j (see Methods). We note here that our sensitivity to rising or fading kilonovae is highly dependent on latency in starting observations and number of follow-up epochs.

For our model-dependent constraints, assuming the kilonova is in the area observed, we take a series of representative median magnitudes for each night of observations and compare them to light curve models from the radiative transfer code POSSIS (Bulla, 2019); we generated them using a new grid of KN spectra tailored to NSBH mergers. These are summarized in Figure 4.4, where we show light curves that are allowed (grey) or ruled out at different distances (light to dark blue) by the median magnitudes achieved with our observations of S200105ae and S200115j (see Methods). We find that the median magnitudes place weak constraints on these models. Specifically, all KN light curves we consider are fainter than the limits for S200105ae while only a few models with large amounts of post-merger ejecta ( $\gtrsim 0.05M_{\odot}$ ) are ruled out for S200115j at polar viewing angles and for the nearest-by portions of the skymap. Additionally, we note that due to our coverage in both skymaps being less than 50%, our model constraints for S200105ae and S200115j only apply within the observed region. For comparison, the right panel of Figure 4.4 shows NSBH models from our new grid that are ruled out by the DECam observations of S190814bv (Andreoni et al., 2020); such limits are more robust than our limits on S200105ae and S200115j due to DECam covering 98% of the skymap (compared to 48% and 22%). For that well-localized event, the deeper DECam limits and the closer distance for S190814bv ( $d=267\pm 52$  Mpc (LIGO Scientific Collaboration & Virgo Collaboration, 2019b)) lead to a larger number of models ruled out.

To understand the scientific performance and potential of meter-class, wide field-of-view imagers as powerful tools in EM-GW follow-up, we determine what constraints are possible on the viewing angle of a potential counterpart, the dynamical ( $M_{\text{ej,dyn}}$ ) and post-merger ( $M_{\text{ej,pm}}$ ) ejecta and the binary parameters with the deepest ZTF exposures on each night (see Methods). For S200105ae, with five-minute ex-

posures reaching a depth of  $m_{AB} \gtrsim 22$  mag, ZTF would be sensitive to a large fraction of KNe with polar and intermediate viewing angles. Non-detection of a kilonova in these circumstances could rule out  $M_{\text{ej,dyn}} \leq 0.02 M_{\odot}$  and  $M_{\text{ej,pm}} \leq 0.04 M_{\odot}$  for polar directions at 283 Mpc (see 4.8). Using these  $M_{\text{ej}}-\theta_{\text{obs}}$  constraints, we could estimate the maximum aligned spin of the BH component for different assumptions on the viewing angle, binary mass ratio and neutron star radius. Non-detection would further rule out low mass ratios, high BH spins, and/or large neutron star radii (see 4.11). For high mass ratios, the limit on  $M_{\text{ej,dyn}}$  would be more constraining than the limit on  $M_{\text{ej,pm}}$ . As  $M_{\text{ej,dyn}}$  is reasonably well known from simulations (Foucart et al., 2018b), our modeling of the ejected mass is not a significant source of uncertainty. For low mass ratios, the limit on  $M_{\text{ej,pm}}$  would be more constraining. Current simulations only allow us to constrain  $M_{\text{ej,pm}}$  to within a factor of 2–3 (Christie et al., 2019), and are in this case an important source of modeling uncertainty. Here, we derive an upper limit on the black hole spin using a conservative estimate of  $M_{\text{ej,pm}}$ . Improved simulations providing better estimates of  $M_{\text{ej,pm}}$  could make these limits more constraining in the future (see 4.13 for the binary parameter region not constrained by our simulations).

Additionally, the available parameter space could be significantly reduced if we knew the chirp mass of the binary (Barbieri et al., 2019), which is not yet published by LIGO-Virgo. For S200115j, whose median distance was  $\sim 60$  Mpc greater than S200105ae, the deepest exposures would only be sensitive to kilonovae at nearby distances, and thus place weak constraints on the binary parameters.

Revisiting the follow-ups of S190814bv with the updated NSBH grid, we find more stringent constraints on the ejecta mass and binary parameters than for S200105ae, even using median observations (Figure 4.4). Polar orientations are ruled out at distances  $\leq 267$  Mpc, limiting the ejecta masses to  $M_{\text{ej,dyn}} \lesssim 0.01 M_{\odot}$  and  $M_{\text{ej,pm}} \lesssim 0.01 M_{\odot}$ . At intermediate orientations ( $46^{\circ} \lesssim \theta_{\text{obs}} \lesssim 53^{\circ}$ ), these constraints are still  $M_{\text{ej,dyn}} \lesssim 0.02 M_{\odot}$  and  $M_{\text{ej,pm}} \lesssim 0.03 M_{\odot}$  (see 4.8). We also find that deep  $i$ - and  $z$ -band exposures contribute significantly towards constraining a larger portion of the  $M_{\text{ej}}-\theta_{\text{obs}}$  and binary parameter-space (see 4.12). Literature on kilonova models (Kawaguchi et al., 2020; Tanaka et al., 2014) have predicted kilonovae from NSBH mergers to be brighter in the  $i$ - and  $z$ -bands compared to  $g$ - and  $r$ -bands. The same reddened emission is evident in our models (see 4.9 and 4.10), and is demonstrated by our re-analysis of the DECam upper limits on S190814bv. Thus observations in redder bands will yield better overall constraints on NSBH kilonova emission.

Several works in the literature (Barbieri et al., 2019; Kawaguchi et al., 2020; Rosswog et al., 2017) have shown that KNe from NSBH mergers are generally brighter than those resulting from BNS mergers. A similar behaviour is found in NSBH and BNS models computed here and in Dietrich et al. (2020a), respectively. Although the comparison is sensitive to the specific binary properties and thus ejecta masses adopted, we identify some general behaviour using typical values from analytical models calibrated to numerical simulations (Foucart et al., 2018b; Krüger & Foucart, 2020) (e.g. for a  $1.2M_{\odot} - 1.4M_{\odot}$  BNS merger with  $R = 12 \text{ km}$ :  $M_{\text{ej,dyn}}^{\text{BNS}} = 0.005 M_{\odot}$ ,  $M_{\text{ej,pm}}^{\text{BNS}} = 0.05 M_{\odot}$ ; for a  $1.2M_{\odot} - 6M_{\odot}$  NSBH merger with BH spin of 0.75:  $M_{\text{ej,dyn}}^{\text{NSBH}} = 0.05 M_{\odot}$  and  $M_{\text{ej,pm}}^{\text{NSBH}} = 0.05 M_{\odot}$ ). At peak, the difference in brightness between NSBH and BNS mergers is relatively small in both  $g$ - and  $r$ -bands. The evolution after peak, however, is significantly different between the two systems. Compared to BNS mergers, NSBH mergers produce  $\sim 10\times$  more massive dynamical ejecta and are thus associated with longer diffusion timescales, as photons take longer to diffuse out of the high-density and lanthanide-rich dynamical ejecta. Consequently, KNe from NSBH mergers evolve more slowly after peak and therefore stay bright longer than those resulting from BNS mergers. The difference can be as large as  $\Delta m \sim 2 \text{ mag}$  about 3 days post-peak for favourable viewing angles. The different evolution post-peak explains why constraints derived above for S190814bv are tighter than those using BNS models (Andreoni et al., 2020). The slower evolution of NSBH compared to BNS mergers makes the former promising candidates for future follow-up studies. This slower evolution is fairly robust to the choice of parameters as long as the NS is disrupted by its BH companion.

Looking forward, achieving increased and consistent depth over our observations, and supplementing  $r$ - and  $g$ -band observations with an  $i$ -band observation will be key to increasing our chances of finding a kilonova and/or discerning properties of the merger (See Methods). NSBH binaries, with a combination of intrinsically longer-lasting emission, higher signal-to-noise ratios and therefore smaller sky areas (sky area  $\sim \frac{1}{\text{SNR}^2}$ ), and high rates based on the three high-significance NSBH candidates observed during O3 makes them ideal for counterpart searches, important for measuring the Hubble Constant given their improved inclination measurements over BNS counterparts (Vitale & Chen, 2018). Furthermore, the uncertainty over the time delay between a merger and its peak light curve motivates obtaining observations one night after the merger; the most constraining limits from our analysis correspond to one night post-merger, when the KN is brightest (see Figure 4.4). While low-latency follow-up is crucial for determining whether an early-time

lanthanide-free component is present in these KNe, observations one night after are equally important for detection or placing ejecta mass constraints. In this work, we have showcased a novel methodology for deriving significant constraints on NSBH kilonova models even in the case of non-detection of a counterpart, and demonstrated that such valuable constraints are within reach of wide field-of-view, meter-class imagers.

To close, we highlight the immense promise of undertaking searches for the kilonova counterparts of NSBH mergers. The dearth of electromagnetic observations of NSBH systems as compared to BNS systems (discovered in X-ray binaries), and the difficulty of distinguishing between a low-mass BBH and a NSBH system from the GWs points to the “smoking gun” nature of KNe in confirming the existence of such systems. KNe are amongst the most valuable probes of the empirical “mass gap” between the stellar mass neutron star and black hole systems, and will allow us to observationally confirm the correlation between the mass ratio of the binary and the fate of the remnant, even in the case of non-detection. These could be jointly addressed by GW and EM facilities that possess a combination of large fields-of-view and deep sensitivity. Continuing follow-ups of NSBH mergers is essential in granting key insights into the nature of the elusive NSBH population as a whole.

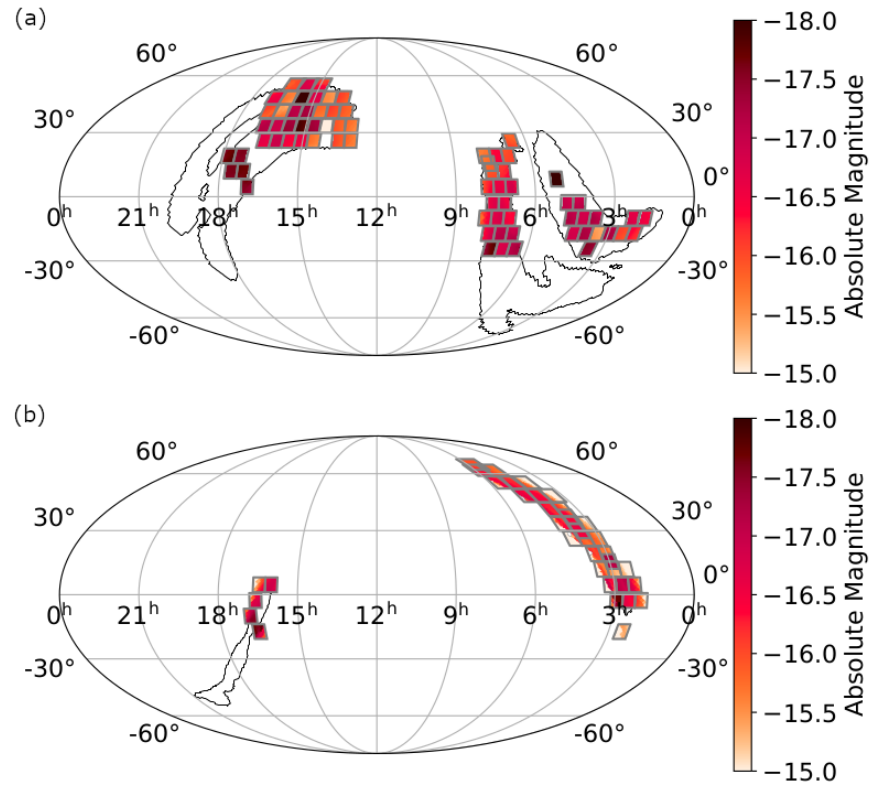
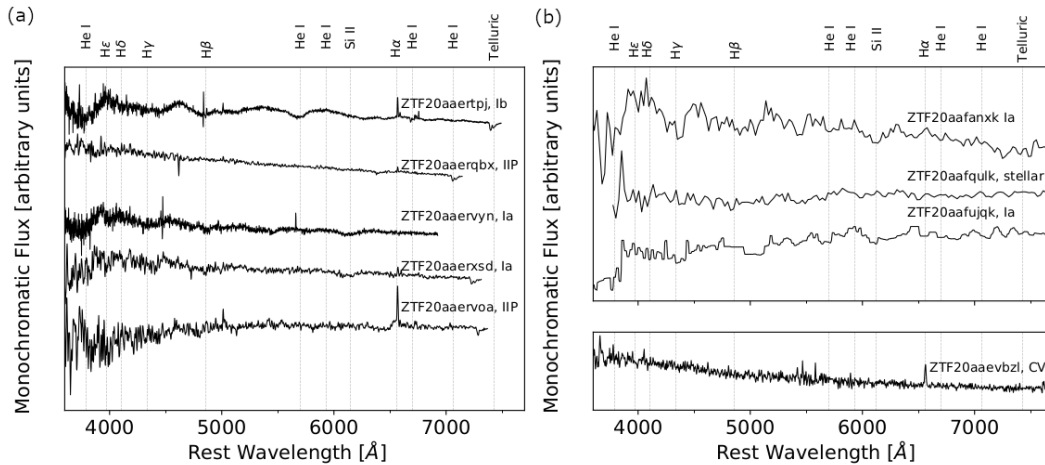
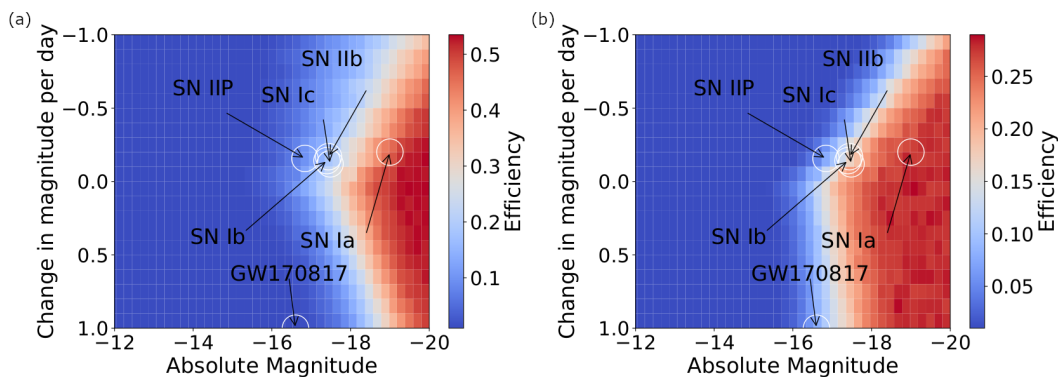


Figure 4.1: **Absolute magnitudes corresponding to ZTF pointings in the skymap.** We map the absolute magnitudes corresponding to the distance provided in the GW LALInference skymap, measured at the center of each field, and the deepest limiting magnitude in either  $g$ - or  $r$ -bands (computed as a median over the CCDs in a particular field) for S200105ae (a) and S200115j (b). We also show the 90% probability region contours to guide the eye.



**Figure 4.2: Spectra of all of the candidates ruled out spectroscopically during both campaigns.** In order to visualize all the spectra on the same figure, we have applied a vertical offset to the flux, and plotted each spectrum at mean signal-to-noise ratio. The vertical dashed lines correspond to common spectral absorption and emission features in SN spectra. (a) Spectra of five S200105ae candidates taken with the Optical System for Imaging and low Resolution Integrated Spectroscopy (OSIRIS) on the Gran Telescopio Canarias (GTC) of the Roque de los Muchachos Observatory in La Palma, Spain (Castro-Tirado et al., 2020; Valeev et al., 2020). The top three spectra were taken on Jan 11th, and the bottom two were taken on Jan 10th. From top to bottom, ZTF20aaertpj was classified as a SN Ib at  $z(s) = 0.026$ , ZTF20aaerqbx was classified as a SN IIP at  $z(s) = 0.098$ , ZTF20aaervyn was shown to be a SN Ia at  $z(s) = 0.112$ , ZTF20aaerxsd is a SN Ia at  $z(s) = 0.055$ , and ZTF20aaervoa was classified as a SN IIP at  $z(s) = 0.046$ . (b) Top: all spectra taken with the SED Machine (SEDM) on the Palomar 60-inch telescope (P60); from top to bottom, ZTF20aafanxk (S200105ae) was classified as a SN Ia at  $z(s) = 0.103$  on January 18th, the spectrum of ZTF20aafqulk (S200115j), observed on January 24th, indicates that it is likely stellar, and ZTF20aafujqk (S200105ae), also observed on January 18th, was classified as a SN Ia at  $z(s) = 0.074$ . (b) Bottom: The spectrum of ZTF20aaevbz1 (S200105ae) taken by the Double Spectrograph (DBSP) on the Palomar 200-inch telescope (P200) obtained on January 18th, 2020, contains a H $\alpha$  feature in a mostly featureless blue continuum that is indicative of it being a cataclysmic variable.



**Figure 4.3: Detection efficiency of simulated KNe based on ZTF observations.** Ratio of recovered vs injected KNe (efficiency) identified in observations in a skymap for an analytic model varying absolute magnitude and change in magnitude per day for (a) S200105ae and (b) S200115j in both  $g$  and  $r$ -bands. Here, the magnitude corresponds to the peak absolute magnitude of the injected kilonovae for a linear model with a given rise or decay rate. The maximum of the colorbar scale is set to the maximum efficiency achieved (at  $M = -20$ ), which for S200105ae was 53% and 29% for S200115j. We include approximate peak absolute magnitudes and approximate rise rates for some common SNe types; for GW170817, we plot the absolute magnitude at detection and the approximate decline rate to guide the eye.

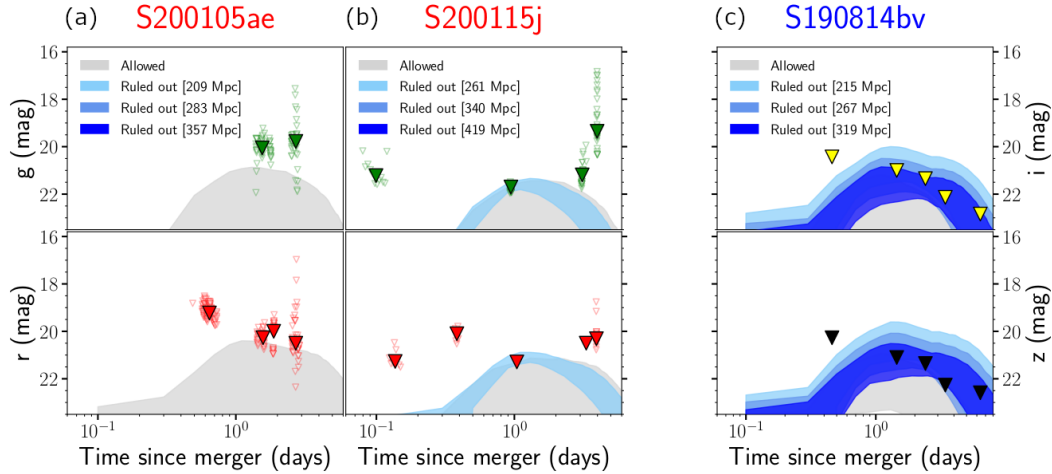


Figure 4.4: **Constraints on kilonova model parameters based on median limiting magnitudes.** We display all KN light curves ruled out by *median*  $5\text{-}\sigma$  limits on (a) S200105ae (ZTF), (b) S200115j (ZTF) and (c) S190814bv (DECam). For S200105ae and S200115j, median AB magnitudes are shown with filled triangles, while individual limits are shown with open triangles. Limits shown for S190814bv are median depth values from table 1 of Andreoni et al. (2020). KN light curves are calculated with POSSIS (Bulla, 2019); we show in blue when they are ruled out by the limits at three different distances (corresponding to median distances and  $\pm 1\sigma$  distance uncertainties from LIGO) and in grey otherwise. For each distance, the shaded area represents the range spanned by different models and different viewing angles (with the brighter end generally corresponding to higher masses and polar orientations while the fainter end to lower masses and equatorial orientations). The median limits for S200105ae do not constrain any kilonova models for any distance assumptions, while for S200115j they place constraints only on the models for nearby kilonovae (light blue). For S190814bv, median limits constrain kilonova models for all distance assumptions.

**Acknowledgements** This work was supported by the GROWTH (Global Relay of Observatories Watching Transients Happen) project funded by the National Science Foundation under PIRE Grant No 1545949. GROWTH is a collaborative project among California Institute of Technology (USA), University of Maryland College Park (USA), University of Wisconsin Milwaukee (USA), Texas Tech University (USA), San Diego State University (USA), University of Washington (USA), Los Alamos National Laboratory (USA), Tokyo Institute of Technology (Japan), National Central University (Taiwan), Indian Institute of Astrophysics (India), Indian Institute of Technology Bombay (India), Weizmann Institute of Science (Israel), The Oskar Klein Centre at Stockholm University (Sweden), Humboldt University (Germany), Liverpool John Moores University (UK) and University of Sydney (Australia).

Based on observations obtained with the Samuel Oschin Telescope 48-inch and the 60-inch Telescope at the Palomar Observatory as part of the Zwicky Transient Facility project. ZTF is supported by the National Science Foundation under Grant No. AST-1440341 and a collaboration including Caltech, IPAC, the Weizmann Institute for Science, the Oskar Klein Center at Stockholm University, the University of Maryland, the University of Washington (UW), Deutsches Elektronen-Synchrotron and Humboldt University, Los Alamos National Laboratories, the TANGO Consortium of Taiwan, the University of Wisconsin at Milwaukee, and Lawrence Berkeley National Laboratories. Operations are conducted by Caltech Optical Observatories, IPAC, and UW. The work is partly based on the observations made with the Gran Telescopio Canarias (GTC), installed in the Spanish Observatorio del Roque de los Muchachos of the Instituto de Astrofísica de Canarias, in the island of La Palma. One of us also acknowledges all co-Is of our GTC proposal.

The KPED team thanks the National Science Foundation and the National Optical Astronomical Observatory for making the Kitt Peak 2.1-m telescope available. We thank the observatory staff at Kitt Peak for their efforts to assist Robo-AO KP operations. The KPED team thanks the National Science Foundation, the National Optical Astronomical Observatory, the Caltech Space Innovation Council and the Murty family for support in the building and operation of KPED. In addition, they thank the CHIMERA project for use of the Electron Multiplying CCD (EMCCD).

SED Machine is based upon work supported by the National Science Foun-

dition under Grant No. 1106171 The ZTF forced-photometry service was funded under the Heising-Simons Foundation grant #12540303 (PI: Graham). M. W. Coughlin acknowledges support from the National Science Foundation with grant number PHY-2010970. S. Anand gratefully acknowledges support from the GROWTH PIRE grant (1545949). Part of this research was carried out at the Jet Propulsion Laboratory, California Institute of Technology, under a contract with the National Aeronautics and Space Administration. E.C. Kool acknowledges support from the G.R.E.A.T research environment and the Wenner-Gren Foundations. F. Foucart gratefully acknowledges support from NASA through grant 80NSSC18K0565, from the NSF through grant PHY-1806278, and from the DOE through CAREER grant DE-SC0020435.

**Competing Interests** The authors declare no competing interests.

**Contributions** SA and MWC were the primary authors of the manuscript. MMK is the PI of GROWTH and the ZTF EM-GW program. MB, ASC, and FF led the theory and modeling. TA, MA, NG, IA, and LPS support development of the GROWTH ToO Marshal and associated program. TA, RS, JS, SBC, VZG, AKHK, HK, ECK, PM, and SR contributed to candidate scanning, vetting, and classification. EB leads the ZTF scheduler and associated interfacing with the ToO program. BB provided interpretation of the asteroid candidates. MDC, AJC, YH, RS, AFV provided GTC data and associated analysis. KD and MJH provided P200 follow-up. RGD, DAD, MF, SRK, ES and RR provided KPED data. MR and RW provided SEDM data. CF, MJG, RRL, FJM, PM, MP, PR, BR, DLS, RS, MTS, and RW are ZTF builders. All authors contributed to edits to the manuscript.

**Correspondence** Correspondence and requests for materials should be addressed to Michael Coughlin (email: cough052@umn.edu) and Shreya Anand (email: sanand@caltech.edu).

## 4.1 Methods

### Gravitational-wave candidates

LIGO/Virgo S200105ae (LIGO Scientific Collaboration & Virgo Collaboration, 2020a), a candidate NSBH event which occurred at 2020-01-05 16:24:26.057 UTC, was discovered by the Advanced LIGO-Livingston detector, with Virgo also observing at the time. The event was initially reported as having 97% terrestrial probability, with a false alarm rate (FAR) of 24 per year, and therefore not generally of interest for follow-up. However, the LIGO and Virgo Collaborations reported that the significance was likely grossly underestimated as a single-instrument event, and the presence of a chirp-like structure in the spectrograms gave confidence in it being a real event (LIGO Scientific Collaboration & Virgo Collaboration, 2020a,d). Unlike other NSBH events, this trigger initially had  $p_{\text{remnant}} > 0\%$ ; this parameter indicates the probability of whether there is remnant matter outside of the merger that could generate an electromagnetic transient counterpart (Chatterjee et al., 2020; Foucart et al., 2018b). Similar to GW190425 (Abbott et al., 2020a), as a single detector event, the 90% credible region spans  $7720 \text{ deg}^2$ , with an all-sky averaged distance to the source of  $265 \pm 81 \text{ Mpc}$ . After our observations on the three following nights were complete, a new LALInference skymap was released (LIGO Scientific Collaboration & Virgo Collaboration, 2020e). The LALInference map slightly reduced the 90% area to  $7373 \text{ deg}^2$  (while making the 50% area larger), modified the all-sky averaged distance to the source to  $283 \pm 74 \text{ Mpc}$ , and shifted more of the probability to be uniform across the lobes (including the one near the sun, which was at  $\sim 19 \text{ hr}$  in RA and  $\sim -22^\circ$  in declination at the time of the trigger, see 4.6). Further parameter estimation maintained that the merger was likely to have contained one object with component masses  $< 3 M_\odot$ , and therefore likely to be a neutron star ( $> 98\%$  probability), but significantly reduced the estimated remnant probability ( $p_{\text{remnant}} < 1\%$ ).

LIGO/Virgo S200115j (LIGO Scientific Collaboration & Virgo Collaboration, 2020b), a candidate NSBH event which occurred at 2020-01-15 04:23:09.742 UTC, was discovered by the two Advanced LIGO interferometers and the Advanced Virgo interferometer. This event was classified as a “MassGap” event, with  $\text{HasNS} > 99\%$ , indicating that one component’s mass fell into the range between 3 and 5 solar masses, and the other component was  $< 3 M_\odot$ , and therefore likely to be a neutron star, respectively. Although S200115j initially had a non-zero terrestrial probability, its revised classification reflected that the trigger was astrophysical ( $\text{MassGap} > 99\%$ ), with a FAR of 1 per 1513 years. As a three-detector localized event, the

skymap was better-constrained than for S200105ae, spanning  $908 \text{ deg}^2$  (at 90% confidence). Additionally, it contained two disjointed lobes, one in each hemisphere, and had a median distance of  $331 \pm 97 \text{ Mpc}$ . Considering all of these factors, along with the remnant probability  $p_{\text{remnant}} = 8.7\%$ , we chose to trigger our program for ZTF follow-up and obtained target-of-opportunity (ToO) observations. Nearly three days later, an updated LALInference skymap reduced the 90% credible region to  $765 \text{ deg}^2$  and shifted most of the probability to the southern-most tip of the lower lobe (LIGO Scientific Collaboration & Virgo Collaboration, 2020c), see 4.6. The median distance was only slightly modified to  $340 \pm 79 \text{ Mpc}$ . This update also distinguished S200115j from other NSBH candidates as an exceptional event for electromagnetic follow-up, with a  $p_{\text{remnant}} > 99\%$  (LIGO Scientific Collaboration & Virgo Collaboration, 2020c).

## Observing Plan

### S200105ae

S200105ae was detected by LIGO and Virgo during the morning Palomar time on 2020-01-05 UT (LIGO Scientific Collaboration & Virgo Collaboration, 2020a). Because it was originally identified as having a FAR above the threshold for automated public release, the skymap was not released until the following day. On 2020-01-06, beginning at 02:21:59 UT (hereafter night 1), only  $\sim 2\%$  of the localization was covered serendipitously by ZTF routine survey operations (Bellm et al., 2018; Dekany et al., 2020; Graham et al., 2019; Masci et al., 2019), which have 30 s observations, emphasizing that the delay in the skymap may have been a critical loss to the chances of detection for any fast fading counterparts.

On 2020-01-07 UT (night 2) following the belated publication of the alert by LIGO and Virgo, we adopted a survey strategy of  $g$ - and  $r$ -band exposure blocks with 180 s exposures for ZTF. The length of the exposures was chosen to balance both the depth required for a relatively distant event and the sky area requiring coverage; specifically, we optimize the exposure times to be as long as possible while covering the 90% sky area consistent with the GW event observable from Palomar and in two filters within the night. We used `gwemopt` (Coughlin et al., 2018b, 2019b), a codebase designed to optimize telescope scheduling for GW follow-up, to schedule the observations. The schedule is designed such that fields have reference images available to facilitate image subtraction, as well as a 30 minute gap between the observations in  $g$ - and  $r$ -bands to identify and remove moving objects.

These observations were submitted from the GROWTH ToO Marshal (Coughlin et al., 2019c), which we use to ingest alerts and plan observations.

Due to poor weather conditions at Palomar, the limiting magnitudes in the first block of night 2 were shallower than expected at a  $5\sigma$  median depth of  $m_{AB} = 19.5$  in  $g$ - and  $r$ -bands (see 4.7), and the second block originally scheduled for the same night was subsequently cancelled because of this (Anand et al., 2020c). Combining the serendipitous and ToO observations, we covered  $2200 \text{ deg}^2$ , corresponding to about 44% of the initial BAYESTAR and 35% of the final LALInference maps on night 2. We adopted a similar strategy on night 3 (2020-01-08 UT), and improved weather led to deeper limits, with a  $5\sigma$  median depth of  $m_{AB} = 20.2$  in  $g$ - and  $r$ -bands (Stein et al., 2020). Combining the serendipitous and ToO observations, we covered  $2100 \text{ deg}^2$  on night 3, corresponding to about 18% of the initial BAYESTAR and 23% of the LALInference maps. In total, over the 3 nights, we covered  $3300 \text{ deg}^2$ , corresponding to about 52% of the initial BAYESTAR and 48% of the LALInference maps.

### **S200115j**

The skymap for S200115j was released during Palomar nighttime on 2020-01-15 UT; we triggered ToO observations with ZTF and were on-sky within minutes. We employed the greedy-slew algorithm, same as for S200105ae, taking 300 s exposures in  $g$ - and  $r$ -bands (Anand et al., 2020b). Because the fields were rapidly setting by the time the skymap arrived, we were only able to cover 36% of the skymap in our ToO observations on that night. Poor weather and seeing conditions prevented us from triggering the following night (2020-01-16 UT). The subsequently released LALInference skymap shifted the innermost probability contour to the Southern lobe (LIGO Scientific Collaboration & Virgo Collaboration, 2020c), which was largely inaccessible to ZTF. While we were unable to obtain further triggered observations due to poor weather, our total serendipitous and triggered coverage within three days of the merger was  $1100 \text{ deg}^2$ , corresponding to about 35% probability of the initial BAYESTAR map and 22% probability of the final LALInference map.

Other teams also performed synoptic follow-up of these two events (Han et al., 2020; LIGO Scientific Collaboration & Virgo Collaboration, 2020a; Lipunov et al., 2020a,b; Noysena et al., 2020; Steeghs et al., 2020; Turpin et al., 2020).

## Candidates

For a transient-event to be considered an “alert,” a source extracted from a difference image must satisfy the following criteria:

1. have a signal-to-noise ratio (SNR)  $\geq 5$  in positive or negative flux;
2. PSF-fit magnitude  $\leq 23.5$  mag;
3. number of bad pixels in 5x5 pixel region centered on transient position is  $\leq 4$  pixels;
4. FWHM of source profile is  $\leq 7$  pixels (where 1 pixel  $\approx 1$  arcsec);
5. source elongation (ratio A/B of ellipse from isophotal fit) is  $\leq 1.6$ ;
6. the difference between flux measurements in a fixed aperture and the PSF-fit ( $\text{mag}_{\text{diff}} = \text{Aper}_{\text{mag}} - \text{PSF}_{\text{mag}}$ ) falls in the range:  $-0.4 \leq \text{mag}_{\text{diff}} \leq 0.75$ .

For details, see Masci et al. (2019) for alert packet contents and Patterson et al. (2018) for the ZTF alert distribution system. Hundreds of thousands of alerts are produced by ZTF every night, and the reader can find nightly alert collections in the ZTF alert archive (<https://ztf.uw.edu/alerts/public/>).

To be considered as candidates, transients must have positive residuals after image subtraction, i.e. they must have brightened relative to the reference image. We require reported transients to have at least two detections separated by at least 15 minutes to remove potential asteroids and other moving objects. In order to remove contributions from likely non-transient point sources (stars in our Galaxy and distant QSOs), we remove any candidates located less than  $2''$  from the Pan-STARRS1 point source catalog (PS1 PSC (Tachibana & Miller, 2018)), relying on star/galaxy classification as described in Miller et al. (2017). We exclude candidates shown to be image artifacts after close inspection. We also remove any events that have detections prior to the trigger or are outside the 95% contour in the localization. The progression in reduction of alerts to be considered for three representative nights covering the events discussed in this paper is shown in 4.5.

For cross-validation purposes, we use three forms of candidate selection, light curve filtering, and visualization tools: (i) the GROWTH Marshal (Kasliwal et al., 2019), a web-based dynamic portal for accessing transients (ii) the Kowalski alert archive (<https://github.com/dmitryduev/kowalski>) (Duev et al., 2019), and (iii)

the AMPEL alert archive (<https://github.com/AmpelProject>) (Nordin et al., 2019; Soumagnac & Ofek, 2018). For our realtime human vetting involving candidates from (i), we selected candidates exhibiting interesting  $g-r$  color initially or rapid photometric evolution. Candidates retrieved via Kowalski and AMPEL (ii and iii) were all manually inspected and announced via GCN notice. As a final check, we performed a late-time Kowalski query within both event skymaps for candidates passing the above criteria, whose forced photometry light curves evolved faster than 0.3 mags/day, and with a baseline of  $<10$  days between the first and last detection.

### Observation-Based NSBH Constraints

In this section, we outline a methodology for converting observational upper limits to constraints on the properties of the associated kilonova and the merging binary. Although our upper limits lack the depth required for placing meaningful constraints on the emission from both of these NSBH mergers, and we covered less than 50% of the skymap in each case, we show that scientifically useful constraints are within reach of ZTF and similar facilities. We first illustrate how to analyze the detectability of kilonovae in a model-independent way using field-by-field ZTF pointings and a survey simulation software. Then, using a new grid of kilonova spectra tailored to NSBH mergers, we show that observations attaining a median depth of  $m_{AB} \sim 22$  with improved coverage could rule out certain portions of the  $M_{ej}-\theta_{obs}$  parameter space, translating to constraints on the mass ratio/NS radius/BH spin. We describe our methodologies in detail, below.

### Model-independent constraints

We begin with a simple, generic model to place the observational limits in context. For this purpose, we use `simsurvey` (Feindt et al., 2019), a software package initially designed and used for assessing the rates of transient discovery in surveys such as ZTF by accounting for both transient and observational parameters. We adopt a toy model for transients here, injecting transients that begin at a particular absolute magnitude and decline at a certain rate measured in magnitudes per day (distributed between  $-1.0$  mag/day and  $1.0$  mag/day, with negative decay rates corresponding to rising sources). We assume the transients have the same luminosity in both  $g$ - and  $r$ -band, and inject them in sky locations and distances consistent with the GW skymaps. Our results show that ZTF would be sensitive to rising or fading kilonovae brighter than  $M \sim -17.5$  within the skymap of S200105ae, and fading kilonovae brighter than  $M \sim -17$  within the skymap of S200115j. Losses in

efficiency in general are due to our requirements that they are “detected” at least once within the fields we observed with ZTF; for this study, we are using both ToO and serendipitous ZTF observations from up-to 72 hours following the merger, including time- and field-dependent limiting magnitudes from those observations. We assume that the simulated transients evolve at the same rate during those 72 hours. However, deeper observations of future NSBH mergers could lead to stronger statements about the minimum luminosity and maximum evolution rate of a kilonova associated with a given GW event. In the future, as the number of NSBH merger detections increases, `simsurvey` could be used to empirically estimate the rates and luminosity function of kilonovae from NSBHs (Kasliwal et al., 2020).

Figure 4.3 shows the percentage of transients that should be identified consistent with the LALInference skymaps for both events, parameterized by their peak absolute magnitude and decline rate.

### Ejecta mass and binary parameter constraints

We combine  $g$ - and  $r$ -band upper limits of S200105ae and S200115j with KN models to place constraints on the possible EM counterpart to these NSBH mergers (Kasen et al., 2017; Metzger et al., 2011; Roberts et al., 2011; Rosswog, 2015). We use the Monte Carlo radiative transfer code POSSIS (Bulla, 2019) and create a grid of spectra from which  $g$ - and  $r$ -band light curves can be extracted and compared to observations. In particular, we explore a 2D-geometry and predict light curves for eleven different viewing angles, from pole (face-on,  $\cos \theta_{\text{obs}} = 1$ ) to equator (edge-on,  $\cos \theta_{\text{obs}} = 0$ ).

While KN models published using POSSIS have so far been focused on BNS mergers, here we present a new grid more tailored to NSBH mergers. We adopt a geometry similar to that in Figure 4 of Kawaguchi et al. (2020) with two distinct ejecta components: one representing the dynamical ejecta and one the post-merger ejecta. The dynamical ejecta are characterized by a mass  $M_{\text{ej,dyn}}$ , concentrated within an angle  $\pm\phi$  about the equatorial plane, with velocities from 0.1 to 0.3  $c$  and are lanthanide-rich in composition (see Bulla (2019) for more details on the adopted opacities). For simplicity, we assume a 2D geometry, where the dynamical ejecta cover an angle  $2\pi$  in the azimuthal direction; we note that this is just an approximation and numerical simulations (Foucart et al., 2017; Kyutoku et al., 2015) suggest that this component might cover only  $\sim$  half of the plane (i.e. a crescent rather than a torus). The post-merger ejecta are modelled as a spherical component with mass

$M_{\text{ej,pm}}$ , extending from 0.025 to 0.1  $c$  and with a composition intermediate between lanthanide-poor and lanthanide-rich material (Dietrich et al., 2020a). Below we discuss the effect of the wind composition on the derived constraints. A density profile scaling as  $\rho \propto r^{-3}$  is assumed for both components. Spectra for this new grid are made available at [https://github.com/mbulla/kilonova\\_models](https://github.com/mbulla/kilonova_models).

To place constraints on the ejected material, we fix  $\phi = 30^\circ$  and run a grid of 81 models with varying ejecta masses for the two components:  $M_{\text{ej,dyn}}, M_{\text{ej,pm}} \in [0.01, 0.09] M_\odot$  (step size  $0.01 M_\odot$ ). The simulated light curves show a strong dependence on the viewing angle, with increasingly fainter KNe when moving the observer from the pole ( $\cos \theta_{\text{obs}} = 1$ ) to the equator ( $\cos \theta_{\text{obs}} = 0$ ). In particular, orientations in the equatorial plane are on average 2–3 mag fainter in  $g$ -band than those along the polar direction due to the blocking effect of the dynamical ejecta (Bulla, 2019; Kawaguchi et al., 2020). This blocking effect may be in part a consequence of the choice of an axisymmetric outflow geometry. For a more realistic geometry of the dynamical ejecta, the post-merger ejecta would remain unobscured for some equatorial observers. 3D radiation transfer simulations with a non-axisymmetric dynamical ejecta may thus provide stronger constraints on the ejected mass for at least some equatorial observers than the 2D simulations performed here. We note that the discrepancy mentioned in Kawaguchi et al. (2020) between their light curves and those in Bulla (2019) is now negligible following an update of POSSIS where the temperature is no longer parameterized and uniform but rather calculated at each time and in each zone from the mean intensity of the radiation field. In addition, here we adopt thermalization efficiencies  $\epsilon_{\text{th}}$  from Barnes et al. (2016) rather than assuming  $\epsilon_{\text{th}} = 0.5$  as in Bulla (2019). For instance, we obtain a  $g$ -band absolute magnitude of  $-15.3$  mag at 1 day for the model with  $M_{\text{ej,dyn}} = M_{\text{ej,pm}} = 0.02 M_\odot$  viewed face-on (cf. with Figure 16 of Kawaguchi et al. 2020). 4.9 provides an example set of light curves in the passbands utilized in observations in this paper. The significantly brighter emission in  $i$ - and  $z$ -band compared to  $g$ - and  $r$ -band implies that better overall constraints on the kilonova emission are expected. To perform this check systematically, we present 4.10, which demonstrates the difference in peak magnitudes between  $g$ - and  $r$ -bands and  $i$ - and  $z$ -bands for the models in the NSBH grid used here. The result of brighter emission in  $i$ - and  $z$ -band compared to  $g$ - and  $r$ -band holds true across the parameter space, with peak  $z$ -band observations generally exceeding  $g$ -band by 1 mag or more.

To demonstrate possible constraints from deeper observations, which would have

been achievable under better weather conditions, we also examine constraints given by the most limiting individual pointings in each set of observations. The aim of this analysis is to guide future follow-up comparisons, showing what constraints could have been achieved should all the observations have been taken with the same depth as in the deepest field. Compared to the median values used above, individual observations reach deeper magnitudes (see open triangles in the left and middle panels of Figure 4.4). Results of this analysis are shown in 4.8, where we highlight the deepest limits for each set of observations.

The left column in 4.8 summarizes results for S200105ae. The top panels show  $g$ - and  $r$ -band light curves that would be ruled out if our median limits had reached the depth of our deepest observations on each night, for different distance assumptions (209, 283 and 357 Mpc from light to dark blue). We could rule out more models at closer compared to farther distances. In particular, all the models can be ruled out by the  $r$ -band upper limit at  $\sim 3$  days,  $m_r > 22.35$  mag, with no improvement found when adding the other observations. The bottom panels show what regions of the  $M_{\text{ej,dyn}} - M_{\text{ej,pm}}$  parameter space are ruled out by observations for three different viewing angle ranges:  $0.9 < \cos \theta_{\text{obs}} < 1$  ( $0 < \theta_{\text{obs}} < 26^\circ$ ),  $0.6 < \cos \theta_{\text{obs}} < 0.7$  ( $46^\circ < \theta_{\text{obs}} < 53^\circ$ ) and  $0 < \cos \theta_{\text{obs}} < 0.1$  ( $84^\circ < \theta_{\text{obs}} < 90^\circ$ ). As expected, polar orientations are more constraining than the other ranges. In particular, our deepest observations could constrain the ejecta masses to  $M_{\text{ej,dyn}} \leq 0.02 M_\odot$  and  $M_{\text{ej,pm}} \leq 0.04 M_\odot$  for polar directions at 283 Mpc. Weaker constraints are found for orientations away from the pole, with all KNe being sufficiently faint and thus not ruled out by upper limits for an equatorial observer (bottom-left panel).

The middle column in 4.8 shows the same analysis for S200115j. For S200115j, the larger distance and shallower limits lead to fewer models ruled out and thus poorer constraints in the  $M_{\text{ej,dyn}} - M_{\text{ej,pm}}$  parameter space. Specifically, models are ruled out only in the optimistic case of 261 Mpc and viewing angle close to the pole. For S200115j, the most (and only) constraining observations are the limits at  $\sim 1$  day.

We also provide updated results for S190814bv using our NSBH-specific KN model. For S190814bv, stronger constraints can be derived even for median observing depths. These constraints are also more reliable, as observations (Andreoni et al., 2020) covered 98% of the LVC skymap. On the other hand, constraints on the parameter space of the binary are unlikely to provide information distinct from that extracted from GW observations, as the LVC already indicates that this event has 0% probability of being EM-bright. We find that all of our KN models are ruled out

for polar orientations at  $\leq 267 \text{ Mpc}$ , effectively limiting the dynamical and post-merger ejecta masses to  $\leq 0.01 M_{\odot}$ . This would lead to constraints on the binary parameters shown on 4.12. For higher inclinations ( $46^{\circ} \leq \theta \leq 53^{\circ}$ ), the constraints are similar to what we just obtained for deep observations of S200105ae, with limits on the binary parameters accordingly close to those displayed on 4.11.

### **Data Availability**

The data that support the plots within this paper and other findings of this study are available from the corresponding author upon reasonable request.

### **Code Availability**

Upon request, the corresponding author will provide code (primarily in python) used to produce the figures.

## **4.2 Extended Data**

Filtering criteria	# of Alerts on Jan-05	# of Alerts on Jan-06	# of Alerts on Jan-15
Alerts	313,550	205,700	48,086
Positive subtraction	246,083	139,153	36,013
Real	223,334	113,402	34,677
Not stellar	198,229	56,999	20,529
Far from a bright source	191,747	32,339	19,802
Not moving	3,439	1,916	389
No previous history	<b>261</b>	<b>170</b>	<b>57</b>

Figure 4.5: **Automatic preliminary filtering criteria for transient detection.** Here we show results for each step of the ZTF filtering scheme for three representative nights covering the events discussed in this paper. Each cell shows the number of candidates that successfully pass a particular filter. The number shown is the result of running a filtering step on the alerts that met previous requirements. We define as “Real” any alert with a real-bogus score greater than 0.25 and “not moving” the candidates that have more than two detections separated by at least 15 minutes. The highlighted numbers represent the amount of candidates that required further vetting, as described in Section 4.1.

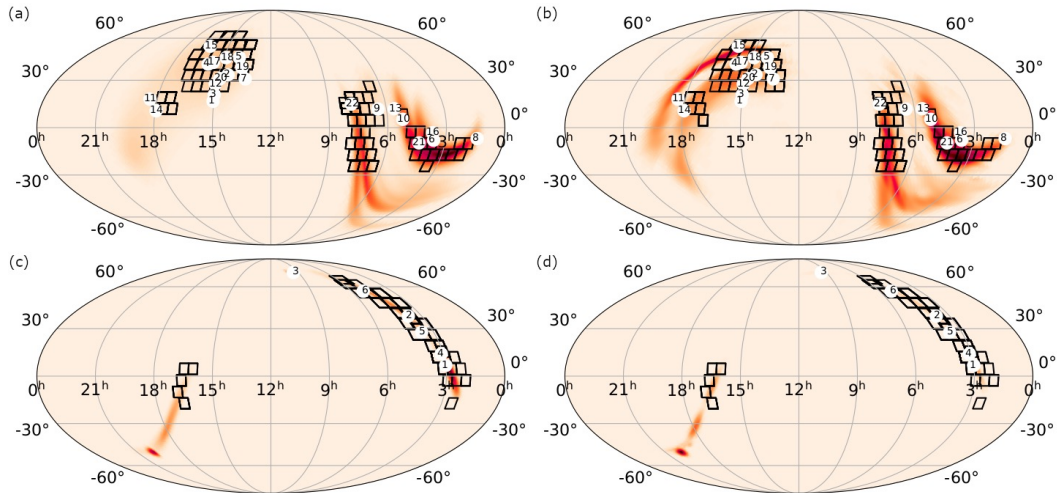


**Figure 4.6: ZTF coverage and candidates discovered within skymap.** Top row: Coverage of S200105ae, showing the tiles on the 90% probability region of the initial BAYESTAR (a) and final LALInference (b) skymaps. The color intensity is proportional to the 2-D probability. The mapping of candidates to numbers is 1: ZTF20aaervoa, 2: ZTF20aaertpj, 3: ZTF20aaervyn, 4: ZTF20aaerqbx, 5: ZTF20aaerxsd, 6: ZTF20aafduvt, 7: ZTF20aaevbzl, 8: ZTF20aafndh, 9: ZTF20aaexpwt, 10: ZTF20aafaoki, 11: ZTF20aafukgx, 12: ZTF20aagijez, 13: ZTF20aafanxk, 14: ZTF20aafujqk, 15: ZTF20aagiiiik, 16: ZTF20aafdxxkf, 17: ZTF20aagiipi, 18: ZTF20aagjemb, 19: ZTF20aafksha, 20: ZTF20aaertil, 21: ZTF20aafexle and 22: ZTF20aafefxe. Bottom row: Same for S200115j, with the BAYESTAR coverage shown in (c) and LALInference coverage shown in (d). The mapping of candidates to numbers is 1: ZTF20aagiqxg, 2: ZTF20aafqvyyc, 3: ZTF20aahenrt, 4: ZTF20aafqpum, 5: ZTF20aafqulk, and 6: ZTF20aahakkp. We note that we include candidates up to and including within the 95% probability region, and therefore some are outside of the fields we plot here.

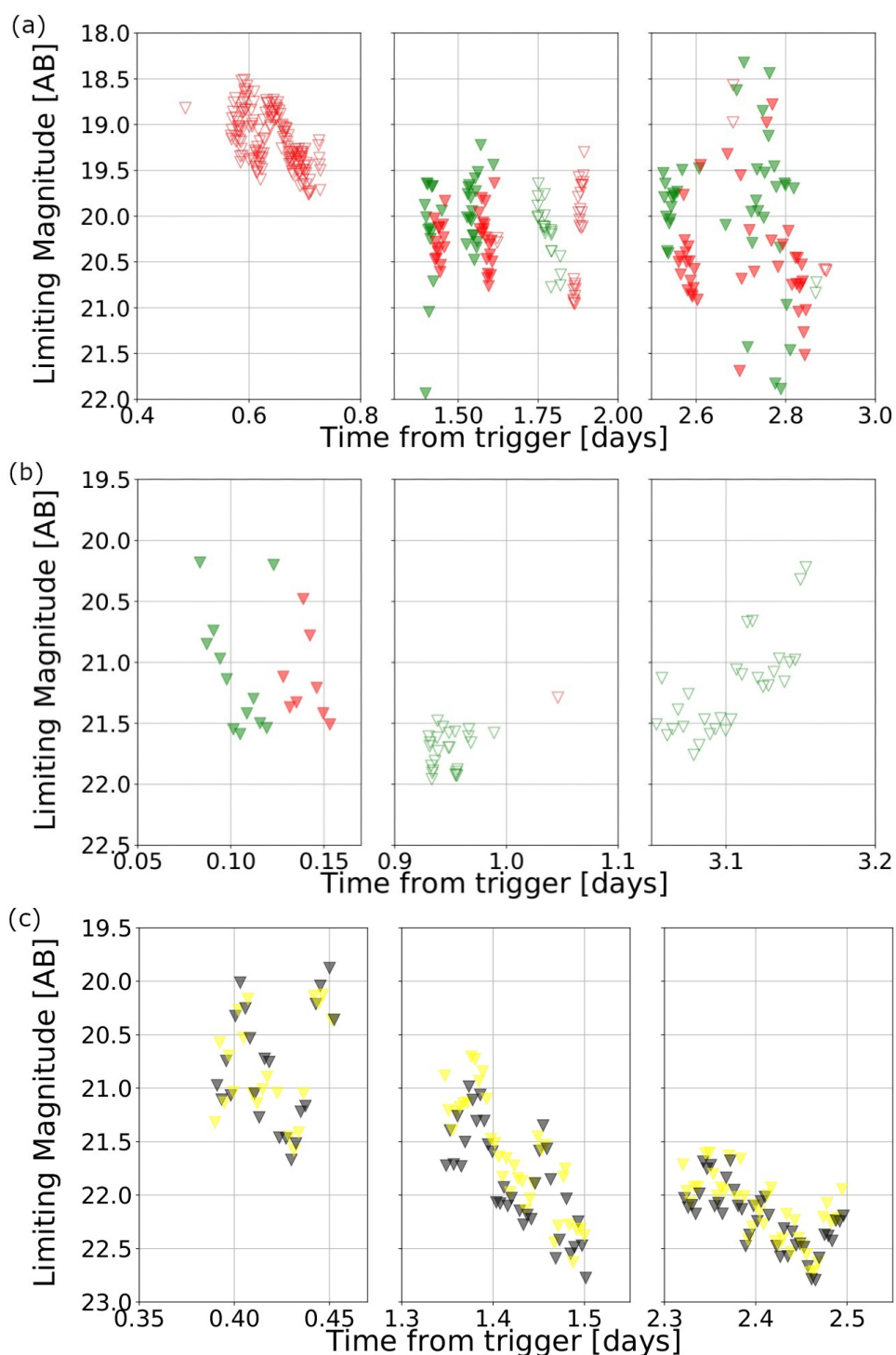


Figure 4.7: **Limiting magnitudes at each epoch of observations.**  $5\text{-}\sigma$  limiting magnitudes as a function of time for (a) S200105ae (ZTF), (b) S200115j (ZTF), and (c) S190814bv (DECAM) with the left, middle, and right panels corresponding to observations on the first, second, and third nights for S200105ae and S190814bv and first, second, and fourth nights for S200115j. The red and green triangles correspond to the  $r$ - and  $g$ -band limits for ZTF, while the yellow and black triangles correspond to the  $i$ - and  $z$ -band limits for DECAM; the open triangles correspond to serendipitous observations and closed ToO observations. The large differences in limiting magnitude from observation to observation are due to poor weather.

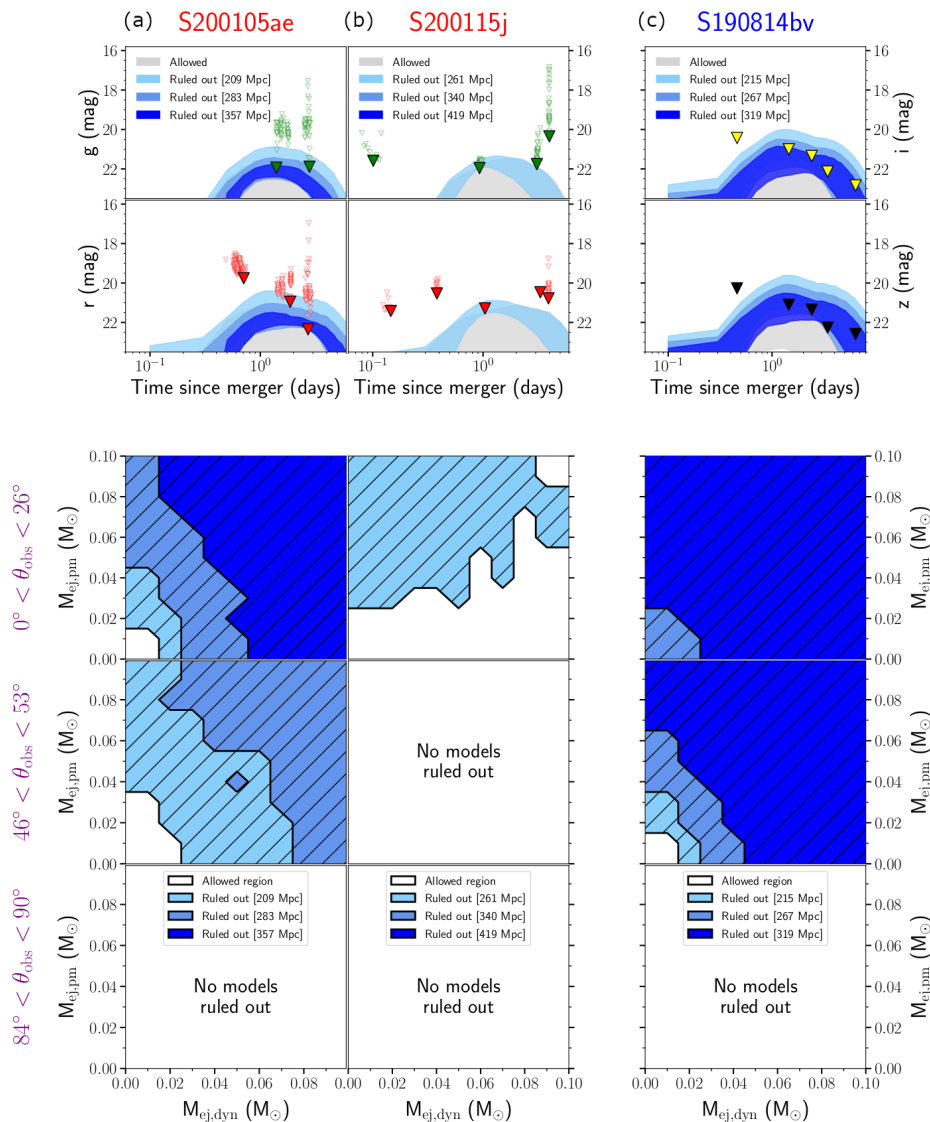


Figure 4.8: **Potential constraints on kilonova model parameters based on the deepest limiting magnitudes.** We display constraints on (a) S200105ae (ZTF), (b) S200115j (ZTF) and (c) S190814bv (DECam) for the models in the NSBH grid used here. *Top panels:* same as Figure 4.4 but using the deepest (filled triangles) rather than the median limits for each set of S200105ae and S200115j observations. The panel for S190814bv is the same as in Figure 4.4, with all limits corresponding to the median magnitudes. *Bottom panels:* regions of the  $M_{ej,dyn} - M_{ej,pm}$  parameter space that are ruled out at different distances and for different viewing angle ranges (moving from pole to equator from top to bottom panel).

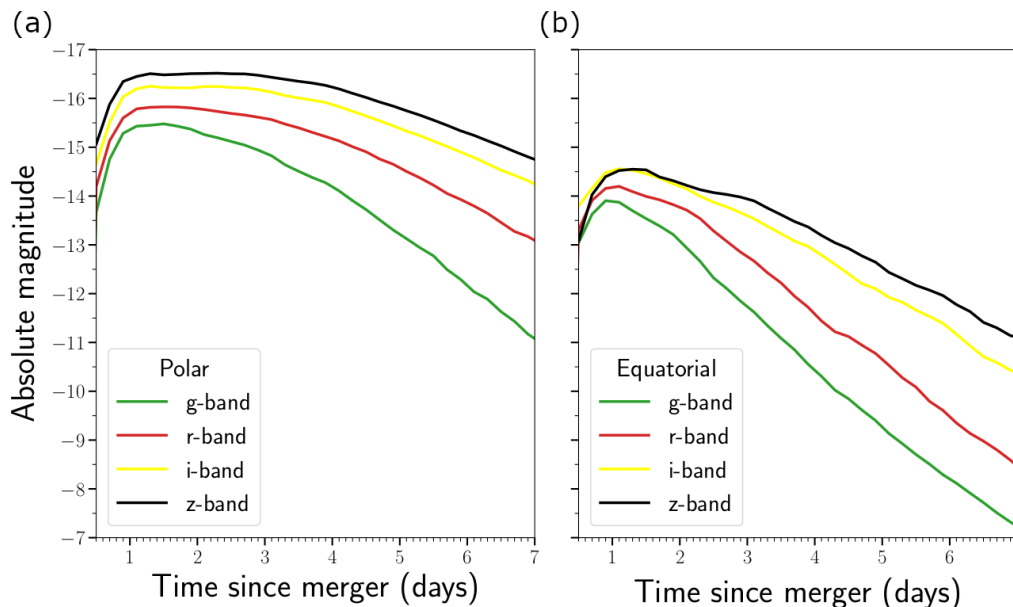


Figure 4.9: **Broadband NSBH light curve models from POSSIS.** Light curves predicted with POSSIS (Bulla, 2019) for a NSBH model with  $M_{\text{dyn}} = 0.05M_{\odot}$  and  $M_{\text{pm}} = 0.05M_{\odot}$  as seen from a polar (a) and equatorial (b) viewing angle.

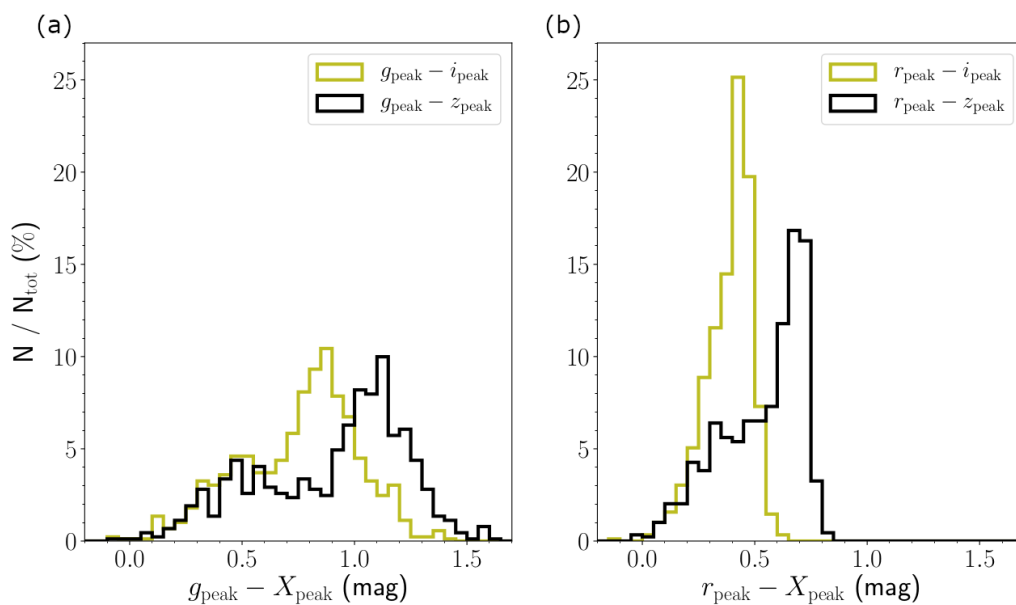


Figure 4.10: **Comparison of peak magnitudes between optical and near-IR bands for NSBH models.** We plot the difference in peak magnitudes between the (a)  $g$ -band and the near-IR  $i$ - and  $z$ -bands for the models in the NSBH grid used here. Similarly, in (b) we show the difference between  $r$ -band and the same near-IR bands.

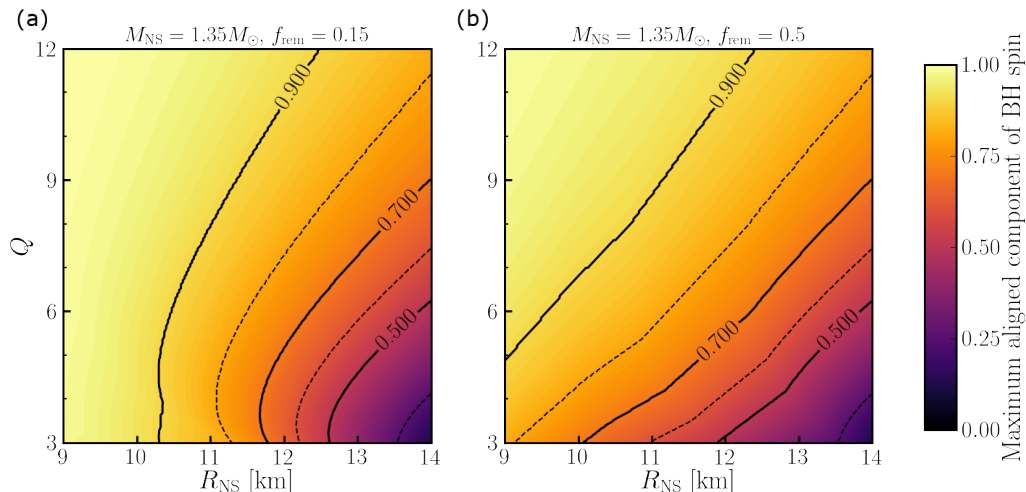


Figure 4.11: **Potential constraints on the parameters of a NSBH binary associated with S200105ae.** Here we assume that  $M_{e,j,dyn} \leq 0.02 M_{\odot}$  and  $M_{e,j,pm} \leq 0.04 M_{\odot}$ , appropriate for the deepest observations of S200105ae in a face-on orientation. We show the maximum value of the aligned component of the BH spin as a function of the neutron star radius  $R_{\text{NS}}$  and the binary mass ratio  $Q = M_{\text{BH}}/M_{\text{NS}}$ . The two panels show results assuming that low (a) and high (b) fractions of the post-merger accretion disk are ejected (see text). Both plots assume  $M_{\text{NS}} = 1.35$ . Results for different neutron star masses can be estimated from this plot simply by considering a binary with the same  $Q, \chi$  and compaction  $M_{\text{NS}}/R_{\text{NS}}$ .

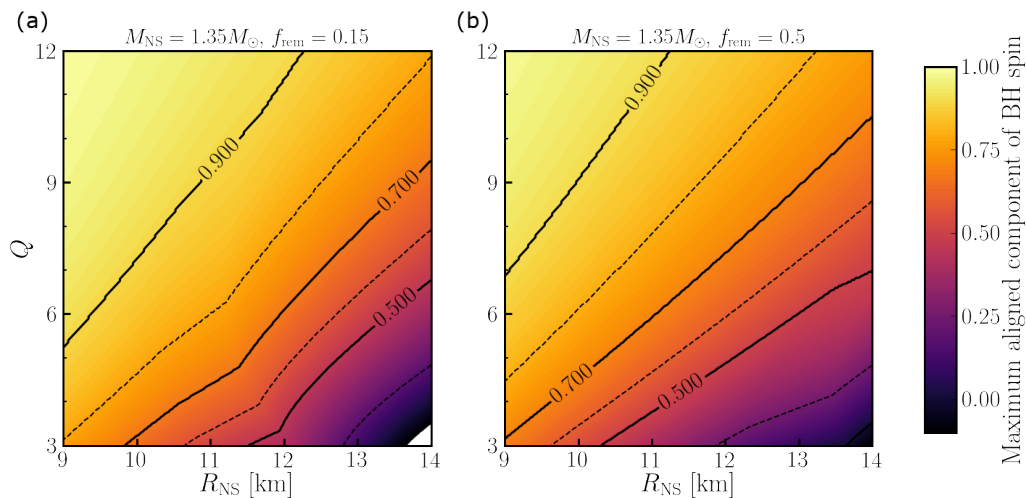


Figure 4.12: **Potential constraints on the parameters of a NSBH binary associated with S190814bv.** Here we assume that  $M_{e,j,dyn} \leq 0.01 M_{\odot}$  and  $M_{e,j,pm} \leq 0.01 M_{\odot}$ , as appropriate for S190814bv in a face-on orientation in a similar fashion to 4.11, with low (a) and high (b) fractions of disk ejecta.

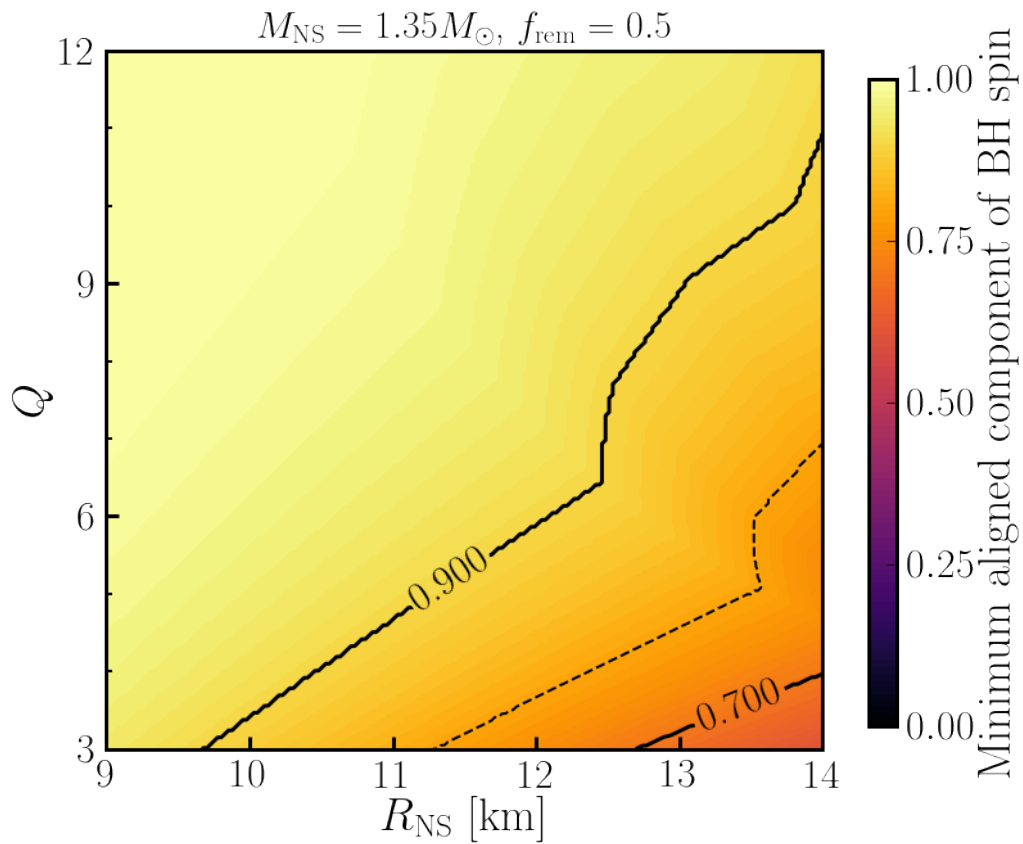


Figure 4.13: **Minimum aligned component of the BH spin above which we cannot rule out the presence of a kilonova.** We cannot exclude this region of parameter space because either the resulting kilonova evolves too slowly, or the ejected mass is outside of the grid of models used in this study. In this plot, we consider the worse-case scenario of  $f_{\text{rem}} = 0.5$ .

### 4.3 Supplementary Information

#### Observational details

##### Photometric Observations

The ZTF observations used to discover potential candidates were primarily obtained with ToO program time, however the public survey (Bellm et al., 2018) provided us with data as well. The nominal exposure time for the ZTF public survey is 30s while for the ToO program varies from 120-300 s depending on the available time and sky area requiring coverage. Our first source of photometry comes from the ZTF alert production pipeline (Masci et al., 2019), however for the purposes of this paper we have performed forced photometry using the package ForcePhot (Yao et al., 2019) on the candidates and reported these values.

For S200105ae, we split the schedule into two blocks of right ascension due to the significantly displaced lobes in the skymap (see 4.6), with observations lasting three hours per block. We additionally utilized the “filter balancing” feature (Almualla et al., 2020), which optimizes for the number of fields that have observations scheduled in all requested filters, and employed the greedy-slew algorithm (Rana et al., 2019) for conducting our search. The ability to split the skymap in right ascension and the use of filter balancing was novel for these observations, and served to help address the previous difficulty with multi-lobed skymaps to make it possible to observe all filters requested for the scheduled fields. Previously, maps of this type created conflicts between the rising/setting times of the lobes, as well as the separation in time between each of the epochs. This problem impacts the transient filtering process as well, for example, resulting in a number of transients failing to satisfy the criteria of 15 minutes between consecutive detections to reject asteroids. With the implementation of these features, both *g*- and *r*-band epochs were successfully scheduled for almost all fields.

For photometric follow-up we used the Gemini Multi-Object Spectrograph (GMOS-N) (Hook et al., 2004) on the Gemini-North 8-meter telescope on Mauna Kea, the Spectral Energy Distribution Machine (SEDM) on the Palomar 60-inch telescope (Blagorodnova et al., 2018b), the Wide-field Infrared Camera (WIRC) (Wilson et al., 2003) on the Palomar 200-inch telescope, as well as telescopes that are part of the Las Cumbres Observatory (LCO) network and the Kitt Peak EMCCD Demonstrator (KPED) (?).

The LCO observations were scheduled using the LCO Observation Portal (<https://lcoobs.org/>):

`//observe.lco.global/`), an online platform designed to coordinate observations. Our imaging plans changed case by case, however our standard requests involved 3 sets of 300s in  $g$ - and  $r$ - band with the 1-m telescopes. For fainter sources we requested 300s of  $g$ - and  $r$ - band with the 2-m telescopes. The reduced images available from the Observation Portal were later stacked and sources were extracted with the SourceExtractor package (Bertin & Arnouts, 1996). We calibrated magnitudes against Pan-STARRS1 (Chambers et al., 2016b) sources in the field. For transients separated  $< 8''$  from their hosts, we aligned a cutout of the transient with a Pan-STARRS1 template using SCAMP (Bertin, 2006b) and performed image subtraction with the High Order Transform of Psf AND Template Subtraction (HOTPANTS) code (Becker, 2015), an enhanced version of the method derived by Alard (2000). Photometry for these candidates comes from an analogous analysis on the residual images. Furthermore, images obtained with the Liverpool telescope (LT) (Steele et al., 2004) were reduced, calibrated and analysed in a similar fashion.

For KPED data, our standard procedure is to stack an hour of  $r$ -band data and reduce the stacked images following to standard bias and flat field calibrations. The photometry is obtained following the same methods as for the LCO data.

The photometric data obtained with GMOS-N was split in four 200 s  $g$ -band images later combined and reduced with DRAGONS (<https://dragons.readthedocs.io/en/stable/>), a Python-base data reduction platform provided by the Gemini Observatory. The data were later calibrated using the methods described for LCO.

Additionally, we scheduled photometric observations with the SEDM automatically through the GROWTH marshal. We acquired  $g$ -,  $r$ -, and  $i$ - band imaging with the Rainbow Camera on SEDM in 300s exposures. SEDM employs a python-based pipeline that performs standard photometric reduction techniques and uses an adaptation of FPipe (Fremling Automated Pipeline; described in detail in Fremling et al. (2016b)) for difference imaging. Data are automatically uploaded to the GROWTH marshal after having been reduced and calibrated.

The near-infrared data obtained with WIRC were reduced using a custom data reduction pipeline described in De et al. (2020c), and involved dark subtraction followed by flat-fielding using sky-flats. The images were then stacked using Swarp (Bertin et al., 2002) and photometric calibration was performed against the 2MASS point source catalog (Skrutskie et al., 2006). Reported magnitudes were derived by performing aperture photometry at the location of the transient using an aperture matched to the seeing at the time of observation, including an aperture correction

to infinite radius.

The photometry presented in the light-curves on this paper was corrected for galactic extinction using dust maps from Schlafly & Finkbeiner (2011).

### **Spectroscopic Observations**

For the candidate dataset described in Section 4.1, we obtained spectroscopic data using the Gran Telescopio Canarias (GTC) and Palomar observatory. We obtained optical spectra of one set of candidates with the 10.4-meter GTC telescope (equipped with OSIRIS). Observations made use of the R1000B and R500R grisms, using typically a slit of width  $1.2''$ . Data reduction was performed using standard routines from the Image Reduction and Analysis Facility (IRAF).

For the second set of candidates, we acquired most of our spectra with the Integral Field Unit (IFU) on SEDM, a robotic spectrograph on the Palomar 60-inch telescope (Blagorodnova et al., 2018b). We scheduled spectroscopic observations for our brighter ( $m_{AB} < 19$ ) and higher priority targets using a tool on the GROWTH Marshal that directly adds the target to the SEDM queue. For each science target, the SEDM robot obtains an acquisition image, solves the astrometry and then sets the target at the center of the integral field unit field of view. At the end of exposure, the automated pysedm pipeline is run (Rigault et al., 2019b). It first extracts the IFU spaxel tracers into a  $x, y, \lambda$  cube accounting for instrument flexures; the target spectrum is then extracted from the cube using a 3D PSF model which accounts for atmospheric differential refractions. The spectrum is finally flux calibrated using the most recent standard star observation of the night, with the telluric absorption lines scaled for the target's airmass. See Rigault et al. (2019b) for more details on the reduction pipeline. The final extracted spectra are then uploaded to the marshal; we use the SNID software (Blondin & Tonry, 2007b) to classify our transients.

Using the Double Spectrograph (DBSP) on the Palomar 200-inch telescope we obtained one transient and one host galaxy spectrum during our classical observing run on 2020-01-18 UT. For the setup configuration, we use  $1.0''$  and  $1.5''$  slitmasks, a D55 dichroic, a B grating of 600/4000 and R grating of 316/7500. Data were reduced using a custom PyRAF DBSP reduction pipeline (<https://github.com/ebellm/pyraf-dbsp>) (Bellm & Sesar, 2016b).

## Candidates

### S200105ae candidates

In this subsection, we provide brief descriptions of candidates identified within the skymap of S200105ae. Due to the poor seeing conditions and moon brightness, there were no candidates that passed all of the criteria after the second night of observations. After the third night of observations of S200105ae, we identified 5 candidates within the skymap (Stein et al., 2020), shown in Supplementary Information Table 4.1 and on 4.6. In addition, we later identified and reported other candidate counterparts (Ahumada et al., 2020b). A late-time query ( $> 1$  month after the mergers) yielded two further candidates of interest, ZTF20aafsnux and ZTF20aaegqfp, that were not already reported via Gamma-ray burst Coordinates Network (GCN).

All the transients are displayed in Supplementary Information Table 4.2; here we briefly describe each set, and show examples of light curves and cutouts for the most well-sampled, slowly photometrically evolving ones in 4.14. For the candidates with spectroscopic redshifts, we compute their distance assuming Planck15 cosmological parameters and use them to estimate the source absolute magnitudes, which we include in the candidate descriptions. When vetting, we prioritized candidates whose distance fell within the  $1\sigma$  LIGO distance uncertainty for each event; however we did not reject any candidates on the basis of redshift.

The redshifts presented in this section come either from the spectra of the transient,  $z(s)$ , or from the Photometric Redshifts for the Legacy Surveys (PRLS) catalog (Zhou et al. in prep.), which is based on Data Release 8 of DESI Legacy Imaging Surveys (Dey et al., 2019),  $z(p)$ .

**Spectroscopic Classification** For this set of spectra, we quote the photometric phase at which the spectrum was taken when the photometry is well-sampled. In all other cases, we derive the spectroscopic phase of the transient using SNID (Blondin & Tonry, 2007b) unless otherwise specified. Most of the spectroscopic classifications were determined using SNID.

*ZTF20aaertpj* - The first  $r$ - and  $g$ -band detections of this transient 3 days after the merger showed a red color  $g - r = 0.4$  mag; it rapidly brightened 1 mag to reach  $g = 18.9$  after 7 days. The Gran Telescopio Canarias (GTC) classified it as a Type Ib SN ( $z(s) = 0.026$ ) on January 10th (Castro-Tirado et al., 2020) a few days before

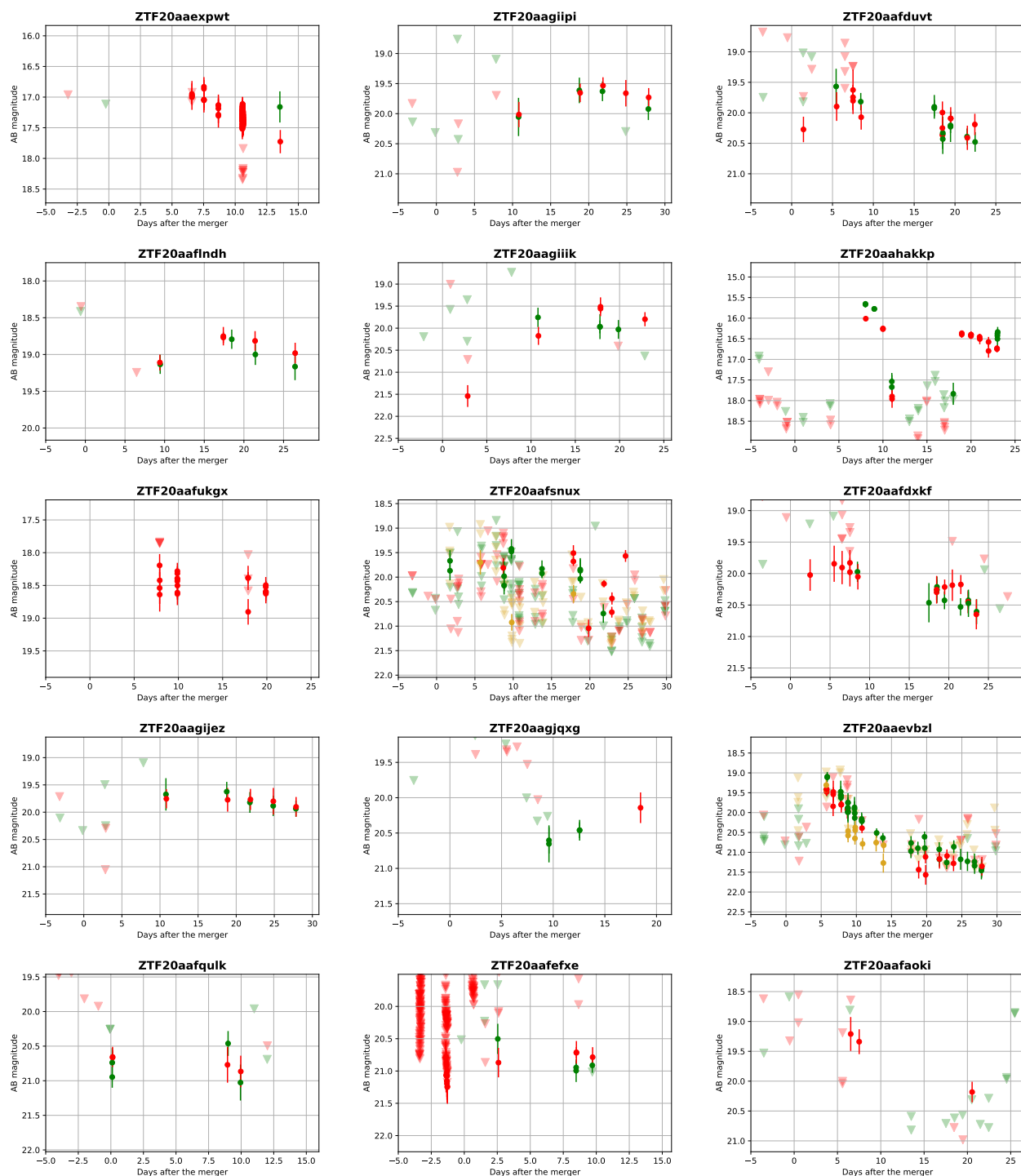


Figure 4.14: **light curves for all objects ruled out photometrically.** In each panel, filled circles represent ZTF forced photometry and the photometry from the ZTF alert production pipeline, with error bars corresponding to  $1\text{-}\sigma$  uncertainties. Filled triangles display  $5\text{-}\sigma$  upper limits for non-detections. The  $r$ -,  $g$ -, and  $i$ -band data is presented in red, green and yellow respectively.

the ZTF light curve reached maximum light, implying an absolute magnitude of  $-15.9$  mag. This supernova is closer than the  $-1\sigma$  LIGO distance.

*ZTF20aaervoa* - This object was found 3 days after the merger at 20.74 mag in  $g$  band with a red color ( $g - r = 0.66$  mag). This field was last observed 1.6 days before the merger. It showed a flat evolution over the first few days. Spectroscopic follow-up with GTC on January 10th classified it as a SN Type IIP ( $z(s) = 0.046$ ),  $\sim 3$  days after maximum (Valeev et al., 2020) using SNID templates. This implied an absolute magnitude of  $-16.4$  mag in  $r$  band. Its redshift is marginally consistent with the LIGO distance uncertainty, though it fell outside the 95% confidence level of the LALInference skymap.

*ZTF20aaervyn* - Its first detection was in the  $g$  band ( $g = 20.62$  mag), 3 days after the merger, which first showed a red color ( $g - r = 0.3$  mag). This field was last visited 3 hours before the LVC alert. It was classified by GTC on January 11th as a Type Ia SN, with  $z(s) = 0.1146$  (Valeev et al., 2020), much farther than  $+1\sigma$  LIGO distance. The spectroscopic phase corresponds to  $\gtrsim 1$  week before the light curve reached maximum light.

*ZTF20aaerxsd* - Similarly, this region was visited 3 hours before the LVC alert and this candidate was first detected 3 days after the merger at  $g = 20.27$  mag and showed a red color of  $g - r = 0.37$  mag. The next couple of detections showed a quickly evolving transient, brightening  $\sim 0.35$  mag/day. GTC spectroscopically classified it as a SN Type Ia ( $z(s) = 0.0533$ ) on January 10th (Valeev et al., 2020); concurrent photometry with ZTF indicates that the spectrum was taken  $> 12$  days before maximum.

*ZTF20aaerqbx* - This transient was first detected in  $g$ -band at  $g = 19.46$  mag 3 days after the merger. It faded 0.5 mag over the first 8 days and was classified by GTC on January 11th as a Type IIP SN ( $z(s) = 0.098$ ) at 5 days before maximum, using SNID (Castro-Tirado et al., 2020). Its redshift places it outside of the LIGO volume.

*ZTF20aafanxk* - This candidate was detected at  $r = 18.52$  mag, 6 days after the merger with galactic latitude  $< 15^\circ$  and offset by  $7''$  from a possible host (Ahumada et al., 2020b); it faded 0.3 mag in the  $r$ -band the first 10 days and a spectrum taken with the P60 SEDM spectrograph revealed its classification to be a SN Ia at  $z(s) = 0.103$ , too far to be consistent with the LIGO distance.

*ZTF20aafujqk* - Offset by  $2.26''$  from the center of a large spiral galaxy host (Ahumada et al., 2020b), *ZTF20aafujqk* was detected in  $r$ -band during serendipitous

observations 10 days after the merger, and later followed up with SEDM photometry in  $g$ - and  $i$ - bands, which showed a steadily declining light curve. SEDM spectroscopy showed that it was also a SN Ia at  $z(s) = 0.06$ , consistent with LIGO distance uncertainties.

*ZTF20aaevbzl* - This region was last observed 3 hours before the LVC alert. *ZTF20aaevbzl* was detected six days after the merger (Ahumada et al., 2020b), this candidate was selected for its atypical rapid decline in its light curve in  $r$ - and  $g$ -bands. This hostless transient faded 1.1 mag in 5 days in the  $g$ -band. We obtained a spectrum of *ZTF20aaevbzl* with P200+DBSP, whose  $H\alpha$  feature at  $z(s) = 0$  amidst a blue, mostly featureless spectrum indicates that it is a galactic cataclysmic variable (See Figure 4.2). Further follow-up with SEDM and LCO showed that the transient was consistently fading at 0.18 magnitudes per day in the  $g$ - band.

### **(Slow) Photometric Evolution**

As mentioned above, we deem candidates to be slowly evolving by checking whether their rise or decay rate is faster than our photometric cut of  $< |0.3|$  mag/day. We justify this cut based on 4.15, a histogram of the evolution rates of KNe from NSBH mergers, which shows that over a baseline of  $\gtrsim 1$  week, which is the case for our candidates, nearly all KN model light curves evolve faster than this cut in both  $g$ - and  $r$ -bands. The decline rate is determined using the photometric band with the longest available baseline. It is calculated by getting the ratio between the  $\Delta m$  and the length of that baseline ( $\Delta t$ ), from the candidate's peak to its last detection. This cut does exclude from our analysis a small part of the physically acceptable parameter space of NSBH binaries (see 4.13), though it significantly reduced the number of false-positive transients. It should thus be seen as a trade-off between parameter space coverage and the cost of EM follow-up that result in a small and known bias in our search.

*ZTF20aafduvt* - The field where this transient lies was observed 12 hours before the LVC alert, and it was detected six days after the merger in  $r$ - and  $g$ - bands (Ahumada et al., 2020b), offset from a possible host at  $z(p) = 0.21 \pm 0.02$  by 51kpc, this candidate faded 0.1 mag in the  $g$ -band during the first 9 days after the discovery. The photometric redshift places this transient at an absolute magnitude of  $M = -21$  mag.

*ZTF20aafndh* - With its last non-detection 12 hours before the GW alert, *ZTF20aafndh* was first detected 10 days after the merger. This source is located  $0.8''$  from the

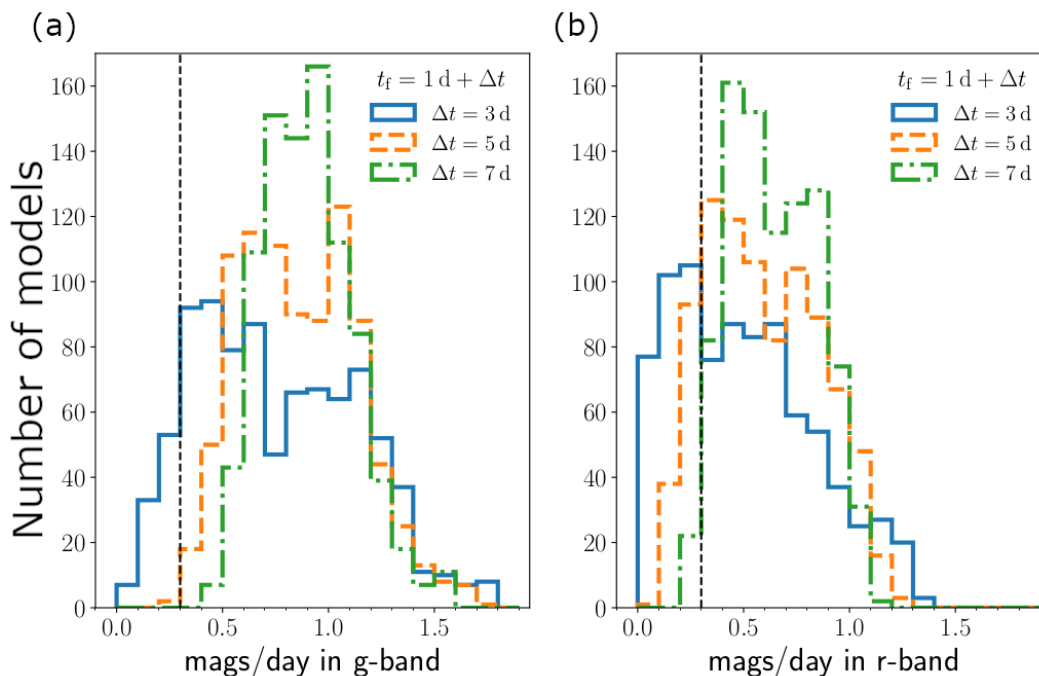


Figure 4.15: **Plot of the decay rate (mag/day) in  $g$ -band (a) and  $r$ -band (b) for all the ejecta masses and viewing angles of the modeled grid presented in Section 4.1.** Blue histograms are for time windows from 1 to 4 days after merger ( $\Delta t = 3$  days), orange from 1 to 6 days ( $\Delta t = 5$  days), green from 1 to 8 days ( $\Delta t = 7$  days). In general, 96 % of models show faster decay than 0.3 mags/day (dashed vertical line) in  $g$ -band, while 82 % of models show faster decay than 0.3 mags/day in  $r$ -band. The more slowly fading models are the higher mass ones. Particularly, our threshold was chosen based on the 7 days baseline, as all the candidates meet that requirement.

center of an apparently small galaxy (Ahumada et al., 2020b) and evolved photometrically to resemble a Type Ia SN light curve; it faded in the  $r$ -band by 0.17 mag in 17 days. Furthermore, the photo- $z$  of the host galaxy is  $z(p) = 0.091 \pm 0.023$  which puts the transient at an absolute magnitude of  $M = -19.06$  mag, consistent with a Type Ia SN.

*ZTF20aaexpwt* - This candidate was first detected one week post-merger, and was one of several hostless candidates identified in a low galactic latitude ( $b_{gal} < 15^\circ$ ) field (Ahumada et al., 2020b). The last non-detection was 5 hours before the LVC alert. Its evolution over the next seven days was 0.12 mag/day in the  $r$ -band, marked by a declining light curve.

*ZTF20aafukgx* - Offset from a potential bright host by  $3.85''$ , at low galactic latitude

(Ahumada et al., 2020b), this candidate was detected at  $r = 18.4$  ten days after the merger but remained flat within error-bars over the next ten days of observations.

*ZTF20aagijez* - First detected 11 days post-merger, this candidate, offset  $3.15''$  from the nucleus of a star-forming galaxy at  $z(s) = 0.061$  (Ahumada et al., 2020b), exhibited a flat light curve for more than 10 days and it was still detectable after 40 days; it photometrically resembles a SN light curve. The spectroscopic host redshift implies an absolute magnitude of  $M = -17.6$  mag. The last visit to the field where this transient lies was 3.6 hours before the GW alert.

*ZTF20aagiiik* - This field was last visited 2 days before the LVC alert. We identified *ZTF20aagiiik* as a candidate of interest due to its rapid rise in  $r$ -band after being detected 11 days after the merger; it is offset by  $5.79''$  from a potential spiral galaxy host (Ahumada et al., 2020b). However, it only faded 0.4 mag in 12 days. Additionally, at the redshift of the potential host galaxy ( $z(s) = 0.13$ , separated by  $5.25''$ ) the absolute magnitude ( $M = -19.24$  mag) is consistent with a Type Ia SN.

*ZTF20aafdxkf* - Detected just three days after the merger, this hostless candidate exhibited a rise in  $r$ -band over the first three days (Ahumada et al., 2020b), but its declining  $g$ -band photometry showed it to be too slow to be a KN. It only faded 0.5 mag in the  $g$ -band during the first 14 days. The last non-detection was 12 hours before the LVC alert.

*ZTF20aagiipi* - Offset by 27 kpc from a potential faint host at  $z(p) = 0.388 \pm 0.016$ , this candidate seemed to be rising when it was detected in the first 11 days after merger. Supplemented with SEDM photometry, its light curve closely resembles that of a typical Type Ia supernova, which at the redshift of the host would peak at  $M = -21.6$  mag. This field was last observed 3.6 hrs before the LVC alert.

*ZTF20aafsnux* - A hostless candidate, *ZTF20aafsnux* appeared to be declining gradually based on its first two  $g$ -band detections two and nine days after the merger. Close monitoring revealed that the source was fluctuating between  $g \sim 19.0$ – $20.0$  mag over a period of 17 days. This region was last visited 3 hours before the GW alert.

*ZTF20aaertil* - This candidate was first detected three days after the merger; it was located  $0.2''$  from the nucleus of a faint galaxy host and appeared to be rising in  $g$ -band (Ahumada et al., 2020b). Our spectrum of the host galaxy with DBSP on Jan 18th demonstrated that the galaxy, at  $z(s) = 0.093$ , was outside the one-sigma distance uncertainty for S200105ae; furthermore, in 40 days, it faded only 0.5 mag in the  $r$ -band. The absolute magnitude at this host redshift is  $M = -18.5$  mag. We

show the light curve and  $r$ -band cutouts for this transient in 4.17. The last non-detection in this field was 3 hours before the LVC alert.

*ZTF20aafksha* - This last non-detection for this transient was 1.2 days before the GW alert. We discovered this candidate nine days after the merger, offset by  $7.92''$  from a possible spiral galaxy host at  $z(s) = 0.167$  at  $g = 20.06$  mag (Ahumada et al., 2020b), corresponding to an absolute magnitude of about  $-19.6$  mag. The steadily declining light curve post-peak in both  $g$ -band and  $r$ -band,  $0.7$  mag in  $g$ -band during the first 19 days, and the bright absolute magnitude, suggests that the candidate is a SN Ia. We display this candidate in 4.17.

*ZTF20aagjemb* - First detected 3 days after merger, this nuclear candidate rose by one magnitude over the course of 5 days in  $g$ -band (Ahumada et al., 2020b). After tracking its evolution over 20 days time, the light curve seems to exhibit a SN-like rise and decline. It presents a slowly-evolving light curve, only fading  $0.1$  mag in the  $r$ -band during the twenty days. This candidate is also displayed in 4.17. The transient is located in a host with a  $z(p) = 0.21 \pm 0.06$ , separated by 6 kpc, implying an absolute magnitude  $M = -19.24$  mag. The last non-detection in this region was 3 hours before the LVC alert.

*ZTF20aafefxe* - This candidate's two detections in  $r$ -band suggest fading behaviour, but subsequently the source has not been detected by the nominal survey observations (Ahumada et al., 2020b). The last non-detection in this region was 5 hours before the LVC alert. The first detection was 9 days after the merger, and there may be a faint host separated by 41 kpc from the transient with  $z(p) = 0.09 \pm 0.05$ , indicating a luminosity of  $M = -17.2$  mag. Forced photometry revealed that it had only evolved  $0.16$  mags in 11 days in the  $g$ -band, placing it clearly into the category of slow evolvers.

*ZTF20aafaoki* - The last non-detection in this region was 12 hours before the LVC alert. This candidate had two  $r$ -band detections at  $19.2$  mag, but had faded below  $21.4$  mag just 5 days later (Ahumada et al., 2020b). Our images taken with KPED do not show any transient or background source up to  $g > 19.55$  mag 6 days after the discovery. Similarly, our LCO follow-up observations showed that 8 days after the discovery, the transient is not detected and there is no visible source at the corresponding coordinate up to  $g > 20.25$  mag and  $r > 21.6$  mag. Our last LCO observations, obtained 72 days after the discovery, show no transient up to  $g > 22.10$  mag. However, after running forced photometry at the transient position, we find a detection 14 days after the initial discovery at  $r = 21.2$  mag, implying

re-brightening of the transient after the non-detection upper limits, or very slow evolution.

**Stellar** *ZTF20aafexle* - This particular region was observed serendipitously 1 hour before the LVC alert. After its initial detection 8 days after the merger, it brightened by nearly one magnitude over four days but returned to its original brightness after 5 days (Ahumada et al., 2020b). We posit that it may be stellar due to the PS1 detections at the source position. Additionally, its evolution over the first 10 days after the discovery is only 0.3 mag in the *r*-band.

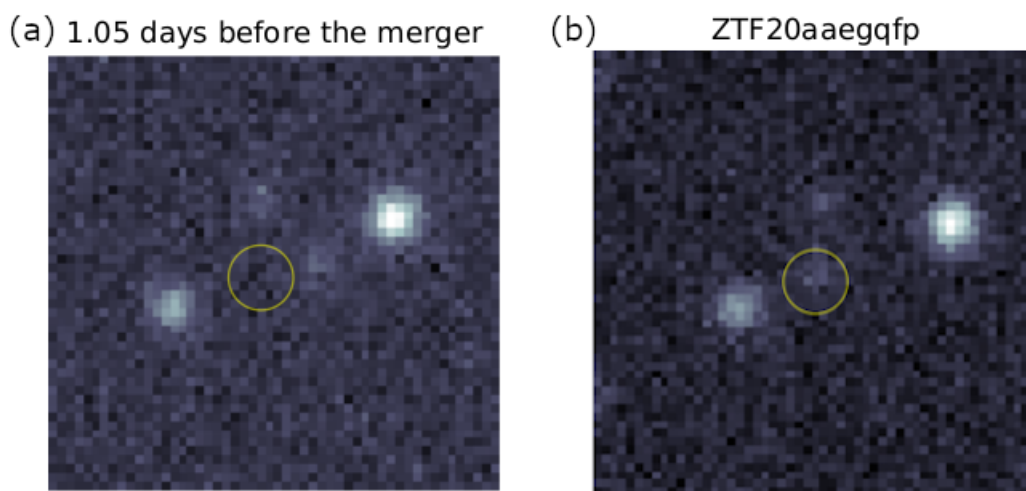


Figure 4.16: **ZTF *r*-band cutouts of the slow moving asteroid ZTF20aaegqfp.** The yellow circles show the position of the ZTF candidate in both cutouts. Panel (a) shows a cutout of the region one day before the trigger. There, it is possible to see a source to the right of ZTF20aaegqfp position, marked with a yellow circle. This source was located at  $7.3''$  from our candidate. Panel (b) shows the discovery image of our candidate ZTF20aaegqfp, which is located within the circle. The cutouts are 0.7 sq. arcmin and north and east are up and to the left respectively.

**Slow-moving asteroids** *ZTF20aaegqfp* - We detected this hostless candidate a day after the merger in *r* band. The last non-detection of this transient was 5 hours before the GW alert. Our pipelines identified it as a fast-evolving transient due to its rise by more than 0.5 mag over the course of the night; subsequently, it was not detected in any of our serendipitous observations. We find non-physical upper limits interspersed with detections, suggesting that the photometry for this transient may not be reliable. Using the Kowalski infrastructure, we queried for alerts in the vicinity of the transient (around  $25''$ ) and found 13 alerts, the oldest of which was

$\sim 4$  days before the trigger, which showed a moving object across the field alerts (see 4.16).

### **S200115j candidates**

In this subsection, we provide brief descriptions of candidates identified within the skymap of S200115j. Most of our candidates were identified during the serendipitous coverage of the map. Some of our transients were discovered within ZTF Uniform Depth Survey (ZUDS; Goldstein et al., in prep) a dedicated survey for catching high-redshift SNe by acquiring and stacking images to achieve greater depth compared to the nominal survey. Intrinsically faint transients ( $m_{AB} \sim -16$  mag) discovered in these fields are more likely to be at redshifts consistent with the distance of this event ( $340 \pm 79$  Mpc).

The relevant candidates circulated by the GROWTH collaboration (Anand et al., 2020b) were found on the first night of observations. Weather issues affected systematic follow-up in the following days; nevertheless, a later deeper search led to more candidates found to be temporally and spatially consistent, which we report here. Additionally, candidates from Evans et al. (2020) were cross-matched with the ZTF database in order to temporally constrain the transients. Only S200115j\_X136 (Evans et al., 2020) had an optical counterpart we could identify, ZTF20aafapey, with a flaring AGN (Andreoni et al., 2020).

Every candidate that was found in the region of interest is listed in Supplementary Information Table 4.3.

**Spectroscopic Classification** *ZTF20aafqpum* - This transient is located at the edge of a host galaxy at  $photz = 0.12 \pm 0.03$  (Anand et al., 2020b). The region was last observed 1 hour before the LVC trigger and the transient. Follow-up with the Liverpool telescope in *r*- and *i*-bands showed this candidate to be red, with  $g - r \sim 0.5$  mag. This transient was then spectroscopically classified by ePESSTO+ as a SN Ia 91-bg, at  $z(s) = 0.09$  (Schulze et al., 2020), placing it at an absolute magnitude of  $M = -17.3$  mag.

### **(Slow) Photometric Evolution**

*ZTF20aahenrt* - This candidate, detected during our serendipitous search 3 days after the merger, is separated from a galaxy host by 8.8 kpc at  $z(p) = 0.16 \pm 0.04$ , giving it an absolute magnitude of  $M = -15.6$  mag. We monitored the transient

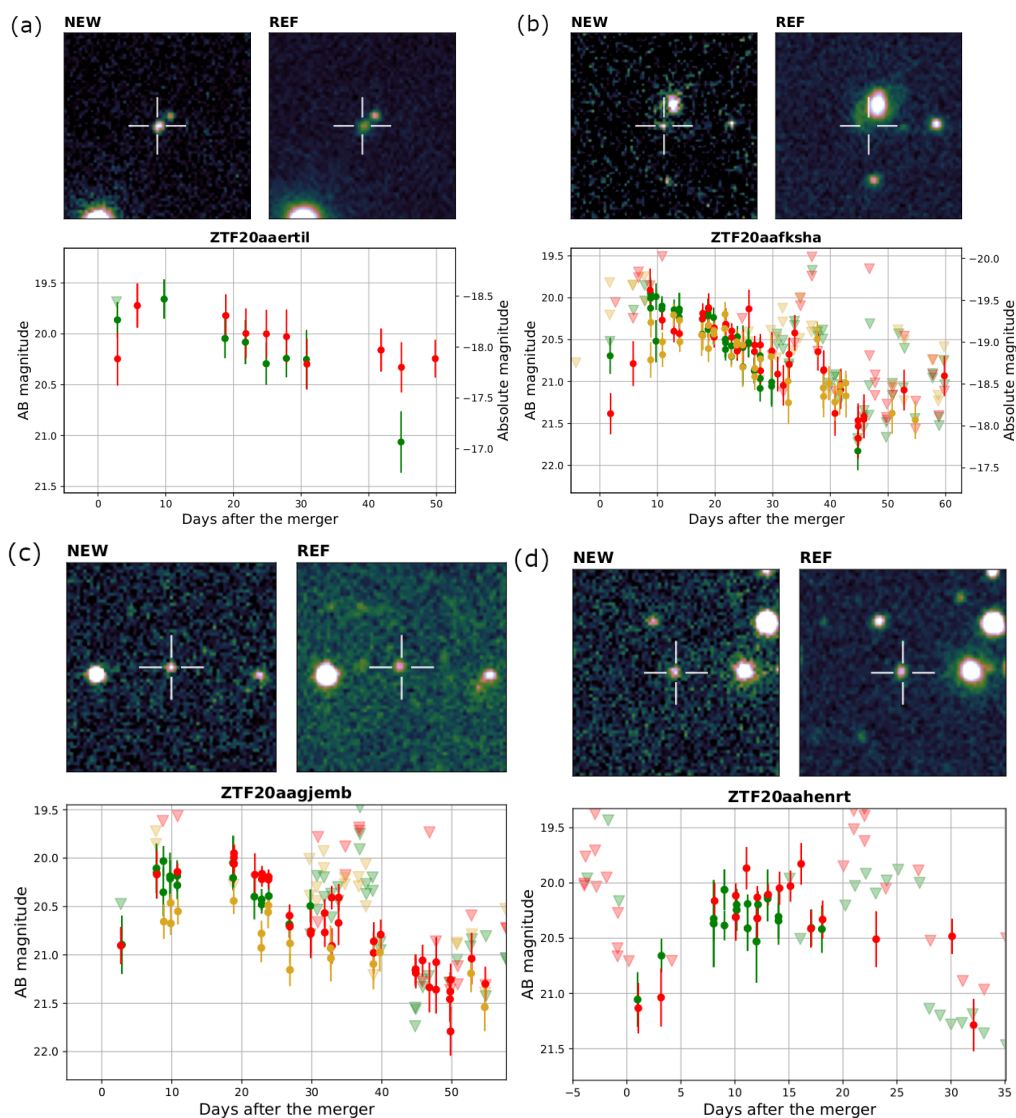


Figure 4.17: **light curves and  $r$ -band cutouts for a subset of the most well-sampled light curves for ZTF candidates that were ruled out photometrically.** Colors were used to represent the different bands: green, red and yellow for  $g$ -,  $r$ - and  $i$ - bands. The triangles in the light curve represent upper limits and filled circles are the detected magnitudes of the object. On each panel, the left cutout is the ZTF discovery image and the right one is the corresponding ZTF reference image. The transient is marked with a cross and the size of the cutouts is 0.7 sq. arcmin with north being up and east to the left. The candidates highlighted here are as follows: (a) ZTF20aaertil, (b) ZTF20aafksha, (c) ZTF20aagjemb, and (d) ZTF20aahernt.

after its initial rise in  $g$ -band, but over 12 days the candidate light curve exhibits very flat evolution, rising by 0.14 mag in 7 days. We highlight it in 4.17 as an example of a very slowly evolving transient identified in our searches. This field

was serendipitously observed 30 min before the LVC alert.

*ZTF20aagjqxg* - We selected this hostless candidate during our scanning due to its faint  $g$ -band detection at  $g = 20.65$  mag and subsequent rise three days after the initial detection two hours after the merger; its detection 11 days later in the  $r$ -band suggests that it was rising or reddening at a rate of  $< 0.1$  mag/day. This field was last observed 3.5 days before the LVC alert.

*ZTF20aahakkp* - This hostless transient was first detected eight days after the merger in  $g = 15.67$  mag and  $r = 16.01$  mag. The last non-detection of this transient was 20 hours before the issue of the LVC alert. While the transient seems to be rapidly fading over the course of a day from  $r = 16.26$  mag to  $r = 17.9$  mag, this detection is likely affected by poor weather and bad seeing on that day (seeing 4"). 20 days later, the light curve is near the original detection magnitude, and exhibits a slow fade since then.

*ZTF20aafqulk* - This region was last observed 1 hour before the issue of the GW alert. This source was detected 2.5 hours after the merger in  $g$ -band and 43 minutes later in  $r$ -band, with a blue color ( $g-r = 0.2$  mag). The candidate is offset by 0.3" from a potential host galaxy at a photometric redshift of  $z(p) = 0.27 \pm 0.04$  (Anand et al., 2020b). Our P60+SEDM spectrum does not offer a clear classification, but we detect a source in our LCO images 5 days after its discovery with  $r = 20.16 \pm 0.1$  mag. When running forced photometry, we find a detection in the  $r$ -band 89 days before the trigger, definitively ruling out its association with the GW event. Furthermore, the light curve appears nearly flat in the  $r$ -band over the course of 10 days.

**Slow-moving asteroids** Solar System asteroids located in the proximity of the stationary points located at  $\sim 60^\circ$  from opposition and low ecliptic latitude (Green, 1985) have slow,  $\lesssim 1''/h$  sky motions (Jedicke et al., 2016).

*ZTF20aafqvyc* - This was first detected as a hostless candidate 2.5 hours after the merger in  $g$ -band, followed by a detection in  $r$ -band just 49 minutes later (Anand et al., 2020b). Due to the transient being faint at  $g = 20.39$  mag, with a  $g-r$  color of 0.34 mag, we pursued follow-up with P200+WIRC on 2020-01-18 with NIR non-detections down to  $J > 21.5$  mag and  $K_s > 20.9$  mag (De et al., 2020a) and LCO on 2020-01-19 with optical non-detections down to  $g > 22.6$  mag,  $r > 21.8$  mag and  $i > 20.9$  mag (Ahumada et al., 2020a). Follow-up reported with AZT-33IK telescope of Sayan observatory (Mondy) revealed non-detections just 13 hours and

one day after the merger, down to upper limits of 21.6 mag and 22.1 mag in the  $r$ -band, suggesting that the source could be fast-fading, if astrophysical (Mazaeva et al., 2020). Finally, we conducted follow-up with Gemini GMOS-N, detecting no source down to an upper limit of  $g > 24.5$  mag (Ahumada & Singer, 2020). Based on the puzzling non-detections, we investigated the possibilities that it could be an artifact or that it was a moving object. Close inspection of the images taken with the Liverpool Telescope, 12.9 hours after the merger in  $g$ - and  $r$ -bands clearly demonstrated that the object had shifted position in the image with a slow angular rate of motion consistent with being an asteroid with an opposition-centric location of  $\pm 60^\circ$  near the evening sky stationary point.

### **Ejecta mass and binary parameter constraints – Implications and caveats**

To further illustrate what we could learn from sufficiently deep observations, we consider potential constraints on the parameters of the NSBH binary powering S200105ae. We assume that the source was located at 283  $Mpc$ , and seen face-on. For the deepest fields reported here, we have seen that this implies  $M_{e,j,dyn} \lesssim 0.02 M_\odot$  and  $M_{e,j,pm} \lesssim 0.04 M_\odot$ . Using semi-analytical formulae calibrated to the results of numerical simulations, we can estimate  $M_{e,j,dyn}$  and  $M_{e,j,pm}$  as functions of the mass ratio of the binary ( $Q = M_{BH}/M_{NS}$ ), the component of the dimensionless black hole spin aligned with the orbital angular momentum ( $\chi$ ), and the neutron star compactness ( $C_{NS} = \frac{GM_{NS}}{R_{NS}c^2}$ ) (see also Refs. (Andreoni et al., 2020; Coughlin et al., 2019; Coughlin et al., 2018a, 2019d; Coughlin et al., 2020b; Dietrich et al., 2020a)). We compute  $M_{e,j,pm}$  using Foucart et al. (2018b), and  $M_{rem}$  using Krüger & Foucart (2020), which are based on, respectively, the work of Foucart (2012) and Kawaguchi et al. (2016). As Foucart et al. (2018b) only predicts the total mass remaining outside of the BH after merger,  $M_{rem}$ , we estimate  $M_{e,j,pm} = f_{rem}(M_{rem} - M_{e,j,dyn})$ , with  $f_{rem} \sim 0.15 - 0.5$  the fraction of the remnant accretion disk that is ejected in the form of disk winds (Christie et al., 2019). The results are shown in 4.11, expressed as the maximum BH spin compatible with the assumed mass constraints. We show results for  $f_{rem} = 0.15$  and  $f_{rem} = 0.5$ , to illustrate the dependence on the (poorly constrained) parameters. While our plots show results at a fixed  $M_{NS} = 1.35 M_\odot$ , they can easily be rescaled to any other choice for the neutron star mass, as the mass predictions only depend on the ratio  $M_{NS}/R_{NS}$ . We note that at high mass ratios, the choice of  $f_{rem}$  has nearly no impact on the constraints. This occurs because the limit on  $M_{e,j,dyn}$  is more constraining than the limit on  $M_{e,j,pm}$ . At lower mass ratios, on the other hand,  $M_{e,j,dyn}$  rapidly decreases

(it asymptotes to the low values predicted for BNS systems in the near equal-mass regime). In that regime, 4.11 shows that the choice of  $f_{rem}$  clearly impacts the constraints that we can place on the binary parameters. Conservative upper limits on the BH spin are obtained by choosing  $f_{rem} \sim 0.15$ . Should more detailed study of post-merger remnants reveal that higher values of  $f_{rem}$  are more realistic, our constraints could become noticeably stronger.

We conclude by mentioning three caveats of this analysis. First, as noted above, KN models adopted here assume axial symmetry and a distribution over a  $2\pi$  azimuthal angle for the dynamical ejecta. In reality, the dynamical ejecta are predicted to cover only  $\sim$  half of the plane and thus  $\sim$  half of the orientations in the equatorial plane are expected to be brighter than predicted here. Accounting for the predicted break of symmetry will therefore produce stronger constraints for equatorial viewing angles than those derived here. The second caveat follows from the fact that the composition of the post-merger ejecta in NSBH mergers is uncertain. This is due in large part to the very approximate treatment of neutrinos used in many simulations (Foucart et al., 2018a; Wanajo et al., 2014), but also to the fact that the post-merger ejecta may contain a number of independent components with different geometry, composition, and temperature (Fernández et al., 2019; Kiuchi et al., 2015; Siegel & Metzger, 2017), and the relative contribution of these various components is strongly affected by the unknown strength and large scale structure of the post-merger magnetic field (Christie et al., 2019). Here we adopted a composition intermediate between lanthanide-poor and lanthanide-rich material but note that a different composition would lead to different constraints in the  $M_{ej,dyn} - M_{ej,pm}$  parameter space. For instance, a lanthanide-poor composition for the post-merger ejecta is expected to lead to brighter KNe and thus to result in stronger constraints. Finally, a third caveat is that binaries leading to extremely massive ejecta are not rigorously excluded by our analysis. This is due to the fact that within the grid of models considered here, the more massive ejecta ( $M_{dyn} \gtrsim 0.07M_{\odot}$  and  $M_{pm} \gtrsim 0.07M_{\odot}$ ) lead to KN that evolve too slowly to pass the observational cuts that we impose on the time evolution of the magnitude of KN, and also because some extreme low-mass systems may have  $M_{pm} \geq 0.1M_{\odot}$ , a region not covered by our grid of simulations. The small regions of parameter space untested by this study is shown in 4.13. We note that on this figure, the excluded region at high NS radii is due to the observational cuts; requiring observations to be sensitive to that region of parameter space may lead to many more false positives. The smaller region at low NS radii and low mass ratio is due to our  $M_{pm} < 0.1M_{\odot}$  limit.

Table 4.1: Follow-up table for all spectroscopically classified transients. Our spectra were obtained with GTC (Castro-Tirado et al., 2020; Valeev et al., 2020), ePESSTO (Schulze et al., 2020), P60+SEDM, and P200+DBSP. The spectroscopic redshifts are listed as well. The objects with a star (\*) were first reported to TNS by ALerCE. Discovery magnitudes reported are extinction-corrected.

Name	RA	Dec	TNS	Discov. Mag.	Classification	Spec. facilities	Spec. Redshift
ZTF20aaertpj	14:27:52	33:34:10	AT2020pv*	$g = 19.88 \pm 0.16$	SN Ib	GTC	0.026
ZTF20aaervoa	15:02:38	16:28:22	AT2020pp*	$g = 20.63 \pm 0.30$	SN Iip	GTC	0.046
ZTF20aaervyn	15:01:27	20:37:24	AT2020pq*	$g = 20.62 \pm 0.26$	SN Ia	GTC	0.112
ZTF20aaerxsd	14:00:54	45:28:22	AT2020py	$g = 20.27 \pm 0.23$	SN Ia	GTC	0.055
ZTF20aaerqbx	15:49:26	40:49:55	AT2020ps*	$g = 19.46 \pm 0.15$	SN Iip	GTC	0.098
ZTF20aafanxk	05:35:36	11:46:15	AT2020adk	$r = 18.52 \pm 0.25$	SN Ia	P60+SEDM	0.133
ZTF20aafujqk	17:57:00	10:32:20	AT2020adg	$r = 18.17 \pm 0.10$	SN Ia	P60+SEDM	0.074
ZTF20aaevbzl	13:26:41	30:52:31	AT2020adf	$i = 19.31 \pm 0.24$	CV	P200+DBSP	0.0
ZTF20aafqpum	03:06:08	13:54:48	SN2020yo	$g = 19.76 \pm 0.20$	SN Ia 91-bg	ePESSTO	0.09

Table 4.2: Follow-up table of the candidates identified for S200105ae, reported in Ahumada et al. (2020b). The ZTF objects with a star (\*) in the TNS column were first reported to TNS by ALerCE. The spectroscopic (s) or photometric (p) redshifts of the respective host galaxies are listed as well. As a reference, the all-sky averaged distance to the source is  $283 \pm 74$  Mpc, corresponding to a redshift range  $z = 0.045\text{--}0.077$ . We use the same rejection criteria described in more detail in section 4.1 here, as follows: slow photometric evolution (slow), hostless, stellar, and slow moving asteroid (asteroid).

Name	RA	Dec	TNS	Discov. Mag.	Host/Redshift	rejection criteria
ZTF20aafduvt	03:36:29	-07:49:35	AT2020ado	$g = 19.57 \pm 0.29$	$0.25 \pm 0.02$ (p)	slow
ZTF20aafndh	01:22:38	-06:49:34	AT2020xzx	$g = 19.11 \pm 0.11$	$0.091 \pm 0.023$ (p)	slow
ZTF20aaexpwt	06:26:01	11:33:39	AT2020adi	$r = 16.95 \pm 0.17$	-	slow
ZTF20aafukgx	18:23:21	17:49:32	AT2020adj	$r = 18.40 \pm 0.15$	-	slow
ZTF20aagijez	15:04:13	27:29:04	AT2020adm	$r = 19.67 \pm 0.3$	0.061 (s)	slow
ZTF20aagiiik	16:19:10	53:45:38	AT2020abl*	$g = 19.76 \pm 0.22$	0.13 (s)	slow
ZTF20aafdxxk	03:42:07	-03:11:39	AT2020ads	$r = 20.02 \pm 0.25$	-	slow
ZTF20aagiipi	15:33:25	42:02:37	AT2020adl	$g = 20.10 \pm 0.32$	$0.39 \pm 0.02$ (p)	slow
ZTF20aafsnux	14:36:01	55:11:49	AT2020dzu	$g = 19.67 \pm 0.22$	-	slow
ZTF20aaertil	14:52:26	31:01:19	AT2020pu*	$g = 19.86 \pm 0.18$	0.093 (s)	slow
ZTF20aafksha	13:43:54	38:25:14	AT2020adr	$g = 20.06 \pm 0.26$	0.167 (s)	slow
ZTF20aagjemb	14:51:26	45:20:41	AT2020adh	$r = 20.90 \pm 0.02$	$0.21 \pm 0.06$ (p)	slow
ZTF20aafefxe	07:47:24	14:42:24	AT2020adt	$g = 21.0 \pm 0.18$	$0.09 \pm 0.05$ (p)	slow
ZTF20aafaoki	05:13:14	05:09:56	AT2020adq	$r = 19.21 \pm 0.28$	-	slow
ZTF20aafexle	04:20:31	-09:30:28	AT2020adn	$r = 19.67 \pm 0.30$	$0.18 \pm 0.02$ (p)	stellar
ZTF20aaegqfp	07:49:02	12:29:26	AT2020dzt	$r = 19.37 \pm 0.27$	-	asteroid

Table 4.3: Follow-up table of the candidates identified for S200115j, reported in Anand et al. (2020b). As a reference, the all-sky averaged distance to the source is  $340 \pm 79$  Mpc, corresponding to a redshift range  $z = 0.056\text{--}0.089$ .

Name	RA	Dec	TNS	Discov. Mag.	Host/Redshift	rejection criteria
ZTF20aaehenrt	09:32:53	72:23:06	AT2020axb	$g = 20.55 \pm 0.29$	$0.16 \pm 0.04$ (p)	slow
ZTF20aagjqxg	02:59:39	06:41:11	AT2020aao	$g = 20.65 \pm 0.26$	-	slow
ZTF20aahakkp	05:07:55	56:27:50	AT2020bbk	$g = 15.67 \pm 0.08$	-	slow
ZTF20aafqulk	03:39:45	27:44:05	AT2020yp	$g = 20.74 \pm 0.21$	-	stellar
ZTF20aafqvyc	03:47:58	38:26:32	AT2020yq	$r = 20.39 \pm 0.19$	-	asteroid

*Chapter 5****r*-PROCESS FROM IGWN-DETECTED NEUTRON STAR  
MERGERS****Searching for Gravitational Wave Optical Counterparts with the Zwicky Transient Facility: Summary of O4a**

Ahumada, T. & Anand, S., Coughlin, M. W., Gupta, V., et al. 2024, Searching for gravitational wave optical counterparts with the Zwicky Transient Facility: summary of O4a, arXiv e-prints, arXiv:2405.12403, . S. A. conducted observations with ZTF, performed candidate vetting and follow-up, simulated KNe with simsurvey and calculated luminosity function constraints, and wrote the manuscript along with T. Ahumada. Submitted to PASP. <https://arxiv.org/abs/2405.12403>

S. A. conducted observations with ZTF, performed candidate vetting and follow-up, simulated KNe with simsurvey and calculated luminosity function constraints, and wrote the manuscript along with T. Ahumada.

## ABSTRACT

During the first half of the fourth observing run (O4a) of the International Gravitational Wave Network (IGWN), the Zwicky Transient Facility (ZTF) conducted a systematic search for kilonova (KN) counterparts to binary neutron star (BNS) and neutron star–black hole (NSBH) merger candidates. Here, we present a comprehensive study of the five high-significance (False Alarm Rate less than 1 per year) BNS and NSBH candidates in O4a. Our follow-up campaigns relied on both target-of-opportunity observations (ToO) and re-weighting of the nominal survey schedule to maximize coverage. We describe the toolkit we have been developing, *Fritz* instance of *SkyPortal*, instrumental in coordinating and managing our GW searches for telescope scheduling, candidate vetting, assigning follow-up observations, and disseminating the results through a user-friendly interface. ZTF covered a total of 2841 deg<sup>2</sup> within the skymaps of the high-significance GW events, reaching a median depth of  $g \approx 20.2$  mag. We circulated 15 candidates, but found no viable KN counterpart to any of the GW events. Based on the ZTF non-detections of the high-significance events in O4a, we used a Bayesian approach, *nimbus*, to quantify the posterior probability of KN model parameters that are consistent with our non-detections. Our analysis favors KNe with initial absolute magnitude fainter than  $-16$  mag. The joint posterior probability of a GW170817-like KN associated with all our O4a follow-ups was 64%. Additionally, we use a survey simulation software, *simsurvey*, to determine that our combined filtered efficiency to detect a GW170817-like KN is 36%, when considering the 5 confirmed astrophysical events in O3 (1 BNS and 4 NSBH events), along with our O4a follow-ups. Following Kasliwal et al. (2020), we derived joint constraints on the underlying KN luminosity function based on our O3 and O4a follow-ups, determining that no more than 76% of KNe fading at 1 mag day<sup>-1</sup> can peak at a magnitude brighter than  $-17.5$  mag.

## 5.1 Introduction

The increased sensitivity of gravitational-wave detector networks have enabled unprecedented discoveries of compact binary mergers in the last decade. The International Gravitational Wave Network (IGWN) detected 102 binary black hole (BBH) mergers, 2 binary neutron star (BNS) mergers and 4 neutron star–black hole (NSBH) mergers between 2015 and 2020 during the first three observing runs (Abbott et al., 2023). The growing population of BBH mergers have challenged the existence of both the upper and lower black hole mass gaps (Abbott et al., 2020b; Abbott et al., 2020b), and have revealed a unique population of low-spin black holes (Tiwari et al., 2018). The second observing run of IGWN marked the discovery of GW170817, the very first GW signal from a binary neutron star merger system (Abbott et al., 2017a), with its short gamma-ray burst (GRB) counterpart (Abbott et al., 2017; Goldstein et al., 2017b), panchromatic afterglow (Balasubramanian et al., 2022; Haggard et al., 2017; Hallinan et al., 2017; Makhathini et al., 2021; Margutti et al., 2017; Mooley et al., 2022, 2018; Pozanenko et al., 2018; Troja et al., 2017), and optical/IR kilonova (KN) (Arcavi, 2018; Coulter et al., 2017a; Drout et al., 2017; Evans et al., 2017a; Kasen et al., 2017; Kasliwal et al., 2017b; Kasliwal et al., 2019; Lipunov et al., 2017a; Soares-Santos et al., 2017; Utsumi et al., 2017; Valenti et al., 2017). IGWN’s third observing run yielded another BNS merger (Abbott et al., 2020a) along with the first ever detections of neutron star–black hole mergers (Abbott et al., 2020b; Abbott et al., 2021, 2023), though no electromagnetic counterpart was found for any of these events.

Many collaborations such as the Zwicky Transient Facility (ZTF; Bellm et al. 2019a; Dekany et al. 2020; Graham et al. 2019), Electromagnetic counterparts of Gravitational wave sources at the Very Large Telescope (ENGRAVE; Levan 2020), Global Rapid Advanced Network Devoted to the Multi-messenger Addicts (GRANDMA; Antier et al. 2020), Gravitational-wave Optical Transient Observer (GOTO; Gompertz et al. 2020), All Sky Automated Survey for SuperNovae (ASAS-SN; Shappee et al. 2014), Asteroid Terrestrial Last Alert System (ATLAS; Tonry et al. 2018), Panoramic Survey Telescope and Rapid Response System (Pan-STARRS; Chambers et al. 2016b), MASTER-Net (Lipunov et al., 2017a), Searches after Gravitational Waves Using ARizona Observatories (SAGUARO; Lundquist et al. 2019), Gravitational-wave Electromagnetic Counterpart Korean Observatory (GECKO; Paek et al. 2024), the Dark Energy Survey Gravitational Wave Collaboration (DESGW; Soares-Santos et al. 2017), Global Relay of Observatories Watching Tran-

sients Happen (GROWTH<sup>1</sup>), Burst Optical Observer and Transient Exploring System (BOOTES; Hu et al. 2023), KM3Net<sup>2</sup> and VINROUGE<sup>3</sup> undertook targeted efforts during IGWN’s third observing run (O3) to identify any associated electromagnetic counterparts. However, despite extensive tiling and galaxy-targeted searches, no EM counterparts were found (Alexander et al., 2021; Andreoni et al., 2019; Andreoni et al., 2020; Antier et al., 2020; Coughlin et al., 2019c; de Wet et al., 2021; Dobie et al., 2022; Goldstein et al., 2019; Kasliwal et al., 2020; Kilpatrick et al., 2021; Rastinejad et al., 2022; Thakur et al., 2021; Tucker et al., 2022; Vieira et al., 2020). Amongst the 6 BNS and 9 NSBH merger candidates announced in O3, only 1 BNS merger (GW190425) and 4 NSBH merger candidates (GW190426, GW190814, GW200105, and GW200115) passed the False Alarm Rate (FAR) threshold for inclusion in the Gravitational Wave Transient Catalog (GWTC-3; Abbott et al. 2023) as high-confidence signals, rendering the remainder of the candidates as subthreshold astrophysical events or noise sources. Nevertheless, the dearth of BNS mergers during O3 revised the projected astrophysical rate of BNS mergers to 50–440  $\text{Gpc}^{-3}\text{yr}^{-1}$  (Abbott et al., 2023), assuming uniform mass and spin distributions, and that the merger rate is constant in comoving volume out to  $z=0.15$ .

IGWN’s fourth observing run (O4) commenced on May 24, 2023 and paused for a commissioning break on January 15, 2024, marking the end of the first half of the observing run (O4a). Based on the sensitivity of the LIGO and Virgo detectors, observing scenarios studies (Weizmann Kiendrebeogo et al., 2023) predicted that  $36_{-22}^{+49}$  BNS and  $6_{-5}^{+11}$  NSBH mergers would be detected at the public alert release threshold during the first year of O4, which is consistent with the number of potential NS merger candidates (including those of low significance, there are 27 events with  $\text{HasNS} > 0.5$  and FAR better than 1 per week) released thus far during O4a (lasting 8 months). These estimates included the Virgo detector as a part of the GW network, whose sensitivity was projected to be between 40–80 Mpc. However, because Virgo has now joined the O4 run since April 2024 at a rough sensitivity of  $\approx 50$  Mpc. The rates are driven by the LIGO interferometers, and the inclusion of Virgo does not affect the predicted rates dramatically; however, it results in better localized NS mergers.

The Zwicky Transient Facility, mounted on the Samuel Oschin 48-inch Telescope

<sup>1</sup><http://growth.caltech.edu/>

<sup>2</sup><https://www.km3net.org/>

<sup>3</sup><https://www.star.le.ac.uk/nrt3/VINROUGE/>

at Palomar Observatory, is a public-private project that routinely acquires 30 s images in the  $g$ -,  $r$ - and  $i$ -band, covering the entire available northern night-sky every two nights. Due to its cadence, ZTF has one of the most complete records of the contemporary dynamic sky. This capability enables the detection of transients at the early stages of their active phase. The use of ZTF for GRB and GW optical counterparts searches, over thousands of square degrees (Ahumada et al., 2022; Kasliwal et al., 2020) has allowed for the discovery of rare GRB afterglows: the shortest burst associated to a collapsar (Ahumada et al., 2021b), an orphan afterglow during O3 (Perley et al., 2024), and the afterglow of one of the brightest GRBs (Srinivasaragavan et al., 2024). We used ZTF (more details in § 5.2) to conduct wide-field tiling searches of 5 high-significance GW candidates (S230518h, S230529ay, S230627c, S230731an, and S231113bw) aiming to detect an EM counterpart. For completeness, we also include 5 other (lower significance) GW candidates for which ZTF has coverage, in the Appendix (see 5.8).

In this paper, we start in § 5.2 describing how ZTF is used to perform searches for EM counterparts to GW sources during O4a. We outline the triggering mechanisms for ZTF in § 5.2. In § 5.3 we give a description of the analysis pipelines and candidate filtering criteria, alongside the new and improved software toolkit for enabling counterpart discovery. In § 5.4 we provide details of the GW events we triggered ZTF on, and in § 5.5 we determine the efficiency of our efforts, and derive constraints to the KN luminosity function. We finalize the paper with conclusions in § 5.6.

## 5.2 Zwicky Transient Facility Follow-up

In this section, we describe the ZTF triggering criteria for GW events during O4a. We start by describing the IGWN public data products that were used to evaluate the relevance of an event, and we continue describing the ZTF triggering criteria and the methods used to trigger and schedule ZTF observations.

### GW metrics

The strain data of the GW events is analyzed in real time by different pipelines. Some pipelines such as GSTLal (Cannon et al., 2021), PyCBC Live (Nitz et al., 2018), the Multi-Band Template Analysis (MBTA; Adams et al. 2016), and the Summed Parallel Infinite Impulse Response (SPIIR; Guo et al. 2018) match the signal to a template bank of compact binaries coalescences (CBCs), while others, such as cWB (Klimenko et al., 2008) and oLIB (Lynch et al., 2017), search for

bursts of power in the GW spectra. These pipelines include the FAR of the event in their public data products, as well as an initial 3D localization map produced by BAYESTAR (Singer & Price, 2016). In addition to this, pipelines searching for CBCs release metrics related to the template matching results, indicating the probability of a merger to have a BBH, BNS, NSBH, or Terrestrial origin in the initial GCN announcement ( $p_{BBH}$ ,  $p_{BNS}$ ,  $p_{NSBH}$ , and  $p_{Terrestrial}$  respectively). This first online pipeline analysis is followed by a machine-learning-based inference (Chatterjee et al., 2020), that sheds light onto whether at least one NS was part of the binary (HasNS), whether the merger is likely to leave a non-zero remnant behind (HasRemnant), or if it involves an object in the 3–5  $M_{\odot}$  mass gap (HasMassGap).

### Triggering criteria

During O3, ZTF conducted a search for optical counterparts for *all* observable BNS, NSBH, and MassGap events Kasliwal et al. (2020, §2). These criteria resulted in 13 campaigns, spanning GW events with FARs between  $10^{-25} - 24 \text{ year}^{-1}$ . The offline GW analysis post-O3 confirmed only five of these candidates as likely CBCs (GW190425, GW190426, GW190814, GW200105, and GW200115), while retracting all other events (Abbott et al., 2023). During O4, we decided to take the FAR and other low-latency GW parameters into consideration at the time of triggering ZTF observations. Given that the FAR depends on the template bank of each pipeline, there are usually discrepancies between the different pipelines that have to be considered case by case. Generally, the ZTF trigger criteria prioritized events with  $\text{FAR} < 1 \text{ year}^{-1}$  and one of the following:  $\text{HasNS} > 0.1$ ,  $\text{pBNS} > 0.1$ , or  $\text{pNSBH} > 0.1$  to avoid BBHs and terrestrial events. These criteria were intended to address the substantial volume of low-significance events, rather than serving as rigid criteria. During O4a, there were 150 events with  $\text{pBNS} > 0.1$  or  $\text{pNSBH} > 0.1$  (for a comprehensive list see Table 5.4). However, only 5 of these had false alarm rates less than  $1 \text{ year}^{-1}$ . We used ZTF to follow-up all 5 of them (see Table 5.1 and § 5.4).

### ZTF strategies

In O4, ZTF developed two observing strategies for GW events that were identified as interesting ( $\text{FAR} < 1 \text{ year}^{-1}$ , and  $\text{HasNS} > 0.1$  or  $\text{pBNS} > 0.1$  or  $\text{pNSBH} > 0.1$ ). The first strategy relied on interrupting the nightly schedule of ZTF through a Target of Opportunity (ToO) trigger, in order to cover the GW region with exposures longer than the nominal 30 s survey exposures. This strategy allowed us to conduct 300 s

observations, and was limited to high confidence and well localized events. Our nominal ToO strategy covers the skymaps in multiple filters during night 0, night 1, night 2, and night 7. To prepare for O4, ZTF developed a set of deep reference images of the ZTF grid, which allowed for robust image subtraction of our deeper ToO observations. The median limiting magnitude of these deeper references is 23.0 mag for the *i*-band, and 23.5 mag for *g*- and *r*-bands.

The second strategy relies on the deliberate rearrangement of the ZTF fields that are part of the regular survey operations. The nightly ZTF schedule is optimized for the discovery and characterization of the dynamic optical sky, while systematically observing different areas of the sky (Bellm et al., 2019b). During O3, we relied on serendipitous ZTF coverage of GW skymaps for low significance or poorly localized events. However, for O4, we developed an alternative approach, referred to as “re-weighting” that makes use of the nominal 30 s exposures of the ZTF public survey and constructs a re-weighted schedule, prioritizing the ZTF fields that overlap with the GW localization area. This strategy conducts observations during the first and second night after a trigger.

### **Triggering ZTF observations**

The scheduling of ZTF observations to tile and cover GW error regions can be done through multiple avenues, and the bulk of our triggers were managed through *Fritz*, an instance of *SkyPortal* (Coughlin et al., 2023; van der Walt et al., 2019). *SkyPortal* combines the functionalities of two separate tools: the GROWTH Marshal (Kasliwal et al., 2019) and the GROWTH Target of Opportunity Marshal (Coughlin et al., 2019c), while providing additional functionalities that further automate the EMGW follow-up process. While the GROWTH Marshal offered the ability to save candidates from different discovery streams and assign follow-up, the GROWTH ToO Marshal allowed for the interaction with skymaps. As a result, *SkyPortal* provides a user-friendly tool that facilitates the management and exploration of astronomical data, allowing one to schedule observations and easily retrieve data associated to a skymap. Particularly, *Fritz* is optimized to interact with ZTF, as it retrieves data from the ZTF database Kowalski (Duvvuri et al., 2019), displays light-curves and spectra of ZTF objects, and enables interaction with multi-messenger events, such as GWs, among other key features. *Fritz* continuously listens to the GCN stream of alerts (Singer & Racusin, 2023) and generates an interactive GCN event page for each new alert, including for GWs, GRBs, and neutrino alerts (see Figure 5.1). Information intrinsic to each GCN, such as  $p_{BNS}$  or HasNS, is read-

ily accessible through this page. Additionally, `Fritz` facilitates the management and execution of ZTF observation plans (as well as for other facilities, such as DE-Cam, WINTER, Palomar Gattini IR, and the GROWTH-India Telescope). As a new event comes in and is added to `Fritz`, a default ZTF observing plan is created with `gwemopt`, a schedule optimizer originally developed to handle GW skymaps (Coughlin et al., 2018b). The default `gwemopt` plan consists of three visits per field, each lasting 300s, in a  $g$ -,  $r$ -,  $g$ -band sequence. However, this default strategy can be modified by requesting a new observing plan with adjusted exposure times and filter sequences, or by targeting a subsection of the GW skymap. For each observing plan, `Fritz` additionally displays the tiling of the region in a dynamic skymap, and a summary of the plan including the duration of the observations, the areal coverage, and the probability enclosed. The finalized plan can be submitted to the ZTF queue through `Fritz`.

For events that required a re-organization and re-weighting of the nominal 30 s ZTF observations, the procedure requires communication with the ZTF scheduler (Bellm et al., 2019b)<sup>4</sup>. This was accomplished by sending fields and their integrated probabilities from the GW skymap to the ZTF scheduler through an integrated API in `Fritz`. Once the fields are received, the scheduler assigns 30 s epochs in  $g$ -,  $r$ -, and  $i$ -bands to the highest probability fields.

Additionally, we developed an open source Simple Nodal Interface for Planning Electromagnetic Reconnaissance of Gravitational Waves (`SniperGW`)<sup>5</sup>, a programmatic avenue to access the ZTF scheduler, as a back-up that can be run on a laptop. `SniperGW` directly downloads maps from `GraceDB`, uses `gwemopt` to generate the schedules, and communicates directly with the ZTF scheduler via API. This serves as an “offline” method for us to submit schedules in real-time in case the `Fritz` database is down, and also allows more flexibility to customize schedules if needed.

### 5.3 Analysis Pipelines

The ZTF pipeline (Masci et al., 2019), running at the Infrared Processing and Analysis Center (IPAC<sup>6</sup>), reduces, calibrates and performs image subtraction in near real time. Any  $5\sigma$  flux deviation from the reference image issues an *alert* (Patterson et al., 2019), containing metadata of the transient, including its light-curve history, real-bogus score (Duvvuri et al., 2019), and cross-matches with PanSTARRS

<sup>4</sup>[https://github.com/ZwickyTransientFacility/ztf\\_sim](https://github.com/ZwickyTransientFacility/ztf_sim)

<sup>5</sup><https://github.com/robertdstein/sniperGW>

<sup>6</sup><https://www.ipac.caltech.edu/>

Figure 5.1: The Fritz page for a GW event displays information in tags located below the date of the event. In the Properties tab, it presents information originally available in the GCN. The page exhibits the most up-to-date information available, as well as the history of changes circulated through GCNs.

(Chambers et al., 2016b), among other useful quantities. These *alerts* are issued to brokers all around the globe, such as ALerCE (Förster et al., 2016), AMPEL (Nordin et al., 2019), ANTARES (Saha et al., 2014), Lasair (Smith et al., 2019), Fink (Möller et al., 2020), and Pitt-Google<sup>7</sup>, where users can manage and filter the alerts in order to recover their transients of interest.

### Transient searches: automatic filtering

Throughout O4a, we relied on four methods to select transients from the ZTF stream: Fritz, nuztf, emgwcafe, and the ZTF REaltime Search and Triggering (ZTFReST; Andreoni et al. 2021). Some of these tools were used during O3, and build on developments following the past IGWN run. Each tool developed a unique alert filtering scheme, however, they have a common core:

<sup>7</sup><https://pitt-broker.readthedocs.io/en/latest/>

- **In the GW skymap:** The candidate is required to be inside the 95% contour of the latest and most up-to-date GW skymap.
- **Positive subtraction:** We focus on sources that have brightened and have a positive residual after image subtraction.
- **Real astrophysical sources:** ZTF has developed a machine learning (ML) model to identify sources that are created by ghosts or artifacts in the CCDs. The model was trained with known ZTF artifacts and it relies on a deep convolutional neural network (Duev et al., 2019). Generally, sources with Real-Bogus score  $> 0.3$  are considered to be of astrophysical origin.
- **Avoid known point sources:** To avoid contamination from stars, we enforce transients to be greater than 3 arcsec from any point source in the PS1 catalog based on Tachibana & Miller (2018).
- **Minimum of two detections:** To reject slow moving solar system objects and cosmic rays, we enforce a minimum of two detections separated by at least 15 min.
- **Far from a bright star:** It is well known that bright sources produce artifacts and ghosts, thus we require a minimum distance of  $> 20$  arcsec from sources with  $m_{AB} < 15$  mag.
- **First detection after the GW event:** KNe and relativistic afterglows are only expected after the merger, thus we filter out sources with activity previous to the GW event.

The majority of the analysis was carried out on `Fritz`: from planning the observing strategy, to the selection of candidates, and the orchestration of their follow-up. For the selection of candidates, we set in place *two* MongoDB filters to interact with `Kowalski`, the ZTF database, via `Fritz`. Both filters followed the points established above, and while the EM+GW filter aims to serve as a thorough census of all the extragalactic sources spatially and temporally consistent with a GW event, the EM+GW PtAu filter was designed to recover transients within 150 kpc of projected distance from a galaxy, either in the Census of the Local Universe (CLU; Cook et al. 2019b) or in the NASA/IPAC Extragalactic Database - Local Volume Sample (NED-LVS; Cook et al. 2023) catalogs. A major development in O4a is the

flexible candidate searches in different skymaps. We used to rely on offline cross-matching for each candidate, in order to determine at what credible level within the GW skymap each candidate was discovered. Now, the searches can be customized through *Fritz*, by selecting a skymap, a credible level, and a detection date, in order to retrieve the candidates that meet the selected criteria. This new feature allows us to easily determine which ZTF sources are inside a skymap, and it has been used to revise candidates when a newly updated GW skymap is circulated (see Figure 5.2).

*Fritz* was intended to provide a stable and reliable way to access, filter, visualize, and interact with ZTF data. It was optimized to cater to multiple science cases with a trade-off in flexibility. Although alert filters can easily be modified, real-time fine-tuning adjustments are difficult to implement. For this reason, we have other software stacks that enable independent queries to *AMPEL* and *Kowalski*, the ZTF databases. Having multiple tools analyzing the ZTF data stream allows us to be meticulously thorough, to increase our completeness, and to understand how the different alert filters affect our results. In this section we describe complementary methods used to filter ZTF alerts.

Firstly, we conducted an independent search using the `nuztf`<sup>8</sup> python package (Stein et al., 2023), originally developed for the ZTF Neutrino Follow-Up Program (see Stein et al. 2023 for further details). `nuztf` uses the *AMPEL* framework to conduct candidate filtering (Nordin et al., 2019), and uses the *AMPEL* broker data archive to retrieve ZTF data at very low latency (Nordin et al., 2019). *AMPEL* provides a direct healpix API query that can return candidates within a given skymap. We perform cuts similar to those listed above to select candidates, and then perform automated cross-matching with various multi-wavelength catalogues to flag likely variable AGN or stars. `nuztf` can export candidates to *Fritz*, as well as produce summary PDFs for quick candidate scanning. `nuztf` uses ZTF observation logs from IPAC to calculate survey coverage of a skymap, accounting for chip gaps and any processing failures in each of the 64 ZTF quadrants.

The *Kowalski* database was queried independently through `emgwcave`<sup>9</sup>, a python-based script that retrieves candidates based on the cuts similar to the ones described above. `emgwcave` offers an extra layer of flexibility, as the queries can be easily modified. Similar to the `nuztf` searches, the candidates are cross-matched with

<sup>8</sup><https://github.com/desy-multimessenger/nuztf>

<sup>9</sup><https://github.com/virajkaram/emgwcave>

The screenshot shows a 'GCN Filtering' panel with the following fields:

- Dateobs/Name:** 2023-10-29T05:23:22 (LVC#S23102...)
- Filter:** bayestar.multiorder.fits,1
- Cumulative Probability:** 0.95
- First Detection After (UTC):** 2023-10-29 05:23:22
- Last Detection Before (UTC):** 2023-11-01 05:23:22
- Minimum Number of Detections:** 2

Figure 5.2: A snapshot illustrating the spatial and temporal constraints set on Fritz for transients selection. This feature is used to refine the candidate query, limiting it to a specific region (Cumulative Probability) on a skymap within a designated time-frame.

multiple catalogs in order to identify AGNs and variable stars. The resulting outcomes are then exported to a PDF file and simultaneously pushed to Fritz.

Finally, we made use of the ZTFReST infrastructure (Andreoni et al., 2021). This open-source code allows the exploration of ZTF data, and the flagging of fast fading transients. ZTFReST derives the evolution of a given transient based on the photometry in the ZTF alerts and forced photometry (Yao et al., 2020). The ranking of transients considers factors such as the galactic latitude, the cross-match to multi-wavelength catalogs, and the magnitude evolution. ZTFReST highlights transients through a user-friendly Slack-bot that enables the scanning of candidates.

All candidates passing the automatic filter are submitted to the Transient Name Server (TNS<sup>10</sup>).

### Transient Vetting: source by source

Once a transient passes either of the filters set in place (EM+GW or EM+GW PtAu), it can be easily retrieved through Fritz where we have implemented an efficient spatial filter through Healpix Alchemy (Singer et al., 2022) that allow us to query transients in a given portion of a specific skymap. If a candidate passes any of the other offline filters (nuztf, emgwcafe, or ZTFReST), it can easily be included in the main Fritz group and be analyzed using the Fritz capabilities. The Fritz interface allows one to easily modify the spatial query and retrieve ZTF transients at different credible levels, as seen in Figure 5.2.

During O3, a key feature to discriminate candidates was the use of ZTF forced photometry (FP). Thanks to a number of modifications and improvements in the IPAC request and retrieval of FP products, Fritz has now integrated forced photometry capabilities. For each transient, there is the option to directly request FP from the

<sup>10</sup><https://www.wis-tns.org/>

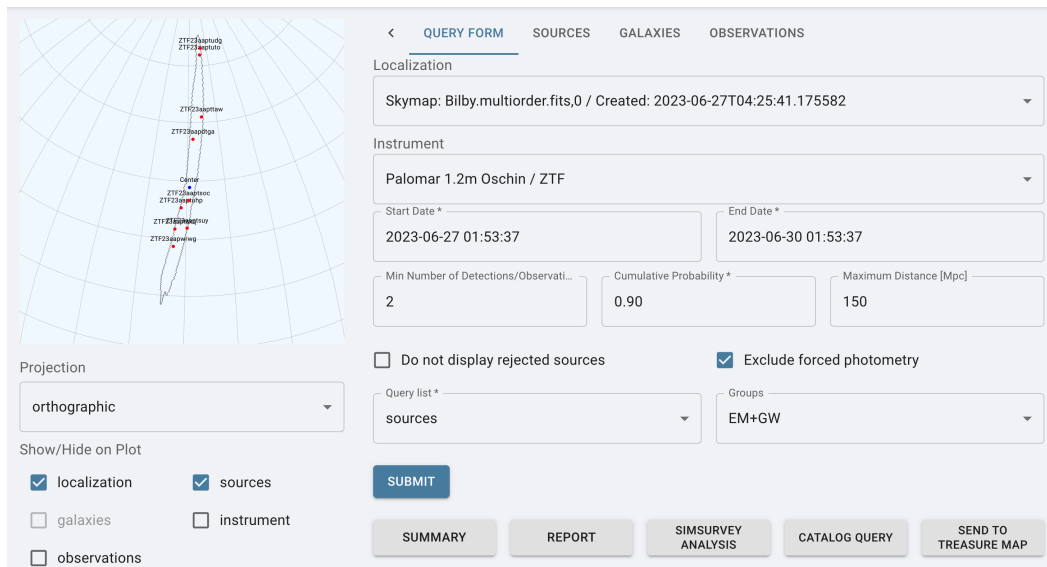


Figure 5.3: Snapshot of the GCN Analysis Fritz page. In this case, we display the sources within the 90% localization of the GW event S230627c passing the EM+GW filter in the corresponding GW skymap.

Fritz source page, and additionally select the time window of interest, that could go back to the start of the survey. Similarly, Fritz has made use of the ATLAS FP service (Shingles et al., 2021), and it has implemented a similar system for data retrieval. For both services, the products include the flux information and its uncertainty. We set a threshold of  $3\sigma$  for detections and we take this information into account when ruling out sources. We also download the ATLAS images associated with the forced photometry for further inspection.

The Fritz alert filters can retrieve additional information for the candidates, as they are ingested in the *Kowalski* database, they are also crossmatched with a number of surveys. Data from the Wide-Field Infrared Survey Explorer (WISE; Wright et al. 2010) and Milliquas (Flesch, 2023) are retrieved and used to assess whether a source is associated to an active galactic nuclei (AGN): for WISE we use the  $W1-W2 > 0.6$  cut (Wright et al., 2010), while for Milliquas we require a quasar probability  $p_{QSO} < 0.8$ . Since the WISE point spread function (PSF) is around 6 arcsec (compared to ZTF’s 1 arcsec PSF), additional human vetting is required to ensure the association to an AGN.

> Source ID	TNS RA (deg)	Dec (deg)	GCN Status	Explanation Notes
> <a href="#">ZTF19aabybn</a>	101.208303	-27.666986	✗ 	STELLAR
> <a href="#">ZTF23aboibmu</a>	121.777133	47.257160	? 	STELLAR
> <a href="#">ZTF23abofcm</a>	289.207379	35.420962	✗ 	SLOW
> <a href="#">ZTF23abojrkp</a>	318.120756	32.835215	✗ 	AGN WISE colors consistent with AGN

Figure 5.4: Snapshot of the GCN Analysis `Fritz` page showing the rejection criteria for candidates discovered within the 90% localization of S231029k.

### Transient Vetting: assigning follow-up

In many cases, the objects discovered in GW search campaigns require additional photometric and/or spectroscopic follow-up in order to discern the nature of the transients and determine whether they could be a viable EM counterpart. Objects passing the filtering criteria outlined in § 5.3 and 5.3 can be assigned external photometric and spectroscopic follow-up through `Fritz`. For example, we triggered the Spectral Energy Distribution Machine (SEDM; Blagorodnova et al. 2018b; Kim et al. 2022b; Rigault et al. 2019a) for both spectroscopy and imaging and Las Cumbres Observatory (LCO; Brown et al. 2013b) for imaging during our O4a GW search campaigns through `Fritz`. We triggered several other external photometric and spectroscopic facilities to photometrically monitor and classify transients found during our GW search campaigns; these facilities are described in Sections 5.8 and 5.8.

After retrieving promising candidates within the GW localization (see Figure 5.3), we used in-built `Fritz` functionality to track the status of each candidate, a novelty during O4a. For each candidate, we can either highlight it, mark it as ambiguous, reject it, or flag it as a source that still needs to be vetted (see Figure 5.4). We can choose a reason for selection or rejection from a dropdown menu spanning the following categories:

- **Local/Far** - based on the photometric/spectroscopic redshift of a potentially associated host galaxy, a candidate appears to be consistent with the GW distance, or too far to be associated with it.
- **New/Old** - based on either alerts or forced photometry, a candidate that is temporally consistent with the GW event (i.e. the first alerts occur after the GW trigger time) or has a history of previous detections.
- **Red** - based on either alerts or forced photometry a candidate exhibits red colors in its light curve ( $g - r > 0.3$  mag), as expected for a KN.
- **Fast/Slow** - based on either alerts or forced photometry, a candidate's light curve evolves more rapidly or slowly than  $0.3 \text{ mag day}^{-1}$  (the minimum decay rate expected for a KN-like transient; ?).
- **Rock** - based on examination of image cutouts or light curve, a candidate is characterized as a moving object.
- **Stellar** - a star lies within 2 arcsec from the candidate position and/or the light curve has stellar-like variability.
- **AGN** - a candidate's host galaxy exhibits WISE colors consistent with an AGN, it shows photometric variability, and/or it is spectroscopically classified as AGN.
- **Bogus** - upon detailed examination of alert image point spread functions, a candidate appears to be an image artifact.
- **Specreject** - the spectroscopic classification of a candidate matches neither a GRB afterglow nor a kilonova.

Optionally, users can also leave a customized note on the candidate, providing additional information not captured in the dropdown menu. Since the selection/rejection

tool is dynamic, users can update the status of a given candidate once additional information (such as forced photometry, or follow-up photometry/spectroscopy) has been obtained. One such example of the candidate selection/rejection tool is shown in Figure 5.4 for the GW event S231029k.

### **Transient Vetting: Dissemination of candidates**

The last step is to disseminate the details of our observations and final candidate selection via GCN circular to the broader astronomical community. Based on the status of candidates marked in the selection/rejection tool, they will be automatically sorted into separate table and displayed in the content of the GCN circular. Furthermore, Fritz generates a summary of the conducted ZTF observations, with probability and areal coverage within the requested time window, along with a detailed table of the ZTF photometry. Examples of auto-generated GCN circular text summarizing ZTF observations as well as tables with highlighted and rejected candidates are shown in Figure 5.5. This new, streamlined system for retrieving transients within the localization, tracking their status, and generating a GCN draft allowed for the timely circulation of interesting candidates discovered with ZTF to the rest of the multi-messenger astronomy (MMA) community. The ZTF fields and the coverage of the gravitational wave skymap is also made available through Treasuremap (Wyatt et al., 2020) to the community.

## **5.4 Summary of ZTF Triggers**

In this section we describe the ZTF observations of 5 O4a GW events that had a probability of BNS or NSBH greater than 0.1 (see Table 5.1) and a FAR  $< 1 \text{ year}^{-1}$ . In Appendix 5.8 we describe the observations of 5 additional GW events with FAR greater than  $1 \text{ year}^{-1}$ . Of the events described in this section, only S230627c passed our criteria to trigger ToO observations. We obtained some serendipitous observations within the skymap of S230518h, but the updated skymap excluded the ZTF-observed regions. The remaining events (GW230529, S230731an, S231113bw) were observed using the re-weighting strategy (see Table 5.1).

### **S230518h**

The first event detected during O4a was during the engineering run, on May 18th, 2023 (LIGO Scientific Collaboration et al., 2023a). This event was a highly significant event (FAR of one per 100 years) and was originally classified as a likely NSBH (86%) and its 90% credible region spanned close to  $460 \text{ deg}^2$ . The majority

```

TITLE: GCN SUMMARY TEST OBS

SUBJECT: Follow-up on GCN Event 2023-05-21T05:30:43

DATE: 2023-05-31 22:45:46.066066

FROM: theophile du laz at ... <theophile.dulaz@gmail.com>

on behalf of the EM+GW, report:

Observations:

Palomar 1.2m Oschin - ZTF:

We observed the localization region of LVC trigger 2023-05-21T05:30:43.000 UTC. We obtained a total of 401 images covering ztfg,ztfi,ztfr bands for a total of 13380 seconds. The observations covered 3048.1 square degrees beginning at 2023-05-21T05:32:51.999 (2 minutes after the burst trigger time) corresponding to ~29% of the probability enclosed in the localization region.
The table below shows the photometry for each observation.

TITLE: EXAMPLE AUTO-GENERATED GCN CIRCULAR

SUBJECT: ZTF Follow-up of the GW event S230521k

DATE: 2024-01-22 21:33:04.877467

FROM: Shreya Anand at ... <sanand@caltech.edu>

T. Ahumada (...), S. Anand (...)

on behalf of the EM+GW, report:

Found 10 sources in the event's localization, 9 of which have been rejected after characterization:

Sources:
+-----+-----+-----+-----+-----+-----+
| id          | tns    | ra      | dec    | redshift | comment |
+-----+-----+-----+-----+-----+-----+
| ZTF23aalcvpw | 2023jfp | 173.4715 | 29.1938 |           | bluer, host, |
+-----+-----+-----+-----+-----+-----+

Rejected sources:
+-----+-----+-----+-----+-----+-----+
| id          | tns    | ra      | dec    | redshift | comment |
+-----+-----+-----+-----+-----+-----+
| ZTF23aalbwxx |         | 176.5481 | -0.9106 |           | redder, no host, rock within 30 arcsec |
| ZTF23aalbypp |         | 179.2981 | 2.1502 |           | redder, no host, rock withi 10 arcsec |
| ZTF23aalcoas |         | 176.3550 | -2.7421 |           | single band data, no host, rock within 10 arcsec |
| ZTF23aalcpv  |         | 175.8908 | 3.0439 |           | bluer, no host, rock within 10 arcsec |
| ZTF23aalcqtq |         | 176.0103 | 6.2305 |           | single band data, no host, rock within 10arcsec |
| ZTF23aaldebi |         | 179.2978 | 2.1501 |           | single band data, no host, rock within 10arcsec |
| ZTF23aaldfpg |         | 177.7096 | 1.4222 |           | single band data, rock within 5 arcsec |
| ZTF23aalbwua |         | 177.6670 | -0.3263 |           | redder, no host, rock within 10 arcsec |
| ZTF23aaldgfi |         | 176.5482 | -0.9103 |           | single band data, no host, rock within 5 arcsec |
+-----+-----+-----+-----+-----+-----+

```

Figure 5.5: Two examples of auto-generated GCN circular text for the GW event S230521k. Top: a summary of the actual ZTF observations conducted. Bottom: selected and rejected candidates within the GW localization.

Trigger	Strategy	FAR [year <sup>-1</sup> ]	$p_{BNS}$	$p_{NSBH}$ prob.	HasNS prob.	HasRemnant prob.	HasMassGap prob.	Distance [Mpc]	Covered prob.	Area covered [deg <sup>2</sup> ]	g-band depth [AB mag]	latency [hr]
S230518h	No coverage	0.01	0.0	0.86	1.0	0.0	0.0	204	–	–	–	–
GW230529	Re-weighting	0.006	0.31	0.62	0.98	0.07	0.73	197	7%	2425	20.6	10
S230627c	ToO	0.01	0.0	0.49	0.0	0.0	0.14	291	74%	72	21.03	2.2
S230731an	Re-weighting	0.01	0.0	0.18	0.0	0.0	0.0	1001	3%	43	18.7	12.4
S231113bw	Re-weighting	0.42	0.0	0.17	0.0	0.0	0.02	1186	11%	301	21.17	7.7

Table 5.1: Summary of ZTF observations and GW properties of the 5 GW events selected and analyzed in this paper. We required their FAR to be less than 1 year<sup>-1</sup>, and one of the following:  $p_{BNS} > 0.1$ ,  $p_{NSBH} > 0.1$ , or  $\text{HasNS} > 0.1$ . We quote other quantities intrinsic to the GW event, such as the mean distance to the merger, the `HasRemnant`, and the `HasMassGap` parameters. For each event we summarize the coverage, depth and latency for the ZTF observations. We include the events with  $\text{FAR} > 1 \text{ year}^{-1}$  in Table 5.2 in the Appendix 5.8. To determine the areal coverage and the enclosed skymap probability observed by ZTF, we require at least two ZTF observations in a given region.

of the region was observable only from the Southern hemisphere, and ZTF covered  $\sim 2\%$  of the initial region. However, IGWN circulated an updated localization 8 days after the event for which the ZTF coverage was negligible.

### GW230529

GW230529 is a highly significant (FAR of 1 per 160 yrs), single detector (LIGO Livingston) event (LIGO Scientific Collaboration et al., 2023b). It was confirmed as an astrophysical event in April 5th, 2024 (The LIGO Scientific Collaboration and the Virgo Collaboration and the KAGRA Collaboration, 2024). The 90% credible region spans over 24000 deg<sup>2</sup>, thus we did not trigger ToO observations and decided to re-weight the ZTF survey fields. The first observation started  $\sim 10$  hours after the GW trigger and based on the first night, the median limiting magnitudes were  $g = 21.1$  and  $r = 21.0$  mag. Over three nights of observations, we covered 2425 deg<sup>2</sup>, that translates to 7% of the localization region. We originally found six candidates in this region; upon follow-up, none of them showed KN-like signatures and hence were rejected (Karambelkar et al., 2023). Details of the candidates are presented in Table 5.3. Although our coverage is only 7%, our limiting magnitudes allow us to set constraints in the properties of the KN, assuming the event was in the ZTF footprint (see Figure 5.6). Specifically, we can rule out KNe with polar viewing angles ( $0^\circ < \theta_{\text{obs}} < 26^\circ$ ) within the observed region, assuming a distance of 105 Mpc (corresponding to the median– $1\sigma$  distance) for the NSBH merger (see Figure 5.6).

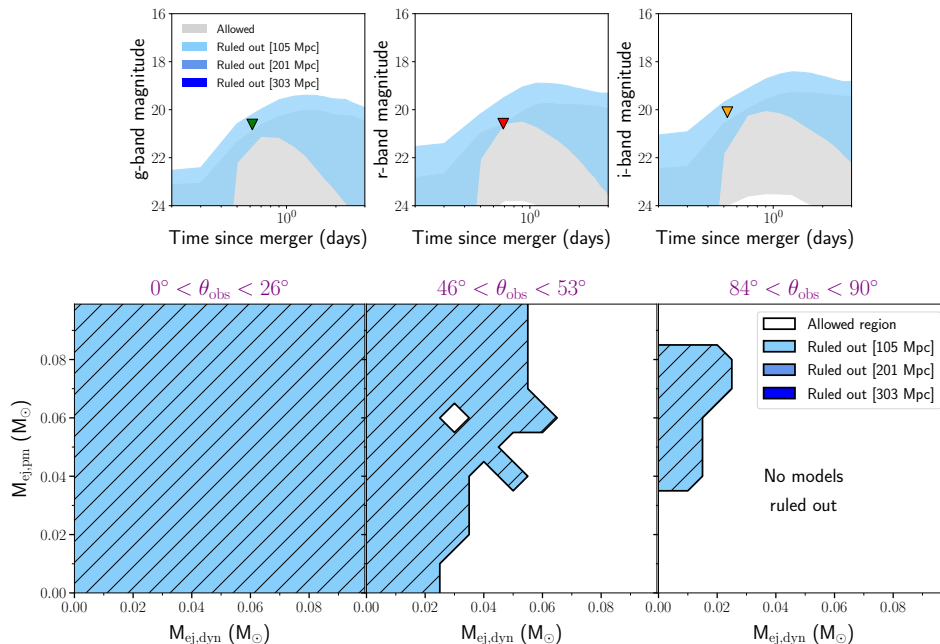


Figure 5.6: Constraints on KN model parameters based on the ZTF limiting magnitudes on GW230529. Top panels. the  $g$  (left),  $r$  (middle) and  $i$  (right) band non-detections are shown together with NSBH KN models: the blue areas encompass light curves that are ruled out by the limits at three different distances (corresponding to median distances and  $\pm 1\sigma$  distance uncertainties from LIGO), while those in grey encompass light curves that are compatible with the limits. These NSBH-specific models are computed with POSSIS (Anand et al., 2020a; Bulla, 2019) and have three free parameters: the mass of the lanthanide-rich dynamical ejecta ( $M_{ej,dyn}$ ), the mass of the post-merger disk-wind ejecta ( $M_{ej,pm}$ ) and the viewing angle ( $\theta_{jobs}$ ). Bottom panels. Regions of the  $M_{ej,pm}$  -  $M_{ej,dyn}$  parameter space that are ruled out at different distances and for different viewing angle ( $\theta_{jobs}$ ) ranges (from a face-on to a edge-on view of the system from left to right), assuming the KN fell within the ZTF footprint.

### S230627c

S230627c, with a FAR of about 1 in 100 years, was classified by the pycbc (Nitz et al., 2018) pipeline as a likely NSBH ( $\sim 50\%$ ) or BBH ( $\sim 50\%$ ) with a relatively small localization: the 90% of the probability spanned  $\sim 82$  deg<sup>2</sup> (LIGO Scientific Collaboration et al., 2023c). Even though the GSTLAL (Cannon et al., 2021) pipeline classified this event as a BBH (100%), we triggered a targeted search with ZTF. The observations started about 2.2 hours after the GW event and covered 74% ( $\sim 72$  deg<sup>2</sup>) of the skymap (see Figure 5.7). After an initial inspection of the candidates (Table 5.3), we ran forced photometry on archival ZTF data, leading to 10 potential counterparts (Anumarlapudi et al., 2023). Further monitoring did not reveal color

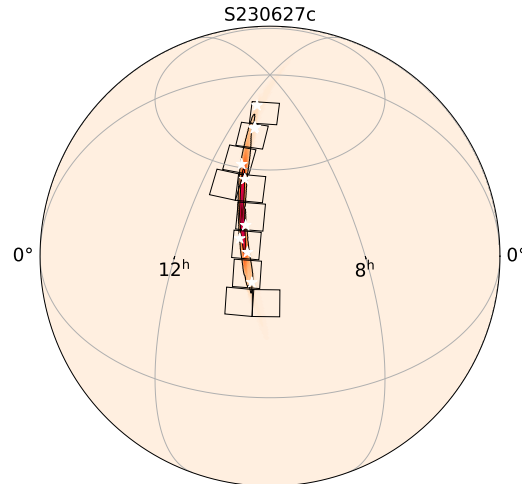


Figure 5.7: Localization of S230627c, overplotted with the ZTF coverage (black squares) and the 90% probability contour. We show the candidates associated to this event as white stars in the localization region. The rest of the skymaps can be found in the Appendix 5.8, in Figs. 5.12-5.18 .

or magnitude evolution consistent with known KN models or an AT2017gfo-like transient. Observations over the first night reached median magnitude limits of  $g = 21.0$  and  $r = 21.2$  mag (Ahumada et al., 2023a).

### S230731an

S230731an, had a FAR of a 1 per 100 years and the 90% credible region of its initial localization covered  $599 \text{ deg}^2$  (LIGO Scientific Collaboration et al., 2023d). It was originally detected by the pycbc pipeline with a NSBH probability of 18% (BBH probability of 81%), while the gstlal pipeline classified it as a probable BBH (99%). Due to its large inferred distance of  $1001 \pm 242$  Mpc, we decided to re-weight the ZTF fields. Due to weather, the ZTF coverage was  $\sim 3\%$  ( $43 \text{ deg}^2$ ), reaching a depth of  $g = 18.7$  mag, and no candidates were found in the region in a 72 hr window.

### S231113bw

Detected by pycbc, this event had a relatively moderate FAR of about 1 per 2.35 years, and was initially classified as a likely BBH (79%), or a NSBH (17%) (LIGO Scientific Collaboration et al., 2023e). Offline analyses by IGWN later classified this event as a likely BBH (96%), and lowered the probability of it being an NSBH to less than 1%. The 90% credible region spanned  $\sim 1713 \text{ deg}^2$ , and although it was mostly a northern hemisphere event, the majority of the error region was in close

proximity to the sun. We covered about 11% of the skymap (301 deg<sup>2</sup>), achieving a depth of  $g = 21.17$  mag, and found no candidates that passed our filters (Ahumada et al., 2023b).

## 5.5 Discussion

In this section, we quantify the efficiency of the ZTF searches during O4a, while also including in the analysis the confirmed astrophysical events from O3. We address this by taking both a Bayesian (§ 5.5) and a frequentist approach (§ 5.5). We use the ZTF observations to constrain the KN luminosity function under different assumptions.

### **nimbus**

In our analysis of the events described above, we have utilised the hierarchical Bayesian framework `nimbus` (Mohite et al., 2022). Briefly, `nimbus` uses a single “average-band” linear model (we will hereafter refer to this model as the *Tophat* model) for the time evolution of the absolute magnitude using  $M(t) = M_0 + \alpha (t - t_0)$ , where  $M_0$  is the initial magnitude and  $\alpha$  is the evolution rate, to determine the likelihood of obtaining the upper limits from ZTF observations given a model  $(M_0, \alpha)$ . The “average-band” model enables us to use ZTF observations across all bands. In order for `nimbus` to infer the intrinsic luminosity parameters, it requires information about the survey observations, which in this case includes the ZTF observation logs with the specific fields targeted, the Milky Way extinction values for each pointing, and a 3D GW skymap.

`nimbus` determines the posterior probability of a KN with a particular model (in this case, with a specific  $M_0$  and  $\alpha$ ) given the ZTF observations within the GW skymap. The framework self-consistently accounts for the probability of a GW event being of astrophysical origin ( $p_{astro}$ ) and also factors in the ZTF coverage within the GW skymap. For every sample in the KN parameter space, `nimbus` calculates the likelihood of obtaining the observed limiting magnitude in the ZTF survey, given the model parameters for every field independently. For this, `nimbus` follows Mohite et al. (2022, § 2.2). We have adopted a uniform distribution for the model priors, and flattened the `multiorder` skymap fits file for all the events to an `nside` of 256. Once the likelihoods have been determined of the observations for each event in all the corresponding ZTF fields, the overall posterior probability of the KN model parameters is determined as in Mohite et al. (2022, Eq. 18).

The combined posterior probability for KN model parameters using events followed

up by ZTF during O4a is shown in Figure 5.8. Based on the ZTF observations of O4a events, *nimbus* shows a preference for models that are fainter than  $M_0 = -16$  mag (at a credible level of 0.9), regardless of evolution rate. The yellow shaded regions in Figure 5.8 correspond to portions of the KN parameter space that ZTF is unable to constrain based on event distances and ZTF upper limits. On the other hand, for fading KNe in the  $-16 < M_0 < -19$  mag range, ZTF is partially sensitive, hence the posterior probability has some support for those models (at a credible level of 0.64). The bright KNe that show a rising behavior have the least preference in *nimbus*, with posterior probabilities less than 0.3. We note that the most constraining event is S230627c, as it has the best combination of coverage and depth, while for other events these numbers are more marginal.

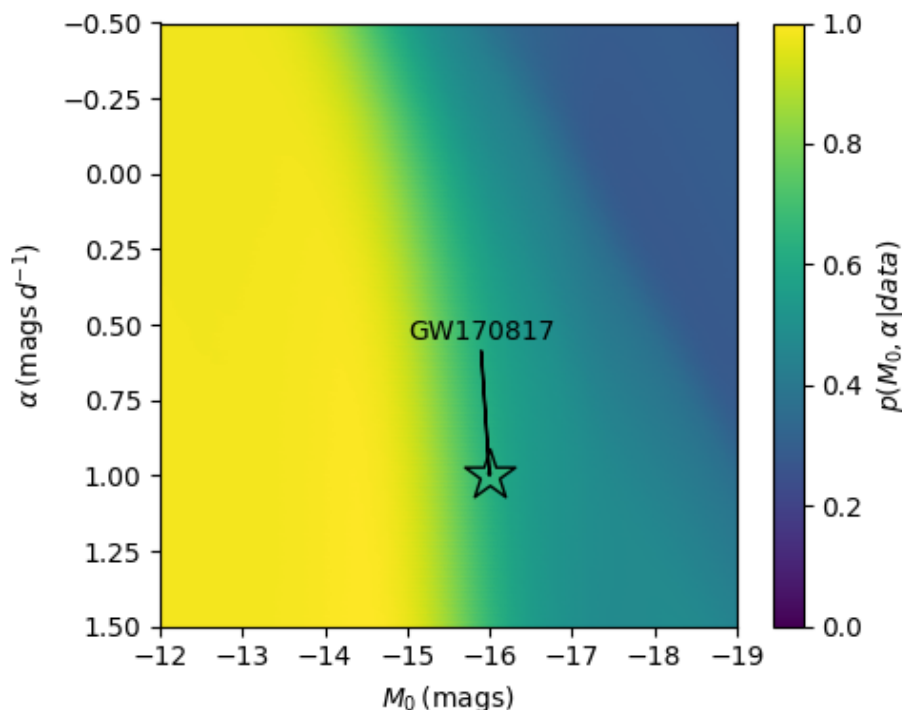


Figure 5.8: The *nimbus* results of the combined posterior probability for KN model parameters assuming the *Tophat* model using events followed up by ZTF only during O4a. The x-axis shows the initial absolute magnitude  $M_0$  of a model, while the y-axis shows its evolution rate  $\alpha$ . The color bar shows the posterior probability of each model, in the combined dataset, where yellow regions show the favored regions of parameter space given the non-detection of KNe from ZTF observations, and the bluer regions show less preferred combinations for initial  $M_0$  and  $\alpha$ . We also mark the position of the average  $r$ -band decay rate for a GW170817-like KN over its first 3 days of evolution.

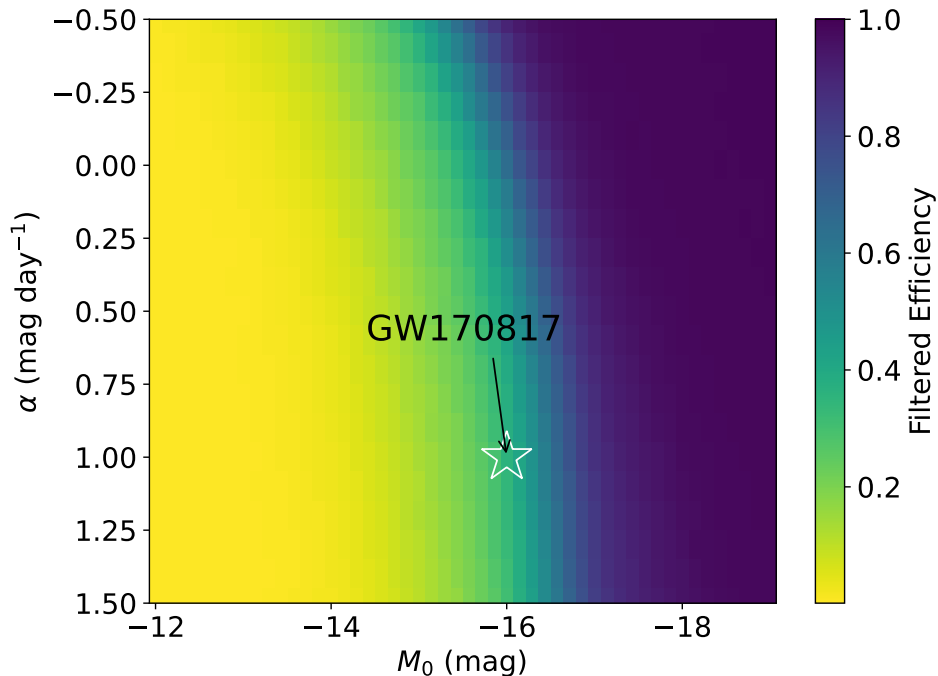


Figure 5.9: Filtered kilonova efficiency with `simsurvey` for the *Tophat* model evolution. The filtering cuts we apply include a requirement of a minimum of two detections separated by 15 minutes at  $5\sigma$ . The color bar shows the fraction of sources detected after the filtering versus the number of sources ingested in the GW volume for the O3 and O4a combined set of skymaps. Similar to Figure 5.8, we mark the position of a GW170817-like KN on this plot. For this dataset, GW170817 has 36% of efficiency.

### **simsurvey**

Similarly to previous optical wide field of view (FoV) studies (Ahumada et al., 2022; Kasliwal et al., 2020), we make use of `simsurvey` to estimate the efficiency of the ZTF searches. The strategy that `simsurvey` takes starts with injecting KN-like light-curves in the GW localization volume, then uses the empirical ZTF coverage to measure the KN recovery rate (number of detected KNe divided by the number of injected KNe). We refer to this KN recovery rate as the KN efficiency. `simsurvey` also has filtering functionality, which we use to mimic our realistic candidate filtering criteria. In particular, for KNe to pass the filtering criteria in `simsurvey`, they must have at least two ZTF detections separated by 15 minutes above  $5\sigma$ . We run separate simulations within the skymaps of each of the 5 GW events listed in Table 5.1 as well as the five surviving O3 candidates for which we conducted ZTF follow-up (GW190425, GW190426, GW190814, GW200105 and GW200115). We chose to include GW190814 despite its ambiguous classification,

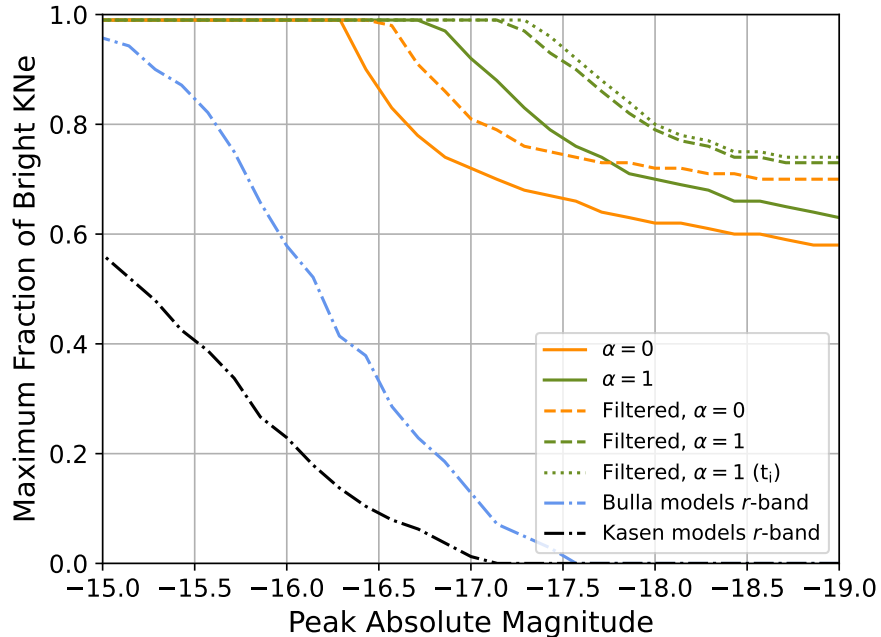


Figure 5.10: Kilonova luminosity function for events surviving O3, and high significance O4a events. We show in orange the models with flat evolution ( $\alpha = 0$ ), and in green the fading models ( $\alpha = 1 \text{ mag day}^{-1}$ ). The solid lines show the unfiltered results, while the dashed lines show the results after selecting sources consistent with the ZTF filtering criteria (i.e. two detections). The green dotted line weights models with fading evolution passing the filtering criteria by the event’s terrestrial probability ( $t_i$ ). The black and blue lines show the fraction of Kasen and Bulla models whose peak magnitudes fall within a particular luminosity bin.

since it remains unclear whether the merger was a BBH or NSBH. We inject three different sets of KN models into `simsurvey`:

1. *Tophat* - an empirical KN model parameterized by initial absolute magnitude ( $M_0$ ) and evolution rate ( $\alpha$ ). This same model was used in the `nimbus` framework.
2. *POSSIS* - the 3-D, radiative transfer *Bu2019lm* KN models described in Bulla (2019) and Dietrich et al. (2020b), parameterized by dynamical ejecta mass, disk wind ejecta mass, half-opening angle of the lanthanide-rich component, and viewing angle.
3. *Kasen* - 1-D, radiative transfer KN models described in Kasen et al. (2017),

parameterized by total ejecta mass, velocity, and lanthanide fraction (no viewing angle dependence).

4. Banerjee - 1-D radiative transfer KN model from (Banerjee et al., 2023, 2022), parameterized by the density, total ejecta mass, and lanthanide fraction (no viewing angle dependence).

In Figure 5.9, we plot the KN efficiency for the *Tophat* model after applying the filtering criteria used in the ZTF searches (i.e. two detections). ZTF would detect a GW170817-like KN with  $M_0 \approx -16.0$  mag and  $\alpha \approx 1.0$  mag day<sup>-1</sup> passing the basic filtering criteria with 36% efficiency. In contrast, during O3, our joint detection efficiency (i.e. one detection in *simsurvey*) for a GW170817-like KN was 93% (Kasliwal et al., 2020). The lower joint efficiency for O3+O4a events compared to Kasliwal et al. (2020) can be attributed to the fact that many GW event candidates we followed up in O3 were retracted (Abbott et al., 2023), and we assess efficiency using more realistic criteria of two detections in *simsurvey* rather than one. In the *simsurvey* simulations, we detect KNe brighter than  $M_0 = -17.5$  mag with > 90% efficiency, indicating that such bright KNe are unlikely to have existed in our dataset.

Next, we determine the efficiency with which we can recover GW170817-like KNe in our ZTF observations for more complex models: POSSIS, *Kasen*, and *Banerjee*. Using the best fit parameters of GW170817, we find that the filtered combined efficiency is 36% and 35% for the POSSIS and the *Kasen* models respectively. The *Banerjee* models, which assume a lanthanide fraction of  $X_{\text{lan}} = 0.1$ , are slightly more pessimistic, predicting a filtered combined efficiency of 20%. We note that the proximity of results from KN models to the approximated *Tophat* model efficiency of 36% shows that the *Tophat* model is a good initial approximation to the KN evolution. In particular, with the *Tophat* model, we can recover GW170817-like KNe with >15% efficiency only in the follow-ups of GW190425 and S230627c, indicating that our most successful EMGW follow-up campaigns with ZTF during O3 and O4a have been of those two events.

While *nimbus*, a Bayesian approach, and *simsurvey*, a frequentist approach, provide independent information about KNe given the ZTF observations, these frameworks are complementary to one another. *nimbus* provides insight into which KN model parameters are more or less favored, given the ZTF observations, while *simsurvey* allows us to assess the recovery efficiency of KNe with particular model

parameters from the ZTF follow-ups. When comparing the two analyses, we note similar overall trends: bright KNe ( $M \lesssim -17.5$  mag) that exhibit rising behavior have the highest efficiencies in `simsurvey` and are the least preferred by `nimbus`, while faint, fast-fading KNe with the poorest detection efficiencies in `simsurvey` have the highest support in `nimbus` given the ZTF non-detections.

### Kilonova Luminosity Function Constraints

Combining all of our EMGW follow-ups in O3 and O4a described above, we follow Kasliwal et al. (2020) in calculating the joint constraints on the KN luminosity function. The luminosity function is given by the following equation:

$$(1 - \text{CL}) = \prod_{i=1}^N (1 - f_b \cdot p_i \cdot (1 - t_i))$$

where CL is the confidence level,  $f_b$  is the maximum allowed fraction of KNe brighter than a given absolute magnitude,  $p_i$  is the probability of KN detection within a given GW event skymap, and  $t_i$  is the terrestrial probability, defined as  $1 - (p_{\text{astro}})$ . We solve for  $f_b$  at 90% confidence for each luminosity bin and plot the results in Figure 5.10. We include separate luminosity function curves corresponding to KNe with flat evolution and declining at  $1 \text{ mag day}^{-1}$ , with two tiers of criteria: KNe recovered with a single detection (solid lines), and KNe passing our filtering criteria of two  $5\sigma$  detections separated by 15 minutes (dashed lines). In all of the curves except for the green dotted line, we set  $t_i$  to zero for all events, meaning that we assume that all of the events are astrophysical in those cases.

For reference, we plot curves corresponding to the fraction of POSSIS (*Bu2019lm*) and *Kasen* models peaking at, or brighter than a particular luminosity bin (see Figure 5.10). The POSSIS models span  $M_{\text{ej,dyn}} = 0.001 - 0.02M_{\odot}$ ,  $M_{\text{ej,wind}} = 0.01 - 0.13M_{\odot}$ , half-opening angles of the lanthanide rich component  $\phi = 15 - 75$  deg, and viewing angles  $\theta = 0 - 90$  deg; we exclude the POSSIS models with half-opening angles of  $\phi = 0$  deg and  $\phi = 90$  deg. With our ZTF observations, we can place constraints on the luminosity function for fading KNe with  $M \lesssim -16.5$  mag, corresponding to  $\sim 35\%$  of the POSSIS *Bu2019lm* grid. The POSSIS models shown here are designed for KNe from BNS (and not NSBH) mergers. We note that though many of the events we followed up have a higher  $p_{\text{NSBH}}$  than  $p_{\text{BNS}}$ , KNe from NSBH mergers are expected to be similar, but redder and fainter on average, compared to those from BNS mergers (Anand et al., 2020a), and hence our ZTF observations

would be much less sensitive to NSBH KNe.

We also plot a subset of the *Kasen* model grid consisting of total ejecta masses of  $M_{ej} = 0.01 - 0.1M_{\odot}$ , velocities of  $v_{ej} = 0.03 - 0.3 c$ , and lanthanide fractions of  $X_{lan} = 10^{-9} - 10^{-1}$ , excluding the very faint KN models with low total ejecta masses (with  $m_{ej} < 0.01M_{\odot}$ ). Approximately 10% of the *Kasen* grid KNe are brighter than  $M \lesssim -16.5$  mag, corresponding to the portion of the KN luminosity function our ZTF observations are sensitive to. Here, we choose to include a larger subset of the Bulla and Kasen grid models as compared to Kasliwal et al. (2020); this choice is largely motivated by the fact that our limits are less constraining, and thus we cannot confidently exclude any portion of the KN model space.

We calculate a maximum fraction of 76% for KNe (detected at least once by ZTF) brighter than  $-17.5$  mag and fading at  $1 \text{ mag day}^{-1}$ . If we take into account only KNe passing ZTF filtering criteria of two detections and fold in the event-by-event terrestrial probability, our maximum fraction of KNe brighter than  $-17.5$  mag and fading at  $1 \text{ mag day}^{-1}$  becomes 92%. At this point, our observations cannot constrain the maximum fraction of GW170817-like KNe (with  $M_{peak} = -16.5$  mag, fading at  $1 \text{ mag day}^{-1}$ ). Compared to the 40% fraction found in Kasliwal et al. (2020) for objects brighter than  $-18.0$  mag with flat evolution and no filtering imposed, our constraints are slightly worse (we find a maximum fraction of 62% for the same criteria). Out of the 13 GW events contributing to the luminosity function in Kasliwal et al. (2020), only 5 survived to make it to GWTC-2 and GWTC-3. In addition to these events, we include 5 events from O4a; however amongst these events, we only triggered ToO observations on S230627c, achieving a skymap coverage  $>70\%$  (all other O4a events have  $<15\%$  skymap coverage). Thus many more GW events with  $>50\%$  ZTF coverage are required in O4b in order to place meaningful constraints on the maximum fraction of GW170817-like KNe.

## 5.6 Conclusion

During the first half of IGWN’s fourth observing run, O4a, we conducted GW follow-ups of five high significance GW events. In this work, we have reported our revised approach to triggering on GW events, novel Fritz machinery for rapidly vetting ZTF candidates found within GW skymaps, and our derived constraints on the properties of KNe.

One of the key developments during O4a is Fritz, a SkyPortal instance to manage ZTF data and coordinate follow-up. This new capability allowed us to receive

the initial GW alert, create an observing plan for ZTF, trigger ZTF observations, display the sources on the GW maps, coordinate follow-up observations for telescopes, vet the candidates, and disseminate our results in an organized fashion. We complemented these searches with offline analyses (*nuzft*, *emgwcafe*, and *ZTFReST*), to leave no stone un-turned in our counterpart searches.

In addition to the ZTF ToO observations, we set in place a novel approach to use the ZTF all-sky survey and observe the GW skymap regions by re-weighting the schedule to maximize the nightly coverage. In total, we conducted observations for 5 high-significance events, and used the re-weighting strategy for 4 of the cases. Only S230518h, S230529ay, S230627c, S230731an, and S231113bw were considered of high significance, as they all had  $\text{FAR} < 1 \text{ year}^{-1}$ , and  $p_{\text{BNS}} > 0.1$  or  $p_{\text{NSBH}} > 0.1$  or  $\text{HasNS} > 0.1$ . We describe in Appendix 5.8 the results for the follow-up of additional events with a  $\text{FAR} > 1 \text{ year}^{-1}$ . In summary, we followed-up over 15 ZTF KN candidates and found no viable GW optical counterpart.

Given the ZTF skymap coverages and limiting depths of these GW events, the lack of an associated KN counterpart is consistent with our non-detection analyses. For this, we used both Bayesian and frequentist frameworks. The Bayesian approach, *nimbus*, allows us to compare which combination of parameters are more likely to have been consistent with the non-detections during our O4a campaigns, and gives preference to KN models with starting absolute magnitudes fainter than  $-16 \text{ mag}$ . Our frequentist approach used *simsurvey* to simulate sources in the GW skymap volumes, leading to an overall combined efficiency of 36% for GW170817-like KNe in O3 and O4a. Both analyses show similar trends, with *nimbus* showing a preference for fainter models, and *simsurvey* exhibiting a high recovery efficiency for bright models, painting a cohesive picture between the two frameworks.

The combination of the ZTF observations during O3 and O4a allow us to set constraints on the KN luminosity function. We find that a maximum fraction of 76% of all KNe can be brighter than  $-17.5 \text{ mag}$ . Our results are less constraining than the ones in Kasliwal et al. (2020), mainly due to the number of high-significance events followed up and the ZTF skymap coverage for the events considered. By observing 9 (17) GW events with  $> 90\%$  ( $50\%$ ) coverage to a sensitivity of  $M_{\text{peak}} > -16 \text{ mag}$ , we would be able to set constraints on the maximum fraction of GW170817-like KNe at the 25% level (Kasliwal et al., 2020).

New near-infrared (NIR) facilities, such as WINTER (Lourie et al., 2020) and PRIME (Kondo et al., 2023), have recently joined the multi-messenger search cam-

paigns. We expect that coordinated efforts in GW searches will lead to the use of these facilities to discriminate candidates based on their NIR evolution, and that they could conduct independent searches for GW events for skymaps in the  $<500$  deg<sup>2</sup> regime. Such well-localized GW events are expected to be routinely detected in O5 (Weizmann Kiendrebeogo et al., 2023). Upcoming wide field surveys, such as the Rubin observatory (Ivezić et al., 2019), ULTRASAT (Shvartzvald et al., 2023), The Nancy Grace Roman Space Telescope, and UVEX (Kulkarni et al., 2021) will open a new window in the GW searches, surveying larger volumes and exploring the UV regime. Wide FoV surveys, such as ZTF, will continue to play a fundamental role in identifying fast fading counterparts that will likely have no previous history in these new data streams.

One of the main challenges we faced during both O3 and O4a was the large localization areas associated with each of the events. We look forward to the second phase of O4, with the re-integration of Virgo to the network of interferometers at an increased sensitivity, which will reduce the sizes of IGWN sky localizations. New events discovered during O4b will likely improve our KN luminosity function constraints, while the verdict on whether the O4a events included in this analysis are recovered in offline GW analysis will also affect the results of this work.

The development of efficient tools to interface with ZTF, such as `Fritz`, has proven to be useful in the broader context of MMA during O4a, and will continue to be a valuable asset to our search efforts during O4b. `Fritz` has allowed multiple astronomers in the same team to analyze the ZTF data stream simultaneously, sharing notes and conclusions about the evolution or behavior of the candidates. `Fritz` also allows for the exploration of new observing strategies using `simsurvey`, as it can determine the KN recovery efficiency given a skymap, distance and latency. The ability to trigger automated follow-up of promising candidates within the `Fritz` interface itself, and generate ready-to-send GCNs summarizing our follow-up efforts are ways in which we have significantly reduced our latency in the GW follow-up process, increasing our chances of detecting the associated KN.

During O4b, we plan to include ZTF forced photometry throughout the candidate filtering stages, rather than post-facto. This is now possible because of the inclusion of forced photometry in the ZTF alert packets which are also accessible to the broader community. Additionally, new tools such as `GWSkyNet` may enhance our ability to target candidates that are less likely to be caused or influenced by detector noise by providing an independent metric that can be consistently inter-

preted across all candidates (Abbott et al., 2022; Cabero et al., 2020; Raza et al., 2024). GWSkyNet annotations are currently expected to be publicly available for LIGO-Virgo events in O4b on GraceDB<sup>11</sup>.

Recent recommendations from the broader EM community (The 2023 Windows on the Universe Workshop White Paper Working Group, 2024) underline the importance of prompt, public access to images and alerts, and not just the vetted counterpart candidates, from surveys conducting MMA search campaigns. Our frequent use of the re-weighting strategy during O4a has ensured immediate access to ZTF images and alerts from those GW follow-ups. This approach could be adopted by future surveys, such as the Vera C. Rubin Observatory’s Legacy Survey of Space and Time survey. For both ToO and re-weighting follow-ups, we report our pointings (and limiting magnitudes) to the TreasureMap as soon as our observations have completed. Furthermore, the development of critical software infrastructure to streamline telescope coordination and efficiency is emphasized in the white paper.

Following these recommendations, we highlight three specific areas where software infrastructure needs to be improved to boost multi-messenger discovery. First, joint querying of heterogeneous discovery streams in real-time (e.g., querying ZTF, WINTER, Rubin and LS4 simultaneously with kowalski) will enable both timely selection of the most promising multi-messenger candidates as well as timely rejection of the false positives. Second, a decentralized communications framework could facilitate active follow-up co-ordination between independent teams. This will enable optimal use of limited follow-up resources that are already the bottleneck in multi-messenger searches (e.g., communication between decentralized SkyPortal instances or similar softwares). Third, incorporating inclination angle constraints into the low-latency GW alert packets could help refine EM counterpart search strategies. For instance, one could tune the targeted depth in optical/IR bands or customize search strategies in radio/high-energy bands based on the expected emission from a KN model with GW inclination constraints applied. Together, such improvements in software infrastructure would amplify the power of collaborative discovery.

Augmenting infrastructure used by the MMA community will make multi-messenger science more accessible to a diverse set of teams around the world. Fritz is an ex-

<sup>11</sup><https://emfollow.docs.ligo.org/userguide/content.html#gwskynet-classification>

ample of an open-source tool, catering to the needs of its users, designed to lower the entry barrier for astronomers into time-domain astronomy and MMA. It serves as an intuitive interface to analyze astronomical data, while exploiting the interactive nature of a number of surveys and online catalogs. We look forward to the infrastructure developments that will address the challenges raised by the MMA community, as they will foster a more inclusive approach to enabling MMA discoveries.

## 5.7 Acknowledgements

We thank Fabio Ragosta, Nidhal Guessoum, and Albert K.H. Kong for the useful comments and suggestions. M.M.K., S.A. and T.A. acknowledge generous support from the David and Lucille Packard Foundation. We acknowledge the support from the National Science Foundation GROWTH PIRE grant No. 1545949. M.W.C, B. F. H., A.T., and T.B. acknowledge support from the National Science Foundation with grant numbers PHY-2308862 and PHY-2117997. This work used Expanse at the San Diego Supercomputer Cluster through allocation AST200029 – “Towards a complete catalog of variable sources to support efficient searches for compact binary mergers and their products” from the Advanced Cyberinfrastructure Coordination Ecosystem: Services & Support (ACCESS) program, which is supported by National Science Foundation grants #2138259, #2138286, #2138307, #2137603, and #2138296. C.M.C. acknowledges support from UKRI with grant numbers ST/X005933/1 and ST/W001934/1.

Based on observations obtained with the Samuel Oschin Telescope 48-inch and the 60-inch Telescope at the Palomar Observatory as part of the Zwicky Transient Facility project. ZTF is supported by the National Science Foundation under Grants No. AST-1440341 and AST-2034437 and a collaboration including current partners Caltech, IPAC, the Oskar Klein Center at Stockholm University, the University of Maryland, University of California, Berkeley, the University of Wisconsin at Milwaukee, University of Warwick, Ruhr University, Cornell University, Northwestern University and Drexel University. Operations are conducted by COO, IPAC, and UW.

SED Machine is based upon work supported by the National Science Foundation under Grant No. 1106171.

The ZTF forced-photometry service was funded under the Heising-Simons Foundation grant #12540303 (PI: Graham).

The Gordon and Betty Moore Foundation, through both the Data-Driven Investigator Program and a dedicated grant, provided critical funding for SkyPortal.

This research has made use of the NASA/IPAC Extragalactic Database (NED), which is funded by the National Aeronautics and Space Administration and operated by the California Institute of Technology.

The Liverpool Telescope is operated on the island of La Palma by Liverpool John Moores University in the Spanish Observatorio del Roque de los Muchachos of the Instituto de Astrofísica de Canarias with financial support from the UK Science and Technology Facilities Council.

This work relied on the use of HTCondor via the IGWN Computing Grid hosted at the LIGO Caltech computing clusters.

## 5.8 Appendix

### Observing and Data Reduction Details for Follow-up Observations

#### Photometric Follow-up

We show the photometric light-curves of all the candidates in Figures 5.19, 5.20, and 5.21.

**Palomar 60-inch** We acquired photometric data utilizing the Spectral Energy Distribution Machine (SEDM; Blagorodnova et al. 2018b; Rigault et al. 2019a) mounted on the Palomar 60-inch telescope. The SEDM is a low resolution ( $R \sim 100$ ) integral field unit spectrometer with a multi-band (*ugri*) Rainbow Camera (RC). The follow-up request process is automated and can be initiated through Fritz. Standard requests typically involved 180 s exposures in the *g*-, *r*-, and *i*-bands, however it can be customized and for some transients we used 300 s exposures. The data undergoes reduction using a Python-based pipeline, which applies standard reduction techniques and incorporates a customized version of FPipe (Fremling Automated Pipeline; Fremling et al. 2016b) for image subtraction.

**GROWTH-India Telescope** We utilized the 0.7-meter robotic GROWTH-India Telescope (GIT) (Kumar et al., 2022), located in Hanle, Ladakh. It is equipped with a 4k back-illuminated camera that results in a  $0.82 \text{ deg}^2$  field of view. Data reduction is performed in real-time using the automated GIT pipeline. Photometric zero points were determined using the PanSTARRS catalogue, and PSF photometry was conducted with PSFEx (Bertin, 2011). In cases where sources exhibited a signif-

Trigger	Strategy	FAR [year <sup>-1</sup> ]	$p_{BNS}$	$p_{NSBH}$ prob.	HasNS prob.	HasRemnant prob.	HasMassGap prob.	Distance [Mpc]	Covered prob.	Area covered [deg <sup>2</sup> ]	g-band depth [AB mag]	latency [hr]
S230521k	Re-weighting	76	0.25	0.14	1.0	0.9	0.0	454	20%	1294	21.37	0.03
S230528a	Re-weighting	9	0.31	0.62	0.98	0.07	0.73	261	4%	315	20.92	3
S230615az	Re-weighting	4.7	0.85	0.0	1.0	1.0	0.01	260	31%	1063	21.25	11
S230729cj	No coverage	3.82	0.0	0.39	0.0	0.61	1.0	344	0%	—	—	—
S231029k	Re-weighting	93	0.68	0.0	1.0	1.0	0.46	571	36%	6836	19.28	0.23

Table 5.2: Summary of ZTF observations and GW properties for 5 GW events additionally followed-up with ZTF, with FAR > 1 year<sup>-1</sup>. Similarly to Table 5.1 we quote other quantities intrinsic to the GW event, such as the mean distance to the merger, the HasRemnant, and the HasMassGap parameters.

icant host background, we performed image subtraction using pyzogy (Guevel & Hosseinzadeh, 2017b), based on the ZOGY algorithm (Zackay et al., 2016).

**Liverpool Telescope** The images acquired with the Liverpool Telescope (LT) were taken using the IO:O (Steele et al., 2004) camera equipped with the Sloan *griz* filterset. These images underwent reduction through an automated pipeline, including bias subtraction, trimming of overscan regions, and flat fielding. Image subtraction occurred after aligning with a PS1 template, and the final data resulted from the analysis of the subtracted image.

### Spectroscopic Follow-up

**Palomar 60-inch:** Through Fritz, we can assign transients for spectroscopic follow-up with SEDM. The low-resolution ( $R \sim 100$ ) integral field unit (IFU) spectrograph is used to characterize sources brighter than 18.5 mag. The classification is done by running SNID (Blondin & Tonry, 2007b) and NGSF (Goldwasser et al., 2022) on the reduced spectra.

**Palomar 200-inch:** We observed ZTF candidates using the Palomar 200-inch Double Spectrograph (DBSP; Oke & Gunn 1982). The setup configuration involved 1 arcsec, 1.5 arcsec, and 2 arcsec slitmasks, a D55 dichroic, a blue grating of 600/4000, and a red grating of 316/7500. We applied a custom PyRAF DBSP reduction pipeline (Bellm & Sesar, 2016a) to process and reduce our data.

### Additional ZTF triggers

Throughout O4a, ZTF covered the region of events detected with a FAR > 1 year<sup>-1</sup>. We triggered observations for S230521k, S230528a, S230615az, S230729cj, and S231029k.

S230521k

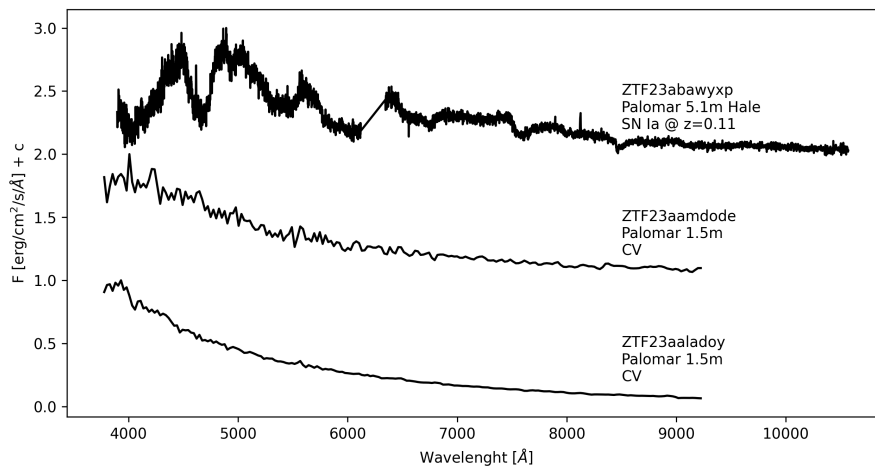


Figure 5.11: Spectra of the counterpart candidates taken during O4a.

S230521k had a source classification with 25% probability of it being a BNS system and 14% being a NSBH system but had a high FAR of  $76 \text{ year}^{-1}$ . S230521k properties did not merit a targeted search, thus we re-weighted the nominal ZTF schedule. The observations spanned a total area of  $1294 \text{ deg}^2$ , covering 20% of the total probability. The first serendipitous observation was taken around  $\sim 5$  minutes after the GW event. The median seeing during the observations is  $\sim 2$  arcsec, and limiting magnitudes of the first night are  $g = 21.37$  and  $r = 21.42$  mag. Based on the first two nights of observations, 13 candidates passed our automatic and manual inspection and upon further monitoring, none of them showed any promising nature (Ahumada et al., 2023c; Swain et al., 2023). Details of the candidates along with the rejection criterion are presented in Table 5.3.

### S230528a

S230528a was issued with a 40% probability of it being an NSBH system and 20% probability for a BNS system with a FAR of  $9 \text{ year}^{-1}$ . Observations included the re-weighting of the ZTF public fields for coverage and the first observation was taken  $\sim 3$  hours after the GW alert. The observations during the first two days which covered  $315 \text{ deg}^2$  and 4% of the total probability. The median limiting magnitudes for the first night of observations was  $g = 20.92$  and  $r = 21.09$  mag. During the real-time search, we found four candidates (Ahumada et al., 2023d). However, forced photometry on the archival ZTF data and ATLAS data revealed fainter detections

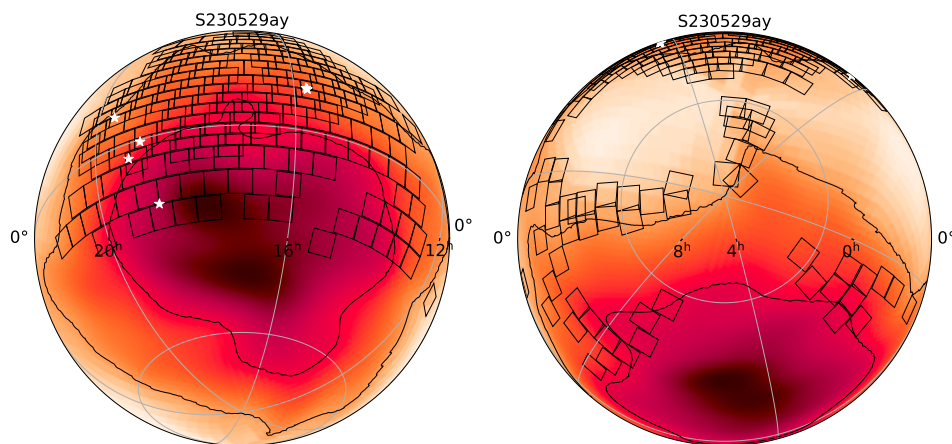


Figure 5.12: Localization of the high-significance event S230529ay, overplotted with the ZTF tiles and the 90% probability contour.

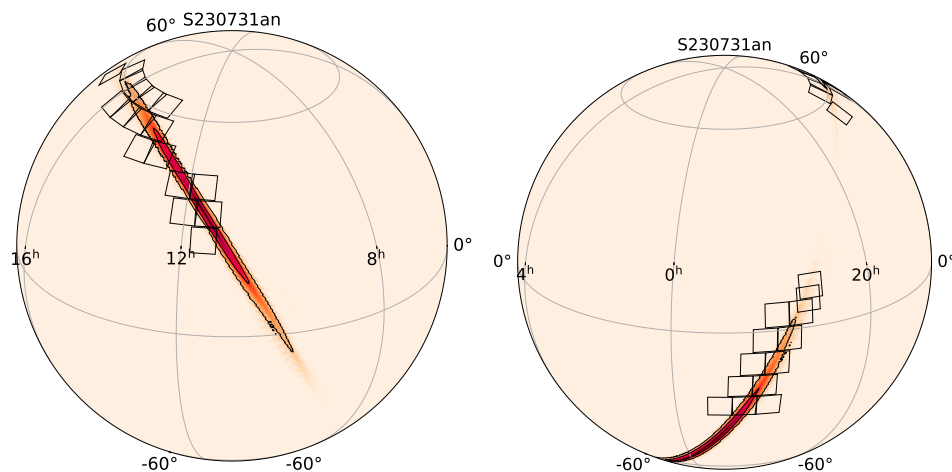


Figure 5.13: Localization of the high-significance event S230731an, overplotted with the ZTF tiles and the 90% probability contour. We show the candidates discovered in the region as white stars. We note that even though we covered  $\sim 2500 \text{ deg}^2$ , the total enclosed probability is only 7%.

in two candidates that predated the GW event and the other two showed flat evolution inconsistent with the expectations for KN emission, so none of the candidates survived for further follow-up (see Table 5.3).

### S230615az

S230615az was classified as a probable BNS event with 85% probability and a FAR of  $\sim \text{four year}^{-1}$ . The initial 90% probability area covered  $\sim 4400 \text{ deg}^2$ . The ZTF strategy for this event relied on the re-weighting of the nominal ZTF fields, cover-

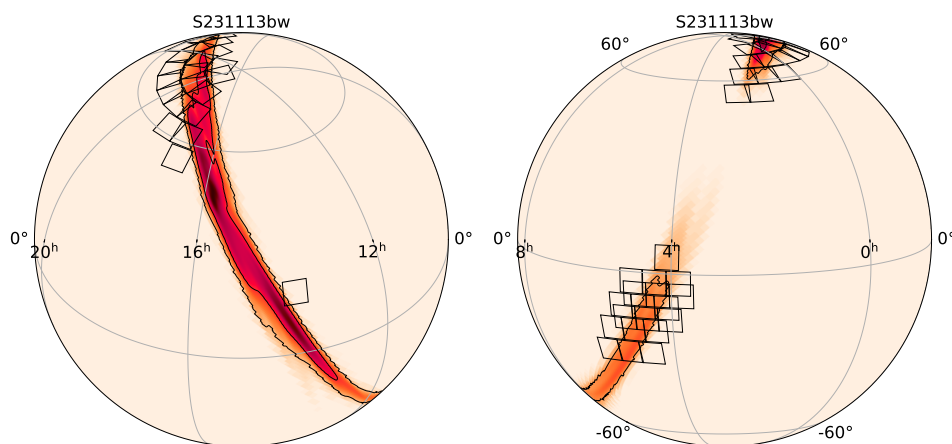


Figure 5.14: Localization of the high-significance event S231113bw, over plotted with the ZTF tiles and the 90% probability contour. No candidates were found in this region.

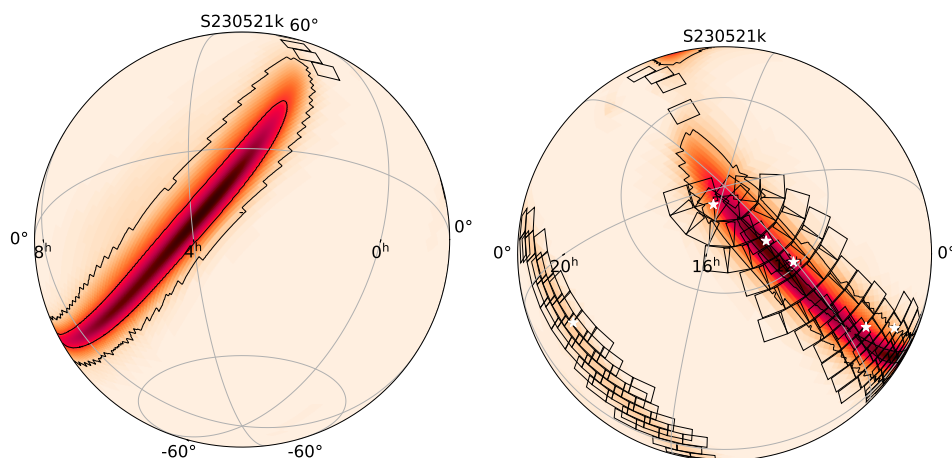


Figure 5.15: Localization of S230521k, overplotted with the ZTF tiles and the 90% probability contour. We show the candidates in the region as white stars.

ing in total 31% of the region. While most of the probability lied in two southern lobes, ZTF was able to observe  $\sim 1063 \text{ deg}^2$ . We found two candidates, but both of them had pre-detections  $\sim 11$  days before the GW trigger. No candidates were selected for further follow-up. Additionally, GOTO found a candidate counterpart to the GW event with an L band magnitude of  $19.43 \pm 0.08$  (Gompertz et al., 2023), but forced photometry on ZTF data revealed that this candidate had a  $g$ -band detections 36 hours before the GW trigger and hence we ruled it out (see Table 5.3 for details). Observations with LBT classified the GOTO transient as a SN Ia (Maiorano et al., 2023). GIT obtained multiple 300-sec exposures in the  $r$  filter by starting to observe

6 min after the GW event, and was able to cover 0.4% of the skymap. GIT found two interesting candidates that passed the cross-checks with Minor Planet Catalog (MPC) — GIT230615aa and GIT230615ab (Kumar et al., 2023). GIT230615aa was later rejected as an interesting candidate due to deep upper-limits reported (Strausbaugh et al., 2023) soon after the first detection.

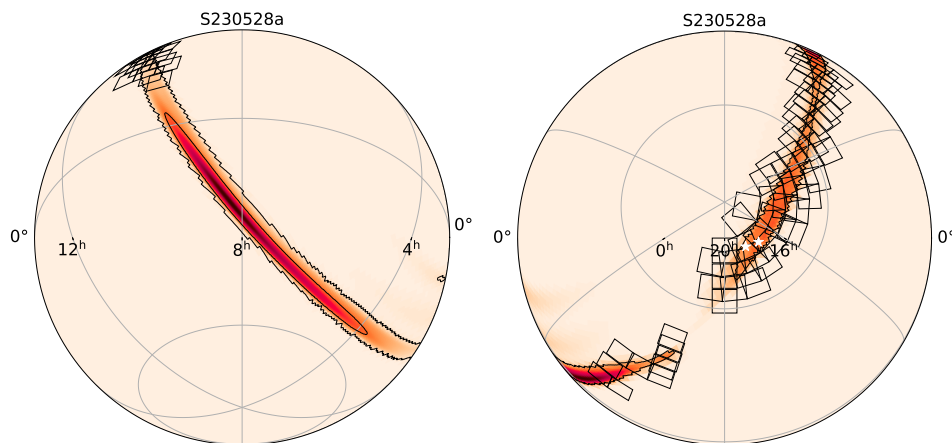


Figure 5.16: Localization of S230528a, overplotted with the ZTF tiles and the 90% probability contour. We show the transients consistent with KNe candidates as white stars.

### **S230729cj**

This event had a FAR of  $3.8 \text{ year}^{-1}$ , however, the region was almost entirely behind the Sun and the ZTF coverage was of only 2% of the skymap. Hence, we recovered no candidates.

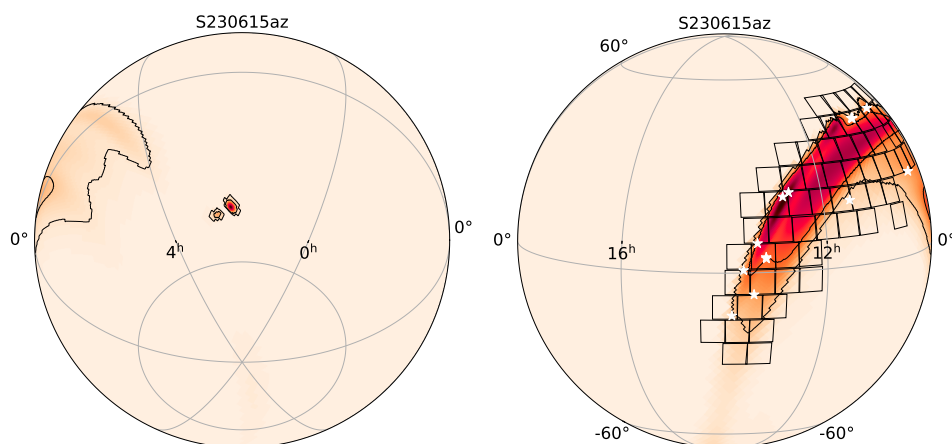


Figure 5.17: Localization of S230615az, overplotted with the ZTF tiles and the 90% probability contour. We show the candidates as white stars.

### S231029k

S231029k, with a relatively high FAR of  $93 \text{ year}^{-1}$ , was detected by the *spair* pipeline (Guo et al., 2018) and was initially classified as a likely BNS (68%), with a terrestrial probability of 32%. The 90% credible level of the skymap covered  $\sim 14968 \text{ deg}^2$ , primarily in the southern hemisphere. Our serendipitous observations started about 15 min after the GW event and covered about 36% ( $\sim 6836 \text{ deg}^2$ ) of the latest skymap. The first night of observations reached magnitude limits of 19.3 mag in the *g* band and 19.5 in the *r* band. No candidates passed our filters.

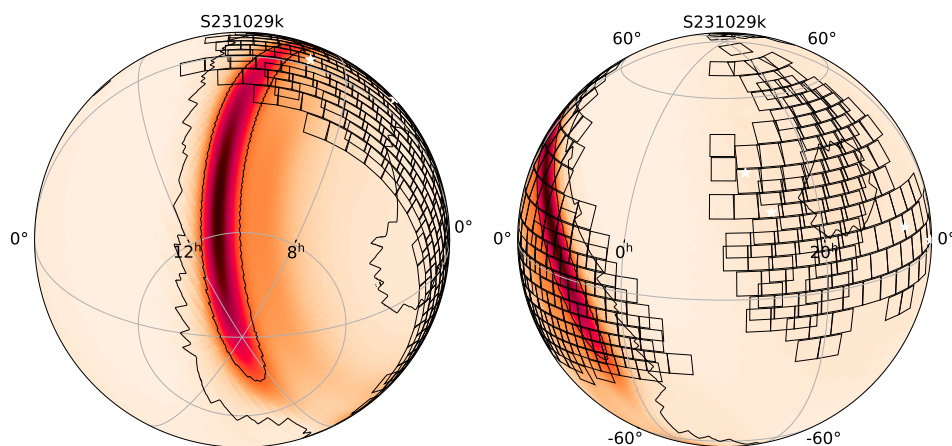


Figure 5.18: Localization of S231029k, overplotted with the ZTF tiles and the 90% probability contour. We show the candidates as white stars.

Event	Candidate	RA [hhmmss]	DEC [ddmmss]	Discovery timea (hours)	Discovery mag. (AB magnitude)	Redshift	Rejection criterion	
Candidates for the <i>High-significance events</i> : FAR < 1 year <sup>-1</sup>								
S230529ay	ZTF23aamnpce	15h43m56.1s	+15d13m29.3s	11.47	$r=20.49\pm0.23$	0.227	Inconsistent with GW distance	
	ZTF23aamnowb	15h45m31.2s	+15d39m03.5s	11.47	$r=18.95\pm0.28$		Slow evolution	
	ZTF23aamnsjs	18h40m49.0s	-20d39m35.6s	14.77	$g=19.20\pm0.14$	Flat evolution		
	ZTF23aamnycd	19h34m57.5s	+11d15m58.8s	15.21	$g=19.28\pm0.15$	Slow evolution		
	ZTF23aamoaji	18h57m55.6s	-0d37m42.5s	15.25	$g=20.15\pm0.20$	Likely galactic		
ZTF23aamnwln	19h13m03.8s	-4d53m51.1s	15.34	$g=19.93\pm0.13$	Flat evolution			
S230627c	ZTF23aaptuhp	10h34m41.1s	+45d25m31.3s	2.23	$g=20.34\pm0.17$	0.15	Slow evolution	
	ZTF23aaptssn	10h21m11.3s	+31d18m05.6s	2.41	$g=20.91\pm0.18$		Slow evolution	
	ZTF23aapwrrwg	10h29m03.6s	+38d44m34.6s	2.49	$g=20.88\pm0.18$	0.577	Slow evolution	
	ZTF23aaptsuy	10h40m48.5s	+41d58m05.3s	2.49	$g=20.2\pm0.11$	Slow evolution		
	ZTF23aaptaw	10h58m45.5s	+60d57m16.4s	2.67	$g=21.12\pm0.19$	0.254	Slow evolution	
	ZTF23aaptudb	11h06m13.5s	+78d33m34.7s	2.75	$g=21.03\pm0.27$	0.188	Slow evolution	
	ZTF23aapdtga	10h46m32.1s	+57d08m54.8s	3.23	$r=21.33\pm0.22$	0.678	Slow evolution	
	ZTF23aaptusa	10h48m10.6s	+71d50m29.1s	3.89	$g=21.32\pm0.2$	0.175	Slow evolution	
	ZTF23aapwtcp	10h49m43.9s	+71d24m34.0s	4.03	$r=21.22\pm0.25$	0.918	Slow evolution	
	Candidates for the <i>Other ZTF triggers</i> : FAR > 1 year <sup>-1</sup>							
S230521k	ZTF23aaladoy	18h40m43.9s	+27d01m24.8s	3.32	$g=15.56\pm0.03$	0.145	Featureless spectrum long-lived (~ 200days).	
	ZTF23aalcvpw	11h33m53.2s	+29d11m37.8s	23.22	$r=20.36\pm0.26$		Pre-detections	
	ZTF23aalczje	12h29m02.8s	+70d51m01.8s	23.26	$r=20.19\pm0.29$	0.201	Slow evolution	
	ZTF23aalkyfsk	12h03m33.6s	+61d23m17.2s	23.94	$g=20.41\pm0.19$	Slow evolution		
	ZTF23aaldkog	17h03m21.3s	+83d56m32.9s	24.24	$g=20.60\pm0.25$	Quasar		
S230528a	ZTF23aamgkz	17h16m51.2s	+75d27m22.8s	3.27	$g=19.24\pm0.11$	0.105	Slow evolution	
	ZTF23aamlhjz	18h17m47.0s	+76d20m35.1s	31.26	$r=20.74\pm0.31$	Slow evolution		
S230615az	GOTO23hu	13h22m55.2s	+08d09m49.5s	-36.7	$g=20.72\pm0.19$	0.095	Pre-detections	
	GIT230615aa	12h50m03.64s	+20d45m21.77s	0.67	$r=20.05\pm0.06$		Asteroid	
	GIT230615ab	12h42m11.65s	+22d03m25.09s	1.05	$r=19.81\pm0.05$	Not rejected		
	ZTF23aaocrh	10h19m00.1s	+41d53m02.8s	11.98	$g=20.12\pm0.31$	Slow evolution		
	ZTF23aaocgns	10h17m01.7s	+41d44m38.9s	11.98	$g=20.05\pm0.22$	Slow evolution		
	ZTF23aaonoan	11h21m35.9s	+18d24m26.8s	12.06	$g=20.27\pm0.25$	Slow evolution		
	ZTF23aaooaro	13h13m14.5s	+3d53m10.4s	12.53	$g=20.21\pm0.22$	Slow evolution		
	ZTF23aaooarp	13h13m29.2s	+4d13m31.1s	12.53	$g=20.72\pm0.32$	Slow evolution		
	ZTF23aaocreh	13h51m44.2s	-12d14m51.7s	12.66	$g=19.27\pm0.21$	Slow evolution		
	ZTF23aaoiixv	9h06m17.9s	+22d29m45.7s	34.23	$r=18.86\pm0.19$	Slow evolution		
	ZTF23aaoiimy	9h16m15.1s	+43d23m41.3s	34.52	$r=18.52\pm0.11$	Slow evolution		
	ZTF23aaonttd	13h27m02.9s	-6d10m06.6s	59.76	$r=19.78\pm0.18$	Slow evolution		
	ZTF23aaoorce	13h38m54.1s	+0d45m34.0s	59.77	$r=20.16\pm0.21$	Slow evolution		
	S231029k	ZTF23abnswdx	6h37m33.6s	+18d16m39.2s	6.34	$r=19.29\pm0.18$	0.074	Slow evolution
		ZTF23aboahri	16h24m19.9s	+1d43m55.8s	20.51	$r=17.97\pm0.28$		Slow evolution
ZTF23abnxbcg		8h42m41.8s	+4d34m02.2s	30.56	$r=18.93\pm0.17$	Slow evolution		
ZTF23aboaisu		17h48m33.8s	+11d34m10.8s	68.79	$r=18.86\pm0.12$	Slow evolution		
ZTF23aboaiui		21h02m41.4s	+24d07m28.7s	69.85	$g=20.0\pm0.22$	Slow evolution		
ZTF23aboapns		21h31m33.2s	+35d42m43.5s	69.87	$g=19.45\pm0.2$	Slow evolution		

aTime relative to the GW event.

Table 5.3: Properties of the candidates that passed manual inspection and their rejection criteria for six of the followed-up LVK events. There are 15 candidates from the follow-up of *High-significance events* (FAR < 1 year<sup>-1</sup>), and 27 candidates for the *Other ZTF triggers* with FAR > 1 year<sup>-1</sup>.

## Candidates from ZTF searches

In this section we summarize all the candidates analyzed during the O4a searches. We include transients not originally detected with ZTF, but later ruled out by us.

## Regression

We develop a Random Forest (RF) regressor to predict kilonova properties using low-latency gravitational wave data.

- We adopt simulations from (Weizmann Kiendrebeogo et al., 2023) as our training dataset. This includes 1189 simulated compact binary coalescences that passed detection criteria for O4. The simulations include binary distance, sky position, p-astro, FAR, and an area of 90% sky localization that we include in our features.

- We compute EM-bright<sup>12</sup> classifications (HasNS, HasRemnant, and HasMassGap) for the simulated data above to include as features.
- We generate the light curves for each of the simulated events using the nuclear multi-messenger astronomy (NMMA)<sup>13</sup> framework, which relies on the POSSIS model (Bu2019km; Bulla 2019; Dietrich et al. 2020b). We restrict our analysis to simulations with peak magnitudes  $> 18$  mag for  $r$  filter. We use the peak of the light curve in  $g$  and  $r$  filters as target.
- We use the features and target (the information from the GW simulated events and the predicted peak magnitude) to train a RF regressor. To make sure that the scale and measurement units were consistent throughout the training dataset, we applied StandardScaler. The data is separated into two groups: an 80/20 ratio is used for training and testing, while a 70/30 ratio is used for validation. We obtain an MSE of 0.25 and an  $R^2$  of 0.76 and an MSE of 0.14 and an  $R^2$  of 0.82 in the  $g$ -band and  $r$ -band for our test data, respectively.
- For the events included in this paper (see Table 5.1), we collect the necessary features (FAR, area(90), distance, longitude, latitude, HasNS, HasRemnant, HasMassGap, and P-astro) and use these to predict the peak magnitude using our RF model. The analysis was conducted offline, after the manual candidate vetting was completed.

Our main finding is the estimated peak magnitude for a KN associated with S230627c. Our model predicts a KN peaking at 21.61 mag in the  $r$ -band and 22.16 mag in the  $g$ -band. According to Table 5.3, ZTF23aapdtga is 21.80 mag in the  $g$ -band and 21.33 mag in the  $r$ -band, making this candidate consistent with our predictions within  $3\sigma$ . No other candidate for any other GW event was within  $3\sigma$  of the predicted peak.

We expect our RF model to have improved performance with larger and more representative training data, and we look forward to including our predictions to aid in real-time searches.

---

<sup>12</sup><https://pypi.org/project/gwemopt>

<sup>13</sup><https://nuclear-multimessenger-astronomy.github.io/nmma/fitting.html>

Trigger	FAR	$p_{BNS}$	$p_{NSBH}$	$p_{BBH}$	$p_{Terrestrial}$	HasNS	HasRemnant	HasMassGap
<i>High-significance: FAR &lt; 1 year<sup>-1</sup></i>								
S230518h	0.01	0.0	0.86	0.04	0.1	1.0	0.0	0.0
S230529ay	0.01	0.31	0.62	0.0	0.07	0.98	0.07	0.73
S230627c	0.01	0.0	0.49	0.48	0.03	0.0	0.0	0.14
S230731an	0.01	0.0	0.18	0.81	0.0	0.0	0.0	0.0
S231113bw	0.43	0.0	0.17	0.79	0.04	0.02	0.0	0.04
<i>Other ZTF triggers</i>								
S230521k	76.34	0.25	0.14	0.0	0.6	1.0	0.9	0.0
S230528a	9.58	0.2	0.44	0.0	0.36	1.0	0.02	0.97
S230615az	4.7	0.85	0.0	0.0	0.15	1.0	1.0	0.01
S230729cj	3.82	0.0	0.39	0.0	0.61	1.0	0.0	0.86
S231029k	93.5	0.68	0.0	0.0	0.32	1.0	1.0	0.46
<i>Not followed with ZTF</i>								
S230615i	411.95	0.02	0.2	0.0	0.78	1.0	0.0	0.06
S230617bc	55.43	0.27	0.07	0.0	0.66	1.0	1.0	0.02
S230618ba	81.1	0.0	0.29	0.14	0.57	0.73	0.0	0.52
S230619aa	248.48	0.36	0.02	0.0	0.62	1.0	0.82	0.55
S230619bd	608.9	0.18	0.0	0.0	0.81	1.0	1.0	0.46
S230620ad	197.28	0.0	0.12	0.02	0.86	0.26	0.0	0.51
S230621ap	497.72	0.1	0.0	0.0	0.9	1.0	1.0	0.0
S230622br	101.94	0.0	0.36	0.1	0.54	1.0	0.0	0.06
S230623ad	80.08	0.49	0.0	0.0	0.51	1.0	1.0	0.0
S230624s	593.36	0.0	0.12	0.01	0.88	1.0	0.0	0.0
S230627v	339.99	0.17	0.0	0.0	0.83	1.0	1.0	0.0
S230627ay	213.68	0.0	0.22	0.03	0.75	1.0	0.0	0.58
S230627bj	245.72	0.0	0.12	0.04	0.84	1.0	0.0	0.0
S230629y	82.07	0.0	0.23	0.09	0.68	0.7	0.0	0.36
S230701z	509.73	0.0	0.12	0.02	0.86	0.82	0.0	0.13
S230703aq	596.07	0.14	0.0	0.0	0.86	1.0	1.0	0.0
S230704bf	312.88	0.12	0.0	0.0	0.88	1.0	1.0	0.01
S230705bd	528.13	0.19	0.0	0.0	0.81	1.0	1.0	0.0
S230706al	61.13	0.07	0.2	0.0	0.73	1.0	0.01	0.63
S230706bv	671.4	0.1	0.04	0.0	0.86	1.0	0.7	0.53
S230708y	317.51	0.18	0.0	0.0	0.82	1.0	1.0	0.46
S230708ay	694.89	0.14	0.0	0.0	0.86	1.0	1.0	0.52

S230708bf	314.04	0.1	0.01	0.0	0.88	1.0	1.0	0.56
S230708bv	167.08	0.0	0.29	0.05	0.66	0.54	0.0	0.12
S230709aq	127.88	0.0	0.16	0.16	0.68	0.13	0.0	0.23
S230709bj	358.29	0.0	0.22	0.13	0.64	0.82	0.0	0.06
S230711j	664.72	0.17	0.05	0.0	0.77	1.0	0.88	0.47
S230711aj	375.04	0.17	0.01	0.0	0.82	1.0	1.0	0.52
S230712ab	545.49	0.04	0.12	0.0	0.84	1.0	0.0	0.53
S230713s	674.74	0.0	0.13	0.0	0.86	1.0	0.0	0.0
S230713x	237.37	0.35	0.01	0.0	0.63	1.0	0.97	0.52
S230714i	89.78	0.2	0.39	0.0	0.41	1.0	0.0	0.31
S230715z	266.79	0.14	0.0	0.0	0.86	1.0	1.0	0.0
S230720a	402.07	0.04	0.1	0.0	0.85	1.0	0.0	0.67
S230721x	484.57	0.16	0.0	0.0	0.84	1.0	1.0	0.46
S230723bl	647.4	0.11	0.0	0.0	0.89	1.0	1.0	0.46
S230726al	355.31	0.0	0.14	0.09	0.76	0.62	0.0	0.02
S230727am	434.43	0.13	0.0	0.0	0.87	1.0	1.0	0.02
S230729p	66.91	0.41	0.0	0.0	0.59	1.0	1.0	0.46
S230729ae	484.22	0.11	0.0	0.0	0.89	1.0	1.0	0.02
S230729bl	719.23	0.03	0.17	0.0	0.8	1.0	0.0	0.06
S230729bv	385.66	0.2	0.0	0.0	0.8	1.0	1.0	0.46
S230729cf	439.08	0.04	0.17	0.0	0.79	1.0	0.0	0.38
S230730av	695.25	0.0	0.11	0.05	0.84	0.91	0.0	0.09
S230805k	594.66	0.12	0.0	0.0	0.88	1.0	1.0	0.0
S230805at	514.49	0.0	0.15	0.02	0.83	0.91	0.0	0.8
S230805ax	112.23	0.0	0.21	0.08	0.71	1.0	0.0	0.0
S230806f	130.82	0.16	0.0	0.0	0.84	1.0	1.0	0.0
S230810r	293.81	0.28	0.0	0.0	0.72	1.0	1.0	0.0
S230812bu	196.26	0.0	0.15	0.06	0.79	1.0	0.0	0.06
S230812cd	501.37	0.11	0.01	0.0	0.88	1.0	0.86	0.52
S230819f	495.6	0.05	0.13	0.0	0.82	1.0	0.0	0.4
S230819h	576.93	0.0	0.11	0.03	0.86	0.68	0.0	0.0
S230820bj	681.63	0.1	0.0	0.0	0.9	1.0	1.0	0.33
S230820bn	100.93	0.0	0.42	0.16	0.43	1.0	0.0	0.06
S230821e	413.82	0.01	0.14	0.0	0.85	1.0	0.0	0.15
S230823ay	158.96	0.0	0.31	0.03	0.66	1.0	0.04	0.0
S230824av	513.48	0.15	0.0	0.0	0.85	1.0	1.0	0.52

S230824ay	607.69	0.14	0.0	0.0	0.86	1.0	1.0	0.0
S230825bf	78.56	0.0	0.12	0.07	0.81	0.8	0.0	0.03
S230826ac	126.26	0.13	0.04	0.0	0.84	1.0	0.11	0.6
S230826al	61.85	0.43	0.0	0.0	0.57	1.0	1.0	0.46
S230826ba	615.77	0.21	0.0	0.0	0.79	1.0	1.0	0.07
S230827au	89.07	0.0	0.2	0.28	0.52	0.39	0.0	0.04
S230827bj	138.75	0.0	0.39	0.11	0.5	0.71	0.0	0.0
S230827bl	524.14	0.13	0.01	0.0	0.86	1.0	1.0	0.4
S230828ah	106.23	0.0	0.18	0.05	0.77	0.74	0.0	0.02
S230830g	105.68	0.0	0.12	0.08	0.8	0.18	0.0	0.41
S230830an	100.02	0.2	0.3	0.0	0.5	1.0	0.0	0.77
S230901h	322.3	0.2	0.0	0.0	0.8	1.0	1.0	0.46
S230902ak	589.69	0.0	0.14	0.03	0.82	0.65	0.0	0.13
S230903aw	353.71	0.21	0.01	0.0	0.79	1.0	1.0	0.33
S230903bk	297.01	0.0	0.15	0.21	0.64	0.27	0.0	0.03
S230904i	138.6	0.0	0.34	0.01	0.64	1.0	0.0	0.0
S230906al	202.08	0.0	0.26	0.09	0.65	0.79	0.0	0.35
S230907ap	512.92	0.0	0.16	0.01	0.83	0.97	0.14	0.0
S230907az	728.0	0.1	0.0	0.0	0.9	1.0	1.0	0.02
S230909an	277.05	0.15	0.0	0.0	0.85	1.0	1.0	0.29
S230910p	378.32	0.14	0.01	0.0	0.85	1.0	1.0	0.46
S230910ay	249.17	0.03	0.29	0.0	0.69	1.0	0.06	0.04
S230911am	162.54	0.25	0.05	0.0	0.7	1.0	1.0	0.02
S230912g	259.7	0.13	0.0	0.0	0.87	1.0	1.0	0.0
S230912y	153.36	0.16	0.02	0.0	0.82	1.0	1.0	0.07
S230918bq	253.07	0.0	0.13	0.09	0.78	0.61	0.0	0.06
S230918bu	201.7	0.11	0.01	0.0	0.88	1.0	1.0	0.0
S230919j	69.33	0.25	0.0	0.0	0.75	1.0	1.0	0.02
S230919m	94.0	0.0	0.16	0.01	0.84	1.0	0.08	0.01
S230920p	377.03	0.22	0.0	0.0	0.77	1.0	1.0	0.0
S230920bc	85.93	0.38	0.0	0.0	0.62	1.0	1.0	0.46
S230923f	566.72	0.11	0.0	0.0	0.89	1.0	1.0	0.0
S230924v	167.54	0.24	0.2	0.0	0.56	1.0	0.05	0.62
S230924ah	485.38	0.0	0.13	0.06	0.81	0.91	0.0	0.0
S230925ac	269.34	0.12	0.0	0.0	0.88	1.0	1.0	0.46
S230925au	89.14	0.23	0.19	0.0	0.57	1.0	0.2	0.53

S230925bx	96.48	0.44	0.0	0.0	0.56	1.0	1.0	0.56
S230928q	400.2	0.0	0.11	0.05	0.84	0.73	0.0	0.2
S230928am	249.42	0.0	0.25	0.06	0.69	0.7	0.0	0.03
S230928cc	239.25	0.0	0.13	0.03	0.84	0.65	0.0	0.09
S230930bt	536.97	0.1	0.0	0.0	0.9	1.0	1.0	0.33
S231003ab	574.58	0.0	0.21	0.07	0.72	0.94	0.0	0.06
S231003bg	97.4	0.0	0.15	0.12	0.74	0.82	0.0	0.03
S231004f	92.6	0.47	0.0	0.0	0.53	1.0	1.0	0.0
S231005bt	387.57	0.24	0.0	0.0	0.76	1.0	1.0	0.46
S231006c	498.88	0.0	0.22	0.07	0.71	0.91	0.0	0.1
S231006ac	341.4	0.0	0.11	0.15	0.74	0.23	0.0	0.03
S231010ak	364.29	0.11	0.01	0.0	0.88	1.0	1.0	0.52
S231013ai	114.44	0.03	0.42	0.0	0.55	1.0	0.0	0.05
S231013bo	502.53	0.21	0.0	0.0	0.79	1.0	1.0	0.0
S231014g	374.43	0.14	0.0	0.0	0.86	1.0	1.0	0.46
S231014w	374.3	0.13	0.03	0.0	0.84	1.0	1.0	0.02
S231014be	163.23	0.1	0.19	0.0	0.71	1.0	0.01	0.85
S231015g	290.21	0.25	0.01	0.0	0.74	1.0	1.0	0.0
S231015by	211.49	0.14	0.0	0.0	0.86	1.0	1.0	0.0
S231016br	220.42	0.0	0.16	0.06	0.78	0.82	0.0	0.01
S231017t	200.55	0.14	0.07	0.0	0.8	1.0	0.0	0.55
S231017z	259.76	0.27	0.05	0.0	0.68	1.0	1.0	0.0
S231018v	203.66	0.2	0.0	0.0	0.79	1.0	1.0	0.0
S231018ax	213.21	0.36	0.01	0.0	0.63	1.0	1.0	0.33
S231019ak	228.54	0.01	0.41	0.02	0.56	1.0	0.0	0.0
S231020br	519.02	0.13	0.05	0.0	0.82	1.0	0.72	0.53
S231021az	7.38	0.0	0.26	0.01	0.73	0.96	0.0	0.02
S231022bk	468.37	0.23	0.0	0.0	0.76	1.0	1.0	0.0
S231022bl	373.51	0.06	0.11	0.0	0.83	1.0	0.0	0.72
S231025a	29.42	0.59	0.0	0.0	0.41	1.0	1.0	0.0
S231025c	578.54	0.0	0.1	0.04	0.85	1.0	0.0	0.09
S231025r	498.2	0.11	0.0	0.0	0.89	1.0	1.0	0.46
S231025t	146.73	0.16	0.33	0.0	0.51	1.0	0.0	0.35
S231025az	551.51	0.17	0.0	0.0	0.83	1.0	1.0	0.02
S231026n	415.8	0.15	0.06	0.0	0.79	1.0	0.3	0.62
S231026z	361.62	0.16	0.01	0.0	0.83	1.0	0.85	0.52

S231027bk	498.81	0.2	0.0	0.0	0.8	1.0	1.0	0.0
S231028r	679.89	0.16	0.0	0.0	0.84	1.0	1.0	0.02
S231028ai	274.01	0.13	0.0	0.0	0.87	1.0	1.0	0.02
S231028aw	306.48	0.3	0.0	0.0	0.7	1.0	1.0	0.0
S231029e	444.94	0.22	0.0	0.0	0.78	1.0	1.0	0.27
S231029ai	160.69	0.0	0.46	0.04	0.5	1.0	0.0	0.0
S231029bd	281.51	0.22	0.0	0.0	0.78	1.0	1.0	0.0
S231030t	707.41	0.16	0.01	0.0	0.82	1.0	1.0	0.0
S231102i	185.19	0.29	0.16	0.0	0.55	1.0	0.98	0.03
S231104s	256.82	0.0	0.21	0.09	0.69	0.91	0.0	0.06
S231107a	410.49	0.21	0.0	0.0	0.78	1.0	1.0	0.0

Table 5.4: Compilation of all the 150 IGWN events that had either a probability of BNS ( $p_{BNS}$ ) greater than 0.1 or their probability of NSBH ( $p_{NSBH}$ ) greater than 0.1. We divide the events into *High-significance* ( $FAR < 1 \text{ year}^{-1}$ ), *Other ZTF triggers*, and *Not followed with ZTF*. The events we did not follow-up with ZTF all have  $FAR > 1 \text{ year}^{-1}$ , and were not used in the ZTF non-detection analysis. We additionally quote their FAR, their probability of BBH merger ( $p_{BBH}$ ), their terrestrial probability ( $p_{Terrestrial}$ ), and their publicly available properties `HasNS`, `HasRemnant`, and `HasMassGap`.

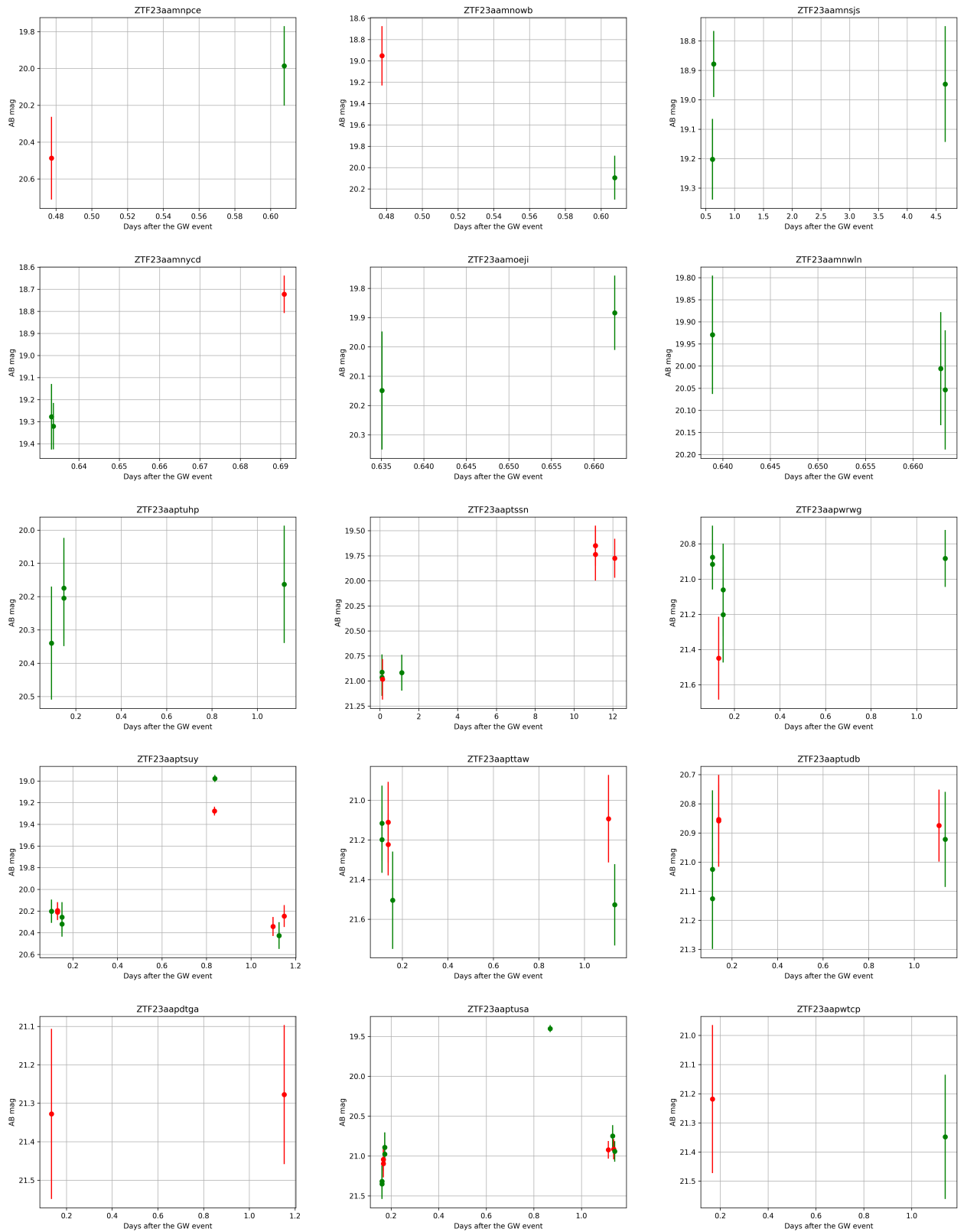


Figure 5.19: Light-curves for ZTF candidates found during O4a. These candidates correspond to the high-significant events S230529ay and S230627c.

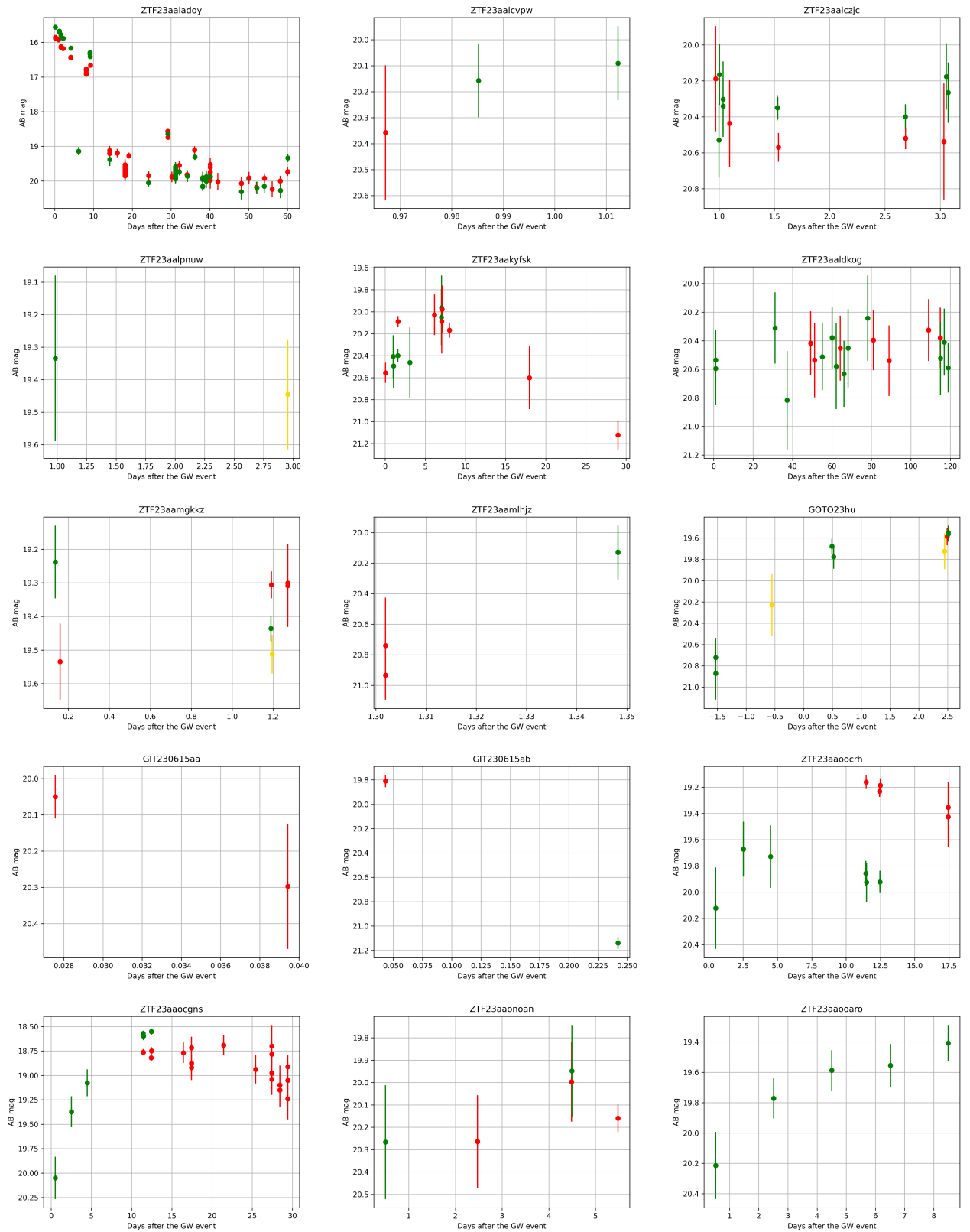


Figure 5.20: Light-curves for ZTF candidates found during O4a. These candidates correspond to the events S230521k and S230528a.

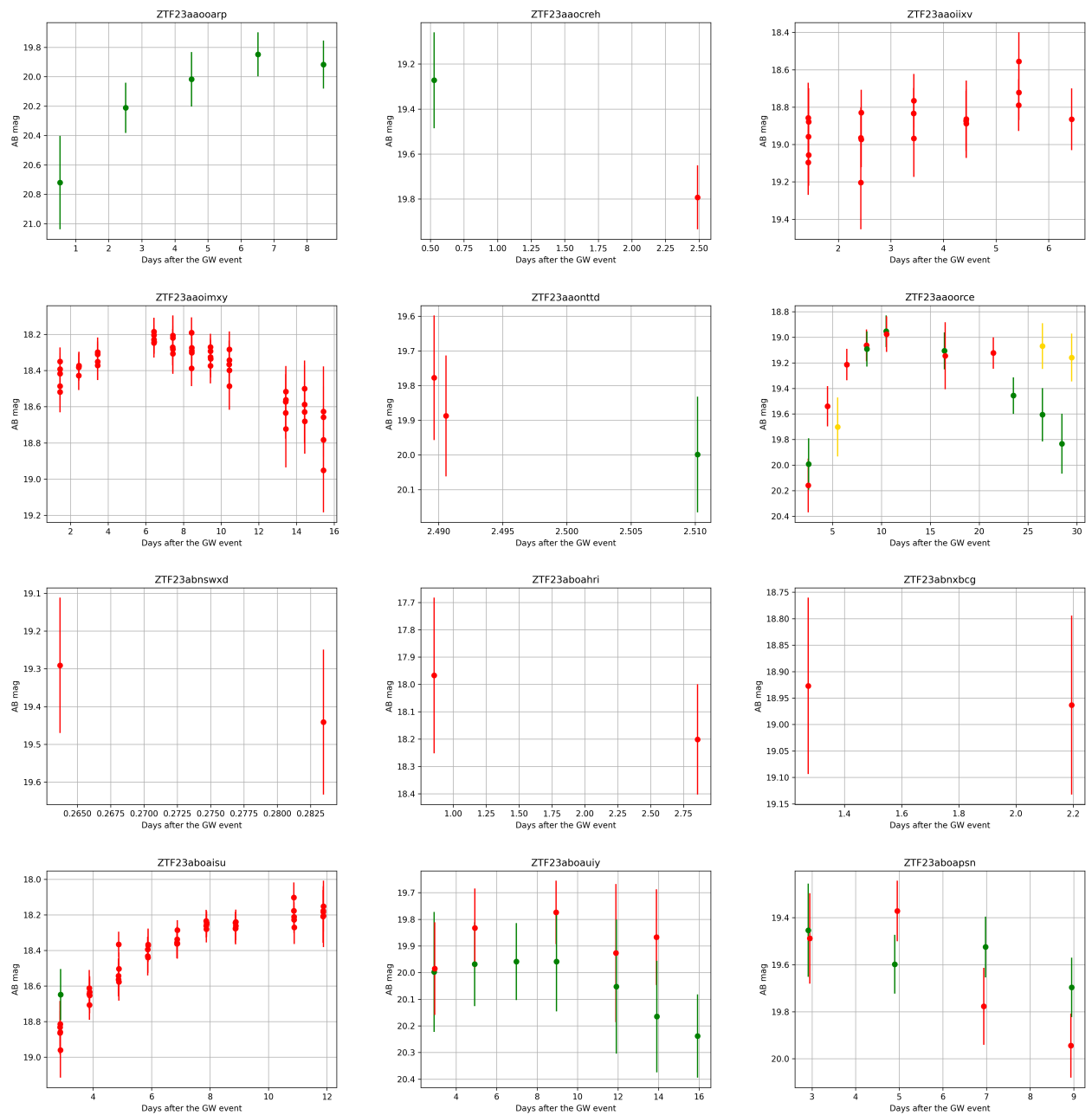


Figure 5.21: These candidates correspond to the events S230521k, S230528a and S231029k.

## *Chapter 6*

### LESSONS LEARNED AND FUTURE OUTLOOK

This PhD thesis began as an eyes-wide-open quest to broaden our understanding of  $r$ -process sites in general, and the bulk of our learning has come from non-detections. Our systematic follow-up of SNe Ic-BL discovered with ZTF revealed no compelling evidence of  $r$ -process production in collapsars. The extensive MMA search campaigns we conducted with ZTF during O3 (Kasliwal et al., 2020) and O4a (Ahumada & Anand 2024) yielded several KN candidates that were all successfully ruled out, resulting in no convincing KN counterpart. However, we have gained insights on 1) techniques for probing  $r$ -process production in neutron star mergers and collapsars, and 2) the nature of  $r$ -process sites in general.

#### 6.1 Collapsars

##### **Summary: $r$ -process production in SNe Ic-BL**

Well-cadenced, *concurrent* optical and NIR observations of SNe Ic-BL light curves are the only way to robustly detect  $r$ -process signatures in these SNe photometrically. Equally important are SN models with and without  $r$ -process and methods for fitting/model comparison. In our study (Anand et al., 2024), we conduct the first ever systematic photometric campaign to search for  $r$ -process production in SNe Ic-BL, and demonstrate a variety of metrics by which to assess whether the data shows any signatures of heavy elements (Chapter 2). However, our work is by no means the final word on  $r$ -process production in collapsars. Though we find no evidence for heavy element nucleosynthesis in the SNe we followed up, it is still possible that some subset of SNe Ic-BL do produce heavy elements, or that the quantity of  $r$ -process ejecta from each SN was too low for our observations (and those we analyzed from the literature) to constrain. Next, we discuss potential future studies of  $r$ -process from collapsars.

##### **Future Work: Constraining $r$ -Process from Collapsars**

The  $r$ -process question, as it pertains to collapsars, long GRBs, and SNe Ic-BL is a multi-faceted one. Over the past few years, this growing field has been fueled by both enigmatic discoveries and somewhat inconclusive non-detections. Following our work (Anand et al., 2024), Rastinejad et al. (2023) conducted a photometric

search with the Hubble Space Telescope for NIR excesses in the light curves of four GRB-SNe: GRB030329, GRB100316D, GRB130427A, and GRB190829A. The study found that while GRB190829A showed no evidence of  $r$ -process production, the remaining GRBs were consistent with either no enrichment, or producing  $r$ -process material in quantities between  $0.01 - 0.15 M_{\odot}$  for low amounts of mixing. These conclusions match those of our work, and do not provide strong evidence for or against  $r$ -process production in SNe Ic-BL.

Nebular-phase spectroscopy in the optical, but more critically in the near-IR wavelengths could lend direct evidence of heavy element nucleosynthesis in these SNe. For many of the ZTF objects in our sample, we obtained nebular-phase spectra with Keck I LRIS or late-phase spectra with Keck II NIRES; we plan to analyze these spectra in a future work in the context of  $r$ -process enrichment. The biggest challenge is in understanding how to theoretically model the observations. Spectroscopic signatures of  $r$ -process may be washed out or blended due to high velocities in the spectra, making clear emission lines difficult to identify. Furthermore, state-of-the-art nebular spectroscopic models with  $r$ -process for SNe Ic-BL currently do not exist. Recently, Blanchard et al. (2024) obtained nebular-phase spectra of GRB221009A, also known as the “B.O.A.T.” (Burns et al., 2023), with NIRSpec on the James Webb Space Telescope. They find no possible emission lines attributed to  $r$ -process production; the spectrum is consistent with that of a standard SN Ic-BL.

There have also been some puzzling discoveries in the past few years that have raised the question of whether compact binary mergers can give rise to long-duration GRBs. Rastinejad et al. (2022) discovered a potential “kilonova” associated with the long-duration GRB 211211A, identified via a faint NIR excess in the light curve relative to the afterglow emission. Many works have debated about whether this source could have arisen from a white dwarf–neutron star merger (Yang et al., 2022), a collapsar origin (Barnes & Metzger, 2023), reddening from dust (Waxman et al., 2022) or a kilonova (Kunert et al., 2024). More recently, Levan et al. (2024) obtained spectra of the long-duration GRB 230307A with JWST NIRSpec, finding Tellurium signatures that could be traced back to an  $r$ -process origin, which the authors argue is a KN. Both of these long GRBs had extended emission lasting several tens of seconds. The ambiguous origin of these particular long GRBs could have at least two possible explanations: 1) compact binary mergers powering relativistic jets that could last for several seconds (Gottlieb et al., 2023), or 2)  $r$ -

process-producing collapsars with peculiar properties that result in fast-fading SNe Ic-BL fainter than  $M \sim -17$  mag. One way to resolve the progenitor question is by crossmatching LGRBs (especially those with tails of extended emission) to GW sources during an IGWN observing run, as a long GRB with a merger origin would be seen by ground-based GW detectors. The soft X-ray mission Einstein Probe (Yuan et al., 2022), which came online this year, will help better characterize these long GRBs. Radio properties could also help distinguish between GRBs with a collapsar vs. merger origin.

Upcoming optical and IR surveys such as Rubin and Roman will unveil new populations of  $r$ -process transients associated with long GRBs, providing key insights into the nature of their progenitors. The increase in volume probed by Rubin will multiply the number of SNe Ic-BL discovered with and without GRBs that could be followed up with dedicated NIR telescopes. WINTER, a near-IR 1 sq. deg. survey telescope in Palomar observatory came online in early 2024 and is routinely following up ZTF transients as well as discovering new IR sources as a part of its survey operations (Lourie et al., 2020). Similarly, PRIME has been operating since 2023, but in the Southern Hemisphere. DREAMS will soon join WINTER as a NIR survey with similar capabilities, while NEWFIRM will complement DECam and Rubin as a NIR follow-up telescope in the Southern Hemisphere. The landscape of NIR astronomy will be enhanced by powerful future surveys, including Cryoscope, which will survey the sky in the K-dark filter, and the Nancy Grace Roman Space telescope (Roman), which will reach unprecedented depths of  $J \approx 27 - 28$  mag in its supernova survey. Detailed observations of SNe Ic-BL with and without GRBs in the optical and NIR bands will shed light on whether or not collapsars synthesize  $r$ -process elements.

## 6.2 Neutron Star Mergers

### Summary: Binary Neutron Star Mergers

Under good weather conditions, KNe from BNS mergers will be within reach of ZTF's limiting magnitudes in 300 s exposures ( $m_{AB} \approx 22$  mag). Since the discovery of GW170817, there has only been one other high-significance BNS merger discovery (GW190425; Abbott et al. 2020a). ZTF undertook a thorough search campaign for a KN counterpart within the colossal ( $\sim 7500$  sq. deg.) localization of GW190425, but ultimately did not find a convincing KN counterpart (Coughlin et al., 2019a). Tens of other facilities conducted searches of the localization; amongst those, ZTF, ATLAS, and GOTO-4 covered the largest fractions of the

probability region (Coulter et al., 2024). We eagerly await the next well-localized BNS merger detection in O4, which will provide exciting prospects for a joint KN discovery.

In Kasliwal et al. (2020), Mohite et al. (2022) and Ahumada & Anand (2024), we focus on model-agnostic approaches to gauge ZTF’s sensitivity to KNe based on observational campaigns. We also constrain the KN luminosity function under different assumptions for the evolution of the KN over the first few days following the merger. Unsurprisingly, our `nimbus` and `simsurvey` analyses indicate that combined ZTF observations over all GW search campaigns are most sensitive to rising KNe brighter than  $M \sim -17.5$  mag. Our joint luminosity function constraints have only just begun to constrain the bright end of the KN model space (see Chapter 5). With nine more bona-fide GW follow-up campaigns covering >90% of the localization to a depth of  $M \sim -16$  mag, ZTF could constrain the maximum fraction of GW170817-like KNe to  $< 25\%$ . Our targeted follow-ups of GW events with ZTF along with observations from regular survey operations have constrained the rate of GW170817-like KNe to  $R < 900 \text{Gpc}^{-3} \text{yr}^{-1}$ , and will continue to provide independent constraints on the rate of KNe from BNS mergers.

### **Summary: Neutron Star-Black Hole Mergers**

LIGO’s third observing run served as the very first confirmation of the existence of NSBH mergers. The first NSBH merger candidate, GW190426, was detected near the start of O3 (Abbott et al., 2023). Following that, O3 yielded two confident NSBH merger detections (GW200105 and GW200115; Abbott et al. 2021) and one mass-gap event that could be a NSBH or a BBH merger (GW190814; Abbott et al. 2020b). So far, O4 has yielded one published NSBH merger discovery (GW230529; The LIGO Scientific Collaboration and the Virgo Collaboration and the KAGRA Collaboration 2024) and another high-significance NSBH merger candidate (S240422ed; LIGO Scientific Collaboration et al. 2024a). Each LIGO detection has prompted extensive EM follow-up campaigns.

Depth, red sensitivity, and well-cadenced observations (spanning a week after the merger) are key to placing constraints on NSBH KN models. One of the deepest and most thorough search campaigns of an NSBH merger was that of GW190814 with the Dark Energy Camera (Andreoni et al., 2020; Morgan et al., 2020). DECam fully targeted its small localization (23 sq. deg.) in the  $i$ - and  $z$ -bands, reaching median depths of  $m_{\text{AB}} \approx 22-23$  mag over the course of six nights. However, further

analysis of GW190814 revealed that it was either a binary black hole merger or a NSBH merger with an extreme mass ratio of  $q \sim 0.11$ , in which the neutron star was likely swallowed whole, yielding no EM counterpart in either scenario (Abbott et al., 2020b). GW200105 and GW200115, on the other hand, had higher mass ratios of  $q \sim 0.22$  and  $q \sim 0.26$ , respectively, and therefore were more promising in terms of EM counterpart prospects (Abbott et al., 2021). Our work (Anand et al., 2020a), building on that of Andreoni et al. (2020), shows that the median upper limits from ZTF can rule out NSBH KNe with the largest ejecta masses at the closest distances within the observed region of the skymap for GW200115 (Chapter 4). These constraints correspond to polar KN viewing angles. We repeated this analysis for GW230529, expected to have produced a detectable EM counterpart based on its component masses (The LIGO Scientific Collaboration and the Virgo Collaboration and the KAGRA Collaboration, 2024) for which we can similarly rule out KNe with polar viewing angles at the median- $1\sigma$  GW distance, within our ZTF observed region (Ahumada & Anand 2024). With deeper observations, meter-class optical facilities like ZTF can place independent constraints on the mass ratio of the system, the radius of the neutron star, and the maximum aligned component of the black hole spin. Together with GW analyses, these EM observations provide valuable insights into the nature of NSBH merger systems.

### **S240422ed**

O4b has so far yielded one high-significance GW event candidate: S240422ed, an NSBH merger candidate ( $p_{\text{NSBH}} > 99\%$ ) at a distance of  $188 \pm 43$  Mpc, and localized to 272 sq. deg. (LIGO Scientific Collaboration et al., 2024a,b). Both ZTF and DECam triggered observations, since the event was localized mostly to the Southern Hemisphere. With ZTF, we covered 70% of the localization (which reduces to 49% accounting for losses due to chip gaps and lack of references) to a median  $r$ -band depth of 20.6 mag over two nights and found no compelling candidates. DECam covered 80% of the localization to a median depth of  $\sim 22.5$  mag, yielding several tens of candidates, which have since been ruled out through follow-up observations.

Given the lack of a KN counterpart discovery, we can factor in our ZTF observations of S240422ed into the luminosity function constraints discussed in Chapter 5. We add an approximate luminosity function constraint using the median depth and total probability coverage from ZTF for all events in O3+O4a, with and without the inclusion of S240422ed (golden curves in Figure 6.1). The inclusion of S240422ed improves our luminosity function constraint by  $\sim 10\%$ . This preliminary calculation

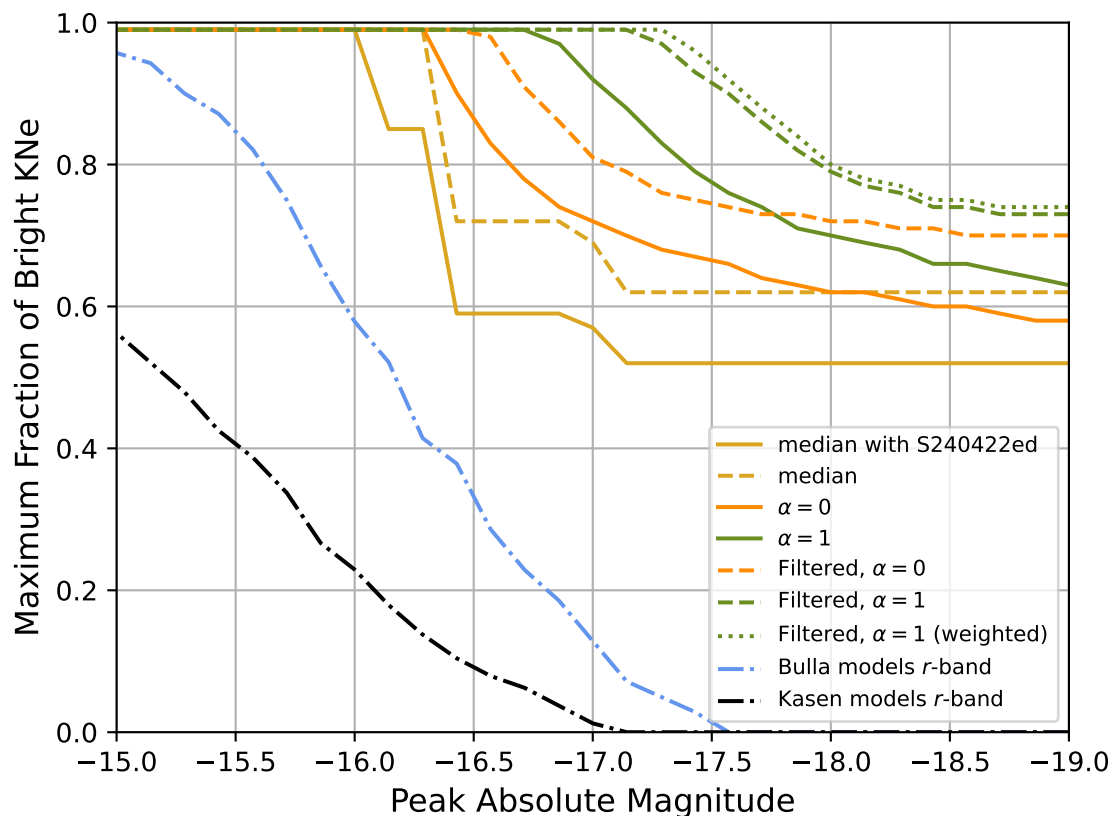


Figure 6.1: Luminosity function from O4a, updated with the inclusion of S240422ed.

indicates that a handful of additional ZTF follow-ups of better localized GW events, now that Virgo is online, will significantly improve our KN luminosity function constraints by the end of O4.

### Machine Learning KN Classifier

During the Rubin era, elevating a KN detection to a confident *discovery* will require sophisticated systems to coordinate follow-up to confirm the nature of the transient. As such, during O4, our team has access to an ecosystem of photometric and spectroscopic resources including Palomar and Keck, and has ongoing programs at Las Cumbres Observatory (PI: Anand), SOAR (PI: Anand), and Gemini. However, the problem of resource allocation is non-trivial. Each search campaign we conducted during O3 with ZTF and the Dark Energy Camera (DECam) yielded candidates

with single detections, missing color information, and lack of evolution rate constraints that we could only rule out after long-term monitoring. Without adequate follow-up, discerning the nature of such candidates in real-time is nearly impossible. Even for candidates whose photometric evolution or colors are consistent with KNe, the decision of *which* follow-up resources to assign and *when* to assign them is a manual process subject to human error.

The first step of solving this problem is to build a robust kilonova classifier. So far, we have created a training dataset for KNe and their common impostors (i.e., GRB afterglows, core-collapse SNe, SNe Ia, CVs, AGN, etc.) using a suite of models implemented in NMMA, sampled at ZTF’s target-of-opportunity and nominal cadence. The KNe are simulated using the IGWN Observing Scenarios (Weizmann Kiendrebeogo et al., 2023) mass distributions along with their GW skymaps. I am building a KN classifier based on an encoder-decoder Long Short Term Memory (LSTM) architecture, which is a type of recurrent neural network. LSTMs can automatically learn features from sequential data and support multi-variate input and output arrays. After imputing missing values and zero-padding the simulated transient light curves, I train the LSTM model on our simulated dataset. Currently, I am working on producing light curve reconstructions using the LSTM, which we will then pass through a simple classifier to output the probability of a given transient in the dataset being a KN. I plan to also incorporate skymap information for the KNe in our dataset in a separate convolutional neural network that will comprise another component of our machine learning model, to see whether skymap information can aid in the ranking KNe with higher probabilities compared to its common impostors. We intend to test out the classifier on real candidates discovered during EMGW observing campaigns to test its effectiveness in identifying potential fast-fading KN candidates. Eventually, we aspire to develop an automatic pipeline for resource allocation that will rely on the KN classifier and incorporate the “cost” of each observation into the decision-making process for assigning follow-up resources. Such classification and resource-allocation pipelines will be essential for KN discovery especially in the Rubin era.

### **O5: ToOs with Rubin**

Looking ahead, IGWN’s fifth observing run, O5, promises BNS and NSBH mergers localized to better than 100 sq. deg (Weizmann Kiendrebeogo et al., 2023). The Vera C. Rubin Observatory (Rubin), expected to begin operations in October 2025, will be one of the very few optical facilities capable of tiling GW localizations of

this size and achieving a sufficient depth to detect KNe to  $\sim 700$  Mpc, commensurate to the median luminosity distance out to which the IGWN will detect BNS mergers. Rubin will be allocating 3% of its time over the course of the 10 year LSST survey for target-of-opportunity (ToO) observations. In March 2024, astronomers gathered at University of California, Berkeley, to draft recommendations for how to use Rubin’s ToO time allocation. I had the opportunity to participate in this workshop and help draft recommendations for the follow-up of BNS and NSBH mergers. The Rubin ToO 2024 workshop recommendations have since been published on the official website.

Based on the IGWN official observing scenarios (Weizmann Kiendrebeogo et al., 2023), we expect  $\sim 18$  BNS mergers and up to 4 NSBH mergers per year, with false alarm rates  $< 1 \text{ yr}^{-1}$  to be localized to  $< 100 \text{ sq. deg}^1$ . Approximately one-third of these mergers will be observable with Rubin, corresponding to 6 BNS mergers and up to 2 NSBH mergers per year of O5. For these “gold” events, the baseline strategy is for Rubin to obtain four consecutive nights of observations. On the first night following the trigger (*night 0*), Rubin would cover the GW localization three times in *gri* filters using 120 s exposures. On the following nights (1, 2, and 3), the recommendation is for Rubin to tile the localization once in the *ri* filters with 180 s exposures. The fourth night of observations (*night 3*) will only take place if no KN counterpart is identified by *night 2*. This strategy maximizes the discovery space for KNe on the first night of observations and prioritizes deeper observations in two of the same filters on subsequent nights to eliminate contaminants and catch fast-fading counterparts (see Figure 6.2 for a summary of the strategies outlined). In case O5 yields mostly poorly localized (area  $\gtrsim 100 \text{ sq. deg.}$ ) mergers, as in previous observing runs, Rubin could trigger on these “silver” GW events localized to  $< 500 \text{ sq. deg.}$  In this case, the strategy will be to scan the skymap in two filters (*gi* or *gz*) once on *night 0* in 30 s exposures, and repeat the observations on *nights 1, 2 and 3* in the same filters in 120 s exposures. The estimated time budget for these observations corresponds to  $< 3\%$  of Rubin’s total survey time. We are optimistic that with Rubin’s ToO capabilities there will be many KN counterpart discoveries within the next decade.

---

<sup>1</sup>These rates do not factor in the number of detected BNS and NSBH mergers so far in O4, and are thus subject to change. See <https://emfollow.docs.ligo.org/userguide/capabilities.html> for the latest updates to the IGWN Public Alerts User Guide.

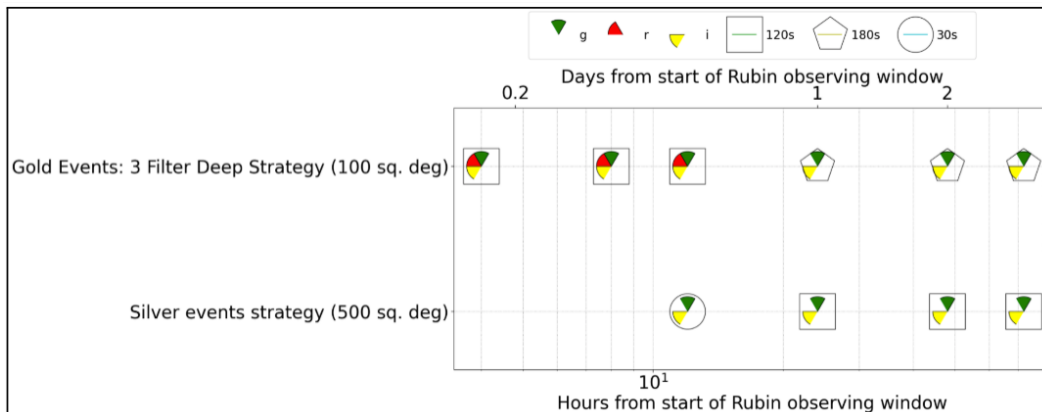


Figure 6.2: A schematic diagram showing the recommended observing strategy with filters and cadence for Rubin during GW ToO observations for both “gold” and “silver” events. Figure credit: Igor Andreoni. Published in the Rubin ToO 2024 workshop final report linked here.

### O5: ToOs with Roman, Cryoscope, and UVEX

Looking farther into the future, Roman, Cryoscope, and the Ultraviolet Explorer (UVEX) will be powerful upcoming missions in discovering KNe during IGWN’s fifth, and potentially sixth observing runs. Both Roman and Cryoscope possess a unique combination of depth, red sensitivity, and wide field of view that will enable them to find KNe that would normally be missed by optical surveys, including those at large distances, with large lanthanide fractions, equatorial viewing angles, and those obscured by line-of-sight dust extinction (Andreoni et al., 2024). Specifically, both Roman and Cryoscope will be advantageous in detecting KNe from NSBH mergers which are expected to be redder and fainter than KNe from BNS mergers. From Roman ToO observations of GW events localized to  $<10$  sq. deg., 1 – 6 KNe are expected to be detected in O5 (and 4 – 21 in O6) (Andreoni et al., 2024). UVEX will possess both far- and near-UV sensitivity to a photometric depth of 24.5 mag, and a wide field-of-view ( $3.5^\circ \times 3.5^\circ$ ) ideal for conducting GW follow-ups (Kulkarni et al., 2021). With its rapid response time, UVEX will be sensitive to the early blue emission expected during the first few hours of a KN’s evolution, thereby distinguishing between shock-powered cocoon emission and radioactivity-powered emission (Gottlieb et al., 2018; Nakar & Piran, 2016). UVEX will follow-up  $\sim 20$  neutron star mergers localized to  $<100$  sq. deg. within hours of the merger (Kulkarni et al., 2021).

We look forward to a bright era in multi-messenger astronomy over the next decade,

with the prospect of exciting EM-GW discoveries that will revolutionize our understanding of KNe and the  $r$ -process as a whole.

## Bibliography

- Abbott, B. P., Abbott, R., Abbott, T. D., et al. 2017a, GW170817: Observation of Gravitational Waves from a Binary Neutron Star Inspiral, *Phys. Rev. Lett.*, 119, 161101. <https://link.aps.org/doi/10.1103/PhysRevLett.119.161101>
- . 2017b, Gravitational Waves and Gamma-Rays from a Binary Neutron Star Merger: GW170817 and GRB 170817A, *The Astrophysical Journal*, 848, L13. <https://doi.org/10.3847/2041-8213/aa920c>
- . 2020a, GW190425: Observation of a Compact Binary Coalescence with Total Mass  $\sim 3.4M_{\odot}$ , *The Astrophysical Journal*, 892, L3. <http://dx.doi.org/10.3847/2041-8213/ab75f5>
- Abbott, B. P., et al. 2020b, GW190814: Gravitational Waves from the Coalescence of a 23 Solar Mass Black Hole with a 2.6 Solar Mass Compact Object, *The Astrophysical Journal, Letters*, 896, L44
- Abbott, B. P., Abbott, R., Abbott, T. D., et al. 2020a, GW190425: Observation of a Compact Binary Coalescence with Total Mass  $\sim 3.4 M_{\odot}$ , *The Astrophysical Journal, Letters*, 892, L3
- Abbott, R., Abbott, T. D., Abraham, S., et al. 2020b, GW190521: A Binary Black Hole Merger with a Total Mass of  $150 M_{\odot}$ , *Physical Review Letters*, 125, 101102
- . 2021, Observation of Gravitational Waves from Two Neutron Star-Black Hole Coalescences, *The Astrophysical Journal, Letters*, 915, L5
- Abbott, R., Abbott, T. D., Abraham, S., et al. 2021, Observation of Gravitational Waves from Two Neutron Star-Black Hole Coalescences, *The Astrophysical Journal Letters*, 915, L5. <https://dx.doi.org/10.3847/2041-8213/ac082e>
- Abbott, R., Abbott, T. D., Acernese, F., et al. 2023, GWTC-3: Compact Binary Coalescences Observed by LIGO and Virgo during the Second Part of the Third Observing Run, *Physical Review X*, 13, 041039
- Abbott, R., Abbott, T. D., Acernese, F., et al. 2023, Population of Merging Compact Binaries Inferred Using Gravitational Waves through GWTC-3, *Phys. Rev. X*, 13, 011048. <https://link.aps.org/doi/10.1103/PhysRevX.13.011048>
- Abbott, T. C., Buffaz, E., Vieira, N., et al. 2022, GWSkyNet-Multi: A Machine-learning Multiclass Classifier for LIGO-Virgo Public Alerts, *The Astrophysical Journal*, 927, 232. <http://dx.doi.org/10.3847/1538-4357/ac5019>
- Abbott et al. 2017, GW170814: A Three-Detector Observation of Gravitational Waves from a Binary Black Hole Coalescence, *Phys. Rev. Lett.*, 119, 141101. <https://link.aps.org/doi/10.1103/PhysRevLett.119.141101>

- Adams, T., Buskulic, D., Germain, V., et al. 2016, Low-latency analysis pipeline for compact binary coalescences in the advanced gravitational wave detector era, *Classical and Quantum Gravity*, 33, 175012
- Ahumada, T., Coughlin, M., & Anand, S. 2020a, LIGO/Virgo S200115j: LCO upper limits for ZTF20aafqvyc/AT2020yq from the McDonald Observatory 1-m telescope, *GRB Coordinates Network*, 26817, 1
- Ahumada, T., & Singer, L. 2020, LIGO/Virgo S200115j: GMOS-N upper limits for ZTF20aafqvyc/AT2020yq from the Gemini Observatory, *GRB Coordinates Network*, 26822, 1
- Ahumada, T., Andreoni, I., Karambelkar, V., et al. 2020b, LIGO/Virgo S200105ae: More candidates from the Zwicky Transient Facility., *GRB Coordinates Network*, 26810, 1
- Ahumada, T., Singer, L. P., Anand, S., et al. 2021a, Discovery and confirmation of the shortest gamma-ray burst from a collapsar, *Nature Astronomy*, arXiv:2105.05067
- . 2021b, Discovery and confirmation of the shortest gamma-ray burst from a collapsar, *Nature Astronomy*, 5, 917
- Ahumada, T., Anand, S., Coughlin, M. W., et al. 2022, In Search of Short Gamma-Ray Burst Optical Counterparts with the Zwicky Transient Facility, *The Astrophysical Journal*, 932, 40
- Ahumada, T., Andreoni, I., Anumarpudi, A., et al. 2023a, LIGO/Virgo/KAGRA S230627c: Additional observations from the Zwicky Transient Facility, *General Coordinates Network*, 34100, 1
- Ahumada, T., Salgundi, A., Stein, R., et al. 2023b, LIGO/Virgo/KAGRA S231113bw: Zwicky Transient Facility observations, *General Coordinates Network*, 35032, 1
- Ahumada, T., Karambelkar, V., Stein, R., et al. 2023c, # LIGO/Virgo/KAGRA S230521k: Zwicky Transient Facility observations, *General Coordinates Network*, 33848, 1
- Ahumada, T., Anumarpudi, A., Karambelkar, V., et al. 2023d, LIGO/Virgo/KAGRA S230528a: Zwicky Transient Facility observations, *General Coordinates Network*, 33899, 1
- Alard, C. 2000, Image subtraction using a space-varying kernel, *Astron. Astrophys.*, 144, 363
- Alexander, K. D., Schroeder, G., Paterson, K., et al. 2021, A Late-time Galaxy-targeted Search for the Radio Counterpart of GW190814, *The Astrophysical Journal*, 923, 66

- Almualla, M., Coughlin, M. W., Anand, S., et al. 2020, Dynamic scheduling: target of opportunity observations of gravitational wave events, *Mon. Not. R. Astron. Soc.*, 495, 4366. <https://doi.org/10.1093/mnras/staa1498>
- Almualla, M., Ning, Y., Salehi, P., et al. 2021, Using Neural Networks to Perform Rapid High-Dimensional Kilonova Parameter Inference, *arXiv e-prints*, arXiv:2112.15470
- Anand, S., Coughlin, M. W., Kasliwal, M. M., et al. 2020a, Optical follow-up of the neutron star-black hole mergers S200105ae and S200115j, *Nature Astronomy*, arXiv:2009.07210
- Anand, S., Kumar, H., Reusch, S., et al. 2020b, LIGO/Virgo S200115j: Candidates from the Zwicky Transient Facility., *GRB Coordinates Network*, 26767, 1
- Anand, S., Coughlin, M., Singer, L., et al. 2020c, LIGO/Virgo S200105ae: Upper Limits from the Zwicky Transient Facility., *GRB Coordinates Network*, 26662, 1
- Anand, S., Barnes, J., Yang, S., et al. 2024, Collapsars as Sites of r-process Nucleosynthesis: Systematic Photometric Near-infrared Follow-up of Type Ic-BL Supernovae, *The Astrophysical Journal*, 962, 68
- Andreoni, I., Kasliwal, M. M., Cenko, S. B., & Yao, Y. 2020, LIGO/Virgo S200115j: Zwicky Transient Facility search for optical counterparts to Swift X-ray sources, *GRB Coordinates Network*, 26863, 1
- Andreoni, I., Ackley, K., Cooke, J., et al. 2017a, Follow Up of GW170817 and Its Electromagnetic Counterpart by Australian-Led Observing Programmes, *PASA*, 34, e069
- . 2017b, Follow Up of GW170817 and Its Electromagnetic Counterpart by Australian-Led Observing Programmes, *PASA*, 34, e069
- Andreoni, I., Goldstein, D. A., Anand, S., et al. 2019, GROWTH on S190510g: DECam Observation Planning and Follow-up of a Distant Binary Neutron Star Merger Candidate, *The Astrophysical Journal, Letters*, 881, L16
- Andreoni, I., Goldstein, D. A., Kasliwal, M. M., et al. 2020, GROWTH on S190814bv: Deep Synoptic Limits on the Optical/Near-infrared Counterpart to a Neutron Star-Black Hole Merger, *The Astrophysical Journal*, 890, 131. <https://doi.org/10.3847/2F1538-4357%2Fab6a1b>
- Andreoni, I., Coughlin, M. W., Kool, E. C., et al. 2021, Fast-transient Searches in Real Time with ZTFReST: Identification of Three Optically Discovered Gamma-Ray Burst Afterglows and New Constraints on the Kilonova Rate, *The Astrophysical Journal*, 918, 63

- Andreoni, I., Coughlin, M. W., Criswell, A. W., et al. 2024, Enabling kilonova science with Nancy Grace Roman Space Telescope, *Astroparticle Physics*, 155, 102904
- Antier, S., Agayeva, S., Almualla, M., et al. 2020, GRANDMA observations of advanced LIGO's and advanced Virgo's third observational campaign, *Monthly Notices of the RAS*, 497, 5518
- Anumarlapudi, A., Ahumada, T., Kasliwal, M., et al. 2023, LIGO/Virgo/KAGRA S230627c: Zwicky Transient Facility observations and candidates, *General Coordinates Network*, 34089, 1
- Arcavi, I. 2018, The First Hours of the GW170817 Kilonova and the Importance of Early Optical and Ultraviolet Observations for Constraining Emission Models, *The Astrophysical Journal, Letters*, 855, L23
- Arcavi, I., Hosseinzadeh, G., Howell, D. A., et al. 2017, Optical emission from a kilonova following a gravitational-wave-detected neutron-star merger, *Nature*, 551, 64
- Arnett, W. D. 1982, Type I supernovae. I - Analytic solutions for the early part of the light curve, *Astrophys. J.*, 253, 785
- Ashall, C., Mazzali, P. A., Pian, E., et al. 2019, GRB 161219B/SN 2016jca: a powerful stellar collapse, *Monthly Notices of the RAS*, 487, 5824
- Balasubramanian, A., Corsi, A., Mooley, K. P., et al. 2022, GW170817 4.5 Yr After Merger: Dynamical Ejecta Afterglow Constraints, *The Astrophysical Journal*, 938, 12
- Banerjee, S., Tanaka, M., Kato, D., & Gaigalas, G. 2023, Diversity of early kilonova with the realistic opacities of highly ionized heavy elements, arXiv e-prints, arXiv:2304.05810
- Banerjee, S., Tanaka, M., Kato, D., et al. 2022, Opacity of the Highly Ionized Lanthanides and the Effect on the Early Kilonova, *The Astrophysical Journal*, 934, 117
- Barbarino, C., Sollerman, J., Taddia, F., et al. 2021, Type Ic supernovae from the (intermediate) Palomar Transient Factory, *Astronomy and Astrophysics*, 651, A81
- Barbieri, C., Salafia, O. S., Colpi, M., et al. 2019, Filling the Mass Gap: How Kilonova Observations can Unveil the Nature of the Compact Object Merging with the Neutron Star, *Astrophys. J.*, 887, L35
- Barnes, J., & Duffell, P. C. 2023, Hydrodynamic Mixing of Accretion Disk Outflows in Collapsars: Implications for r-process Signatures, *The Astrophysical Journal*, 952, 96. <https://dx.doi.org/10.3847/1538-4357/acdb67>

- Barnes, J., Duffell, P. C., Liu, Y., et al. 2018, A GRB and Broad-lined Type Ic Supernova from a Single Central Engine, *The Astrophysical Journal*, 860, 38
- Barnes, J., & Kasen, D. 2013, Effect of a High Opacity on the Light Curves of Radioactively Powered Transients from Compact Object Mergers, *The Astrophysical Journal*, 775, 18
- Barnes, J., Kasen, D., Wu, M.-R., & Martínez-Pinedo, G. 2016, Radioactivity and Thermalization in the Ejecta of Compact Object Mergers and Their Impact on Kilonova Light Curves, *The Astrophysical Journal*, 829, 110
- Barnes, J., & Metzger, B. D. 2022, Signatures of R-process Enrichment in Supernovae from Collapsars, arXiv e-prints, arXiv:2205.10421
- . 2023, A Collapsar Origin for GRB 211211A Is (Just Barely) Possible, *The Astrophysical Journal*, 947, 55
- Bauswein, A., Baumgarte, T. W., & Janka, H. T. 2013, Prompt Merger Collapse and the Maximum Mass of Neutron Stars, *Physical Review Letters*, 111, 131101
- Becker, A. 2015, HOTPANTS: High Order Transform of PSF ANd Template Subtraction, *Astrophysics Source Code Library*, , , ascl:1504.004
- Becker, A. 2015, HOTPANTS: High Order Transform of PSF ANd Template Subtraction, *Astrophysics Source Code Library*
- Bellm, E. C., & Sesar, B. 2016a, pyraf-dbsp: Reduction pipeline for the Palomar Double Beam Spectrograph, *Astrophysics Source Code Library*, , , ascl:1602.002
- . 2016b, pyraf-dbsp: Reduction pipeline for the Palomar Double Beam Spectrograph, , , ascl:1602.002
- Bellm, E. C., Kulkarni, S. R., Graham, M. J., et al. 2018, The Zwicky Transient Facility: System Overview, Performance, and First Results, *Pub. Astron. Soc. Pac.*, 131, 018002. <https://doi.org/10.1088%2F1538-3873%2Faae6be>
- Bellm, E. C., Kulkarni, S. R., Graham, M. J., et al. 2019a, The Zwicky Transient Facility: System Overview, Performance, and First Results, *Publications of the ASP*, 131, 018002
- Bellm, E. C., Kulkarni, S. R., Barlow, T., et al. 2019b, The Zwicky Transient Facility: Surveys and Scheduler, *Publications of the ASP*, 131, 068003
- Ben-Ami, S., Gal-Yam, A., Mazzali, P. A., et al. 2014, SN 2010mb: Direct Evidence for a Supernova Interacting with a Large Amount of Hydrogen-free Circumstellar Material, *The Astrophysical Journal*, 785, 37
- Beniamini, P., Hotokezaka, K., & Piran, T. 2016, Natal Kicks and Time Delays in Merging Neutron Star Binaries: Implications for r-process Nucleosynthesis in Ultra-faint Dwarfs and in the Milky Way, *The Astrophysical Journal*, Letters, 829, L13

- Bertin, E. 2006a, in *Astronomical Society of the Pacific Conference Series*, Vol. 351, *Astronomical Data Analysis Software and Systems XV*, ed. C. Gabriel, C. Arviset, D. Ponz, & S. Enrique, 112
- Bertin, E. 2006b, *Astron. Soc. Pac. Conf. Ser.*, Vol. 351, *Automatic Astrometric and Photometric Calibration with SCAMP*, ed. C. Gabriel, C. Arviset, D. Ponz, & S. Enrique, 112–115
- . 2010, *SWarp: Resampling and Co-adding FITS Images Together*, *Astrophysics Source Code Library*, , , ascl:1010.068
- Bertin, E. 2011, in *Astronomical Society of the Pacific Conference Series*, Vol. 442, *Astronomical Data Analysis Software and Systems XX*, ed. I. N. Evans, A. Accomazzi, D. J. Mink, & A. H. Rots, 435
- Bertin, E., & Arnouts, S. 1996, *SExtractor: Software for source extraction.*, *Astron. Astrophys.*, 117, 393
- . 2010, *SExtractor: Source Extractor*, *Astrophysics Source Code Library*, , , ascl:1010.064
- Bertin, E., Mellier, Y., Radovich, M., et al. 2002, in *Astronomical Society of the Pacific Conference Series*, Vol. 281, *Astronomical Data Analysis Software and Systems XI*, ed. D. A. Bohlender, D. Durand, & T. H. Handley, 228
- Bianco, F. B., Modjaz, M., Hicken, M., et al. 2014, *Multi-color Optical and Near-infrared Light Curves of 64 Stripped-envelope Core-Collapse Supernovae*, *The Astrophysical Journal, Supplement*, 213, 19
- Bissaldi, E., Calura, F., Matteucci, F., Longo, F., & Barbiellini, G. 2007, *The connection between gamma-ray bursts and supernovae Ib/c*, *Astronomy and Astrophysics*, 471, 585
- Blagorodnova, N., Neill, J. D., Walters, R., et al. 2018a, *The SED Machine: A Robotic Spectrograph for Fast Transient Classification*, *Publications of the ASP*, 130, 035003
- . 2018b, *The SED Machine: A Robotic Spectrograph for Fast Transient Classification*, *Publications of the ASP*, 130, 035003
- Blanchard, P. K., Villar, V. A., Chornock, R., et al. 2024, *JWST detection of a supernova associated with GRB 221009A without an r-process signature*, *Nature Astronomy*, arXiv:2308.14197
- Blondin, S., & Tonry, J. L. 2007a, *Determining the Type, Redshift, and Age of a Supernova Spectrum*, *The Astrophysical Journal*, 666, 1024
- . 2007b, *Determining the Type, Redshift, and Age of a Supernova Spectrum*, *The Astrophysical Journal*, 666, 1024

- Bonetti, M., Perego, A., Dotti, M., & Cescutti, G. 2019, Neutron star binary orbits in their host potential: effect on early r-process enrichment, *Monthly Notices of the RAS*, 490, 296
- Bradley, L., Sipőcz, B., Robitaille, T., et al. 2020, *astropy/photutils: 1.0.0, v1.0.0*, Zenodo, doi:10.5281/zenodo.4044744. <https://doi.org/10.5281/zenodo.4044744>
- Brown, T. M., Baliber, N., Bianco, F. B., et al. 2013a, *Las Cumbres Observatory Global Telescope Network*, *Publications of the ASP*, 125, 1031
- . 2013b, *Las Cumbres Observatory Global Telescope Network*, *Publications of the ASP*, 125, 1031
- Buchner, J., Georgakakis, A., Nandra, K., et al. 2014, X-ray spectral modelling of the AGN obscuring region in the CDFS: Bayesian model selection and catalogue, *Astronomy and Astrophysics*, 564, A125
- Bufano, F., Pian, E., Sollerman, J., et al. 2012, The Highly Energetic Expansion of SN 2010bh Associated with GRB 100316D, *The Astrophysical Journal*, 753, 67
- Bulla, M. 2019, POSSIS: predicting spectra, light curves, and polarization for multidimensional models of supernovae and kilonovae, *Monthly Notices of the RAS*, 489, 5037
- . 2023, The critical role of nuclear heating rates, thermalization efficiencies, and opacities for kilonova modelling and parameter inference, *Monthly Notices of the RAS*, 520, 2558
- Burbidge, E. M., Burbidge, G. R., Fowler, W. A., & Hoyle, F. 1957, Synthesis of the Elements in Stars, *Rev. Mod. Phys.*, 29, 547. <https://link.aps.org/doi/10.1103/RevModPhys.29.547>
- Burke, J., Hiramatsu, D., Howell, D. A., et al. 2020, *Global SN Project Transient Classification Report for 2020-06-02*, *Transient Name Server Classification Report*, 2020-1666, 1
- Burns, E., Svinkin, D., Fenimore, E., et al. 2023, GRB 221009A: The Boat, *The Astrophysical Journal Letters*, 946, L31
- Cabero, M., Mahabal, A., & McIver, J. 2020, GWSkyNet: A Real-time Classifier for Public Gravitational-wave Candidates, *The Astrophysical Journal Letters*, 904, L9. <http://dx.doi.org/10.3847/2041-8213/abc5b5>
- Cameron, A. G. 1957, *Stellar evolution, nuclear astrophysics, and nucleogenesis*. Second edition, ed. A. G. Cameron (Atomic Energy of Canada Limited)
- Cannon, K., Caudill, S., Chan, C., et al. 2021, GstLAL: A software framework for gravitational wave discovery, *SoftwareX*, 14, 100680

- Cano, Z., Wang, S.-Q., Dai, Z.-G., & Wu, X.-F. 2017a, The Observer's Guide to the Gamma-Ray Burst Supernova Connection, *Advances in Astronomy*, 2017, 8929054
- Cano, Z., Izzo, L., de Ugarte Postigo, A., et al. 2017b, GRB 161219B/SN 2016jca: A low-redshift gamma-ray burst supernova powered by radioactive heating, *Astronomy and Astrophysics*, 605, A107
- Casey, A. R., & Schlaufman, K. C. 2017, The Universality of the Rapid Neutron-capture Process Revealed by a Possible Disrupted Dwarf Galaxy Star, *The Astrophysical Journal*, 850, 179
- Castro-Tirado, A. J., Valeev, A. F., Hu, Y.-D., et al. 2020, LIGO/Virgo S200105ae: AT2020pq, AT2020ps and AT2020pv 10.4m GTC spectroscopy, GRB Coordinates Network, 26703
- Chambers, K. C., Magnier, E. A., Metcalfe, N., et al. 2016a, The Pan-STARRS1 Surveys, arXiv e-prints, arXiv:1612.05560
- . 2016b, The Pan-STARRS1 Surveys, arXiv e-prints, arXiv:1612.05560
- Chatterjee, D., Ghosh, S., Brady, P. R., et al. 2020, A Machine Learning-based Source Property Inference for Compact Binary Mergers, *Astrophys. J.*, 896, 54. <http://dx.doi.org/10.3847/1538-4357/ab8dbe>
- Chatterjee, D., Ghosh, S., Brady, P. R., et al. 2020, A Machine Learning-based Source Property Inference for Compact Binary Mergers, *The Astrophysical Journal*, 896, 54
- Chatziioannou, K. 2020, Neutron-star tidal deformability and equation-of-state constraints, *General Relativity and Gravitation*, 52, 109
- Chornock, R., Berger, E., Kasen, D., et al. 2017, The Electromagnetic Counterpart of the Binary Neutron Star Merger LIGO/Virgo GW170817. IV. Detection of Near-infrared Signatures of r-process Nucleosynthesis with Gemini-South, *The Astrophysical Journal*, 848, L19. <https://doi.org/10.3847/2041-8213/aa905c>
- Christie, I. M., Lalakos, A., Tchekhovskoy, A., et al. 2019, The Role of Magnetic Field Geometry in the Evolution of Neutron Star Merger Accretion Discs, *Mon. Not. R. Astron. Soc.*, 490, 4811
- Chu, M., Dahiwalé, A., & Fremling, C. 2021, ZTF Transient Classification Report for 2021-09-28, Transient Name Server Classification Report, 2021-3339, 1
- Chugai, N. N. 2000, Monte Carlo Simulations of Supernova Light Curves and the Hypernova SN1998bw, *Astronomy Letters*, 26, 797
- Clocchiatti, A., Suntzeff, N. B., Covarrubias, R., & Candia, P. 2011, The Ultimate Light Curve of SN 1998bw/GRB 980425, *AJ*, 141, 163

- Colgate, S. A., & McKee, C. 1969, Early Supernova Luminosity, *The Astrophysical Journal*, 157, 623
- Cook, D. O., Kasliwal, M. M., Van Sistine, A., et al. 2019a, Census of the Local Universe (CLU) Narrowband Survey. I. Galaxy Catalogs from Preliminary Fields, *The Astrophysical Journal*, 880, 7
- . 2019b, Census of the Local Universe (CLU) Narrowband Survey. I. Galaxy Catalogs from Preliminary Fields, *The Astrophysical Journal*, 880, 7
- Cook, D. O., Mazzarella, J. M., Helou, G., et al. 2023, Completeness of the NASA/IPAC Extragalactic Database (NED) Local Volume Sample, *The Astrophysical Journal*, Supplement, 268, 14
- Corsi, A., & Lazzati, D. 2021, Gamma-ray burst jets in supernovae, *New A Rev.*, 92, 101614
- Corsi, A., Ho, A. Y. Q., Cenko, S. B., et al. 2023, A Search for Relativistic Ejecta in a Sample of ZTF Broad-lined Type Ic Supernovae, *The Astrophysical Journal*, 953, 179. <https://dx.doi.org/10.3847/1538-4357/acd3f2>
- Côté, B., Fryer, C. L., Belczynski, K., et al. 2018, The Origin of r-process Elements in the Milky Way, *The Astrophysical Journal*, 855, 99. <https://doi.org/10.3847/1538-4357/aaad67>
- Côté, B., Eichler, M., Arcones, A., et al. 2019, Neutron Star Mergers Might Not Be the Only Source of r-process Elements in the Milky Way, *The Astrophysical Journal*, 875, 106
- Coughlin, M. W., Dietrich, T., Margalit, B., & Metzger, B. D. 2019, Multimessenger Bayesian parameter inference of a binary neutron star merger, *Monthly Notices of the RAS*, 489, L91
- Coughlin, M. W., T., A., S., A., et al. 2019a, GROWTH on S190425z: Searching thousands of square degrees to identify an optical or infrared counterpart to a binary neutron star merger with the Zwicky Transient Facility and Palomar Gattini IR, *Astrophys. J. Lett.*, 885, L19
- Coughlin, M. W., Dietrich, T., Doctor, Z., et al. 2018a, Constraints on the neutron star equation of state from AT2017gfo using radiative transfer simulations, *Monthly Notices of the Royal Astronomical Society*, 480, 3871. <https://doi.org/10.1093/mnras/sty2174>
- Coughlin, M. W., Tao, D., Chan, M. L., et al. 2018b, Optimizing searches for electromagnetic counterparts of gravitational wave triggers, *Monthly Notices of the Royal Astronomical Society*, 478, 692. <http://dx.doi.org/10.1093/mnras/sty1066>

- Coughlin, M. W., Antier, S., Corre, D., et al. 2019b, Optimizing Multi-Telescope Observations of Gravitational-Wave Counterparts, *Mon. Not. R. Astron. Soc.*, <http://oup.prod.sis.lan/mnras/advance-article-pdf/doi/10.1093/mnras/stz2485/29808472/stz2485.pdf>, stz2485. <https://doi.org/10.1093/mnras/stz2485>
- Coughlin, M. W., Ahumada, T., Cenko, S. B., et al. 2019c, 2900 Square Degree Search for the Optical Counterpart of Short Gamma-Ray Burst GRB 180523B with the Zwicky Transient Facility, *Publications of the Astronomical Society of the Pacific*, 131, 048001
- Coughlin, M. W., Dietrich, T., Antier, S., et al. 2019d, Implications of the search for optical counterparts during the first six months of the Advanced LIGO's and Advanced Virgo's third observing run: possible limits on the ejecta mass and binary properties, *Mon. Not. R. Astron. Soc.*, 492, 863. <https://doi.org/10.1093/mnras/stz3457>
- Coughlin, M. W., Dietrich, T., Heinzel, J., et al. 2020, Standardizing kilonovae and their use as standard candles to measure the Hubble constant, *Phys. Rev. Research*, 2, 022006. <https://link.aps.org/doi/10.1103/PhysRevResearch.2.022006>
- Coughlin, M. W., Dietrich, T., Heinzel, J., et al. 2020a, Standardizing kilonovae and their use as standard candles to measure the Hubble constant, *Physical Review Research*, 2, 022006
- Coughlin, M. W., Dietrich, T., Antier, S., et al. 2020b, Implications of the search for optical counterparts during the second part of the Advanced LIGO's and Advanced Virgo's third observing run: lessons learned for future follow-up observations, *Monthly Notices of the RAS*, 497, 1181
- Coughlin, M. W., Bloom, J. S., Nir, G., et al. 2023, A Data Science Platform to Enable Time-domain Astronomy, *The Astrophysical Journal, Supplement*, 267, 31
- Coughlin et al. 2019, GROWTH on S190425z: Searching Thousands of Square Degrees to Identify an Optical or Infrared Counterpart to a Binary Neutron Star Merger with the Zwicky Transient Facility and Palomar Gattini-IR, *Astrophys. J.*, 885, L19. <https://doi.org/10.3847/2041-8213/ab4ad8>
- Coulter, D. A., Foley, R. J., Kilpatrick, C. D., et al. 2017a, Swope Supernova Survey 2017a (SSS17a), the optical counterpart to a gravitational wave source, *Science*, 358, 1556
- . 2017b, Swope Supernova Survey 2017a (SSS17a), the optical counterpart to a gravitational wave source, *Science*, 358, 1556

- Coulter, D. A., Kilpatrick, C. D., Jones, D. O., et al. 2024, The Gravity Collective: A Comprehensive Analysis of the Electromagnetic Search for the Binary Neutron Star Merger GW190425, arXiv e-prints, arXiv:2404.15441
- Cowan, J. J., Sneden, C., Lawler, J. E., & Den Hartog, E. A. 2006, r-Process Enhanced Halo Stars, arXiv e-prints, astro
- Cowperthwaite, P. S., Berger, E., Villar, V. A., et al. 2017, The Electromagnetic Counterpart of the Binary Neutron Star Merger LIGO/Virgo GW170817. II. UV, Optical, and Near-infrared Light Curves and Comparison to Kilonova Models, *The Astrophysical Journal*, 848, L17. <https://doi.org/10.3847/2F2041-8213%2Faa8fc7>
- Dahiwale, A., Dugas, A., & Fremling, C. 2019, ZTF Transient Classification Report for 2019-08-15, Transient Name Server Classification Report, 2019-1505, 1
- Dahiwale, A., & Fremling, C. 2020a, ZTF Transient Classification Report for 2020-08-25, Transient Name Server Classification Report, 2020-2608, 1
- . 2020b, ZTF Transient Classification Report for 2020-06-25, Transient Name Server Classification Report, 2020-1935, 1
- Davies, M. B., Benz, W., Piran, T., & Thielemann, F. K. 1994, Merging Neutron Stars. I. Initial Results for Coalescence of Noncorotating Systems, *The Astrophysical Journal*, 431, 742
- De, K., Hankins, M., & Kasliwal, M. M. 2020a, LIGO/Virgo S200115j: NIR upper limits for ZTF20aafqvyc/AT2020yq from the Palomar 200-inch telescope, GRB Coordinates Network, 26814, 1
- De, K., Kasliwal, M. M., Tzanidakis, A., et al. 2020b, The Zwicky Transient Facility Census of the Local Universe. I. Systematic Search for Calcium-rich Gap Transients Reveals Three Related Spectroscopic Subclasses, *The Astrophysical Journal*, 905, 58
- De, K., Hankins, M. J., Kasliwal, M. M., et al. 2020c, Palomar Gattini-IR: Survey Overview, Data Processing System, On-sky Performance and First Results, *Publications of the ASP*, 132, 025001
- de Wet, S., Groot, P. J., Bloemen, S., et al. 2021, GW190814 follow-up with the optical telescope MeerLICHT, *Astronomy and Astrophysics*, 649, A72
- Dekany, R., Smith, R. M., Riddle, R., et al. 2020, The Zwicky Transient Facility: Observing System, *Publications of the ASP*, 132, 038001
- Della Valle, M., Chincarini, G., Panagia, N., et al. 2006, An enigmatic long-lasting  $\gamma$ -ray burst not accompanied by a bright supernova, *Nature*, 444, 1050

- Desai, D. K., Siegel, D. M., & Metzger, B. D. 2023, Three-dimensional General-relativistic Simulations of Neutrino-driven Winds from Magnetized Proto-Neutron Stars, *The Astrophysical Journal*, 954, 192
- Dey, A., Schlegel, D. J., Lang, D., et al. 2019, Overview of the DESI Legacy Imaging Surveys, *Astron. J.*, 157, 168. <http://dx.doi.org/10.3847/1538-3881/ab089d>
- Dichiara, S., Bernadini, M., & Burrows, D. 2019, GRB 190829A: Swift detection of a burst consistent with a galaxy at  $z=0.08$ , *GRB Coordinates Network*, 25552, 1
- Dietrich, T., Coughlin, M. W., Pang, P. T. H., et al. 2020a, Multimessenger constraints on the neutron-star equation of state and the Hubble constant, *Science*, 370, 1450
- . 2020b, New Constraints on the Supranuclear Equation of State and the Hubble Constant from Nuclear Physics – Multi-Messenger Astronomy, *arXiv e-prints*, arXiv:2002.11355
- Dobie, D., Stewart, A., Hotokezaka, K., et al. 2022, A comprehensive search for the radio counterpart of GW190814 with the Australian Square Kilometre Array Pathfinder, *Monthly Notices of the RAS*, 510, 3794
- Drout, M. R., Piro, A. L., Shappee, B. J., et al. 2017, Light curves of the neutron star merger GW170817/SSS17a: Implications for r-process nucleosynthesis, *Science*, 358, 1570
- Duev, D. A., Mahabal, A., Masci, F. J., et al. 2019, Real-bogus classification for the Zwicky Transient Facility using deep learning, *Monthly Notices of the RAS*, 489, 3582
- Duev, D. A., Mahabal, A., Masci, F. J., et al. 2019, Real-bogus classification for the Zwicky Transient Facility using deep learning, *Mon. Not. R. Astron. Soc.*, 489, 3582. <https://doi.org/10.1093/mnras/stz2357>
- Duggan, G. E., Kirby, E. N., Andrievsky, S. M., & Korotin, S. A. 2018, Neutron Star Mergers are the Dominant Source of the r-process in the Early Evolution of Dwarf Galaxies, *The Astrophysical Journal*, 869, 50
- Evans, P. A., Cenko, S. B., Kennea, J. A., et al. 2017a, Swift and NuSTAR observations of GW170817: Detection of a blue kilonova, *Science*, 358, 1565
- . 2017b, Swift and NuSTAR observations of GW170817: Detection of a blue kilonova, *Science*, 358, 1565
- Evans, P. A., Page, K. L., Kennea, J. A., et al. 2020, LIGO/Virgo S200115j: Swift-XRT sources, *GRB Coordinates Network*, 26798, 1

- Feindt, U., Nordin, J., Rigault, M., et al. 2019, *simsurvey: estimating transient discovery rates for the Zwicky transient facility*, *J. Cosmol. Astropart. Phys.*, 2019, 005. <http://dx.doi.org/10.1088/1475-7516/2019/10/005>
- Fernández, R., Tchekhovskoy, A., Quataert, E., Foucart, F., & Kasen, D. 2019, *Long-term GRMHD simulations of neutron star merger accretion discs: implications for electromagnetic counterparts*, *Mon. Not. R. Astron. Soc.*, 482, 3373
- Feroz, F., Hobson, M. P., & Bridges, M. 2009, *MULTINEST: an efficient and robust Bayesian inference tool for cosmology and particle physics*, *Monthly Notices of the RAS*, 398, 1601
- Fields, B. D., Olive, K. A., Yeh, T.-H., & Young, C. 2020, *Big-Bang Nucleosynthesis after Planck*, *Journal of Cosmology and Astroparticle Physics*, 2020, 010. <https://dx.doi.org/10.1088/1475-7516/2020/03/010>
- Flesch, E. W. 2023, *The Million Quasars (Milliquas) Catalogue, v8*, *The Open Journal of Astrophysics*, 6, 49
- Flewelling, H. 2018, in *American Astronomical Society Meeting Abstracts, Vol. 231*, *American Astronomical Society Meeting Abstracts #231*, 102.02
- Fong, W., Berger, E., Margutti, R., & Zauderer, B. A. 2015, *A Decade of Short-duration Gamma-Ray Burst Broadband Afterglows: Energetics, Circumburst Densities, and Jet Opening Angles*, *The Astrophysical Journal*, 815, 102
- Fong, W., Blanchard, P. K., Alexander, K. D., et al. 2019, *The Optical Afterglow of GW170817: An Off-axis Structured Jet and Deep Constraints on a Globular Cluster Origin*, *The Astrophysical Journal, Letters*, 883, L1
- Forster, F. 2021, in *American Astronomical Society Meeting Abstracts, Vol. 53*, *American Astronomical Society Meeting Abstracts*, 423.03
- Förster, F., Maureira, J. C., San Martín, J., et al. 2016, *The High Cadence Transient Survey (HITS). I. Survey Design and Supernova Shock Breakout Constraints*, *The Astrophysical Journal*, 832, 155
- Förster, F., Bauer, F. E., Pignata, G., et al. 2019, *ALeRCE/ZTF Transient Discovery Report for 2019-12-19*, *Transient Name Server Discovery Report*, 2019-2642, 1
- Förster, F., Bauer, F. E., Galbany, L., et al. 2020a, *ALeRCE/ZTF Transient Discovery Report for 2020-08-18*, *Transient Name Server Discovery Report*, 2020-2527, 1
- . 2020b, *ALeRCE/ZTF Transient Discovery Report for 2020-05-25*, *Transient Name Server Discovery Report*, 2020-1550, 1
- Förster, F., Bauer, F. E., Muñoz-Arancibia, A., et al. 2021, *ALeRCE/ZTF Transient Discovery Report for 2021-01-10*, *Transient Name Server Discovery Report*, 2021-96, 1

- Foucart, F. 2012, Black-hole-neutron-star mergers: Disk mass predictions, *Phys. Rev. D*, 86, 124007
- Foucart, F., Desai, D., Brege, W., et al. 2017, Dynamical ejecta from precessing neutron star-black hole mergers with a hot, nuclear-theory based equation of state, *Class. Quant. Grav.*, 34, 044002
- Foucart, F., Duez, M. D., Kidder, L. E., et al. 2018a, Evaluating radiation transport errors in merger simulations using a Monte Carlo algorithm, *Phys. Rev.*, D98, 063007
- Foucart, F., Hinderer, T., & Nissanke, S. 2018b, Remnant baryon mass in neutron star-black hole mergers: Predictions for binary neutron star mimickers and rapidly spinning black holes, *Phys. Rev.*, D98, 081501
- Foucart, F., O'Connor, E., Roberts, L., et al. 2015, Post-merger evolution of a neutron star-black hole binary with neutrino transport, *Phys. Rev. D*, 91, 124021. <https://link.aps.org/doi/10.1103/PhysRevD.91.124021>
- Freiburghaus, C., Rosswog, S., & Thielemann, F.-K. 1999, r-Process in Neutron Star Mergers, *The Astrophysical Journal*, 525, L121. <https://dx.doi.org/10.1086/312343>
- Fremming, C. 2018, ZTF Transient Discovery Report for 2018-12-25, Transient Name Server Discovery Report, 2018-1979, 1
- . 2019, ZTF Transient Discovery Report for 2019-06-18, Transient Name Server Discovery Report, 2019-1032, 1
- Fremming, C., Dahiwal, A., & Dugas, A. 2019a, ZTF Transient Classification Report for 2019-09-26, Transient Name Server Classification Report, 2019-1923, 1
- Fremming, C., Dugas, A., & Sharma, Y. 2018, ZTF Transient Classification Report for 2018-12-18, Transient Name Server Classification Report, 2018-1946, 1
- . 2019b, ZTF Transient Classification Report for 2019-06-17, Transient Name Server Classification Report, 2019-1029, 1
- . 2019c, ZTF Transient Classification Report for 2019-06-18, Transient Name Server Classification Report, 2019-1033, 1
- . 2019d, ZTF Transient Classification Report for 2019-01-04, Transient Name Server Classification Report, 2019-29, 1
- Fremming, C., Sollerman, J., Taddia, F., et al. 2016a, PTF12os and iPTF13bvn. Two stripped-envelope supernovae from low-mass progenitors in NGC 5806, *Astronomy and Astrophysics*, 593, A68

- . 2016b, PTF12os and iPTF13bvn. Two stripped-envelope supernovae from low-mass progenitors in NGC 5806, *Astronomy and Astrophysics*, 593, A68
- Fremling, C., Miller, A. A., Sharma, Y., et al. 2020, The Zwicky Transient Facility Bright Transient Survey. I. Spectroscopic Classification and the Redshift Completeness of Local Galaxy Catalogs, *The Astrophysical Journal*, 895, 32
- Fujibayashi, S., Sekiguchi, Y., Shibata, M., & Wanajo, S. 2022, Collapse of rotating massive stars leading to black hole formation and energetic supernovae, arXiv e-prints, arXiv:2212.03958
- Fujimoto, S.-i., Hashimoto, M.-a., Kotake, K., & Yamada, S. 2007, Heavy-Element Nucleosynthesis in a Collapsar, *The Astrophysical Journal*, 656, 382
- Fynbo, J. P. U., Hjorth, J., Sollerman, J., et al. 2004, in *American Institute of Physics Conference Series*, Vol. 727, *Gamma-Ray Bursts: 30 Years of Discovery*, ed. E. Fenimore & M. Galassi (AIP), 301–306
- Fynbo, J. P. U., Watson, D., Thöne, C. C., et al. 2006, No supernovae associated with two long-duration  $\gamma$ -ray bursts, *Nature*, 444, 1047
- Gal-Yam, A. 2017, in *Handbook of Supernovae*, ed. A. W. Alsabti & P. Murdin, 195
- Galama, T. J., Vreeswijk, P. M., van Paradijs, J., et al. 1998, An unusual supernova in the error box of the  $\gamma$ -ray burst of 25 April 1998, *Nature*, 395, 670
- . 1999, On the possible association of SN 1998bw and GRB 980425, *Astronomy and Astrophysics*, Supplement, 138, 465
- Gehrels, N., Norris, J. P., Barthelmy, S. D., et al. 2006, A new  $\gamma$ -ray burst classification scheme from GRB060614, *Nature*, 444, 1044
- Ghirlanda, G., Salafia, O. S., Paragi, Z., et al. 2019, Compact radio emission indicates a structured jet was produced by a binary neutron star merger, *Science*, 363, 968
- Gillanders, J. H., McCann, M., Sim, S. A., Smartt, S. J., & Ballance, C. P. 2021, Constraints on the presence of platinum and gold in the spectra of the kilonova AT2017gfo, *Monthly Notices of the RAS*, 506, 3560
- Goldstein, A., Veres, P., Burns, E., et al. 2017a, An Ordinary Short Gamma-Ray Burst with Extraordinary Implications: Fermi-GBM Detection of GRB 170817A, *The Astrophysical Journal*, 848, L14
- . 2017b, An Ordinary Short Gamma-Ray Burst with Extraordinary Implications: Fermi-GBM Detection of GRB 170817A, *The Astrophysical Journal*, 848, L14

- Goldstein, D. A., Andreoni, I., Nugent, P. E., et al. 2019, GROWTH on S190426c: Real-time Search for a Counterpart to the Probable Neutron Star-Black Hole Merger using an Automated Difference Imaging Pipeline for DECam, *The Astrophysical Journal, Letters*, 881, L7
- Goldwasser, S., Yaron, O., Sass, A., et al. 2022, The Next Generation SuperFit (NGSF) tool is now available for online execution on WISeREP, *Transient Name Server AstroNote*, 191, 1
- Gompertz, B., Kotak, R., Lyman, J., et al. 2023, LIGO/Virgo/KAGRA S230615az: GOTO candidate counterparts, *General Coordinates Network*, 33979, 1
- Gompertz, B. P., Cutter, R., Steeghs, D., et al. 2020, Searching for electromagnetic counterparts to gravitational-wave merger events with the prototype Gravitational-Wave Optical Transient Observer (GOTO-4), *Monthly Notices of the RAS*, 497, 726
- Goriely, S. 1999, Uncertainties in the solar system r-abundance distribution, *Astronomy and Astrophysics*, 342, 881
- Gottlieb, O., Nakar, E., Piran, T., & Hotokezaka, K. 2018, A cocoon shock breakout as the origin of the  $\gamma$ -ray emission in GW170817, *Monthly Notices of the RAS*, 479, 588
- Gottlieb, O., Issa, D., Jacquemin-Ide, J., et al. 2023, Large-scale Evolution of Seconds-long Relativistic Jets from Black Hole-Neutron Star Mergers, *The Astrophysical Journal, Letters*, 954, L21
- Graham, M. J., Kulkarni, S. R., Bellm, E. C., et al. 2019, The Zwicky Transient Facility: Science Objectives, *Publications of the ASP*, 131, 078001
- Graham, M. J., Kulkarni, S. R., Bellm, E. C., et al. 2019, The Zwicky Transient Facility: Science Objectives, *Pub. Astron. Soc. Pac.*, 131, 078001
- Green, R. M. 1985, *Spherical Astronomy*
- Guevel, D., & Hosseinzadeh, G. 2017a, Dguevel/Pyzogy: Initial Release, vv0.0.1, Zenodo, doi:10.5281/zenodo.1043973
- . 2017b, Dguevel/Pyzogy: Initial Release, vv0.0.1, Zenodo, doi:10.5281/zenodo.1043973
- Guo, X., Chu, Q., Chung, S. K., et al. 2018, GPU-acceleration on a low-latency binary-coalescence gravitational wave search pipeline, *Computer Physics Communications*, 231, 62
- Haggard, D., Nynka, M., Ruan, J. J., et al. 2017, A Deep Chandra X-Ray Study of Neutron Star Coalescence GW170817, *The Astrophysical Journal, Letters*, 848, L25

- Hallinan, G., Corsi, A., Mooley, K. P., et al. 2017, A radio counterpart to a neutron star merger, *Science*, 358, 1579
- Han, X. H., Wei, J. Y., Guillot, S., Wang, J., & Basa, S. 2020, LIGO/Virgo S200115j: no counterpart candidate in SVOM/GWAC observations, GRB Coordinates Network, 26786, 1
- Heinzel, J., Coughlin, M. W., Dietrich, T., et al. 2021, Comparing inclination-dependent analyses of kilonova transients, *Monthly Notices of the Royal Astronomical Society*, 502, 3057. <https://doi.org/10.1093/mnras/stab221>
- Ho, A. Y. Q., Goldstein, D. A., Schulze, S., et al. 2019, Evidence for Late-stage Eruptive Mass Loss in the Progenitor to SN2018gep, a Broad-lined Ic Supernova: Pre-explosion Emission and a Rapidly Rising Luminous Transient, *The Astrophysical Journal*, 887, 169
- Ho, A. Y. Q., Kulkarni, S. R., Perley, D. A., et al. 2020a, SN2020bvc: a Broad-lined Type Ic Supernova with a Double-peaked Optical Light Curve and a Luminous X-ray and Radio Counterpart, arXiv e-prints, arXiv:2004.10406
- Ho, A. Y. Q., Corsi, A., Cenko, S. B., et al. 2020b, The Broad-lined Ic Supernova ZTF18aaqjovh (SN 2018bvw): An Optically Discovered Engine-driven Supernova Candidate with Luminous Radio Emission, *The Astrophysical Journal*, 893, 132
- Hodgkin, S. T., Breedt, E., Delgado, A., et al. 2020, GaiaAlerts Transient Discovery Report for 2020-09-16, Transient Name Server Discovery Report, 2020-2816, 1
- Hook, I., Jørgensen, I., Allington-Smith, J., et al. 2004, The Gemini–North Multi-Object Spectrograph: Performance in imaging, long-slit, and multi-object spectroscopic modes, *Pub. Astron. Soc. Pac.*, 116, 425
- Hotokezaka, K., Beniamini, P., & Piran, T. 2018, Neutron star mergers as sites of r-process nucleosynthesis and short gamma-ray bursts, *International Journal of Modern Physics D*, 27, 1842005
- Hotokezaka, K., Kyutoku, K., Okawa, H., Shibata, M., & Kiuchi, K. 2011, Binary neutron star mergers: Dependence on the nuclear equation of state, *Physical Review D*, 83, 124008
- Hotokezaka, K., Kyutoku, K., Tanaka, M., et al. 2013, Progenitor Models of the Electromagnetic Transient Associated with the Short Gamma Ray Burst 130603B, *The Astrophysical Journal, Letters*, 778, L16
- Hotokezaka, K., Tanaka, M., Kato, D., & Gaigalas, G. 2021, Nebular emission from lanthanide-rich ejecta of neutron star merger, *Monthly Notices of the RAS*, 506, 5863

- Hoyle, F. 1954, On Nuclear Reactions Occuring in Very Hot STARS.I. the Synthesis of Elements from Carbon to Nickel., *The Astrophysical Journal, Supplement*, 1, 121
- Hu, Y. D., Fernández-García, E., Caballero-García, M. D., et al. 2023, The burst observer and optical transient exploring system in the multi-messenger astronomy era, *Frontiers in Astronomy and Space Sciences*, 10, 952887
- Huang, Y. F., Dai, Z. G., & Lu, T. 2002, Failed gamma-ray bursts and orphan afterglows, *Monthly Notices of the RAS*, 332, 735
- Hughes, J. P., Rakowski, C. E., Burrows, D. N., & Slane, P. O. 2000, Nucleosynthesis and Mixing in Cassiopeia A, *The Astrophysical Journal, Letters*, 528, L109
- Hughes, J. P., & Singh, K. P. 1994, Elemental Abundances of the Supernova Remnant G292.0+1.8: Evidence for a Massive Progenitor, *The Astrophysical Journal*, 422, 126
- Hulse, R. A., & Taylor, J. H. 1975, Discovery of a pulsar in a binary system., *The Astrophysical Journal, Letters*, 195, L51
- Hunter, D. J., Valenti, S., Kotak, R., et al. 2009, Extensive optical and near-infrared observations of the nearby, narrow-lined type Ic <ASTROBJ>SN 2007gr</ASTROBJ>: days 5 to 415, *Astronomy and Astrophysics*, 508, 371
- Ivezić, Ž., Kahn, S. M., Tyson, J. A., et al. 2019, LSST: From Science Drivers to Reference Design and Anticipated Data Products, *The Astrophysical Journal*, 873, 111
- Izzo, L., de Ugarte Postigo, A., Maeda, K., et al. 2019, Signatures of a jet cocoon in early spectra of a supernova associated with a  $\gamma$ -ray burst, *Nature*, 565, 324
- Jedicke, R., Bolin, B., Granvik, M., & Beshore, E. 2016, A fast method for quantifying observational selection effects in asteroid surveys, *Icarus*, 266, 173
- Ji, A. P., Frebel, A., Chiti, A., & Simon, J. D. 2016a, R-process enrichment from a single event in an ancient dwarf galaxy, *Nature*, 531, 610
- Ji, A. P., Frebel, A., Simon, J. D., & Chiti, A. 2016b, Complete Element Abundances of Nine Stars in the r-process Galaxy Reticulum II, *The Astrophysical Journal*, 830, 93
- Johnson, J. A., Fields, B. D., & Thompson, T. A. 2020, The origin of the elements: a century of progress, *Philosophical Transactions of the Royal Society A: Mathematical, Physical and Engineering Sciences*, 378, 20190301. <https://royalsocietypublishing.org/doi/abs/10.1098/rsta.2019.0301>
- Jones, D. O., French, K. D., Agnello, A., et al. 2021, YSE/Pan-STARRS1 Transient Discovery Report for 2021-07-17, *Transient Name Server Discovery Report*, 2021-2481, 1

- Jordi, K., Grebel, E. K., & Ammon, K. 2006, Empirical color transformations between SDSS photometry and other photometric systems, *Astronomy and Astrophysics*, 460, 339
- Just, O., Aloy, M. A., Obergaulinger, M., & Nagataki, S. 2022, r-process Viable Outflows are Suppressed in Global Alpha-viscosity Models of Collapsar Disks, *The Astrophysical Journal Letters*, 934, L30. <https://doi.org/10.3847/2041-8213/ac83a1>
- Just, O., Bauswein, A., Ardevol Pulpillo, R., Goriely, S., & Janka, H. T. 2015, Comprehensive nucleosynthesis analysis for ejecta of compact binary mergers, *Monthly Notices of the RAS*, 448, 541
- Kajino, T., Aoki, W., Balantekin, A., et al. 2019, Current status of r-process nucleosynthesis, *Progress in Particle and Nuclear Physics*, 107, 109. <http://dx.doi.org/10.1016/j.pnpnp.2019.02.008>
- Käppeler, F., Gallino, R., Bisterzo, S., & Aoki, W. 2011, The s process: Nuclear physics, stellar models, and observations, *Reviews of Modern Physics*, 83, 157
- Karambelkar, V., Ahumada, T., Stein, R., et al. 2023, LIGO/Virgo/KAGRA S230529ay: Zwicky Transient Facility observations, *General Coordinates Network*, 33900, 1
- Kasen, D., Badnell, N. R., & Barnes, J. 2013, Opacities and Spectra of the r-process Ejecta from Neutron Star Mergers, *The Astrophysical Journal*, 774, 25
- Kasen, D., Metzger, B., Barnes, J., Quataert, E., & Ramirez-Ruiz, E. 2017, Origin of the heavy elements in binary neutron-star mergers from a gravitational-wave event, *Nature*, 551, 80
- Kashiyama, K., Murase, K., Bartos, I., Kiuchi, K., & Margutti, R. 2016, Multimessenger Tests for Fast-spinning Newborn Pulsars Embedded in Stripped-envelope Supernovae, *The Astrophysical Journal*, 818, 94
- Kashyap, R., Raman, G., & Ajith, P. 2019, Can Kilonova Light curves be Standardized?, *Astrophys. J. Lett.*, 886, L19
- Kasliwal, M. M., Nakar, E., Singer, L. P., et al. 2017a, Illuminating gravitational waves: A concordant picture of photons from a neutron star merger, *Science*, 358, 1559
- . 2017b, Illuminating gravitational waves: A concordant picture of photons from a neutron star merger, *Science*, 358, 1559
- Kasliwal, M. M., Kasen, D., Lau, R. M., et al. 2019, Spitzer Mid-Infrared Detections of Neutron Star Merger GW170817 Suggests Synthesis of the Heaviest Elements, *Monthly Notices of the Royal Astronomical Society: Letters*, <http://oup.prod.sis.lan/mnrasl/advance-article->

- [pdf/doi/10.1093/mnrasl/slz007/27503647/slz007.pdf](https://doi.org/10.1093/mnrasl/slz007/27503647/slz007.pdf). <https://doi.org/10.1093/mnrasl/slz007>
- Kasliwal, M. M., Cannella, C., Bagdasaryan, A., et al. 2019, The GROWTH Marshal: A Dynamic Science Portal for Time-domain Astronomy, Publications of the ASP, 131, 038003
- Kasliwal, M. M., Anand, S., Ahumada, T., et al. 2020, Kilonova Luminosity Function Constraints Based on Zwicky Transient Facility Searches for 13 Neutron Star Merger Triggers during O3, *The Astrophysical Journal*, 905, 145
- Kasliwal, M. M., Kasen, D., Lau, R. M., et al. 2022, Spitzer mid-infrared detections of neutron star merger GW170817 suggests synthesis of the heaviest elements, *Monthly Notices of the RAS*, 510, L7
- Kasliwal et al. 2019, The GROWTH Marshal: A Dynamic Science Portal for Time-domain Astronomy, *Pub. Astron. Soc. Pac.*, 131, 038003
- Kawaguchi, K., Fujibayashi, S., Hotokezaka, K., Shibata, M., & Wanajo, S. 2022, Electromagnetic Counterparts of Binary-neutron-star Mergers Leading to a Strongly Magnetized Long-lived Remnant Neutron Star, *The Astrophysical Journal*, 933, 22
- Kawaguchi, K., Kyutoku, K., Shibata, M., & Tanaka, M. 2016, Models of Kilonova/Macronova Emission from Black Hole-Neutron Star Mergers, *The Astrophysical Journal*, 825, 52
- Kawaguchi, K., Kyutoku, K., Shibata, M., & Tanaka, M. 2016, Models of Kilonova/macronova Emission From Black Hole–neutron Star Mergers, *Astrophys. J.*, 825, 52
- Kawaguchi, K., Shibata, M., & Tanaka, M. 2020, Diversity of Kilonova Light Curves, *The Astrophysical Journal*, 889, 171
- Kawaguchi, K., Shibata, M., & Tanaka, M. 2020, Constraint on the Ejecta Mass for Black Hole–Neutron Star Merger Event Candidate S190814bv, *Astrophys. J.*, 893, 153. <http://dx.doi.org/10.3847/1538-4357/ab8309>
- Kilpatrick, C. D., Foley, R. J., Kasen, D., et al. 2017, Electromagnetic evidence that SSS17a is the result of a binary neutron star merger, *Science*, 358, 1583
- Kilpatrick, C. D., Coulter, D. A., Arcavi, I., et al. 2021, The Gravity Collective: A Search for the Electromagnetic Counterpart to the Neutron Star-Black Hole Merger GW190814, *The Astrophysical Journal*, 923, 258
- Kim, Y. L., Rigault, M., Neill, J. D., et al. 2022a, New Modules for the SED-Machine to Remove Contaminations from Cosmic Rays and Non-target Light: BYECR and CONTSEP, Publications of the ASP, 134, 024505

- . 2022b, New Modules for the SEDMachine to Remove Contaminations from Cosmic Rays and Non-target Light: BYECR and CONTSEP, Publications of the ASP, 134, 024505
- Kiuchi, K., Sekiguchi, Y., Kyutoku, K., et al. 2015, High resolution magnetohydrodynamic simulation of black hole-neutron star merger: Mass ejection and short gamma ray bursts, *Phys. Rev. D*, 92, 064034. <https://link.aps.org/doi/10.1103/PhysRevD.92.064034>
- Klimenko, S., Yakushin, I., Mercer, A., & Mitselmakher, G. 2008, A coherent method for detection of gravitational wave bursts, *Classical and Quantum Gravity*, 25, 114029
- Kocevski, D., Modjaz, M., Bloom, J. S., et al. 2007, Multicolor Infrared Observations of SN 2006aj. I. The Supernova Associated with XRF 060218, *The Astrophysical Journal*, 663, 1180
- Komiya, Y., & Shigeyama, T. 2016, Contribution of Neutron Star Mergers to the r-Process Chemical Evolution in the Hierarchical Galaxy Formation, *The Astrophysical Journal*, 830, 76
- Kondo, I., Sumi, T., Koshimoto, N., et al. 2023, Prediction of Planet Yields by the PRime-focus Infrared Microlensing Experiment Microlensing Survey, *AJ*, 165, 254
- Krüger, C. J., & Foucart, F. 2020, Estimates for disk and ejecta masses produced in compact binary mergers, *Physical Review D*, 101, 103002. <http://dx.doi.org/10.1103/PhysRevD.101.103002>
- Kulkarni, S. R., Frail, D. A., Wieringa, M. H., et al. 1998, Radio emission from the unusual supernova 1998bw and its association with the  $\gamma$ -ray burst of 25 April 1998, *Nature*, 395, 663
- Kulkarni, S. R., Harrison, F. A., Grefenstette, B. W., et al. 2021, Science with the Ultraviolet Explorer (UVEX), arXiv e-prints, arXiv:2111.15608
- Kumar, H., Swain, V., Salgundi, A., et al. 2023, LIGO/Virgo/KAGRA S230615az: GROWTH-India candidates, *General Coordinates Network*, 33974, 1
- Kumar, H., Bhalerao, V., Anupama, G. C., et al. 2022, India's First Robotic Eye for Time-domain Astrophysics: The GROWTH-India Telescope, *The Astronomical Journal*, 164, 90. <https://dx.doi.org/10.3847/1538-3881/ac7bea>
- Kumar, H., Bhalerao, V., Anupama, G. C., et al. 2022, India's First Robotic Eye for Time-domain Astrophysics: The GROWTH-India Telescope, *AJ*, 164, 90
- Kuncarayakti, H., Maeda, K., Dessart, L., et al. 2022, Late-time H/He-poor Circumstellar Interaction in the Type Ic Supernova SN 2021ocs: An Exposed Oxygen-Magnesium Layer and Extreme Stripping of the Progenitor, *The Astrophysical Journal, Letters*, 941, L32

- Kuncarayakti, H., Sollerman, J., Izzo, L., et al. 2023, The broad-lined Type-Ic supernova SN 2022xxf with extraordinary two-humped light curves, arXiv e-prints, arXiv:2303.16925
- Kunert, N., Antier, S., Nedora, V., et al. 2024, Bayesian model selection for GRB 211211A through multiwavelength analyses, *Monthly Notices of the RAS*, 527, 3900
- Kyutoku, K., Ioka, K., Okawa, H., Shibata, M., & Taniguchi, K. 2015, Dynamical mass ejection from black hole-neutron star binaries, *Phys.Rev.D*, 92, 044028
- Lamb, G. P., Lyman, J. D., Levan, A. J., et al. 2019, The Optical Afterglow of GW170817 at One Year Post-merger, *The Astrophysical Journal, Letters*, 870, L15
- Lattimer, J. M., & Schramm, D. N. 1974a, Black-Hole-Neutron-Star Collisions, *The Astrophysical Journal, Letters*, 192, L145
- . 1974b, Black-hole-neutron-star collisions, *Astrophys. J. Lett.*, 192, L145
- Lattimer, J. M., & Schramm, D. N. 1976, The tidal disruption of neutron stars by black holes in close binaries, *Astrophys. J.*, 210, 549
- Lee, J., Bahri, Y., Novak, R., et al. 2017, Deep Neural Networks as Gaussian Processes, arXiv e-prints, arXiv:1711.00165
- Levan, A. 2020, ENGRAVE: Electromagnetic counterparts of gravitational wave sources at the Very Large Telescope, *PoS, Asterics2019*, 044
- Levan, A. J., Gompertz, B. P., Salafia, O. S., et al. 2024, Heavy-element production in a compact object merger observed by JWST, *Nature*, 626, 737
- Li, J.-Y., Wang, S.-Q., Gan, W.-P., et al. 2022, Using the Optical-NIR Spectral Energy Distributions to Search for the Evidence of Dust Formation of 66 Supernovae, *The Astrophysical Journal*, 928, 77
- Li, L.-X., & Paczynski, B. 1998, Transient Events from Neutron Star Mergers, *Astrophys. J. Lett.*, 507, L59. <http://stacks.iop.org/1538-4357/507/i=1/a=L59>
- LIGO Scientific Collaboration, & Virgo Collaboration. 2019a, LIGO/Virgo S190426c: Identification of a GW compact binary merger candidate., *GRB Coordinates Network*, 24237, 1
- . 2019b, LIGO/Virgo S190814bv: Identification of a GW compact binary merger candidate., *GRB Coordinates Network*, 25324, 1
- . 2020a, LIGO/Virgo S200105ae: A subthreshold GW compact binary merger candidate, *GRB Coordinates Network*, 26640

- . 2020b, LIGO/Virgo S200115j: Identification of a GW compact binary merger candidate, GRB Coordinates Network, Circular Service, No. 26759, #1 (2020/Jan-0), 26759
  - . 2020c, LIGO/Virgo S200115j: Updated Sky Localization and source properties, GRB Coordinates Network, 26807, 1
  - . 2020d, LIGO/Virgo S200105ae: Further study ongoing for GW compact binary merger candidate, GRB Coordinates Network, 26657
  - . 2020e, LIGO/Virgo S200105ae: Updated Sky Localization and EM-Bright Probabilities, GRB Coordinates Network, 26688
- LIGO Scientific Collaboration, VIRGO Collaboration, & Kagra Collaboration.
- 2023a, LIGO/Virgo/KAGRA S230518h: Identification of a GW compact binary merger candidate, General Coordinates Network, 33813, 1
  - . 2023b, LIGO/Virgo/KAGRA S230529ay: Identification of a GW compact binary merger candidate, General Coordinates Network, 33889, 1
  - . 2023c, LIGO/Virgo/KAGRA S230627c: Identification of a GW compact binary merger candidate, General Coordinates Network, 34086, 1
  - . 2023d, LIGO/Virgo/KAGRA S230731an: Identification of a GW compact binary merger candidate, General Coordinates Network, 34303, 1
  - . 2023e, LIGO/Virgo/KAGRA S231113bw: Identification of a GW compact binary merger candidate, General Coordinates Network, 35016, 1
  - . 2024a, LIGO/Virgo/KAGRA S240422ed: Identification of a GW compact binary merger candidate, GRB Coordinates Network, 36236, 1
  - . 2024b, LIGO/Virgo/KAGRA S240422ed: Updated Sky localization and EM Bright Classification, GRB Coordinates Network, 36240, 1
- Liljegren, S., Jerkstrand, A., Barklem, P. S., et al. 2022, The molecular chemistry of Type Ibc supernovae, and diagnostic potential with the James Webb Space Telescope, arXiv e-prints, arXiv:2203.07021
- Lipunov, V., Gorbovskey, E., Kornilov, V., et al. 2020a, LIGO/Virgo S200105ae: Global MASTER-Net observations report, GRB Coordinates Network, 26646, 1
- . 2020b, LIGO/Virgo S200115j: Global MASTER-Net observations report, GRB Coordinates Network, 26755
- Lipunov, V. M., Gorbovskey, E., Kornilov, V. G., et al. 2017a, MASTER Optical Detection of the First LIGO/Virgo Neutron Star Binary Merger GW170817, The Astrophysical Journal, Letters, 850, L1

- . 2017b, MASTER Optical Detection of the First LIGO/Virgo Neutron Star Binary Merger GW170817, *The Astrophysical Journal, Letters*, 850, L1
- Liu, Y.-Q., Modjaz, M., Bianco, F. B., & Graur, O. 2016, Analyzing the Largest Spectroscopic Data Set of Stripped Supernovae to Improve Their Identifications and Constrain Their Progenitors, *The Astrophysical Journal*, 827, 90
- Lodders, K. 2003, Solar System Abundances and Condensation Temperatures of the Elements, *The Astrophysical Journal*, 591, 1220
- Lourie, N. P., Baker, J. W., Burruss, R. S., et al. 2020, in *Society of Photo-Optical Instrumentation Engineers (SPIE) Conference Series*, Vol. 11447, *Ground-based and Airborne Instrumentation for Astronomy VIII*, ed. C. J. Evans, J. J. Bryant, & K. Motohara, 114479K
- Lucy, L. B. 1999, Computing radiative equilibria with Monte Carlo techniques, *Astronomy and Astrophysics*, 344, 282
- Lundquist, M. J., Paterson, K., Fong, W., et al. 2019, Searches after Gravitational Waves Using ARizona Observatories (SAGUARO): System Overview and First Results from Advanced LIGO/Virgo’s Third Observing Run, *The Astrophysical Journal, Letters*, 881, L26
- Lyman, J. D., Bersier, D., & James, P. A. 2014, Bolometric corrections for optical light curves of core-collapse supernovae, *Monthly Notices of the RAS*, 437, 3848
- Lyman, J. D., Bersier, D., James, P. A., et al. 2016, Bolometric light curves and explosion parameters of 38 stripped-envelope core-collapse supernovae, *Monthly Notices of the RAS*, 457, 328
- Lynch, R., Vitale, S., Essick, R., Katsavounidis, E., & Robinet, F. 2017, Information-theoretic approach to the gravitational-wave burst detection problem, *Physical Review D*, 95, 104046
- MacFadyen, A. I., & Woosley, S. E. 1999, Collapsars: Gamma-Ray Bursts and Explosions in “Failed Supernovae”, *The Astrophysical Journal*, 524, 262
- MacFadyen, A. I., Woosley, S. E., & Heger, A. 2001, Supernovae, Jets, and Collapsars, *The Astrophysical Journal*, 550, 410
- Magee, M., Terwel, J., Prentice, S., Harvey, L., & Strotjohann, N. L. 2021, ePESSTO+ Transient Classification Report for 2021-02-03, *Transient Name Server Classification Report*, 2021-327, 1
- Mahabal, A., Rebbapragada, U., Walters, R., et al. 2019, Machine Learning for the Zwicky Transient Facility, *Publications of the ASP*, 131, 038002
- Maiorano, E., Rossi, A., Palazzi, E., et al. 2023, LIGO/Virgo/KAGRA S230615az: LBT spectroscopic classification of GOTO23hn, *General Coordinates Network*, 34066, 1

- Makhathini, S., Mooley, K. P., Brightman, M., et al. 2021, The Panchromatic Afterglow of GW170817: The Full Uniform Data Set, Modeling, Comparison with Previous Results, and Implications, *The Astrophysical Journal*, 922, 154
- Margalit, B., & Metzger, B. D. 2019, The Multi-messenger Matrix: The Future of Neutron Star Merger Constraints on the Nuclear Equation of State, *The Astrophysical Journal, Letters*, 880, L15
- Margutti, R., Berger, E., Fong, W., et al. 2017, The Electromagnetic Counterpart of the Binary Neutron Star Merger LIGO/Virgo GW170817. V. Rising X-Ray Emission from an Off-axis Jet, *The Astrophysical Journal, Letters*, 848, L20
- Margutti, R., Alexander, K. D., Xie, X., et al. 2018, The Binary Neutron Star Event LIGO/Virgo GW170817 160 Days after Merger: Synchrotron Emission across the Electromagnetic Spectrum, *The Astrophysical Journal, Letters*, 856, L18
- Martínez-Pinedo, G., Fischer, T., Lohs, A., & Huther, L. 2012, Charged-Current Weak Interaction Processes in Hot and Dense Matter and its Impact on the Spectra of Neutrinos Emitted from Protoneutron Star Cooling, *Physical Review Letters*, 109, 251104
- Masci, F. J., Laher, R. R., Rusholme, B., et al. 2019, The Zwicky Transient Facility: Data Processing, Products, and Archive, *Publications of the ASP*, 131, 018003
- Mazaeva, E., Pozanenko, A., Belkin, S., Klunko, E., & Volnova, A. 2020, LIGO/Virgo S200115j: Mondy upper limits for ZTF20aafqvyc/AT2020yq, GRB Coordinates Network, 26819, 1
- Mazzali, P. A., Deng, J., Maeda, K., et al. 2002, The Type Ic Hypernova SN 2002ap, *The Astrophysical Journal, Letters*, 572, L61
- McCully, C., Hiramatsu, D., Howell, D. A., et al. 2017, The Rapid Reddening and Featureless Optical Spectra of the Optical Counterpart of GW170817, AT 2017gfo, during the First Four Days, *The Astrophysical Journal, Letters*, 848, L32
- Meneguzzi, M., Audouze, J., & Reeves, H. 1971, The production of the elements Li, Be, B by galactic cosmic rays in space and its relation with stellar observations., *Astronomy and Astrophysics*, 15, 337
- Metzger, B. D. 2019, Kilonovae, *Living Reviews in Relativity*, 23
- Metzger, B. D., & Berger, E. 2012, What is the Most Promising Electromagnetic Counterpart of a Neutron Star Binary Merger?, *The Astrophysical Journal*, 746, 48
- Metzger, B. D., & Fernandez, R. 2014, Red or blue? A potential kilonova imprint of the delay until black hole formation following a neutron star merger, *Mon. Not. R. Astron. Soc.*, 441, 3444. <http://dx.doi.org/10.1093/mnras/stu802>

- Metzger, B. D., Giannios, D., & Horiuchi, S. 2011, Heavy nuclei synthesized in gamma-ray burst outflows as the source of ultrahigh energy cosmic rays, *Monthly Notices of the RAS*, 415, 2495
- Metzger, B. D., Piro, A. L., & Quataert, E. 2008, Time-dependent models of accretion discs formed from compact object mergers, *Monthly Notices of the RAS*, 390, 781
- . 2009, Neutron-rich freeze-out in viscously spreading accretion discs formed from compact object mergers, *Monthly Notices of the RAS*, 396, 304
- Metzger, B. D., Thompson, T. A., & Quataert, E. 2018, A Magnetar Origin for the Kilonova Ejecta in GW170817, *The Astrophysical Journal*, 856, 101
- Metzger, B. D., Martínez-Pinedo, G., Darbha, S., et al. 2010, Electromagnetic counterparts of compact object mergers powered by the radioactive decay of r-process nuclei, *Monthly Notices of the RAS*, 406, 2650
- Miller, A. A., Kulkarni, M. K., Cao, Y., et al. 2017, Preparing for Advanced LIGO: A Star-Galaxy Separation Catalog for the Palomar Transient Factory, *Astrophys. J.*, 153, 73
- Miller, J. M., Sprouse, T. M., Fryer, C. L., et al. 2020, Full Transport General Relativistic Radiation Magnetohydrodynamics for Nucleosynthesis in Collapsars, *The Astrophysical Journal*, 902, 66
- Misner, C. W., Thorne, K. S., & Wheeler, J. A. 1973, *Gravitation*
- Modjaz, M., Liu, Y. Q., Bianco, F. B., & Graur, O. 2016, The Spectral SN-GRB Connection: Systematic Spectral Comparisons between Type Ic Supernovae and Broad-lined Type Ic Supernovae with and without Gamma-Ray Bursts, *The Astrophysical Journal*, 832, 108
- Modjaz, M., Kewley, L., Kirshner, R. P., et al. 2008, Measured Metallicities at the Sites of Nearby Broad-Lined Type Ic Supernovae and Implications for the Supernovae Gamma-Ray Burst Connection, *AJ*, 135, 1136
- Mohite, S. R., Rajkumar, P., Anand, S., et al. 2022, Inferring Kilonova Population Properties with a Hierarchical Bayesian Framework. I. Nondetection Methodology and Single-event Analyses, *The Astrophysical Journal*, 925, 58. <https://dx.doi.org/10.3847/1538-4357/ac3981>
- Möller, A., Peloton, J., Ishida, E. E. O., et al. 2020, <scp>fink</scp>, a new generation of broker for the LSST community, *Monthly Notices of the Royal Astronomical Society*, 501, 3272. <http://dx.doi.org/10.1093/mnras/staa3602>
- Mooley, K. P., Anderson, J., & Lu, W. 2022, Optical superluminal motion measurement in the neutron-star merger GW170817, *Nature*, 610, 273

- Mooley, K. P., Frail, D. A., Dobie, D., et al. 2018, A Strong Jet Signature in the Late-time Light Curve of GW170817, *The Astrophysical Journal, Letters*, 868, L11
- Morgan, R., Soares-Santos, M., Annis, J., et al. 2020, Constraints on the Physical Properties of GW190814 through Simulations Based on DECam Follow-up Observations by the Dark Energy Survey, *The Astrophysical Journal*, 901, 83
- Naidu, R. P., Ji, A. P., Conroy, C., et al. 2021, Evidence from Disrupted Halo Dwarfs that *r*-process Enrichment via Neutron Star Mergers is Delayed by *rsim*500 Myrs, arXiv e-prints, arXiv:2110.14652
- Nakamura, K., Kajino, T., Mathews, G. J., Sato, S., & Harikae, S. 2015, *r*-process nucleosynthesis in the MHD+neutrino-heated collapsar jet, *Astronomy and Astrophysics*, 582, A34
- Nakamura, T., Mazzali, P. A., Nomoto, K., & Iwamoto, K. 2001, Light Curve and Spectral Models for the Hypernova SN 1998bw Associated with GRB 980425, *The Astrophysical Journal*, 550, 991. <https://doi.org/10.1086/319784>
- Nakar, E. 2015, A Unified Picture for Low-luminosity and Long Gamma-Ray Bursts Based on the Extended Progenitor of IIGRB 060218/SN 2006aj, *The Astrophysical Journal*, 807, 172
- Nakar, E., & Piran, T. 2016, THE OBSERVABLE SIGNATURES OF GRB COCOONS, *The Astrophysical Journal*, 834, 28. <https://dx.doi.org/10.3847/1538-4357/834/1/28>
- Narayan, R., Paczynski, B., & Piran, T. 1992, Gamma-Ray Bursts as the Death Throes of Massive Binary Stars, *The Astrophysical Journal, Letters*, 395, L83
- Nedora, V., Bernuzzi, S., Radice, D., et al. 2021, Numerical Relativity Simulations of the Neutron Star Merger GW170817: Long-term Remnant Evolutions, Winds, Remnant Disks, and Nucleosynthesis, *The Astrophysical Journal*, 906, 98
- Nicholl, M., Berger, E., Kasen, D., et al. 2017, The Electromagnetic Counterpart of the Binary Neutron Star Merger LIGO/Virgo GW170817. III. Optical and UV Spectra of a Blue Kilonova from Fast Polar Ejecta, *The Astrophysical Journal, Letters*, 848, L18
- Nitz, A. H., Dal Canton, T., Davis, D., & Reyes, S. 2018, Rapid detection of gravitational waves from compact binary mergers with PyCBC Live, *Physical Review D*, 98, 024050
- Nordin, J., Brinnel, V., Giomi, M., et al. 2018, ZTF Transient Discovery Report for 2018-11-26, Transient Name Server Discovery Report, 2018-1827, 1
- . 2019, ZTF Transient Discovery Report for 2019-06-04, Transient Name Server Discovery Report, 2019-930, 1

- . 2020, ZTF Transient Discovery Report for 2020-02-24, Transient Name Server Discovery Report, 2020-613, 1
- Nordin, J., Brinnel, V., Santen, J. V., et al. 2021, AMPEL/ZTF Transient Discovery Report for 2021-09-14, Transient Name Server Discovery Report, 2021-3174, 1
- Nordin, J., Brinnel, V., van Santen, J., et al. 2019, Transient processing and analysis using AMPEL: alert management, photometry, and evaluation of light curves, *Astron. Astrophys.*, 631, A147. <http://dx.doi.org/10.1051/0004-6361/201935634>
- Nordin, J., Brinnel, V., van Santen, J., et al. 2019, Transient processing and analysis using AMPEL: alert management, photometry, and evaluation of light curves, *Astronomy and Astrophysics*, 631, A147
- Noysena, K., Antier, S., Blazek, M., et al. 2020, LIGO/Virgo S200115j : No significant candidates in TAROT - FRAM - GRANDMA observations, GRB Coordinates Network, 26820, 1
- Ochsenbein, F., Bauer, P., & Marcout, J. 2000, The VizieR database of astronomical catalogues, *Astronomy and Astrophysics, Supplement*, 143, 23
- Oke, J. B., & Gunn, J. E. 1982, An Efficient Low Resolution and Moderate Resolution Spectrograph for the Hale Telescope, *Publications of the Astronomical Society of the Pacific*, 94, 586. <https://doi.org/10.1086/131027>
- Oke, J. B., Cohen, J. G., Carr, M., et al. 1995, The Keck Low-Resolution Imaging Spectrometer, *Publications of the Astronomical Society of the Pacific*, 107, 375. <https://doi.org/10.1086/133562>
- Olivares E., F., Greiner, J., Schady, P., et al. 2012, The fast evolution of SN 2010bh associated with XRF 100316D, *Astronomy and Astrophysics*, 539, A76
- Omand, C. M. B., & Jerkstrand, A. 2022, Towards Nebular Spectral Modeling of Magnetar-Powered Supernovae, arXiv e-prints, arXiv:2211.04502
- Omand, C. M. B., Kashiyama, K., & Murase, K. 2019, Dust formation in embryonic pulsar-aided supernova remnants, *Monthly Notices of the RAS*, 484, 5468
- Ono, M., Hashimoto, M., Fujimoto, S., Kotake, K., & Yamada, S. 2012, Explosive Nucleosynthesis in Magnetohydrodynamical Jets from Collapsars. II — Heavy-Element Nucleosynthesis of s, p, r-Processes, *Progress of Theoretical Physics*, 128, 741
- Paek, G. S. H., Im, M., Kim, J., et al. 2024, Gravitational-wave Electromagnetic Counterpart Korean Observatory (GECKO): GECKO Follow-up Observation of GW190425, *The Astrophysical Journal*, 960, 113

- Pang, P. T. H., Dietrich, T., Coughlin, M. W., et al. 2022, NMMA: A nuclear-physics and multi-messenger astrophysics framework to analyze binary neutron star mergers, arXiv e-prints, arXiv:2205.08513
- Patat, F., Cappellaro, E., Danziger, J., et al. 2001, The Metamorphosis of SN 1998bw, *The Astrophysical Journal*, 555, 900
- Patterson, M. T., Bellm, E. C., Rusholme, B., et al. 2019, The Zwicky Transient Facility Alert Distribution System, *Publications of the ASP*, 131, 018001
- Patterson et al. 2018, The Zwicky Transient Facility Alert Distribution System, Accepted by PASP
- Perego, A., Rosswog, S., Cabezón, R. M., et al. 2014, Neutrino-driven winds from neutron star merger remnants, *Monthly Notices of the RAS*, 443, 3134
- Perley, D. A. 2019, Fully Automated Reduction of Longslit Spectroscopy with the Low Resolution Imaging Spectrometer at the Keck Observatory, *Publications of the ASP*, 131, 084503
- Perley, D. A., Fremling, C., Sollerman, J., et al. 2020, The Zwicky Transient Facility Bright Transient Survey. II. A Public Statistical Sample for Exploring Supernova Demographics, *The Astrophysical Journal*, 904, 35
- Perley, D. A., Ho, A. Y. Q., Fausnaugh, M., et al. 2024, AT2019pim: A Luminous Orphan Afterglow from a Moderately Relativistic Outflow, arXiv e-prints, arXiv:2401.16470
- Pessi, P. J., Gromadski, M., & Strotjohann, N. L. 2021, ePESSTO+ Transient Classification Report for 2021-08-02, *Transient Name Server Classification Report*, 2021-2659, 1
- Pian, E., D'Avanzo, P., Benetti, S., et al. 2017a, Spectroscopic identification of r-process nucleosynthesis in a double neutron-star merger, *Nature*, 551, 67
- . 2017b, Spectroscopic identification of r-process nucleosynthesis in a double neutron-star merger, *Nature*, 551, 67
- Podsiadlowski, P., Mazzali, P. A., Nomoto, K., Lazzati, D., & Cappellaro, E. 2004, The Rates of Hypernovae and Gamma-Ray Bursts: Implications for Their Progenitors, *The Astrophysical Journal, Letters*, 607, L17
- Pooley, D., Kumar, P., Wheeler, J. C., & Grossan, B. 2018, GW170817 Most Likely Made a Black Hole, *The Astrophysical Journal, Letters*, 859, L23
- Pozanenko, A. S., Barkov, M. V., Minaev, P. Y., et al. 2018, GRB 170817A Associated with GW170817: Multi-frequency Observations and Modeling of Prompt Gamma-Ray Emission, *The Astrophysical Journal*, 852, L30. <https://doi.org/10.3847/2F2041-8213/2Faa2f6>

- Prantzos, N. 2012, Production and evolution of Li, Be, and B isotopes in the Galaxy, *Astronomy and Astrophysics*, 542, A67
- Prentice, S. J., Maguire, K., Skillen, K., Magee, M. R., & Clark, P. 2019, TCD Transient Classification Report for 2019-12-20, Transient Name Server Classification Report, 2019-2659, 1
- Pritchard, T. A., Bensch, K., Modjaz, M., et al. 2021, The Exotic Type Ic Broad-lined Supernova SN 2018gep: Blurring the Line between Supernovae and Fast Optical Transients, *The Astrophysical Journal*, 915, 121
- Prochaska, J. X., Hennawi, J., Cooke, R., et al. 2019, PypeIt: Python spectroscopic data reduction pipeline, *Astrophysics Source Code Library*, record ascl:1911.004, , ascl:1911.004
- Qian, Y. Z., & Woosley, S. E. 1996, Nucleosynthesis in Neutrino-driven Winds. I. The Physical Conditions, *The Astrophysical Journal*, 471, 331
- Radice, D., Perego, A., Hotokezaka, K., et al. 2018, Binary Neutron Star Mergers: Mass Ejection, Electromagnetic Counterparts, and Nucleosynthesis, *The Astrophysical Journal*, 869, 130
- Rana, J., Anand, S., & Bose, S. 2019, Optimal Search Strategy for Finding Transients in Large-sky Error Regions under Realistic Constraints, *Astrophys. J.*, 876, 104. <http://dx.doi.org/10.3847/1538-4357/ab165a>
- Rank, D. M., Pinto, P. A., Woosley, S. E., et al. 1988, Nickel, argon and cobalt in the infrared spectrum of SN1987A: the core becomes visible, *Nature*, 331, 505
- Rastinejad, J. C., Gompertz, B. P., Levan, A. J., et al. 2022, A Kilonova Following a Long-Duration Gamma-Ray Burst at 350 Mpc, arXiv e-prints, arXiv:2204.10864
- Rastinejad, J. C., Paterson, K., Fong, W., et al. 2022, A Systematic Exploration of Kilonova Candidates from Neutron Star Mergers during the Third Gravitational-wave Observing Run, *The Astrophysical Journal*, 927, 50. <https://dx.doi.org/10.3847/1538-4357/ac4d34>
- Rastinejad, J. C., Fong, W., Levan, A. J., et al. 2023, A Hubble Space Telescope Search for r-Process Nucleosynthesis in Gamma-ray Burst Supernovae, arXiv e-prints, arXiv:2312.04630
- Raza, N., Chan, M. L., Haggard, D., et al. 2024, Explaining the GWSkyNet-Multi Machine Learning Classifier Predictions for Gravitational-wave Events, *The Astrophysical Journal*, 963, 98
- Reggiani, H., Schlaufman, K. C., Casey, A. R., Simon, J. D., & Ji, A. P. 2021, The Most Metal-poor Stars in the Magellanic Clouds Are r-process Enhanced, *AJ*, 162, 229

- Rigault, M., Neill, J. D., Blagorodnova, N., et al. 2019a, Fully automated integral field spectrograph pipeline for the SEDMachine: pypedm, *Astronomy and Astrophysics*, 627, A115
- . 2019b, A Fully Automated Integral Field Spectrograph Pipeline for the SEDMachine: pypedm, arXiv e-prints, arXiv:1902.08526
- Roberson, M., Fremling, C., & Kasliwal, M. 2022, DBSP\_DRP: A Python package for automated spectroscopic data reduction of DBSP data, *The Journal of Open Source Software*, 7, 3612
- Roberts, L. F., Kasen, D., Lee, W. H., & Ramirez-Ruiz, E. 2011, Electromagnetic Transients Powered by Nuclear Decay in the Tidal Tails of Coalescing Compact Binaries, *Astrophys. J. Lett.*, 736, L21. <http://stacks.iop.org/2041-8205/736/i=1/a=L21>
- Roberts, L. F., Woosley, S. E., & Hoffman, R. D. 2010, Integrated Nucleosynthesis in Neutrino-driven Winds, *The Astrophysical Journal*, 722, 954
- Roederer, I. U., Mateo, M., Bailey, John I., I., et al. 2016, Detailed Chemical Abundances in the r-process-rich Ultra-faint Dwarf Galaxy Reticulum 2, *AJ*, 151, 82
- Rosswog, S. 2015, The multi-messenger picture of compact binary mergers, *Int. J. Mod. Phys.*, D24, 1530012
- Rosswog, S., Feindt, U., Korobkin, O., et al. 2017, Detectability of compact binary merger macronovae, *Class. Quant. Grav.*, 34, 104001
- Rosswog, S., & Korobkin, O. 2022, Heavy elements and electromagnetic transients from neutron star mergers, arXiv e-prints, arXiv:2208.14026
- Rosswog, S., Liebendörfer, M., Thielemann, F. K., et al. 1999, Mass ejection in neutron star mergers, *Astronomy and Astrophysics*, 341, 499
- Saha, A., Matheson, T., Snodgrass, R., et al. 2014, in *Society of Photo-Optical Instrumentation Engineers (SPIE) Conference Series*, Vol. 9149, *Observatory Operations: Strategies, Processes, and Systems V*, ed. A. B. Peck, C. R. Benn, & R. L. Seaman, 914908
- Savchenko, V., Ferrigno, C., Kuulkers, E., et al. 2017, INTEGRAL Detection of the First Prompt Gamma-Ray Signal Coincident with the Gravitational-wave Event GW170817, *The Astrophysical Journal*, 848, L15
- Schlafly, E. F., & Finkbeiner, D. P. 2011, Measuring reddening with Sloan Digital Sky Survey stellar spectra and recalibrating SFD, *Astrophys. J.*, 737, 103
- Schulze, S., & Sollerman, J. 2021, ZTF Transient Classification Report for 2021-01-25, *Transient Name Server Classification Report*, 2021-244, 1

- Schulze, S., Irani, I., Zimmerman, E., et al. 2020, ePESSTO+ spectroscopic classification of optical transients, *Transient Name Server AstroNote*, 13, 1
- Schutz, B. F. 1986, Determining the Hubble constant from gravitational wave observations, *Nat*, 323, 310
- Sekiguchi, Y., Kiuchi, K., Kyutoku, K., Shibata, M., & Taniguchi, K. 2016, Dynamical mass ejection from the merger of asymmetric binary neutron stars: Radiation-hydrodynamics study in general relativity, *Physical Review D*, 93, 124046
- Setzer, C. N., Peiris, H. V., Korobkin, O., & Rosswog, S. 2023, Modelling populations of kilonovae, *Monthly Notices of the RAS*, 520, 2829
- Shappee, B. J., Prieto, J. L., Grupe, D., et al. 2014, The Man behind the Curtain: X-Rays Drive the UV through NIR Variability in the 2013 Active Galactic Nucleus Outburst in NGC 2617, *Astrophys. J.*, 788, 48
- Shappee, B. J., Simon, J. D., Drout, M. R., et al. 2017, Early spectra of the gravitational wave source GW170817: Evolution of a neutron star merger, *Science*, 358, 1574
- Shibata, M., & Taniguchi, K. 2006, Merger of binary neutron stars to a black hole: Disk mass, short gamma-ray bursts, and quasinormal mode ringing, *Physical Review D*, 73, 064027
- Shingles, L., Smith, K. W., Young, D. R., et al. 2021, Release of the ATLAS Forced Photometry server for public use, *Transient Name Server AstroNote*, 7, 1
- Shvartzvald, Y., Waxman, E., Gal-Yam, A., et al. 2023, ULTRASAT: A wide-field time-domain UV space telescope, *arXiv e-prints*, arXiv:2304.14482
- Siegel, D. M. 2019, GW170817—the first observed neutron star merger and its kilonova: implications for the astrophysical site of the r-process, *Eur. Phys. J. A*, 55, 203
- Siegel, D. M., Barnes, J., & Metzger, B. D. 2019, Collapsars as a major source of r-process elements, *Nature*, 569, 241
- Siegel, D. M., & Metzger, B. D. 2017, Three-Dimensional General-Relativistic Magnetohydrodynamic Simulations of Remnant Accretion Disks from Neutron Star Mergers: Outflows and r-Process Nucleosynthesis, *Phys. Rev. Lett.*, 119, 231102. <http://dx.doi.org/10.1103/PhysRevLett.119.231102>
- Singer, L., & Racusin, J. 2023, in *American Astronomical Society Meeting Abstracts*, Vol. 55, American Astronomical Society Meeting Abstracts, 108.02
- Singer, L. P., Parazin, B., Coughlin, M. W., et al. 2022, HEALPix Alchemy: Fast All-Sky Geometry and Image Arithmetic in a Relational Database for Multimesenger Astronomy Brokers, *The Astronomical Journal*, 163, 209

- Singer, L. P., & Price, L. R. 2016, Rapid Bayesian position reconstruction for gravitational-wave transients, *Phys. Rev. D*, 93, 024013. <https://link.aps.org/doi/10.1103/PhysRevD.93.024013>
- Siqueira Mello, C., Hill, V., Barbuy, B., et al. 2014, High-resolution abundance analysis of very metal-poor r-I stars, *Astronomy and Astrophysics*, 565, A93
- Skrutskie, M. F., Cutri, R. M., Stiening, R., et al. 2006, The Two Micron All Sky Survey (2MASS), *Astrophys. J.*, 131, 1163
- Smartt, S. J., Chen, T. W., Jerkstrand, A., et al. 2017, A kilonova as the electromagnetic counterpart to a gravitational-wave source, *Nature*, 551, 75
- Smith, K. W., Williams, R. D., Young, D. R., et al. 2019, Lasair: The Transient Alert Broker for LSST:UK, *Research Notes of the AAS*, 3, 26. <https://dx.doi.org/10.3847/2515-5172/ab020f>
- Soares-Santos, M., Holz, D., Annis, J., Chornock, R., & Herner, K. 2017, The Electromagnetic Counterpart of the Binary Neutron Star Merger LIGO/Virgo GW170817. I. Discovery of the Optical Counterpart Using the Dark Energy Camera, *Astrophys. J. Lett.*, 848, L16
- Soares-Santos et al. 2017, The Electromagnetic Counterpart of the Binary Neutron Star Merger LIGO/Virgo GW170817. I. Discovery of the Optical Counterpart Using the Dark Energy Camera, *Astrophys. J. Lett.*, 848, L16. <http://stacks.iop.org/2041-8205/848/i=2/a=L16>
- Soker, N., & Gilkis, A. 2017, Magnetar-powered Superluminous Supernovae Must First Be Exploded by Jets, *The Astrophysical Journal*, 851, 95
- Soumagnac, M. T., & Ofek, E. O. 2018, catsHTM: A Tool for Fast Accessing and Cross-matching Large Astronomical Catalogs, *Pub. Astron. Soc. Pac.*, 130, 075002
- Srinivasaragavan, G. P., Swain, V., O'Connor, B., et al. 2024, Characterizing the Ordinary Broad-line Type Ic SN 2023pel from the Energetic GRB 230812B, *The Astrophysical Journal, Letters*, 960, L18
- Srivastav, S., Smartt, S. J., McBrien, O., et al. 2020, Transient Classification Report for 2020-09-22, *Transient Name Server Classification Report*, 2020-2903, 1
- Steeghs, D., Ulaczyk, K., Lyman, J., et al. 2020, LIGO/Virgo S200115j: No notable candidates in GOTO imaging, *GRB Coordinates Network*, 26794, 1
- Steele, I. A., Smith, R. J., Rees, P. C., et al. 2004, in *Society of Photo-Optical Instrumentation Engineers (SPIE) Conference Series*, Vol. 5489, *Ground-based Telescopes*, ed. J. Oschmann, Jacobus M., 679–692
- Steele, I. A., Smith, R. J., Rees, P. C., et al. 2004, in *Ground-based Telescopes*, Vol. 5489, *International Society for Optics and Photonics*, 679–692

- Stein, R., Reusch, S., & Necker, J. 2023, desy-multimessenger/nuztf: v2.7.1 Release, vv2.7.1, Zenodo, doi:10.5281/zenodo.7990902. <https://doi.org/10.5281/zenodo.7990902>
- Stein, R., Anand, S., Coughlin, M., et al. 2020, LIGO/Virgo S200105ae: Candidates from the Zwicky Transient Facility., GRB Coordinates Network, 26673, 1
- Stein, R., Reusch, S., Franckowiak, A., et al. 2023, Neutrino follow-up with the Zwicky transient facility: results from the first 24 campaigns, Monthly Notices of the RAS, 521, 5046
- Strausbaugh, R., Pyshna, O., Du Laz, T., et al. 2023, LIGO/Virgo/KAGRA S230615az: GRANDMA observations of GOTO and GIT candidates, General Coordinates Network, 34020, 1
- Stritzinger, M. D., Taddia, F., Burns, C. R., et al. 2018a, The Carnegie Supernova Project I. Methods to estimate host-galaxy reddening of stripped-envelope supernovae, *Astronomy and Astrophysics*, 609, A135
- Stritzinger, M. D., Anderson, J. P., Contreras, C., et al. 2018b, The Carnegie Supernova Project I. Photometry data release of low-redshift stripped-envelope supernovae, *Astronomy and Astrophysics*, 609, A134
- Surman, R., McLaughlin, G. C., & Hix, W. R. 2006, Nucleosynthesis in the Outflow from Gamma-Ray Burst Accretion Disks, *The Astrophysical Journal*, 643, 1057
- Suzuki, A., & Maeda, K. 2021, Two-dimensional Radiation-hydrodynamic Simulations of Supernova Ejecta with a Central Power Source, *The Astrophysical Journal*, 908, 217
- Swain, V., Kumar, H., Karambelkar, V., et al. 2023, LIGO/Virgo/KAGRA S230521k: Additional candidates from Zwicky Transient Facility, General Coordinates Network, 33858, 1
- Symbalysty, E., & Schramm, D. N. 1982, Neutron Star Collisions and the r-Process, *Astrophysics Letters*, 22, 143
- Tachibana & Miller. 2018, A Morphological Classification Model to Identify Unresolved PanSTARRS1 Sources: Application in the ZTF Real-time Pipeline, *Publications of the Astronomical Society of the Pacific*, 130, 128001
- Tachibana, Y., & Miller, A. A. 2018, A Morphological Classification Model to Identify Unresolved PanSTARRS1 Sources: Application in the ZTF Real-time Pipeline, *Publications of the ASP*, 130, 128001
- Taddia, F., Stritzinger, M. D., Bersten, M., et al. 2018, The Carnegie Supernova Project I. Analysis of stripped-envelope supernova light curves, *Astronomy and Astrophysics*, 609, A136

- Takahashi, K., Wittig, J., & Janka, H. T. 1994, Nucleosynthesis in neutrino-driven winds from protoneutron stars II. The r-process, *Astronomy and Astrophysics*, 286, 857
- Tanaka, M., Hotokezaka, K., Kyutoku, K., et al. 2014, Radioactively Powered Emission from Black Hole-Neutron Star Mergers, *Astrophys. J.*, 780, 31
- Tanaka, M., Kato, D., Gaigalas, G., & Kawaguchi, K. 2020, Systematic opacity calculations for kilonovae, *Monthly Notices of the RAS*, 496, 1369
- Tanga, M., Krühler, T., Schady, P., et al. 2018, The environment of the SN-less GRB 111005A at  $z = 0.0133$ , *Astronomy and Astrophysics*, 615, A136
- Tanvir, N. R., Levan, A. J., González-Fernández, C., et al. 2017, The Emergence of a Lanthanide-rich Kilonova Following the Merger of Two Neutron Stars, *The Astrophysical Journal, Letters*, 848, L27
- Tartaglia, L., Sollerman, J., Barbarino, C., et al. 2021, SN 2018ijp: the explosion of a stripped-envelope star within a dense H-rich shell?, *Astronomy and Astrophysics*, 650, A174
- Tarumi, Y., Yoshida, N., & Inoue, S. 2020, R-process enrichment in ultrafaint dwarf galaxies, *Monthly Notices of the RAS*, 494, 120
- Tatischeff, V., & Gabici, S. 2018, Particle Acceleration by Supernova Shocks and Spallogenic Nucleosynthesis of Light Elements, *Annual Review of Nuclear and Particle Science*, 68, 377
- Terreran, G., Margutti, R., Bersier, D., et al. 2019, SN 2016coi (ASASSN-16fp): An Energetic H-stripped Core-collapse Supernova from a Massive Stellar Progenitor with Large Mass Loss, *The Astrophysical Journal*, 883, 147
- Thakur, A. L., Dichiaro, S., Troja, E., et al. 2021, Erratum: A search for optical and near-infrared counterparts of the compact binary merger GW190814, *Monthly Notices of the RAS*, 501, 2821
- The 2023 Windows on the Universe Workshop White Paper Working Group. 2024, Windows on the Universe: Establishing the Infrastructure for a Collaborative Multi-messenger Ecosystem, arXiv e-prints, arXiv:2401.02063
- The LIGO Scientific Collaboration and the Virgo Collaboration and the KAGRA Collaboration. 2024, Observation of Gravitational Waves from the Coalescence of a 2.5–4.5 M Compact Object and a Neutron Star, LIGO P2300352-v9
- Thoennessen, M. 2004, Reaching the limits of nuclear stability, *Reports on Progress in Physics*, 67, 1187
- Thompson, T. A., Burrows, A., & Meyer, B. S. 2001, The Physics of Proto-Neutron Star Winds: Implications for r-Process Nucleosynthesis, *The Astrophysical Journal*, 562, 887

- Tissot, F. L. H., Dauphas, N., & Grossman, L. 2016, Origin of uranium isotope variations in early solar nebula condensates, *Science Advances*, 2, e1501400
- Tiwari, V., Fairhurst, S., & Hannam, M. 2018, Constraining Black Hole Spins with Gravitational-wave Observations, *The Astrophysical Journal*, 868, 140
- Tomita, H., Deng, J., Maeda, K., et al. 2006, The Optical/Near-Infrared Light Curves of SN 2002ap for the First 1.5 Years after Discovery, *The Astrophysical Journal*, 644, 400
- Tonry, J., Denneau, L., Heinze, A., et al. 2019a, ATLAS Transient Discovery Report for 2019-09-17, Transient Name Server Discovery Report, 2019-1841, 1
- . 2019b, ATLAS Transient Discovery Report for 2019-08-04, Transient Name Server Discovery Report, 2019-1407, 1
- . 2021, ATLAS Transient Discovery Report for 2021-02-02, Transient Name Server Discovery Report, 2021-312, 1
- Tonry, J. L., Denneau, L., Heinze, A. N., et al. 2018, ATLAS: A High-cadence All-sky Survey System, *Pub. Astron. Soc. Pac.*, 130, 064505. <http://stacks.iop.org/1538-3873/130/i=988/a=064505>
- Troja, E., Piro, L., van Eerten, H., et al. 2017, The X-ray counterpart to the gravitational-wave event GW170817, *Nature*, 551, 71
- Tucker, D. L., Wiesner, M. P., Allam, S. S., et al. 2022, SOAR/Goodman Spectroscopic Assessment of Candidate Counterparts of the LIGO/Virgo Event GW190814, *The Astrophysical Journal*, 929, 115
- Turpin, D., Coleiro, A., Karpov, S., et al. 2020, LIGO/Virgo S200105ae : No significant candidates in TAROT - FRAM - GRANDMA observations., *GRB Coordinates Network*, 26687, 1
- Urey, H. C. 1952, ABUNDANCES OF THE ELEMENTS, *Annals of the New York Academy of Sciences*, 194. <https://api.semanticscholar.org/CorpusID:84296907>
- Utsumi, Y., Tanaka, M., Tominaga, N., et al. 2017, J-GEM observations of an electromagnetic counterpart to the neutron star merger GW170817, *PASJ*, 69, 101
- Valeev, A. F., Castro-Tirado, A. J., Hu, Y.-D., et al. 2020, LIGO/Virgo S200105ae: AT2020pp and AT2020py 10.4m GTC spectroscopy, *GRB Coordinates Network*, 26702
- Valenti, S., David, J. S., Yang, S., et al. 2017, The Discovery of the Electromagnetic Counterpart of GW170817: Kilonova AT 2017gfo/DLT17ck, *The Astrophysical Journal*, 848, L24. <https://doi.org/10.3847/2041-8213/2Faa8edf>

- Vallely, P. J., Kochanek, C. S., Stanek, K. Z., Fausnaugh, M., & Shappee, B. J. 2021, High-cadence, early-time observations of core-collapse supernovae from the TESS prime mission, *Monthly Notices of the RAS*, 500, 5639
- van der Walt, S., Crellin-Quick, A., & Bloom, J. 2019, SkyPortal: An Astronomical Data Platform, *The Journal of Open Source Software*, 4, 1247
- van der Walt, S. J., Crellin-Quick, A., & Bloom, J. S. 2019, SkyPortal: An Astronomical Data Platform, *Journal of Open Source Software*, 4, doi:10.21105/joss.01247. <http://joss.theoj.org/papers/10.21105/joss.01247>
- Vieira, N., Ruan, J. J., Haggard, D., et al. 2020, A Deep CFHT Optical Search for a Counterpart to the Possible Neutron Star-Black Hole Merger GW190814, *The Astrophysical Journal*, 895, 96
- Villar, V. A., Guillochon, J., Berger, E., et al. 2017, The Combined Ultraviolet, Optical, and Near-infrared Light Curves of the Kilonova Associated with the Binary Neutron Star Merger GW170817: Unified Data Set, Analytic Models, and Physical Implications, *The Astrophysical Journal, Letters*, 851, L21
- Villar, V. A., Guillochon, J., Berger, E., et al. 2017, The Combined Ultraviolet, Optical, and Near-infrared Light Curves of the Kilonova Associated with the Binary Neutron Star Merger GW170817: Unified Data Set, Analytic Models, and Physical Implications, *Astrophys. J. Lett.*, 851, L21. <http://stacks.iop.org/2041-8205/851/i=1/a=L21>
- Vitale, S., & Chen, H.-Y. 2018, Measuring the Hubble Constant with Neutron Star Black Hole Mergers, *Phys. Rev. Lett.*, 121, 021303. <https://link.aps.org/doi/10.1103/PhysRevLett.121.021303>
- Wallner, A., Faestermann, T., Feige, J., et al. 2015, Abundance of live  $^{244}\text{Pu}$  in deep-sea reservoirs on Earth points to rarity of actinide nucleosynthesis, *Nature Communications*, 6, 5956
- Wallner, A., Froehlich, M. B., Hotchkis, M. A. C., et al. 2021,  $^{60}\text{Fe}$  and  $^{244}\text{Pu}$  deposited on Earth constrain the r-process yields of recent nearby supernovae, *Science*, 372, 742. <https://science.sciencemag.org/content/372/6543/742>
- Wanajo, S., Sekiguchi, Y., Nishimura, N., et al. 2014, Production of All the r-process Nuclides in the Dynamical Ejecta of Neutron Star Mergers, *Astrophys. J. Lett.*, 789, L39. <http://stacks.iop.org/2041-8205/789/i=2/a=L39>
- Watson, D., Hansen, C. J., Selsing, J., et al. 2019, Identification of strontium in the merger of two neutron stars, *Nature*, 574, 497

- Waxman, E., Ofek, E. O., & Kushnir, D. 2022, Strong NIR emission following the long duration GRB 211211A: Dust heating as an alternative to a kilonova, arXiv e-prints, arXiv:2206.10710
- Weizmann Kiendrebeogo, R., Farah, A. M., Foley, E. M., et al. 2023, Updated observing scenarios and multi-messenger implications for the International Gravitational-wave Network's O4 and O5, arXiv e-prints, arXiv:2306.09234
- Wilson, J. C., Eikenberry, S. S., Henderson, C. P., et al. 2003, in Society of Photo-Optical Instrumentation Engineers (SPIE) Conference Series, Vol. 4841, Proceedings of the SPIE, ed. M. Iye & A. F. M. Moorwood, 451–458
- Wollaeger, R. T., Korobkin, O., Fontes, C. J., et al. 2018, Impact of ejecta morphology and composition on the electromagnetic signatures of neutron star mergers, *Monthly Notices of the RAS*, 478, 3298
- Woosley, S. E., & Bloom, J. S. 2006, The Supernova Gamma-Ray Burst Connection, *ARA&A*, 44, 507
- Woosley, S. E., Wilson, J. R., Mathews, G. J., Hoffman, R. D., & Meyer, B. S. 1994, The r-Process and Neutrino-heated Supernova Ejecta, *The Astrophysical Journal*, 433, 229
- Wright, E. L., Eisenhardt, P. R. M., Mainzer, A. K., et al. 2010, The Wide-field Infrared Survey Explorer (WISE): Mission Description and Initial On-orbit Performance, *Astron. J.*, 140, 1868. <http://stacks.iop.org/1538-3881/140/i=6/a=1868>
- Wyatt, S. D., Tohuvavohu, A., Arcavi, I., et al. 2020, The Gravitational Wave Treasure Map: A Tool to Coordinate, Visualize, and Assess the Electromagnetic Follow-up of Gravitational-wave Events, *The Astrophysical Journal*, 894, 127
- Xu, F., Huang, Y.-F., & Geng, J.-J. 2023, Possible origin of AT2021any: a failed GRB from a structured jet, arXiv e-prints, arXiv:2304.09051
- Yang, J., Ai, S., Zhang, B.-B., et al. 2022, A long-duration gamma-ray burst with a peculiar origin, *Nature*, 612, 232
- Yang, S., & Sollerman, J. 2023, HAFET: Hybrid Analytic Flux Fitter for Transients, arXiv e-prints, arXiv:2302.02082
- Yao, Y., Miller, A. A., Kulkarni, S. R., et al. 2019, ZTF Early Observations of Type Ia Supernovae. I. Properties of the 2018 Sample, *The Astrophysical Journal*, 886, 152
- Yao, Y., De, K., Kasliwal, M. M., et al. 2020, SN2019dge: a Helium-rich Ultra-Stripped Envelope Supernova, arXiv e-prints, arXiv:2005.12922
- Yong, D., Kobayashi, C., Da Costa, D., Bessell, M., & Chiti, A. 2021, r-Process elements from magnetorotational hypernovae, *Nature*, 595, 223

- Yoon, S.-C., Chun, W., Tolstov, A., Blinnikov, S., & Dessart, L. 2019, Type Ib/Ic Supernovae: Effect of Nickel Mixing on the Early-time Color Evolution and Implications for the Progenitors, *The Astrophysical Journal*, 872, 174
- Yoshii, Y., Tomita, H., Kobayashi, Y., et al. 2003, The Optical/Near-Infrared Light Curves of SN 2002ap for the First 140 Days after Discovery, *The Astrophysical Journal*, 592, 467. <https://doi.org/10.1086/375572>
- Yu, Y.-W., Liu, L.-D., & Dai, Z.-G. 2018, A Long-lived Remnant Neutron Star after GW170817 Inferred from Its Associated Kilonova, *The Astrophysical Journal*, 861, 114
- Yuan, W., Zhang, C., Chen, Y., & Ling, Z. 2022, in *Handbook of X-ray and Gamma-ray Astrophysics*, 86
- Zackay, B., Ofek, E. O., & Gal-Yam, A. 2016, Proper Image Subtraction—Optimal Transient Detection, Photometry, and Hypothesis Testing, *The Astrophysical Journal*, 830, 27
- Zackay, B., Ofek, E. O., & Gal-Yam, A. 2016, PROPER IMAGE SUBTRACTION—OPTIMAL TRANSIENT DETECTION, PHOTOMETRY, AND HYPOTHESIS TESTING, *The Astrophysical Journal*, 830, 27. <http://dx.doi.org/10.3847/0004-637X/830/1/27>

